Surface Functionalisation Effects in Liquid Crystal Nanocomposites

Harry James Litt

University of Leeds

School of Physics and Astronomy

Submitted in accordance with the requirements for the degree of

Doctor of Philosophy

April 2023

The candidate confirms that the work submitted is his own, except where work which has formed part of jointly authored publications has been included. The contribution of the candidate and the other authors to this work has been explicitly indicated below. The candidate confirms that appropriate credit has been given within the thesis where reference has been made to the work of others.

Acknowledgements

Firstly, thank you to my supervisors Prof. Cliff Jones and Dr. Johan Mattsson, without whom, this project would not have been possible. Cliff has been a fantastic supervisor throughout the project and deserves a special thank you for his continual ideas, including the many ”quick-look-see” or ”Friday afternoon” experiments, as well as the motivating discussions and of course for the long hard hours spent poring over this thesis (which unfortunately for him was written in LaTeX rather than Word!). Johan has also been a pleasure to work with, always being available for technical discussions and guidance when needed. Not only did Cliff and Johan enable this work to be undertaken though, but they also made it worthwhile, from both a personal and professional development perspective, even under the unprecedented circumstances of the past few years, for which I am very grateful.

I would also like to thank Dr. Haifa Ojaym and Prof. Georg Mehl from the University of Hull for kindly providing some of the materials used in this work. Additionally, a massive thank you to Dr. Daniel Baker, the Soft Matter Physics group experimental officer for keeping the labs running smoothly and maintaining our equipment, who, without doubt, made my time in the lab considerably easier to navigate and more enjoyable. I would also like to thank a number of other researchers from the Soft Matter Physics group; Dr. Peter Wyatt, Dr. Rowan Morris, Dr. James Bailey and (soon to be Dr.) Tom Moorhouse who all contributed in some form or another to helping perform the experimental work in this thesis and for countless invaluable discussions. Specifically, I would also like to thank several members of the Jones team; Dr. James Bailey for the development of the equipment used in the device fabrication process, as well as Dr. Rowan Morris and Dr. Peter Wyatt for their contribution to the device fabrication process and their continual guidance on both fabrication and characterisation techniques. And of course, thank you to everyone who attended the countless trips to the pub on a Friday night!

None of this though, would have been possible at all, without the network of amazing people around me outside of work. From my friends in Leeds and numerous housemates over the years, making sure I remained sane during this lengthy process. Whether that be joining me climbing or just checking how things were going. To my family for being so supportive over the years, Mum, Dad and Alex, thank you for always being there for me. And last but not least, I'd like to thank Sophie, for seeing me through the worst part of it all, writing up, for that, I will always be incredibly grateful.

COVID-19 and Building Move Impact Statement

The COVID-19 pandemic caused unprecedented disruption to all research degrees, but in particular, experimental projects requiring access to laboratory facilities. The COVID work and travel restrictions imposed from March 2022 had a significant impact on the undertaking of this research project. Between March and September 2020, there was no laboratory access at all, during which period, all work was being undertaken from home. From October 2020 to August 2021, significant disruption to work was still being experienced due to limited access to laboratory facilities as a result of the continued COVID working restrictions. In addition to the COVID working restrictions during this period of time, access to laboratory facilities was again rescinded due to moving buildings between March and August 2021. Thus, essentially a total of five full months of laboratory access was completely lost due to the initial COVID lockdown and an additional four full months of laboratory access was completely lost due to moving buildings, totaling 9 months where absolutely no laboratory work could be performed. On top of this, the additional COVID restrictions between October 2020 and March 2021 where laboratory access was resumed following the initial COVID lockdown prior to moving buildings severely limited progress in this time. Hence, it is fair to say, a total of approximately a full year of experimental time was lost as a result of both the COVID-19 pandemic and moving buildings.

To mitigate the effects of the COVID-19 pandemic, a two month funded extension was granted by the UKRI and to mitigate the effects of the building move, a three month funded extension was provided by the School of Physics and Astronomy. Both of which are greatly appreciated and without them, it would not have been possible to complete this work.

Abstract

Doping of liquid crystal (LC) materials with nanomaterials is of great interest for tuning the optical, dielectric and elastic properties of the LC nanocomposites which are of particular importance for device applications. Additionally, the self-organising nature of LCs can be used to self-assemble nanomaterials into mesoscale structures. This thesis aims to report on the effect that functionalised nanoparticles (NPs) have on the properties of the LC (nanocomposites) and understand how this influences the process of NP self-assembly in the LC host. Sensitive measurements of the LC nanocomposite properties are therefore necessary, particularly at low NP concentrations. Thus, the work presented in this thesis is comprised of two parts. The first describes an investigation of the methodology used to perform accurate dielectric spectroscopy measurements of liquid crystal (LC) materials and subsequent data analysis procedure. The effects of the LC test cell on dielectric spectroscopy measurements of LC materials is found to have a considerable impact on the measured dielectric properties. In particular, for high dielectric anisotropy materials, the thin-film polymeric layers, required to provide homogeneous alignment of the LC are shown to significantly alter the measured permittivities at certain frequencies. An equivalent circuit approach is therefore proposed and used in order to model not only the dielectric spectra obtain using LC test cells, but also correct for the effects of the test cells in order to more accurately determine the properties of the LC.

The second part of the work performed in this thesis is concerned with the characterisation of LC nanocomposites. In particular, quantum dots (QDs) are used as the nano dopant due to their photoluminescence properties. The effect of using different QD surface functionalisation is studied and the influence on the phase behaviour, order and physical properties of the QD-LC nanocomposites directly compared. The phase transition driven QD self-assembly of QD micro-structures is also studied and the process of which, directly related to the surface functionalisation effects on the order and phase behaviour of the nanocomposites. Two different types of surface functionalisation are used in this work. The first is a side-on mesogenic surface functionalisation, where the mesogenic group is attached with the long molecular axis connected tangentially to the surface of the QD by a flexible alkyl linker. This type of surface functionalisation is thought to allow the mesogenic group to freely align with the director of the host LC, therefore reducing the distortion of the director. The second is the alkyl chain, octadecylamine, which is thought to homeotropically anchor the LC and therefore create significant distortion of the director as a result.

Through a combination of studying the phase behaviour and measuring the order parameter, permittivities and elastic constants of the nanocomposites, it is deduced that the mesogenic QD surface functionalisation behaves as expected and the mesogenic group freely aligns with the director of the host LC. The alkyl chain functionalisation, unlike the mesogenic functionalisation, was found to significantly reduce the order parameter and thus also reduce the nematic-isotropic phase transition temperature (T_{NI}) of the nanocomposites compared to the pure LC host. Measurement of the permittivities and elastic constants also confirmed the order preserving nature of the mesogen functionalised QD and the disordering nature of the alkyl chain functionalised QD. The disordering alkyl chain surface functionalisation and the order preserving mesogenic surface functionalisation had a profound effect on the QD self-assembly through the isotropic to nematic phase transition. Using the side-on mesogenic surface functionalisation, 'tubular worm-like' QD networks could be formed, whereas the alkyl chain functionalisation produced 'solid' QD micro-structures. These results confirm the use of side-on mesogen functionalisation of nanomaterials is capable of preserving the order and physical properties of the host LC when forming LC nanocomposites. On the other hand, the alkyl chain functionalisation is actively disordering, thus the phase behaviour and physical properties of the nanocomposites are significantly altered compared to the pure LC.

Further investigation into the dielectric and elastic properties of the QD-LC nanocomposites with consideration of the alignment effects of the different QDs were also performed. The measurement and data analysis methods developed and outlined in the first part of the results in this thesis were used to do so. In agreement with the phase behaviour and order of the mesogen functionalised QD nanocomposites, the elastic constants and permittivities were found to be unchanged compared to the pure LC host. An increase in pretilt with increasing QD concentration in planar aligned LC test cells was found, however. Permittivity measurements of the alkyl chain functionalised QD nanocomposites also agreed with the reduction in order and T_{NI} by showing a decrease in the permittivity parallel to the director and the dielectric anisotropy. Interestingly, however, interpretation of the permittivity-voltage curves, even when accounting for the effect of pretilt did not reveal a reduction in the elastic constants as would be expected due to the reduced order.

Nomenclature

Acronyms and Abbreviations

AL	Alignment Layer
CB	Cyano Biphenyl
CdSe	Cadmium Selenide
CTAB	Cetyltrimethyl ammonium bromide
EP	Electrode Polarisation
GR	Guard Ring
HT	Homeotropic
I	Isotropic Phase
IP	Interfacial Polarisation
IPS	In-Plane Switching
ITO	Indium Tin Oxide
LC	Liquid Crystal
LCD	Liquid Crystal Display
N	Nematic Phase
NP	Nanoparticle
PEDOT:PSS	poly(3,4-ethylenedioxythiophene) polystyrene sulfonate
PH	Planar Homogeneous

QD	Quantum Dot
TBATPB	Tetra butyl ammonium tetra phenyl borate
UV	Ultra-Violet
Vis	Visible
ZBD	Zenithal Bistable Device

Physical Constants

ϵ_0	Permittivity of free space	$8.8541878128 \times 10^{-12}\,\mathrm{F\,m^{-1}}$
$\hbar$	Reduced Planck constant	$6.582119569 \times 10^{-16}\,\mathrm{eVs}$
c	Speed of light in a vacuum	$299\,792\,458\,\mathrm{m\,s^{-1}}$
h	Planck constant	$6.62607015 \times 10^{-34}\,\mathrm{J\,Hz^{-1}}$
K_B	Boltzmann constant	$1.380649 \times 10^{-23}\,\mathrm{J\,K^{-1}}$

Symbols

α	Isotropic Molecular Polarisability
χ	Electric Susceptibility
Δn	Birefringence
$\Delta\epsilon$	Dielectric Anisotropy
ϵ	Dielectric Permittivity
$\epsilon_{\parallel}$	Dielectric Permittivity Parallel to Director
$\epsilon_{\perp}$	Dielectric Permittivity Perpendicular to Director
λ	Wavelength of Light
μ	Dipole Moment
$\mu_{\parallel}$	Dipole Moment parallel to the long molecular axis
$\mu_{\perp}$	Dipole Moment perpendicular to the long molecular axis
ω	Angular frequency

ω_c	Characteristic Angular Frequency
ρ	Density
τ_c	Characteristic Timescale
$\mathbf{E}$	Electric Field Strength
$\mathbf{P}$	Polarisation Density
d	Cell Gap
M	Molar Mass
N	Number of X
n	Refractive Index
N_A	Avogadro's Constant
n_e	Extraordinary Refractive Index
n_o	Ordinary Refractive Index
T	Temperature
T_{NI}	Nematic-Isotropic Phase Transition Temperature
V	Volume
$\mathbf{n}$	Director
S	Scalar Orientational Order Parameter

Contents

List of Figures

List of Tables

Chapter 1

Introduction to Nematic Liquid Crystals and Nanomaterials

This chapter introduces the fundamental physics of Nematic Liquid crystals (NLCs) and nanomaterials required to perform and understand the work carried out for this thesis. The latter part of this chapter will discuss why LC Nanocomposites are of scientific interest, with a discussion of the various types of LC nanocomposites reported elsewhere, such as their properties and applications, as well as how the ordered nature of LCs can be utilised in the self-assembly of nanomaterials within LC nanocomposites.

LC nanocomposites could be useful for a range of different applications, such as improving the performance of LCD technologies to the self-assembly of nanomaterials. Hence, the motivation for this work arises from the need to further understand the behaviour of LC nanocomposites to enable their use in such applications. In particular, it is the role of nanomaterial surface functionalisation that is investigated here, both in terms of how the physical properties of the LC nanocomposites are affected, and how, as a result, this also influences the nanomaterial self-assembly.

1.1 Nematic Liquid Crystals

1.1.1 Liquid Crystallinity

The LC phases also known as mesophases are partially ordered phases of matter that exist between that of a solid crystal with translational/positional order and the disordered state of an isotropic liquid. LC mesophases are therefore fluid-like, but possess some degree of long range orientational order, which leads to their interesting and useful anisotropic properties [1]. The molecules that form such mesophases are known as mesogens. LCs can be split into two categories, thermotropic and lyotropic; the former are mesophases formed through changes in temperature of the mesogens and the latter are mesophases formed both through changes in the concentration of the amphiphilic mesogens in a host solvent. In this work, no lyotropic LCs are used and thus the following will be limited to only thermotropic LCs.

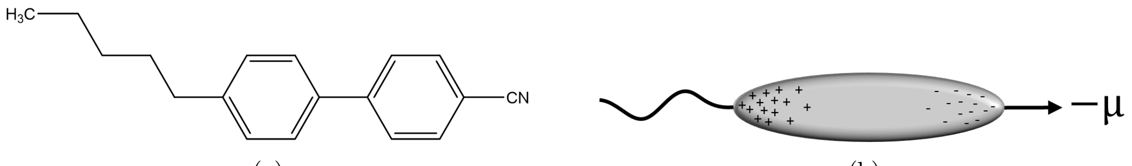

(a) (b)

Figure 1.1: a) Chemical structure of the calamitic nematic mesogen 5CB and b) schematic representation of 5CB.

Thermotropic mesogens are geometrically anisotropic molecules, typically with either a rod-like (calamitic) or disc-like (discotic) shape; both of which can show a range of different mesophases depending on their molecular structure [2]. The most common mesophase is the nematic phase, which will be the focus of this thesis. For a recent review of the history and development of thermotropic nematic mesogens (also known as nematogens) as well as more recent progress in the area, see the article by Goodby and Cowling [3].

The first stable, room temperature nematic phase forming calamitic mesogen, 4-cyano-4’pentylbiphenyl (5CB), which is shown in figure 1.1(a), was first synthesised by G. W. Gray, K. Harrison, and J.A. Nash at the University of Hull in 1972 [4] for use in LC display (LCD) technology and is now probably the most well characterised LC material. The molecular structure consists of two benzene rings (biphenyl group) which make up the rigid rod-like core of the molecule, providing the geometrical anisotropy required to form a mesophase. A cyano group situated on one end of the biphenyl, provides a permanent dipole moment parallel to the long molecular axis of the molecule and an alkyl chain on the other end of biphenyl group influences the mesophase formation and transition temperature, depending on its length.

Nematic phase forming mesogens also form a crystalline solid at low enough temperatures, which not only posses, long range orientational order, but also long range positional order of the mesogens, as a crystalline lattice structure is formed, see figure 1.2. The temperature at which the phase transition between the crystalline solid (X) and nematic liquid crystal (N) phases takes place is the crystal to nematic phase transition temperature (T_{XN}). The temperature at which the nematic phase transitions into the isotropic liquid (I) phase is the nematic to isotropic phase transition temperature (T_{NI}). Both of these phase transitions are typically first order, meaning a discontinuity in the first derivative of the free energy occurs at the transition. It should be noted, however, that not only can the crystalline solid phase be formed on cooling from the nematic or isotropic phase, but also a glassy state can be formed if the mesogens are quenched (cooled rapidly enough) so that they are unable to arrange into a periodic lattice structure, but are instead randomly positioned in space with the orientatrional order of the nematic phase retained but the mesogens are stuck and can no longer flow as they did in the nematic liquid phase.

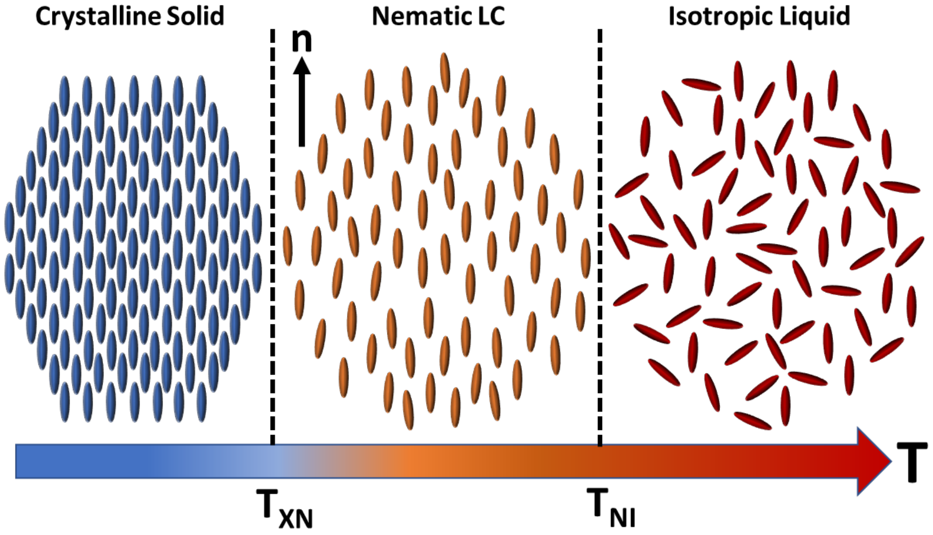

Figure 1.2: Schematic representation of the arrangement of thermotropic mesogens with their corresponding phase changes on heating from crystalline solid to isotropic liquid with the nematic liquid crystal phase between the two.

1.1.2 Order in Nematic Liquid Crystals

In the nematic phase, the average direction in which the long molecular axes are aligned is defined as the orientational director **n** as shown in figure 1.2; which is defined as a pseudo-vector which varies in both space **r** and time t:

$$\mathbf{n} = n(\mathbf{r}, t) = -\mathbf{n}. \tag{1.1}$$

It should be noted, however, that in addition to the cylindrical symmetry of the nematic phase, the distinction between **n** and−**n** is not possible due to the lack of net polarity within the nematic phase; mesogens with net dipole moments arrange in an 'up'/'down' fashion [1].

Due to molecular fluctuations, not all mesogens will be perfectly aligned with **n** at any given time but will instead be oriented with the long molecular axis at some angle θ to **n** [5]. To describe the probability of a mesogen being oriented at an angle θ to **n** the orientational distribution function is used [6, 7]:

$$p(\theta) = \sum_{l(even)} \left(\frac{2l+1}{2} < P_l cos\theta > P_l cos\theta \right). \tag{1.2}$$

For a uniaxial calamitic nematic, an appropriate approximation can be made to give the scalar order parameter S:

$$S \approx < P_2 > = \frac{1}{2} < 3cos^2\theta - 1 > . \tag{1.3}$$

In the case $< cos^2\theta > = 1/3$, $S = 0$, which indicates a complete loss of orientational order, as one would expect to see in the isotropic phase. When $S = 1$, $< cos^2\theta > = 1$ and therefore $\theta = 0°$, meaning that the long molecular axes of all mesogens are perfectly aligned with one another which one would expect to see in the crystalline solid phase at $T = 0K$. Between these two states within the nematic phase range, S follows an approximate temperature dependence of [8]:

$$S = \left(1 - \frac{T}{T^*}\right)^{\beta}, \tag{1.4}$$

where T^* is a temperature slightly above T_{NI} (typically $1°C$ higher), and β is a material dependent value ($\beta \sim 0.2$) [8]. Of course, equation 1.4 gives a continuous reduction of S from $T = 0K$ where $S = 1$ to $T = T^*$ where $S = 0$, whereas in reality, experiments do not show this same temperature dependence across the full temperature range, but instead the first order transitions at T_{XN} and T_{NI} create the discontinuities seen in S. Experiments have shown that S at T_{XN} jumps from $S_{XN} \sim 0.65$ in the nematic phase to $S \sim 1$ in the crystalline solid phase at the transition, and similarly at T_{NI}, a jump between $S = 0$ and $S \sim 0.35$ [9, 10].

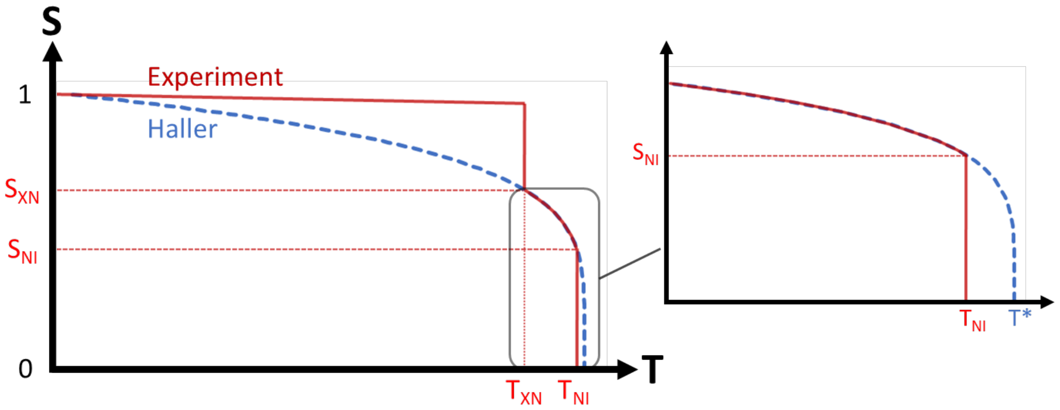

Figure 1.3: Temperature (T) dependence of orientational order parameter (S) using equation 1.4 to plot the blue dashed line for a typical NLC such as 5CB. The solid red lines show the experimentally observed order parameter with the discontinuities in S observed at the first order phase transitions T_{XN} and T_{NI} shown with the dashed red lines.

Maier-Saupe theory predicts this weakly first order transition, from isotropic to nematic and subsequently the jump in S seen at T_{NI}. The nematic free energy F, which is derived from the long range interactions between hard rods using a mean field approach with cylindrical symmetry, whilst neglecting short-range repulsive forces and permanent dipole interactions is [11, 12]:

$$F = -\frac{1}{2}U_0 S^2 + K_B T \int_0^1 f(cos\theta)[lnf(cos\theta)]d(cos\theta), \tag{1.5}$$

where U_0 is the interaction potential of a single molecule, S is the orientational order parameter and θ is the angle between the long molecular axes of the mesogens. The first term in this equation is the contribution to the total free energy from the interaction potential between molecules (i.e. the potential energy term) and the second term in this equation is the entropic contribution which comes from the Boltzmann definition of the orientational entropy. By solving the nematic free energy equation 1.5, a first order transition is predicted at:

$$T_{NI} = 0.22\frac{U_0}{Nk_B}, \tag{1.6}$$

where N is the number density of molecules. The theory also predicts that at this T_{NI}, S jumps from 0 to 0.43, a value slightly above typical nematogens [9].

1.1.3 Elasticity in Nematic Liquid Crystals

1.1.3.1 Nematic Continuum Theory

Since the nematic phase behaves as a fluid, there are no elastic restoring forces opposing the application of any linear stresses such as those found in Hookean solids. However, elastic restoring forces do arise upon the application of torsional and bending stresses, which cause changes in the director orientation through the sample. The nature and magnitude of these restoring forces is dependant upon the type of deformation and the properties of the LC material. The deformation of an LC is described by the 3x3 curvature strain tensor $\left[\frac{dn}{dx}\right]_{ij}$, which for a system with cylindrical symmetry about the z axis i.e. an achiral nematic phase with the director parallel to the z axis, this gives six non-zero curvature strains for splay (s_i), twist (t_i) and bend (b_i), which are depicted in figure 1.4.

$$s_x = \frac{\partial n_x}{\partial x}; \qquad s_y = \frac{\partial n_y}{\partial y} \tag{1.7a}$$

$$t_x = \frac{\partial n_x}{\partial y}; \qquad t_y = \frac{\partial n_y}{\partial x} \tag{1.7b}$$

$$b_x = \frac{\partial n_x}{\partial z}; \qquad b_y = \frac{\partial n_y}{\partial z}. \tag{1.7c}$$

To describe the restoring forces to these deformations, the orientational equivalent of Hooke's law can be used, which requires the 6x6 symmetrical elastic strain tensor K_{ij}. The individual components of this tensor represent the strength and direction of the restoring forces characteristic of the specific material. The diagonal components, K_{11}, K_{22} and K_{33}, correspond to the splay twist and bend deformations respectively. For most calamitic NLCs, these elastic constants are on the order of pN and $K_{33} > K_{11} > K_{22}$, as is the case for 5CB [13]. By considering the symmetry of the system in the achiral calamitic NLC case, Frank formulated an expression for the nematic free energy [14, 15]:

$$\begin{aligned} F = \int_V \frac{1}{2}\Big[K_{11}(\nabla\cdot\mathbf{n})^2 + K_{22}(\mathbf{n}\cdot\nabla\times\mathbf{n})^2 + K_{33}(\mathbf{n}\times\nabla\times\mathbf{n})^2\Big] \\ -(K_{22}+K_{24})\Big[(\nabla\cdot\mathbf{n})^2 + (\nabla\times\mathbf{n})^2 - \nabla\mathbf{n}\cdot\nabla\mathbf{n}\Big]dV, \end{aligned} \tag{1.8}$$

where K_{24} is the saddle-splay elastic constant which describes the resistance to deformation to curvature in two, orthogonal directions. To describe the free energy including the interactions of the LC at a surface, which becomes important in device applications where thin films of materials which anchor the mesogens in specific orientations are used. Nehring and Saupe introduced a number of higher order curvature strain terms ($\frac{\partial^2 n_x}{\partial x \partial z}$ and $\frac{\partial^2 n_y}{\partial x \partial z}$) to the free energy. Using the same symmetry arguments as those used to obtain equation 1.8 the free energy can be split into two components, a volume and a surface integral, which are associated with the free energy of the bulk F_{Bulk} and the surface respectively $F_{Surface}$ [16]:

$$F = F_{Bulk} + F_{Surface}, \tag{1.9a}$$

where:

$$F_{Bulk} = \int_V \frac{1}{2}\Big[K_{11}(\nabla \cdot \mathbf{n})^2 + K_{22}(\mathbf{n} \cdot \nabla \times \mathbf{n})^2 + K_{33}(\mathbf{n} \times \nabla \times \mathbf{n})^2\Big] dV, \tag{1.9b}$$

and

$$F_{Surface} = \int_S \Big[K_{13}(S \cdot \mathbf{n})(\nabla \cdot \mathbf{n}) - K_{24} S\Big((\mathbf{n} \cdot \nabla \mathbf{n}) + (\mathbf{n} \times \nabla \times \mathbf{n})\Big)\Big] dS, \tag{1.9c}$$

where K_{13} is the splay-bend elastic constant. It is common to consider just the K_{11}, K_{22} and K_{33} elastic constants, thus just the expression for F_{Bulk} is used to describe the free energy of the system. K_{13} and K_{24} can be subsumed into the surface anchoring energy $F_{Surface}$, which in the case of defect formation has a significant contribution to the overall free energy.

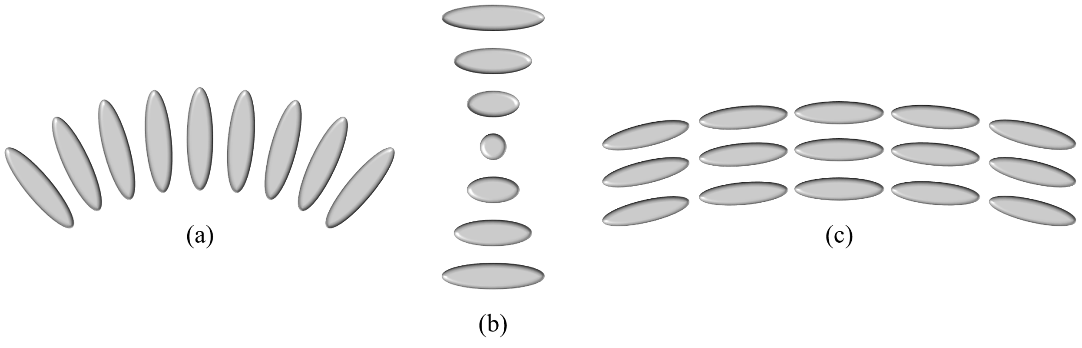

Figure 1.4: Schematic showing the three main forms of deformation for a calamitic nematic LC, a) splay (K_{11}), b) twist (K_{22}) and c) bend (K_{33}).

1.1.3.2 Nematic Defects

Nematic defects arise when the elastic distortion is so great that the free energy of the system is minimised by creating a region of localised disorder, where the orientational order changes discontinuosly between the bulk LC and the defect. Defects can form as points, lines or sheets depending on the LC phase, director profile and sample geometry. The type of defect formed depends on the orientation of the director around the defect, or vice versa, the director profile can depend on the type of defect formed. For the simple case of a line defect, also known as a disclination, and assuming that the splay twist and bend elastic constants are the only non-zero components of the elastic tensor, which can be approximated by a single valued elastic constant $K = K_{11} = K_{22} = K_{33}$ [17]. The free energy per unit volume can be defined as:

$$F_V = \frac{1}{2}K\left[\left(\frac{\partial\theta}{\partial x}\right)_y^2 + \left(\frac{\partial\theta}{\partial y}\right)_x^2\right]. \tag{1.10}$$

Integrating across the x-y plane, an expression for the free energy per unit length is obtained. Using calculus of variations to minimise equation 1.10, an expression for the two dimensional director profile around the disclination, centred at the origin and running parallel to the plane normal can be written as:

$$\theta(x,y) = \theta_0(x,y) + \alpha\eta(x,y), \tag{1.11}$$

where $\alpha \ll 1$. Differentiating equation 1.11 with respect to x and y, then substituting into equation 1.10 and then differentiating again but with respect to α, the rate of change of the free energy per unit length with α can be found:

$$\frac{\partial F_L}{\partial\alpha} = K\int\int\left[\left(\frac{\partial\eta}{\partial x}\right)\left(\frac{\partial\theta}{\partial x}\right) + \left(\frac{\partial\eta}{\partial y}\right)\left(\frac{\partial\theta}{\partial y}\right)\right]. \tag{1.12}$$

Setting this equal to 0 and integrating by parts gives the Laplace equation in two dimensions:

$$\left(\frac{\partial^2\theta}{\partial x^2}\right) + \left(\frac{\partial^2\theta}{\partial y^2}\right) = 0, \tag{1.13a}$$

$$\left(\frac{\partial^2\theta}{\partial\rho^2}\right) + \frac{1}{\rho}\left(\frac{\partial\theta}{\partial\rho}\right) + \frac{1}{\rho^2}\left(\frac{\partial^2\theta}{\partial\phi^2}\right) = 0. \tag{1.13b}$$

This can also be written in cylindrical coordinates (as shown in equation 1.13b), where $\theta(\rho,\phi)$, which has a solution describing the director orientation around the disclination:

$$\theta(\phi) = m\phi + \theta_0, \tag{1.14}$$

where m and θ_0 are constants, the former of which must only take the values of $m = \pm\frac{1}{2}$, ± 1, $\pm\frac{3}{2}$, etc. because θ must change by a multiple of π through a full rotation around the

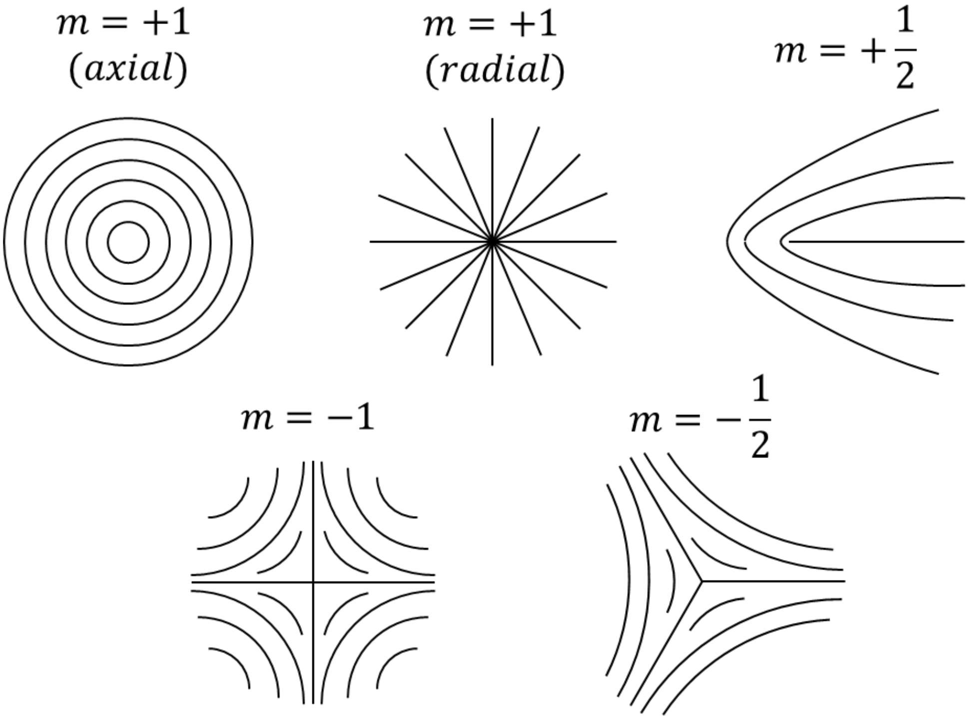

Figure 1.5: Schematic diagram showing several different types of LC defects.

disclination (when ϕ changes by 2π). This is due to $\mathbf{n}$ being able to point in either of two directions. The strength of the disclination m, gives the direction and rate at which $\mathbf{n}$ rotates when traversing around the disclination. If a counter-clockwise path is traversed around the disclination, $\mathbf{n}$ will also rotate in a counter clockwise direction provided m is positive and vice versa when m is negative. The free energy per unit volume in cylindrical coordinates is:

$$F_V = \frac{1}{2}\left[\left(\frac{\partial\theta}{\partial\rho}\right)^2 + \frac{1}{\rho^2}\left(\frac{\partial\theta}{\partial\phi}\right)^2\right]. \tag{1.15}$$

Thus, using 1.14 substituted into 1.15, the free energy per unit volume is therefore:

$$F_V = \frac{1}{2}K\frac{m^2}{\rho^2}, \tag{1.16}$$

and the free energy per unit length in cylindrical coordinates is:

$$F_L = \pi K m^2 \ln\left(\frac{\rho_2}{\rho_1}\right). \tag{1.17}$$

1.1.4 Dielectric Properties of Nematic Liquid Crystals

This section will discuss the dielectric properties of NLCs which are of particular importance for any electro-optic applications. Firstly, a general background to dielectric materials and their interaction with electric fields is given. This is then followed by a description of the behaviour of isotropic molecular dielectric liquids, and finally, the effects of anisotropy in molecular dielectric liquids such as NLCs will be covered.

1.1.4.1 Isotropic Dielectric Media in Static Fields

Dielectric media/dielectric materials, are materials which become polarised under an applied electric field. This means they are able to store electrical energy, unlike a conductive material, which will conduct/dissipate electrical energy. The polarisation in dielectric media arises from bound charges which become displaced, forming dipole moments; these may be permanent, instantaneously induced, or both, depending on the (molecular) structure of the material. The polarisation density $\mathbf{P}$ induced in a dielectric medium is related to the number of individual dipole moments $\mathbf{p}$ enclosed by the volume V and the applied field $\mathbf{E}$:

$$\mathbf{P} = \frac{d\mathbf{p}}{dV} = \frac{dq_b}{dV}\mathbf{l} = \epsilon_0 \chi \mathbf{E}, \tag{1.18}$$

where q_b is the bound charge that is displaced by the distance $\mathbf{l}$, the displacement vector in the volume V, ϵ_0 is the permittivity of free space and χ is the electric susceptibility which is related to the total dielectric permittivity ϵ_t and relative permittivity ϵ_r:

$$\epsilon_t = \epsilon_r \epsilon_0 = (1+\chi)\epsilon_0. \tag{1.19}$$

The electric displacement field $\mathbf{D}$ in the dielectric medium is the sum of the polarisation density $\mathbf{P}$, arising from induced/permanent dipoles and the applied electric field $\mathbf{E}$:

$$\mathbf{D} = \mathbf{P} + \epsilon_0 \mathbf{E} = \epsilon_t \mathbf{E}. \tag{1.20}$$

For molecules with a permanent dipole moment μ which orient with the field, the total polarisation density within the material can be written as the sum of the permanent $\mathbf{P}_p$ and induced $\mathbf{P}_i$ dipole moments:

$$\mathbf{P} = \mathbf{P}_p + \mathbf{P}_i = \frac{N}{V} < \boldsymbol{\mu} > + \frac{N}{V}\alpha \mathbf{E}, \tag{1.21}$$

where N is the number of molecules/dipole moments in the volume V and α is the isotropic molecular polarisability. From Boltzmann statistics, it is known that:

$$<\boldsymbol{\mu}>=\frac{\mu^2}{3K_BT}\mathbf{E}, \tag{1.22}$$

where μ is the magnitude of the dipole moment. Thus, equation 1.21 becomes:

$$\mathbf{P}=\left(\frac{\mu^2}{3K_BT}+\alpha\right)\frac{N}{V}\mathbf{E}. \tag{1.23}$$

However, the effect of dipole orientation within a dielectric medium acts to reduce the local electric field within the medium; the dipole causes the surrounding medium to become polarised and the orientation of any dipoles in the surrounding medium are also affected. Thus it is necessary to account for this when considering the strength of the electric field acting on dipoles within the medium. Lorentz proposed a solution to this problem by considering the polarisation of a spherical cavity (Lorentz sphere) and assumed that the electric field due to the sphere $\mathbf{E}_S$ must be proportional to this polarisation, and thus the local electric field strength $\mathbf{E}_L$ is [18]:

$$\mathbf{E}_L=\mathbf{E}+\mathbf{E}_S=\mathbf{E}+\frac{\mathbf{P}_S}{3\epsilon_0}=\frac{\epsilon+2}{3}\mathbf{E}, \tag{1.24}$$

where $\mathbf{P}_S$ is the polarisation of the spherical cavity and $\epsilon=\epsilon_r$ which will be used from now on. By re-writing equation 1.18 in terms of the relative permittivity using 1.19 and equating to 1.23 with corrected local electric field (1.24),

$$\frac{\epsilon-1}{\epsilon+2}=\frac{N}{3V\epsilon_0}\left(\frac{\mu^2}{3K_BT}+\alpha\right)=\frac{\rho N_A}{3M\epsilon_0}\left(\frac{\mu^2}{3K_BT}+\alpha\right), \tag{1.25}$$

where ρ is the density of the dielectric medium, N_A is Avogadro's constant and M is the molar mass. For the case of apolar molecules, equation 1.25 is reduced to the Cluassius-Mossotti equation [19, 20]:

$$\frac{\epsilon-1}{\epsilon+2}=\frac{N\alpha}{3V\epsilon_0}=\frac{\rho N_A\alpha}{3M\epsilon_0}. \tag{1.26}$$

Further considerations of dipole interactions with the surrounding dielectric medium were made by Onsager [21], whereby the enhancement of the permanent dipole moment by the reaction field of the surrounding medium was accounted for. Further discussion of the Onsager reaction field and the implications for the dielectric properties of NLCs will be discussed in due course.

1.1.4.2 Isotropic Dielectric Media in Oscillating Fields

So far only the static case has been considered; when the electric field is constant and does not vary in time. When the field changes in time, as is the case when performing dielectric spectroscopy, where a sinusoidal field is applied across a dielectric medium, the above case becomes more complex.

Different contributions to the polarisation, albeit from permanent or induced dipole moments, each relax at their own characteristic timescale, therefore the total polarisation which consists of the contributions of all of these polarisations will depend on the frequency of the applied field. This occurs, since a finite time is required to either form the dipole moment (induced dipoles) or for the dipole to rotate/orient with the field (permanent dipoles). Thus if the applied electric field $\mathbf{E}$ takes a frequency dependent sinusoidal form, $\mathbf{E}(\omega)$ then it can be seen from equation 1.18 that the polarisation density must do too $\mathbf{P}(\omega)$, and since different dipole moments will relax at different characteristic timescales/frequencies (τ_c/ω_c), then the total frequency dependent polarisation $\mathbf{P}_{total}(\omega)$ can be written as the sum of N polarisations:

$$\mathbf{P}_{total}(\omega) = \Sigma_{n=1}^{N}\mathbf{P}_n(\omega), \tag{1.27}$$

where $\mathbf{P}_n$ are the individual frequency dependent polarisations, and when $\omega >> \omega_{c,n}$ then $\mathbf{P}_n(\omega) \rightarrow 0$. Hence as the frequency of the applied field is increased above the characteristic frequency for a particular polarisation, this polarisation is relaxed and no longer contributes to the total polarisation as it did below this frequency. Meaning that according to equation 1.20, the electric displacement field within the material must be reduced and therefore so too must the pemittivity of the material, thus, the permittivity must take a frequency dependent complex form:

$$\epsilon^*(\omega) = \epsilon'(\omega) + \epsilon''(\omega), \tag{1.28}$$

where $\epsilon'(\omega)$ is the real permittivity, which we have so far been referring to when talking about permittivity in the static case and $\epsilon''(\omega)$ is the imaginary permittivity. $\epsilon'(\omega)$ represents the (reversible) storage of electrical energy within the dielectric medium and $\epsilon''(\omega)$ represents the loss/dissipation of electrical energy, each of which being proportional to the amount of energy stored or dissipated per cycle.

To model the frequency dependence of $\epsilon^*(\omega)$ with a relaxation process at the characteristic

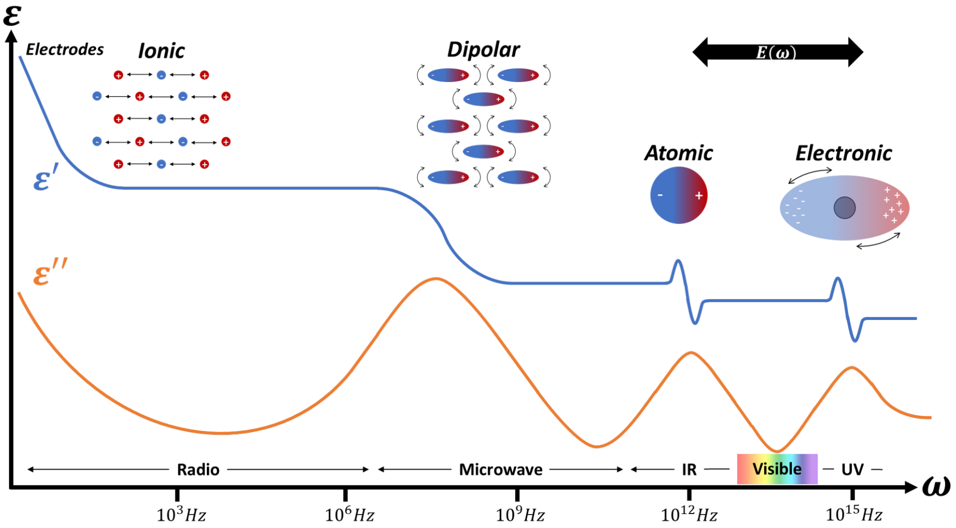

Figure 1.6: Schematic cartoon of typical dielectric spectra showing the different types of dielectric loss/relaxation and their characteristic frequencies. The blue line shows the real ($\epsilon'(\omega)$) and the orange line shows the imaginary ($\epsilon''(\omega)$) part of the complex dielectric functions ($\epsilon^*(\omega)$).

timescale τ_c, the Debeye model of simple harmonic dielectric relaxation can be used [22]:

$$\epsilon^*(\omega) = \epsilon_\infty + \frac{\epsilon_s - \epsilon_\infty}{1 + i\omega\tau_c}, \tag{1.29a}$$

where ϵ_s is the permittivity at the low frequency limit ($\omega << \omega_c$) and ϵ_∞ is the permittivity at the frequency limit ($\omega >> \omega_c$). Splitting into the real and imaginary parts gives:

$$\epsilon'(\omega) = \epsilon_\infty + \frac{\epsilon_s - \epsilon_\infty}{1 + \omega^2\tau_c^2}, \tag{1.29b}$$

$$\epsilon''(\omega) = \frac{(\epsilon_s - \epsilon_\infty)\omega\tau}{1 + \omega^2\tau_c^2}. \tag{1.29c}$$

To account for the broadening of the dielectric relaxation/loss process, the Cole-Cole equation [23] or the Cole-Davidson [24] equations can be used depending on whether this broadening is symmetric or assymmetric respectively. To further generalise the Debye relaxation equation to account for either symmetric or asymmetric broadening, the empirical Havriliak-Negami relaxation equation can be used [25]:

$$\epsilon^*(\omega) = \epsilon_\infty + \frac{\epsilon_s - \epsilon_\infty}{(1 + (i\omega\tau_c)^\alpha)^\beta}, \tag{1.30a}$$

where the exponents α and β describe the asymmetry and broadness of the dielectric loss peak.

Splitting into the real and imaginary parts:

$$\epsilon'(\omega) = \epsilon_\infty + (\epsilon_s - \epsilon_\infty)\bigg(1 + 2(\omega\tau_c)^\alpha cos(\pi\alpha/2) + (\omega\tau_c)^{2\alpha}\bigg)^{-\beta/2} cos(\beta\phi) \tag{1.30b}$$

$$\epsilon'(\omega) = (\epsilon_s - \epsilon_\infty)\bigg(1 + 2(\omega\tau_c)^\alpha cos(\pi\alpha/2) + (\omega\tau_c)^{2\alpha}\bigg)^{-\beta/2} sin(\beta\phi). \tag{1.30c}$$

It should be noted that when $\alpha = 1$, 1.30a reduces to the Cole-Davidson equation, when $\beta = 1$, 1.30a reduces to the Cole-Cole equation, and when both $\alpha = 1$ and $\beta = 1$, equation 1.30a reduces to the Debeye relaxation equation (1.29a).

1.1.4.3 Anisotropy of Dielectric Media - Nematic Liquid Crystals

To understand the dielectric behaviour and response to electric fields of LCs, it is necessary to introduce the effect of anisotropy to the so far discussed properties of dielectric media. Since the nematic phase is cylindrically symmetric around **n**, the dielectric permittivity of the NLC is anisotropic, with two different permittvities, one parallel ($\epsilon_{||}$) and one perpendicular ($\epsilon_\perp$) to **n**. One can then define the dielectric anisotropy as:

$$\Delta\epsilon = \epsilon_{||} - \epsilon_\perp \tag{1.31}$$

Similarly, the microscopic molecular properties of nematogens are anisotropic:

$$\Delta\alpha = \alpha_{||} - \alpha_\perp, \tag{1.32}$$

where $\Delta\alpha$ is the molecular polarisability anisotropy, $\alpha_{||}$ is the molecular polarisability parallel to and $\alpha_\perp$ is the polarisability perpendicular to the long molecular axis. Additionally, the permanent molecular dipole moment, which in the case of 5CB, is created by the electronegative cyanobiphenyl group, can be resolved into its components parallel ($\mu_{||}$) and perpendicular ($\mu_\perp$) to the long molecular axis. Considering these anisotropic properties of NLCs and using the mean field theory developed by Onsager for a dipole in a spherical cavity, Maier and Meier derived expressions for $\epsilon_{||}$and $\epsilon_\perp$, relating to the microscopic anisotropic molecular properties of α and $\boldsymbol{\mu}$ through the orientational order parameter S [12]. The cavity field factor h and the reaction factor f can therefore be written as [26]:

$$h = \frac{3\bar{\epsilon}}{2\bar{\epsilon}+1}, \tag{1.33a}$$

$$f = \frac{2(\bar{\epsilon}+1)}{\epsilon_0(2\bar{\epsilon}+1)}\frac{1}{4\pi a^3}, \tag{1.33b}$$

where $\bar{\epsilon} = \frac{(\epsilon_{||}+2\epsilon_{\perp})}{3}$ is the mean dielectric permittivity and $\Delta\epsilon$ is neglected, which provided $|\epsilon_{||} - \epsilon_{\perp}| << \bar{\epsilon}$ is allowed and the Onsager factor is written as:

$$F = \frac{1}{1-\bar{\alpha}f}, \tag{1.33c}$$

where $\bar{\alpha} = \frac{(\alpha_{||}+2\alpha_{\perp})}{3}$. Using these definitions, Maier and Meier expressed the permittivities of an NLC as:

$$\epsilon_{||} = 1 + \frac{NhF}{\epsilon_0}\left(\bar{\alpha} + \frac{2}{3}\Delta\alpha S + \frac{F}{3k_BT}\left[\mu_{||}^2(1+2S) + \mu_{\perp}^2(1-S)\right]\right), \tag{1.34a}$$

$$\epsilon_{\perp} = 1 + \frac{NhF}{\epsilon_0}\left(\bar{\alpha} - \frac{1}{3}\Delta\alpha S + \frac{F}{3k_BT}\left[\mu_{||}^2(1-S) + \mu_{\perp}^2(1+\frac{1}{2}S)\right]\right), \tag{1.34b}$$

$$\Delta\epsilon = \frac{NhF}{\epsilon_0}\left(\Delta\alpha S + \frac{F}{3k_BT}\left[\mu_{||}^2 - \frac{1}{2}\mu_{\perp}^2\right]\right), \tag{1.34c}$$

$$\bar{\epsilon} = 1 + \frac{NhF}{\epsilon_0}\left(\bar{\alpha} + \frac{F\mu^2}{3k_BT}\right). \tag{1.34d}$$

If $\boldsymbol{\mu}$ is oriented at an angle ζ to the long molecular axis, then from equation 1.34c $\mu_{||}^2 - \frac{1}{2}\mu_{\perp}^2 = \frac{\mu^2}{2}(3cos^2\zeta - 1)$ and it can be seen that when $cos^2\zeta = \frac{1}{3} \Rightarrow \zeta \approx 54.7^{\circ}$ then $\mu_{||}^2 = 2\mu_{\perp}^2$and the contribution to $\Delta\epsilon$ is purely due to $\Delta\alpha$. Additionally, if $S = 0$, it can be seen from equations 1.34a and 1.34b that $\epsilon_{||} = \epsilon_{\perp} = 1 + \frac{NhF}{\epsilon_0}\bar{\alpha} \Rightarrow \Delta\epsilon = 0$, as one would expect.

1.1.5 Optics of Nematic Liquid Crystals

1.1.5.1 Refractive Indices

In the previous section, (1.1.4.3), expressions for the dielectric permittivitieis of an NLC in terms of their microscopic anisotropic molecular properties and the order were introduced. Similarly, one can do the same for the refractive indices of an NLC by using the approximation $n^2 \approx \epsilon$ at optical frequencies:

$$n_e^2 = n_{\parallel}^2 = 1 + \frac{NhF}{\epsilon_0}\left(\bar{\alpha} + \frac{2}{3}\Delta\alpha S\right), \tag{1.35a}$$

$$n_o^2 = n_{\perp}^2 = 1 + \frac{NhF}{\epsilon_0}\left(\bar{\alpha} - \frac{1}{3}\Delta\alpha S\right), \tag{1.35b}$$

$$\Delta n = \frac{NhF}{\epsilon_0}\Delta\alpha, \tag{1.35c}$$

$$\bar{n}^2 = 1 + \frac{NhF}{\epsilon_0}\Delta\alpha. \tag{1.35d}$$

where n_o is the ordinary and n_e is extraordinary refractive index. Note that to obtain 1.35a 1.35b, the dipole parts of 1.34a and 1.34b have been neglected, since at optical frequencies, dipole reorientations are fully relaxed (1.6). The anisotropy in the refractive indices, also known as the birefringence is defined in the same way as $\Delta\epsilon$ in 1.31:

$$\Delta n = n_e - n_o, \tag{1.36}$$

and again, similarly to $\bar{\epsilon}$ the average refractive index is defined as:

$$\bar{n} = \frac{(n_e + 2n_o)}{3}. \tag{1.37}$$

Since density is linear with temperature, one predicts $\bar{n}$ to be also linear and continuous from the isotropic phase. From equations 1.35a and1.35b, the Vuks equation can be found [27, 28]:

$$\frac{n_e^2 - n_o^2}{\bar{n^2} - 1} = \frac{\Delta\alpha}{\bar{\alpha}}S, \tag{1.38}$$

where $\bar{n^2}$ is the mean square refractive index, defined in the same way as $\bar{n}$ (1.37) but with the square of n_e and n_o. Thus, the macroscopic refractive indices are related to the microscopic molecular polarisabilities through the order parameter. Haller utilised this relationship along with equation 1.4 to find [8]:

$$log\left(\frac{n_e^2 - n_o^2}{\bar{n^2} - 1}\right) = log\left(\frac{\Delta\alpha}{\bar{\alpha}}\right) + \beta log\left(1 - \frac{T}{T^*}\right). \tag{1.39}$$

By measuring n_e and n_o as a function of temperature, this enables a straight line extrapolation of $log\left(\frac{n_e^2-n_o^2}{\bar{n^2}-1}\right)$ against $log\left(1-\frac{T}{T^*}\right)$ to find both the intercept with the y-axis at $log\left(\frac{\Delta\alpha}{\bar{\alpha}}\right)$ and the gradient β. Where T^* is typically a °C above T_{NI} (as mentioned earlier in section 1.1.2) and is related by $T^* = T_{NI}/\gamma$, where typically $\gamma = 0.98$. Hence $S(T)$ can be calculated from $n_e(T)$ and $n_o(T)$, which will be used in later chapters.

1.1.5.2 Interaction With Polarised Light

When polarised light is incident on a birefringent medium, the polarisation state of the light is changed provided that the optic axis of the medium is not oriented either parallel to the direction of propagation, or in the case of linearly polarised light, oriented such that the optic axis is parallel to the polarisation direction.

Any plane wave of light can be resolved into two orthogonal components describing the polarisation state of the light in terms of the electric field components in the x and y directions propagating in the z direction:

$$\mathbf{E} = \begin{pmatrix} E_x \\ E_y \end{pmatrix} = \begin{pmatrix} A_x e^{-i(\omega t + \delta_x)} \\ A_y e^{-i(\omega t + \delta_y)} \end{pmatrix}, \tag{1.40}$$

where A_j are the amplitudes in the x and y directions, ω is the frequency and δ_j is the phase, which is related to the wavelength and refractive index:

$$\delta_j = \frac{2\pi n_j d}{\lambda}, \tag{1.41}$$

where n_j is the effective refractive index in either the x or y direction which depends on the orientation of the birefringent slab and d is the thickness of the slab. Thus the maximum phase difference $(\delta_y - \delta_x)$, for an NLC when n_o and n_e are aligned parallel to the x and y directions respectively, can be written as:

$$\Gamma = \frac{2\pi \Delta n d}{\lambda} \tag{1.42}$$

When passing through a linear polariser aligned at an angle ϕ to the x direction, the new polarisation state **E'** can be expressed as:

$$\mathbf{E'} = \mathbf{R}(\phi) \cdot \mathbf{P}_x \cdot \bar{\mathbf{R}}(\phi) \cdot \mathbf{E}, \tag{1.43}$$

where $\mathbf{P}_x$ is the Jones matrix for a linear polariser aligned in the x direction, $\mathbf{R}(\phi)$ is the rotation matrix and $\bar{\mathbf{R}}(\phi)$ is its transpose:

$$\begin{aligned}
\implies \begin{pmatrix} E'_x \\ E'_y \end{pmatrix} &= \begin{pmatrix} cos\phi & -sin\phi \\ sin\phi & cos\phi \end{pmatrix} \begin{pmatrix} 1 & 0 \\ 0 & 0 \end{pmatrix} \begin{pmatrix} cos\phi & sin\phi \\ -sin\phi & cos\phi \end{pmatrix} \begin{pmatrix} E_x \\ E_y \end{pmatrix} \\
&= \begin{pmatrix} cos^2\phi & cos\phi sin\phi \\ cos\phi sin\phi & sin^2\phi \end{pmatrix} \begin{pmatrix} E_x \\ E_y \end{pmatrix} \\
&= \begin{pmatrix} 1 & 0 \\ 0 & 0 \end{pmatrix} \begin{pmatrix} E_x \\ E_y \end{pmatrix} = \begin{pmatrix} E_x \\ 0 \end{pmatrix} \quad when \quad \phi = 0^\circ \\
&= \begin{pmatrix} 0 & 0 \\ 0 & 1 \end{pmatrix} \begin{pmatrix} E_x \\ E_y \end{pmatrix} = \begin{pmatrix} 0 \\ E_y \end{pmatrix} \quad when \quad \phi = 90^\circ
\end{aligned}$$

which means that for light passing through cross polarisers:

$$\mathbf{E'} = \mathbf{P}_x \cdot \mathbf{E} \cdot \mathbf{P}_y, \tag{1.44}$$

where $\mathbf{P}_y$ is the first polariser aligned in the y direction and $\mathbf{P}_x$ is the analyser aligned with the y direction. Therefore, in the absence of any birefringent media between the polariser and analyser, the analyser will block any light that was transmitted through the first polariser and the transmitted intensity will be 0. The Jones matrix for a birefringent retarder is defined as:

$$\mathbf{M} = \begin{pmatrix} e^{-i\frac{\Gamma}{2}} & 0 \\ 0 & e^{i\frac{\Gamma}{2}} \end{pmatrix} \tag{1.45}$$

Thus for a birefringent slab at an angle θ between two orthogonal polarisers (aligned in x and y directions):

$$\mathbf{E'} = \mathbf{P}_x \cdot \mathbf{R}(\theta) \cdot \bar{\mathbf{R}}(\theta) \cdot \mathbf{P}_y \cdot \mathbf{E} \tag{1.46}$$

$$\begin{aligned}
\implies \begin{pmatrix} E'_x \\ E'_y \end{pmatrix} &= \begin{pmatrix} 1 & 0 \\ 0 & 0 \end{pmatrix} \begin{pmatrix} cos\theta & -sin\theta \\ sin\theta & cos\theta \end{pmatrix} \begin{pmatrix} e^{-i\frac{\Gamma}{2}} & 0 \\ 0 & e^{i\frac{\Gamma}{2}} \end{pmatrix} \begin{pmatrix} cos\theta & sin\theta \\ -sin\theta & cos\theta \end{pmatrix} \begin{pmatrix} 0 & 0 \\ 0 & 1 \end{pmatrix} \begin{pmatrix} E_x \\ E_y \end{pmatrix} \\
&= \begin{pmatrix} cos\theta & -sin\theta \\ 0 & 0 \end{pmatrix} \begin{pmatrix} e^{-i\frac{\Gamma}{2}} & 0 \\ 0 & e^{i\frac{\Gamma}{2}} \end{pmatrix} \begin{pmatrix} E_y sin\theta \\ E_y cos\theta \end{pmatrix} \\
&= E_y cos\theta sin\theta \begin{pmatrix} e^{-i\frac{\Gamma}{2}} - e^{i\frac{\Gamma}{2}} \\ 0 \end{pmatrix} = \begin{pmatrix} -2iE_y cos\theta sin\theta \sin\frac{\Gamma}{2} \\ 0 \end{pmatrix} = \begin{pmatrix} -iE_y sin2\theta \sin\frac{\Gamma}{2} \\ 0 \end{pmatrix}.
\end{aligned}$$

The intensity of transmission is therefore given by:

$$T = |\mathbf{E}| = E_y^2 sin^2 2\theta \sin^2\left(\frac{\pi \Delta n d}{\lambda}\right), \tag{1.47}$$

which shows that independent of λ, T is at a maximum when $\theta = 45°, 135°, 225°, 315°$ and at a minimum when $\theta = 0°, 90°, 180°, 270°$; this is the law of Malus. This describes how the orientation of the optic axis (**n**) in the x-y plane affects the intensity of light transmitted through the analyser. However, to understand what happens when (**n**) no longer lies in the x-y plane, but instead is oriented to some extent into the z direction, then Γ will be affected by a change in the effective birefringence $\Delta n'$.

$$\Delta n' = n_e' - n_o = \frac{n_e n_o}{(n_e^2 cos^2\psi + n_o^2 sin^2\psi)^{\frac{1}{2}}} - n_o, \tag{1.48}$$

where ψ is the angle between **n** and the z axis, which in the case of an LC device would be the angle to the substrate normal. Equation 1.48 shows that as ψ increases, $\Delta n'$ decreases until $\psi = 90°$, at which point $n_e' = n_o$ and $\Delta n' = 0$. Thus the wavelength of light transmitted through the device changes as **n** tilts into the device until $\psi = 90°$ and no light is transmitted at all, which is the basic operating principle of any LCD.

1.1.6 Nematic Liquid Crystal Alignment and Reorientation

1.1.6.1 Alignment

For effective use in device applications, or to perform characterisation of LC materials, it is necessary to control the LC alignment. Homogeneous alignment of LCs can be readily achieved with external electric or magnetic fields applied across the LC. However, to achieve homogeneous alignment in the absence of any applied fields, surface treatment of the glass substrates can be used, whereby the LC molecules interact with the surface in such a way that **n** becomes anchored in a preferred direction of orientation. Further discussion of this kind of surface treatment, the materials typically used and its practical application is given in the following section 1.1.6.1.

A variety of different in-homogeneous director configurations can also be achieved using surface treatment techniques, patterns and surface relief gratings, which can enable the formation of a variety of LC defects. For now, however, it is sufficient to only consider the two simple cases of planar homogeneous (PH) and homeotropic (HT) alignment, shown in figures 1.7(a) and 1.7(b)

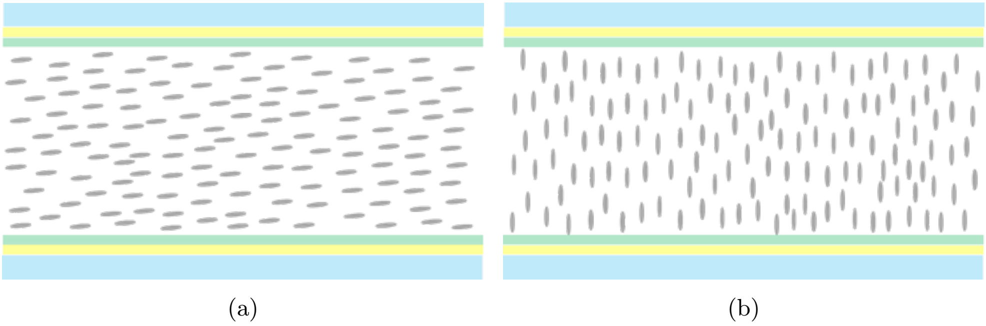
(a) (b)

Figure 1.7: Schematic cartoon of the two most common types of LC alignment used in LC test cells, a) Planar Homogeneous (PH) and b) Homeotropic (HT) alignment.

respectively. When the LC molecules are anchored in the plane of the substrate, this is referred to as PH alignment, although, there is generally some pretilt θ_p associated with this kind of alignment which provides a measure of the out of plane tilt of the LC molecules (typically $\theta_p < 10°$).

The free energy associated with the oriented anchoring of **n** at the substrate surfaces can be expressed as a linear combination of the anchoring energies associated with the anchoring to a specific angle out of the plane θ_p and orientation in the plane ψ_p:

$$\begin{aligned} F_{Anch}(\theta,\psi) &= F_{Anch}(\theta) + F_{Anch}(\psi) \\ &= \int_{\Sigma} \Big(W_\theta sin^2(\theta-\theta_p) + W_\psi sin^2(\psi-\psi_p) \Big) d\Sigma, \end{aligned} \tag{1.49}$$

where W_θ and W_ψ are the anchoring energies associated with the out of plane and in plane anchoring orientations respectively. Typically, the anchoring energies are much larger than the energetic cost of deforming the liquid crystal under applied fields, and hence, even when the bulk LC reorients to minimise the free energy, the LC at the substrate surface will be unaffected.

1.1.6.2 Fréedericksz Transition

The process of director reorientation in homogeneously aligned cells under applied fields is known as the Fréedericksz transition, and is key to the operation of LCDs. Both magnetic and electric field induced Fréedericksz transitions are possible, but here only the latter will be discussed as the use of magnetic fields is generally less practical in comparison to electric fields and less relevant to LCDs. The electric field in an LC cell forming a parallel plate capacitor is

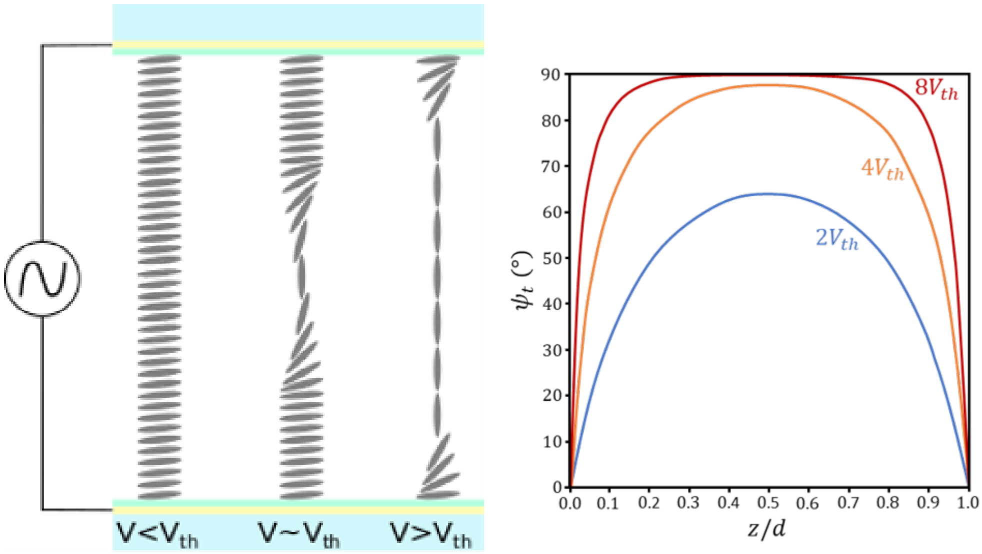

(a) (b)

Figure 1.8: a) Schematic diagram showing the reorientation of the director at various applied voltages relative to V_{th} in an LC cell for a $\Delta\epsilon > 0$ NLC (*Note that the director reorientation depicted here is exaggerated for ease of visualisation). b) Plot of director tilt (ψ_t) measured from the orientation at $V = 0V$ as a function of the normalised depth in the cell (z/d)

.

given by:

$$\mathbf{E} = \frac{\mathbf{V}}{d}, \tag{1.50}$$

where $\mathbf{V}$ is the applied voltage and d is the cell gap; hence for a typical $d \sim 10\mu m$ cell with $1V$ applied across it, then the electric field strength would be $E \sim 100KV/m$. The free energy for an NLC under an applied electric field can be written as the sum of the elastic free energy of the bulk (1.9b) and the electro-static free energy:

$$\begin{aligned} F &= F_{Bulk} + F_{Elec} \\ &= \frac{1}{2}\int_0^d \frac{1}{2}\Big[K_{11}(\nabla\cdot\mathbf{n})^2 + K_{22}(\mathbf{n}\cdot\nabla\times\mathbf{n})^2 + K_{33}(\mathbf{n}\times\nabla\times\mathbf{n})^2 - \epsilon_0\Delta\epsilon(\mathbf{n}\cdot\mathbf{E})^2\Big]dz, \end{aligned} \tag{1.51a}$$

where:

$$F_{Elec} = \frac{1}{2}\int_0^d \Big[-\epsilon_0\Delta\epsilon(\mathbf{n}\cdot\mathbf{E})^2\Big]dz. \tag{1.51b}$$

Hence, from equation 1.51b, it can be seen that for $\Delta\epsilon > 0$, F_{Elec} is at a minimum when $\mathbf{n}$ is parallel to $\mathbf{E}$ and for $\Delta\epsilon > 0$, F_{Elec} is at a minimum when $\mathbf{n}$ is parallel to $\mathbf{E}$. So to minimise the total free energy of the system, the Fréedericksz transition is an interplay between the elastic distortion and the electrostatic forces. This is why below the threshold voltage V_{th} there is no director reorientation at all; the elastic forces are dominant throughout the cell. However, as V is increased to V_{th} and above, director reorientation begins in the central plane of the cell and starts to spread outwards towards the two substrates, as shown schematically in figure 1.8(a). The director tilt angle (from its starting position at $V < V_{th}$) as a function of depth through the cell is plotted in figure 1.8(b) [29].

The threshold voltage V_{th} can be found by solving equation 1.51a for the director configuration through the cell $\psi(z)$ in terms of the voltage applied across the cell [30]:

$$V_{th} = \pi\sqrt{\frac{K_{ii}}{\epsilon_0 \Delta\epsilon}}, \tag{1.52}$$

where $i = 1$ for $\Delta\epsilon > 0$ starting in PH alignment and $i = 3$ for $\Delta\epsilon < 0$ starting in HT alignment.

1.2 Nanomaterials

This section will first cover what nanomaterials are and how they are classified, both by their dimensions and the material they are made from. Following this, the interesting properties of some of these nanomaterials which arises from their nanoscale size are briefly discussed, as well as some possible applications and associated challenges. Finally, the properties of semiconductor nanomaterials, specifically 0D quantum dots (QDs) will be discussed in further detail since these are the specific types of nanomaterials used in this work.

1.2.1 Nanomaterial Classification

Nanomaterials are materials which on at least one dimension are on the nanometer scale (i.e. $<< 1\mu m$). Depending on how many of the dimensions are on the nanoscale and also how similar their dimensions are, they can be categorised as 0D, 1D, 2D, or 3D. 0D nanomaterials have all dimensions on the nanoscale and are of approximately the same size as one another, thus forming quasi-spherical nanoparticles (NPs). 1D nanomaterials have at least two dimensions on the nanoscale, but the third dimension is significantly larger than the other two therefore forming large rod-like or tube-like shapes. 2D nanomaterials on the other hand only have at least one dimension on the nanoscale, but the other two dimensions are significantly larger thus forming disc-like shapes or platelets. 3D nanomaterials are generally formed from organised 0, 1 and/or 2D nanomaterials to form a 3D structure which has features on the nanoscale.

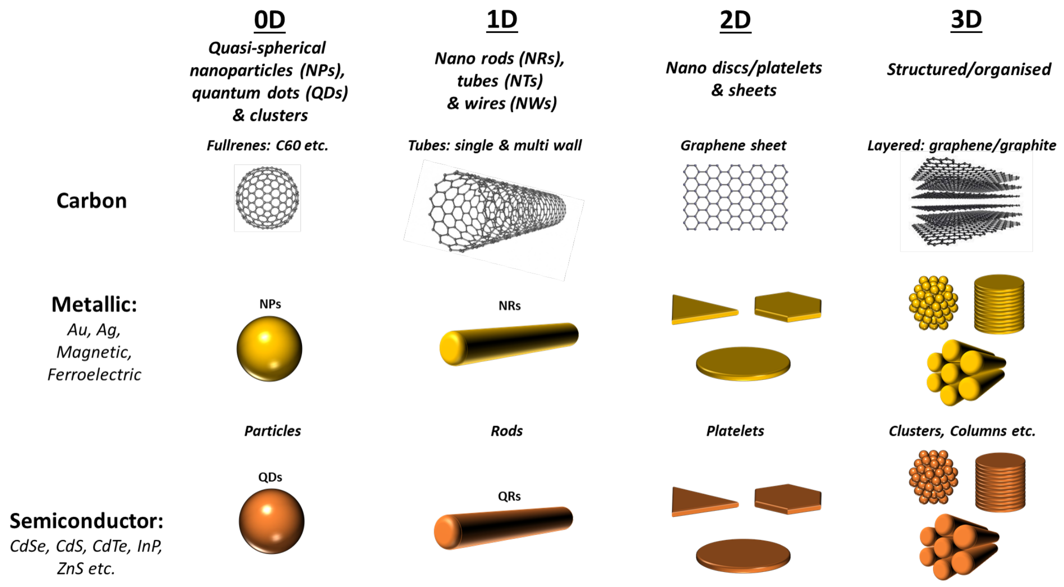

Figure 1.9: Classification of nanomaterials by their dimensions and material.

This classification of nanomaterials by their dimensionality and the material they are made from is shown schematically in Figure 1.9. some of the most commonly used nanomaterials are made from carbon, metallic or semiconductor materials; each of which display their own unique properties and can be used for a variety of different applications.

1.2.2 Nanomaterial Properties and Applications

As already mentioned, the unique properties of nanomaterials depends on both the material they are comprised of and their dimensionality. The dimensionality of the nanomaterial can determine whether the properties are anisotropic or not; for instance, carbon nanotubes show very high conductivities, both thermal ($3kW/mK$) and electrical ($10^6 - 10^7 S/m$) as well as impressive mechanical strength ($0.63TPa$) along the long axis of the tube [31].

Metallic NPs such as gold NPs (AuNPs), exhibit the useful property of surface plasmon resonance (SPR), which is the collective oscillation of the free conduction electrons when interacting with an electric field such as that of visible light. Thus, visible light of a specific wavelength is absorbed by the AuNPs and this wavelength is determined by the size of the AuNPs, with larger sizes absorbing at longer wavelengths [32, 33]. This property of AuNPs, however, is not seen in either the bulk material or AuNPs of smaller sizes ($d < 2nm$). Gold nanorods (AuNRs) still exhibit these same properties that are shown by spherical AuNPs, except, due to the geometrical anisotropy of the AuNRs, the properties parallel and perpendicular to the long axis of the AuNRs differ. Both the absorption wavelength and extinction are affected by the geometry of the AuNRs, thus these anisotropic properties can be tuned through controlling the AuNRs aspect ratio [34].

In addition to the size and geometry of AuNPs and AuNRs, their dielectric environment also affects their plasmonic properties. Primarily this is due to the surface functionalisation, but to some extent also the solvent they are dispersed in and also the presence of other AuNPs/AuNRs in close proximity, thus enabling AuNPs and AuNRs to be used for plasmonic sensing. These properties combined with the low toxicity of AuNPs and AuNRs make them ideal for both diagnostic (labelling, visualisation and imaging, contrast agents, plasmonic sensing etc.) and therapeutic (drug/gene delivery, photothermal and photodynamic therapy) biomedical applications [35, 36].

The organisation of nanomaterials such as NPs, NRs and nanodiscs (NDs) into self-assembled structures is a useful method for bottom up fabrication of nano structured and meta materials [37, 38, 39, 40]. Additionally, similar bottom up fabrication techniques using metallic NPs are commonly used to create surface enhanced raman scattering (SERS) substrates [41], which can enhance the the raman scattering intensity by up to $10^{14} - 10^{15}$ times, enabling the incredible sensitivity required to detect single molecules [42, 43]. Thus, controlling the position and orientation of NPs and NRs is of significant importance for a range of different practical applications in different areas of materials science, nanotechnology and sensing.

1.2.3 Quantum Dots

One class of nanomaterials that has not yet been discussed in detail are 0D quasi-spherical semiconductor NPs also known as quantum dots (QDs). These nanomaterials get their name from the quantum confinement effect that they exhibit due to their geometry. The nm scale in all three dimensions means that the electron hole pairs (excitons) generated in the semiconductor material are confined by the dimensions of the particle; this happens when the dimensions of the semiconductor nanocrystal approach the de Broglie wavelength of the charge carriers.

In bulk semiconductor materials, there exists band like structure of energy levels in which there is a valence band (VB) and conduction band (CB) where there is an energy gap between the two, known as the band gap (E_g). The band gap is a forbidden range of energy states in which no holes or electrons can exist, thus in order for conduction to take place in a semiconductor, an electron must be sufficiently excited to jump to the conduction band, where it can freely conduct, and likewise, the hole that is left behind in the valence band is also able to conduct.

As a result of the quantum confinement effect, discretised energy levels are formed, which can be modelled as a particle with a potential which inside the box and is infinite at the edges of the box:

$$\begin{aligned} V(x,y,z) &= 0 \quad \text{for} \quad 0 < x < L_x \wedge 0 < y < L_y \wedge 0 < z < L_z \\ V(x,y,z) &= \infty \quad \text{for} \quad 0 \geq x \leq L_x \vee 0 \geq y \leq L_y \vee 0 \geq z \leq L_z, \end{aligned} \tag{1.53}$$

where L_x, L_y, L_z are the dimensions of the box in the x, y and z directions. The wavefunction can be written as:

$$\psi_{n_x,n_y,n_z} = \sqrt{\frac{8}{L_x L_y L_z}} sin\left(\frac{n_x \pi x}{L_y}\right) sin\left(\frac{n_y \pi y}{L_y}\right) sin\left(\frac{n_z \pi z}{L_z}\right), \tag{1.54}$$

where n_x, n_y, n_z are the integer energy levels in the x, y and z directions. Thus by solving Schrödinger's equation, the discretised energies of the particle in the box can be found:

$$E_{n_x,n_y,n_z} = \frac{\hbar^2 \pi^2}{2m}\left[\left(\frac{n_x}{L_x}\right)^2 + \left(\frac{n_y}{L_y}\right)^2 + \left(\frac{n_z}{L_z}\right)^2\right], \tag{1.55}$$

where m is the effective mass of the particle and $\hbar$ is the reduced Planck constant. It can be seen then, that due to the inverse square dependence of the particles energy on the dimensions of the box, QD size has a strong influence on the exciton energy levels.

On the nanoscale, where the quantum confinement effects take place, the energies of the CB and VB are shifted, known as band edge shifting, and as a result, the band gap energy is increased at the nanoscale. To model this effect, Brus derived an equation by applying the particle in a sphere model (not a box) to the bulk Wannier Hamiltonian to find the band gap energy in a QD [44, 45]:

$$E_g^{QD} = E_g^{Bulk} + \left(\frac{h^2}{8R^2}\right)\left(\frac{1}{m_e} + \frac{1}{m_h}\right) - \left(\frac{1.8e^2}{4\pi\epsilon_0\epsilon R}\right), \tag{1.56}$$

where E_g^{Bulk} is the bulk semiconductors bandgap, R is the QD radius, m_e and m_h are the effective electron and hole masses and ϵ is the bulk semiconductors materials relative permittivity. It can be seen from the Brus equation (1.56) that E_g^{QD} is a quadratic function in $\frac{1}{R}$, therefore as R increases, E_g^{QD} decreases. This has the implication that when excited with light of sufficient energy to excite electrons to the CB ($h\nu > E_g^{QD}$), then upon relaxation back to the VB, light will be re-emitted with energy $h\nu = E_g^{QD}$. By relating this energy to the wavelength of light through $E = \frac{hc}{\lambda}$, it can be seen that QDs will fluoresce with a wavelength of light that depends on their size, with larger QDs emitting at longer wavelengths as depicted in figure 1.10.

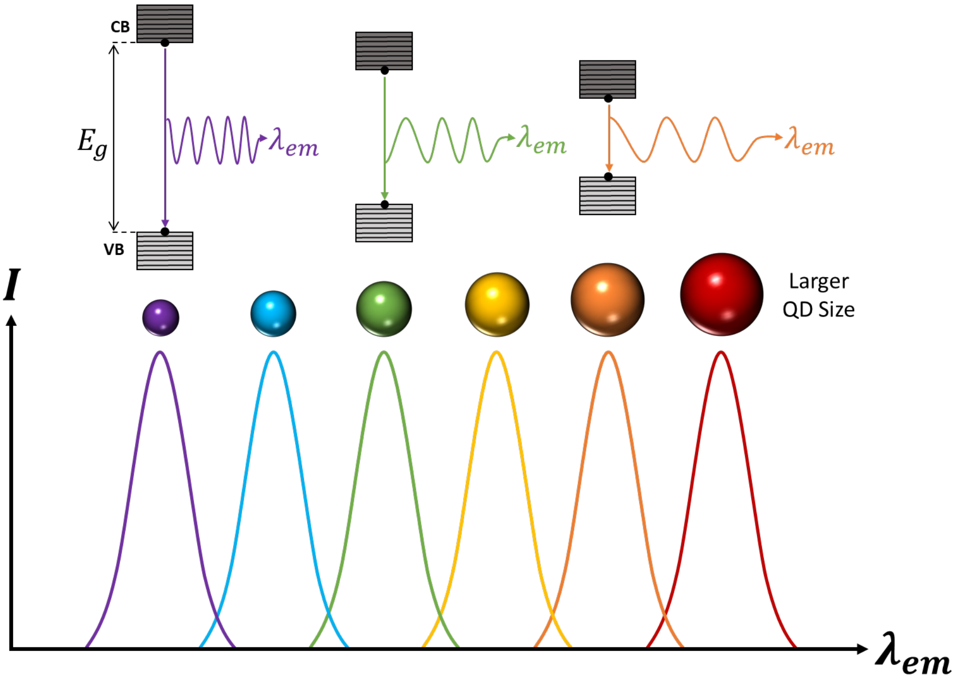

Figure 1.10: Schematic showing changing fluorescence emission spectra with different QD core sizes.

1.3 Liquid Crystal Nanocomposites

Now that the fundamentals of LCs and nanomaterials have been covered, the final section of the introduction will cover the amalgamation of the two: LC nanocomposites. To begin, the various types of nanocomposites will be introduced and categorised, similarly to nanomaterials in the previous section. Following this, the properties and applications of these different LC nanocomposites are discussed, as well as the self-assembly of nanomaterials in LC materials.

The different types of surface functionalisation that have been used in LC nanocomposites will also be discussed, along with their effects on the nanocomposite properties, particle self-assembly and compatibility with the host LC phase; which will help contextualise the following work on QD-LC nanocomposites. For a number of good review articles covering LC nanocomposites including the use of a variety of nano dopants to tune the properties of LCs as well as utilising LC ordering to self-assemble nanomaterials, see references [46, 47, 48, 49, 50, 51, 52, 53, 54].

1.3.1 Types of LC Nanocomposites

An LC nanocomposite is comprised of an LC host material which has been doped with a nanomaterial. There are a plethora of different types of nanocomposites, depending on the type of LC host and nanomaterial used. LC Nanocomposites can therefore be classified in the same way as the pure nanomaterials are classified, except with the addition of the type of LC phase the nanomaterials have been dispersed into.

Generally speaking, there are two ways of perceiving LC nanocomposites, either by the effect that the doped nanomaterials have on the host LC phase or the effect the host LC phase has on the nanomaterials. For instance, nano dopants can be used to tune the physical properties of the host LC, but also, the host LC can be used to self-assemble the nanomaterials and/or alter their properties through the interaction between the nanomaterials and the ordered LC phase. In some circumstances, as will be discussed later in this thesis (Chapter 4), the two are not mutually exclusive; the effect that the nanomaterial has on the LC host can also impact the self-assembly of the nanomaterial by the LC. The material, dimensions and anisotropy of the nano dopants can affect the properties of the LC and the self-assembly, which will be discussed in the following sections.

The primary focus of this work is placed on thermotropic NLC hosts, doped with quasi-spherical NPs, in particular, QDs. However, there will be discussion in this section regarding the use of various types of nanomaterial dopants used in mainly thermotropic NLCs, but also other LC phases too, as this provides a more holistic view of the field as well as generating the context for the work performed.

1.3.2 Surface Functionalisation

It is common to functionalise the surface of nanomaterials so that they can be dissolved or suspended in an appropriate solvent without readily aggregating due to the attractive forces between them. The addition of surface functional groups that are in themselves soluble in the host solvent enables a stable suspension of NPs or other nanomaterials to be formed. This occurs by promoting solvation and inhibiting aggregation by preventing the NP cores from coming in close enough proximity to one another for the attractive forces to become dominant. Thus, to dissolve nanomaterials into organic solvents, an organic surface functionalisation is used, such as alkyl thiols or amines. Conversely, to form an aqueous dispersion, hydrophilic

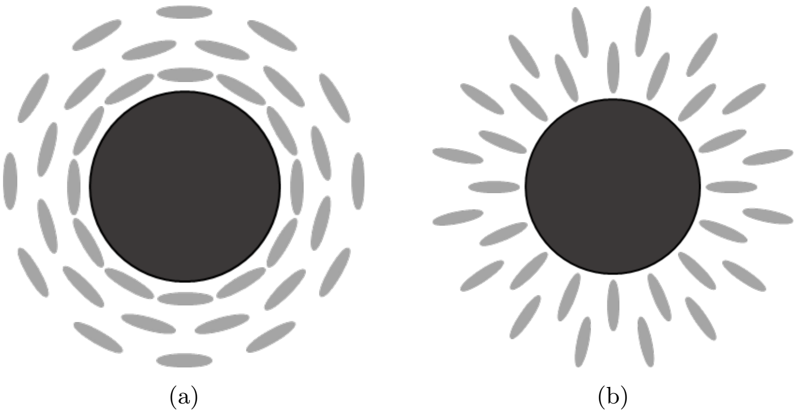
(a) (b)

Figure 1.11: Schematic representation of the two principle anchoring regimes around the 2D cross sections of spherical particles (or a cylindrical particle) in an NLC; a) planar and b) HT anchoring.

surface functionalisation is used, such as polyethyleneglycol or carboxylic acid.

When dispersing nanomaterials into an LC material, however, there is the additional complication of the anisotropic nature of the LC phase. Consider a 2D cross section of a spherical particle (or cylindrical particle) in an NLC host, where the LC molecules are anchored to the surface of the NP in a particular orientation. Figures 1.11(a) and 1.11(b) shows the two principle anchoring conditions (in two dimensions) around a particle in an NLC, planar and homeotropic (HT). These two alignment configurations mean the particles are topologically equivalent to +1 axial and +1 radial (hedeghog) defects.

If the host NLC is homogeneously aligned (as in an aligned LC test cell), this anchoring around the particles create distortions to the director field of the LC, which results in different types of defects/disclinations depending on the size of the particle and the anchoring conditions [55]. In the case of HT anchoring at the particle surface, three possible director configurations around the particle are possible. A hyperbolic hedgehog (figure 1.12(a)) defect, a hyperbolic disclination ring (figure 1.12(b)), or a saturn ring disclination (figure 1.12(c)), [56, 57]. The particle defect pairs behave topologically as a dipole in the case of the hyperbolic hedgehog or hyperbolic ring or as a quadrupole in the case of the Saturn ring defect [58, 56, 59]. In the case of planar anchoring, a pair of +1 boojum defects are formed either side of the particle aligned along the nematic director of the bulk (figure 1.12(d)) [56]. The particle defect pair with this alignment configuration is expected to act as a quadrupole at long ranges [56, 60].

Particles in NLCs forming particle defect pairs interact with one another through long range

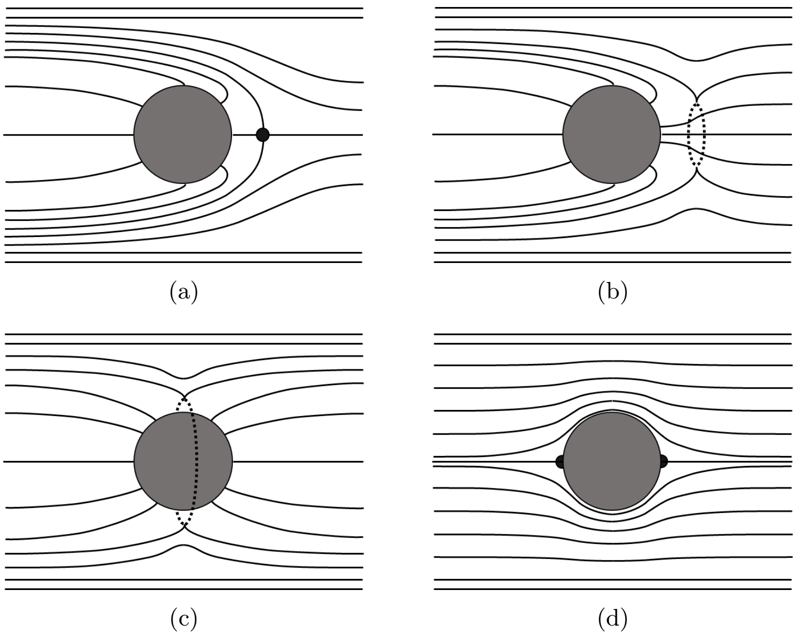

Figure 1.12: Schematic diagram of the various types of defects formed by particles with HT (a, b, c) and Planar (d) anchoring in a homogeneously aligned NLC. Particles forming a topological dipole with a) a hyperbolic hedgehog defect or b) a hyperbolic disclination ring. Particles forming a topological quadrupole with c) a saturn ring defect or d) a pair of boojum defects.

forces. Such interactions between particles can be attractive at long ranges and repulsive at short ranges, leading to the formation of particle chains in homogeneously aligned NLCs [61]. Depending on whether the particle defect pairs behave as dipoles or quadrupoles determines the orientation of these forces relative to the director of the homogeneously aligned bulk NLC [62]. Thus, particle chains may form parallel (for dipolar) or perpendicular (for quadrupolar) to the bulk director depending on the particle size and anchoring conditions [63]. A more detailed discussion of particle self-assembly is given in a following section.

The anchoring conditions at particle surfaces can be controlled using their surface functionalisation. The most commonly used surface functionalisation consisting of a monolayer of alkyl chains such as thiols [64, 65] or amines [66] (see Figure 1.13a)), are known to induce HT anchoring. In attempts to improve the miscibility of NPs in NLCs and subsequently increase the overall nanocomposite stability, a range of mesogenic and promesogenic surface functionalisation have previously been employed [67, 68, 69, 70, 71]. It has been reported that up to $25wt\%$ GNPs with mesogenic functionalisation are completely miscible in the isotropic phase of 5CB [72]. In broad terms, mesogenic/promesogenic surface functionalisation can be categorised either by end on [67], or side on orientation of the mesogens/promesogens [73, 74] (see Figures 1.13b) and 1.13c) respectively), which typically lead to HT or planar anchoring respectively.

To connect the mesogenic moeities to the NP surface, alkyl linkers are used. The length and flexibility of these alkyl linkers can change the anchoring strength; a longer chain enables more movement and reorientation of the mesogen, to the point where a long enough chain could allow the orientation of the mesogens with the hosts director [73]. It is also common for a mixed monolayer of alkyl chains and mesogenic groups to be used as opposed to a purely mesogenic surface functionalisation.

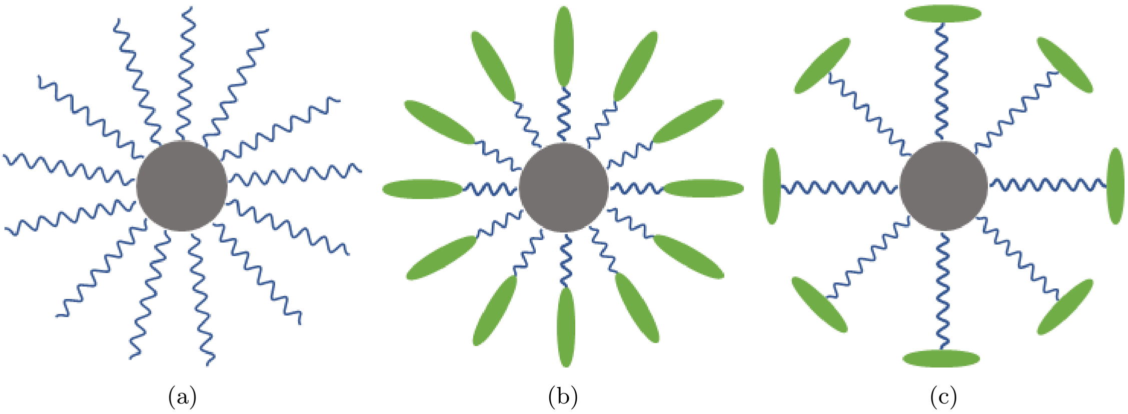
(a) (b) (c)

Figure 1.13: Cartoon showing the different types of typical NP surface functionalisation used for LC nanocomposites. a) Non-mesogenic alkyl chains, b) end on mesogenic and c) side on mesogenic surface functionalisation.

It has been found in some cases, however, that mesogenic surface functionalisation does not always improve the stability of the nanocomposite when compared to alkyl chain surface functionalisation [65]. GNPs functionalised with a mixed monolayer of mesogens (connected end on by dodecanethiol linkers) and either hexane or decanethiol co-ligands, were compared to GNPs functionalised with a homogeneous monolayer of either hexane or decanethiols. It was found that the mesogenic NPs were less miscibile in both 5CB and 8CB than the either of the alky thiol NPs, and interestingly produced uniform HT alignment between untreated glass slides as one would expect from HT NPs, but did not in PH cells, unlike the alkyl thiol NPs. Additionally, the length of the alkyl thiol co-ligands also had an impact on the NP miscibility and aggregation. The shorter chains presumably allow more flexibility and movement of the alkyl linker groups, enabling better reorientation of the mesogens with the host LC, thus improving miscibility and reducing the size of aggregates formed.

Dendritic (end on) promesogenic surface functionalisation of CdS/ZnS QDs has been shown to significantly increase the stability of the QD-LC nanocomposite and prevent QD aggregation, even over the course of a year [67]. It was also found, however, that this was strongly dependent on the use of co-ligands with the appropriate chain length and ratio compared to the promesogenic functional groups. Thus, it is clear that mesogenic and/or promesogenic surface functionalisation (in an end on orientation) can be used to help improve NP miscibility and prevent aggregation in NLCs, but the use of an additional shorter chain co-ligand is essential to do so. It is thought that the short chain co-ligands help to space out the mesogenic/promesogenic groups on the surface, which enables molecules of the host LC to penetrate closer to the NP core as well as allow more motion and fluidity of the mesogenic/promesogenic groups, reducing the disruption to the host director.

1.3.3 Properties and Applications

1.3.3.1 Phase Behaviour

Nanomaterial dopants in NLCs are known to significantly alter the physical properties of the LC as well as the characteristics of LC devices. The mechanism behind most of these alterations varies depending on the type of nanomaterial used and the property of the LC nanocomposite being affected. The LC phase behaviour is often affected by the addition of nanomaterials to the LC, with both increases [75, 76] and reductions [77, 70, 78] of T_{NI} having been reported. It is thought that these increases or reductions in T_{NI} arise from either an enhancement of the nematic ordering or a disordering effect induced by the NPs.

For isotropic quasi-spherical NPs, a disordering effect is not so surprising, particularly if HT anchoring is imposed on the particle surface. An enhancement of nematic ordering from 0D NPs on the other hand seems less likely, and generally arises from an interaction between the material properties of the NP cores and the host LC. For instance, it is believed that when dispersing ferroelectric NPs into an LC, the **E** field created by the spontaneous polarisation of the NPs leads to a local field induced enhancement of the orientational order and hence an increase in T_{NI} [79]. The reduction of T_{NI} seen when doping NLCs with spherical isotropic NPs results from the disordering effect these NPs have on the host; the anchoring conditions at the NP surface create distortions to the host director around the NPs. One would therefore expect this effect to be strongly dependent upon the type of surface functionalisation used on the NPs.

Similarly to ferroelectric NPs, doping LCs with anisotropic nanomaterials such as 1D NRs or NTs can induce additional ordering within the host, resulting in an increase of T_{NI} as has been theoretically predicted [80] and shown experimentally [81]. It should also be noted, a T_{NI} reduction is generally observed for the addition of dopants in LCs due to the 'dilution' effect. The inclusion of isotropic particles within the LC increases the mean distance between the host mesogens, thus reducing the anisotropic interactions between them, thereby reducing the order and phase transition temperature [80].

1.3.3.2 Electro-Optics

Not only does the ordering of LCs affect the phase transitions, but it also affects other macroscopic physical properties such as the permittivities/dielectric anisotropy [82, 83, 76], elastic constants [66, 82], refractive indices/birefringence [76] and also the visco-elastic/switching response times [84, 85, 86]. These alterations and enhancements to the LCs electro-optic properties are of particular interest for display applications. The threshold voltage for a Fréedericksz transition V_{th} in a homogeneously aligned cell (1.52) depends on the dielectric anisotropy $\Delta\epsilon$ and elastic constant K_{ii} of the material. Thus by increasing $\Delta\epsilon$ or by decreasing K_{11} (for $\Delta\epsilon > 0$), V_{th} is reduced. Since $K_{ii} \propto S^2$ and $\Delta\epsilon \propto S$, a reduction in order therefore means that V_{th} is reduced as $V_{th} \propto S^{1/2}$. By doping LCs with isotropic disordering NPs or QDs, the orientational order of the LC nanocomposite can therefore be reduced, which in turn reduces V_{th}. There a numerous reports of isotropic NP or QD doping of NLCs causing a reduction of V_{th} due to this disordering effect [87, 88, 89, 90].

There are, however, very few investigations into this effect, where a reduction in V_{th} has been found but also accompanied by measurements of S. One example of such measurements have been been performed for CdS QD in 5CB where a reduction in V_{th} and T_{NI} was found, measurements of S also showed the same monotonic reduction with increasing QD concentration, although the type of surface functionalisation used was not reported [91].

Quite contradictory results have also been reported [92], where an increase of $\Delta\epsilon$ but decrease of K_{11} was found for alkyl thiol functionalised GNPs in an NLC, and depending on the GNP concentration. Both a reduction (at $0.2wt\%$) or increase (at $0.5wt\%$) of T_{NI} was also reported [92]. Elsewhere [93], doping of an NLC with thiol capped silver NPs was found to reduce T_{NI} for all NP concentrations measures (0.2, 0.5 and $1.0wt\%$) whilst $\Delta\epsilon$, Δn and K_{ii} all increased with increasing NP concentration. In one case, where a reduction of V_{th} was found, an increase in T_{NI} and $\Delta\epsilon$ were attributed to a increase in orientational order, but K_{11} was also reported to be significantly reduced [89].

1.3.3.3 Conductivity

The use of metallic NPs [78] and NRs [94] as well as CNTs [47] have also been shown to increase the conductivity and conductivity anisotropy of LCs. The origin of the increased electrical conductivity is not entirely obvious, since in some cases, it has been reported that NP doping leads to ion trapping by the NPs [95]. In the cases where an increase ion conductivity is reported for isotropic NP doping, it is thought the increase arises from an increase in ionic charge carriers that were initially trapped by the organic surface functionalisation of the NP and released upon solvation by the alkyl chains of the LC host [96]. Thus, one would expect electrode polarisation effects and low frequency dielectric behaviour to be altered by the doping of NPs and for there to be a dependence on the type of surface functionalisation used. This was also shown to be the case by the same authors, who compared the effect of doping LCs with GNPs capped using either a dodecanethiol monolayer or a mesogenic capping agent [97].

1.3.3.4 Alignment

An added complication that must be considered when characterising LC nanocomposites is the alteration of alignment within LC devices. NPs are known to be able to induce alignment changes in addition to altering other properties of the LC, either from the bulk [98], or by segregation to the surfaces [66]. NPs functionalised with either alkyl chains or with mesogens in an end on orientation have been shown to induce uniform HT alignment in LC nanocomposites between plain glass slides [99, 82]. Alkyl chain functionalisation has even been shown to induce HT alignment in PH cells, completely overcoming the anchoring conditions imposed by the ALs on the substrate surfaces [99, 66, 82].

Birefringent stripes formed by twist disclinations at the substrate surfaces have also been reported in these cells with induced HT alignment from the NPs [100, 101]. These alignment effects can be favourable and enable interesting new device applications, such as a dual alignment cell [102]. Ink jet printing of NPs to produce patterned alignment layers has also been employed [103]. However, when trying to determine material properties of LC nanocomposites, these effects must be considered. Depending on where the NPs reside, whether in the bulk or at the surfaces, and how they affect the LC alignment is also an important factor for the reliable determination of the LC nanocomposite properties [104]. For a detailed up to date review of the various approaches to using NP induced LC alignment for display applications and photonic devices, see [105].

1.3.4 Self-Assembly

Particle and nanomaterial self-assembly in LCs is of great interest; the self-organising nature of LCs can be imparted onto the unorganised NPs in range of different ways. As already briefly discussed in 1.3.2, the defects formed around particles in LCs can lead to particle chaining [61, 62, 63]. An obvious way in which the ordered nature of LCs can be used to organise/self-assemble nanomaterials is through the orientation of anisotropic NRs or NTs. Not discussed so far and covered in detail within this section, is the confinement of particles into defects/disclinations and the use of the isotropic-nematic phase transition to self-assemble NP structures.

1.3.4.1 Self-Assembly into Defects

There is a continually extending body of research on the confinement/trapping of particles within defects of various types formed in a variety of LC phases. The electrostatic analogy used to describe the assembly of colloidal particles which was discussed in section 1.3.2, can also be used to describe the interaction between colloidal particles and LC defects, as Pires et al. did when using particle tracking to analyse the motion of colloidal particles in the vicinity of a -1/2 disclination [106].

The -1/2 disclination was formed through surface treatment of the device substrates; polymeric ALs were rubbed in orthogonal directions in neighbouring regions on each of the adjacent substrates, inducing a highly frustrated region at the interface between the different alignment domains. The particles were attracted to the disclination lines and became trapped on them. Using a similar method of patterned rubbing to form disclination lines in an NLC, the same group were able to self-assemble colloidal particles to form a set of 3D micro-wires [107]. Elsewhere it has also been shown that smaller colloidal particles can be self-assembled into the disclinations surrounding larger colloidal particles [108].

It was originally believed that the self-assembly processes described above would only occur for particles of a sufficiently large size, since the smallest particles around which elastic distortions of the director had been exhibited were only approximately $125nm$ in diameter [61]. This has since been contradicted by multiple groups that have been able to show the self-assembly of NPs with diameters as small as $\sim 5nm$ into defects formed by smectic LCs [109, 110]. Coursault et al. used 8CB as the LC host deposited onto MoS_2 substrates as a $300nm$ thick film, which formed a structure with grain boundaries, disclination lines and curvature walls, into which, the GNPs were self-assembled[109].

Polarisation dependent optical extinction spectra of linear Au NPs was used to confirm the formation of linear NP chains. A significant red-shift in the extinction spectra was seen when the incident polarisation was oriented parallel to the length of the curvature walls and disclinations compared to no observed red-shift when the polarisation was oriented in the perpendicular direction. It was also found that the GNPs preferentially resided in the grain boundaries compared to the curvature walls and disclination lines, thus showing that different defect types exhibit different 'trapping efficiencies'. Similarly, Milette et al. also used 8CB as the LC host, but were able to show reversible self-assembly into linear arrays by employing a mesogenic surface functionalisation of the GNPs [110].

Blue phase LCs (BPLCs) are formed in chiral nematic LCs, where chiral nematic domains form what are known as double twist cylinders which have a 90° twisted structure radiating from the centre of the cylinder. Under specific thermodynamic conditions, these cylinders self organise into a lattice structure where disclinations form in the regions between the cylinders. These structures, however, are generally unstable, existing over narrow temperature ranges of $< 1K$. Therefore, methods for stabilising these phases have been explored, such as the dispersion of NPs into the LC [111]. The NPs are thought to become confined to the cores of the lattice disclinations between the double-twist cylinders, which subsequently stabilises the BP over a wider temperature range [112, 113].

The efficacy of NP induced phase stabilisation of BPLCs has been shown through both theoretical predictions and experimental observations to strongly depend on the NP size and surface functionalisation, which determine the tendency of the NP to reside in the disclination cores [114, 115]. The type of surface functionalisation determines the anchoring conditions imposed on the LC, which in turn determines where is energetically most favourable for the NP to reside. The NPs will thus migrate to regions with naturally similar structure to that imposed by the NP. By using a mesogenic NP surface functionalisation, reversible self-assembly into the disclinations of BPLCs has also been shown [116].

Direct observation of the self-assembly of particles into defects is possible by doping the LC

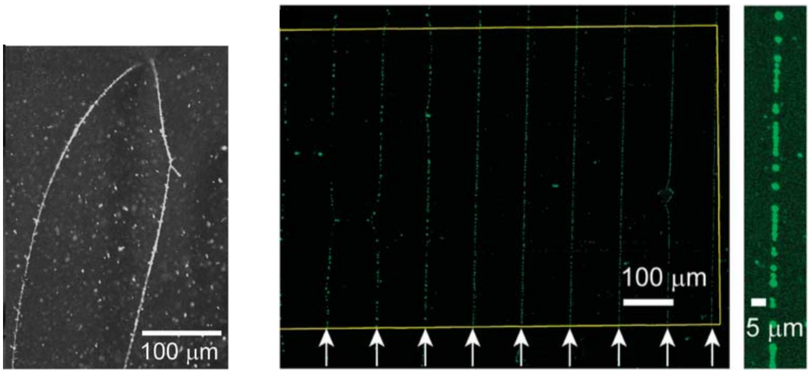

(a) (b)

Figure 1.14: (a) Fluorescence microscopy image of polymer NPs trapped in disclinations. (b) POM image (left) of defect array in wedge cell and fluorescence microscopy image (right) of polymer NPs trapped by a defect [117].

with QDs, or particles functionalised with a fluorescent species. These LC nano/composites can then be filled into an appropriately designed device and the distribution of the fluorescent particles examined through a combination of polarising optical microscopy (POM) and fluorescence microscopy (FM). Using this method, Higashiguchi et al. were able to exhibit the assembly of mesogenic shelled polymer nanoparticles labelled with fluorescent perylene molecules into organised structures [117].

They dispersed the polymer NPs into 5CB and upon cooling from the isotropic to nematic phase, a Schlieren texture was formed, and the polymer NPs became concentrated in the disclinations of strength 1/2 (see figure 1.14(a)). The same procedure was then repeated using a chiral nematic mixture doped with the polymer NPs filled into a Grandjean-Cano wedge cell to form an array of evenly spaced defects, within which, the NPs were confined (figure 1.14(b)). The NPs were observed to move randomly under Brownian motion in the isotropic phase, whereas their motion was directed towards the defects once cooled into the nematic phase and trapping within the defects then resulted in their motion became limited to one dimension along the length of the disclinations.

More recently, similar NP self assembly behaviour using a rather different approach has been demonstrated [118]. A dispersion of fluorescent amphiphiles and silica microparticles in 5CB was filled into a cell with opposing substrates imposing perpendicular LC anchoring to one another, which induce a 90° twist of the director through the cell forming a TN device. A combination of the twisted director orientation and the homeotropic anchoring at the silica microparticle surface, enabled the formation of a single -1/2 disclination loop that ran around and

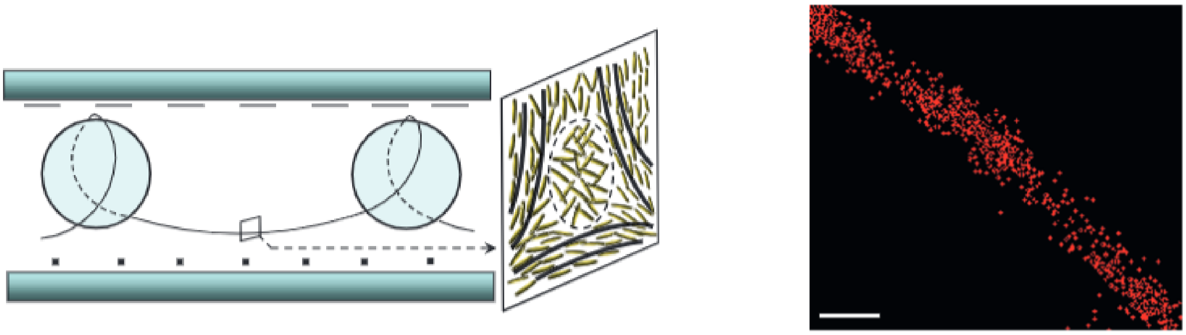
(a)

(b)

Figure 1.15: (a) Schematic illustration of disclination formation between silica microparticles. (b) STORM image of fluorescent amphiphiles trapped in disclination, scale bar 100nm [118]

joined adjacent microparticles (see figure 1.15(a)). By using a boron-dipyrromethene (BODIPY) molecule as the fluorescent label, whose fluorescent properties change upon aggregation, the self assembly into defects could only be seen above a critical concentration of the amphiphiles in the LC. By using cryogenic transmission electron microscopy, the mean diameter of the amphiphile assemblies was found to be $\sim 28nm$. A freely standing polymeric ring was then formed from the polymerisation of the photoreactive amphiphile assemblies.

Since the forces exerted on particles dispersed into an LC depend on the distortion of the local director field around the particle, the type and strength of surface anchoring therefore has a significant impact on the interaction between particles and also the interaction between particles and defects. Evidence for this can be found in the value of the diffusion coefficients for surface functionalised NPs in the isotropic phase of 5CB [119]. The diffusion coefficients were found to change by a factor of up to 1.5 as a result of different chemical surface modifications to the NPs causing different anchoring conditions of the LC at the NP surface. This is a result that is again supported by theoretical predictions which show a dependence of the diffusion coefficient on surface anchoring conditions[120][121]. Other experimental studies on the interaction of 125nm silica particles surface functionalised with N,N-dimethyl-N-octadecyl-3-aminopropyl trimethoxysilyl chloride (DMOAP) dispersed into 5CB, have shown that such particles behave effectively, as much larger particles; which is due to the strong anchoring of the LC imposed by DMOAP layer causing significantly greater distortion of the director field around them [122].

1.3.4.2 Phase Transition Driven Self-Assembly

Another method of self-assembling nanomaterials in LCs utilises the isotropic-nematic phase transition. Consider an NLC in the isotropic phase with a sufficiently large concentration of NPs homogeneously dispersed within it. On cooling, regions of nematic phase begin to nucleate and grow. The NPs, which are initially homogeneously dispersed through the entire sample in the isotropic phase, migrate out of the nematic domains into the remaining isotropic regions as the nematic domains grow. This process of enrichment of NPs in the isotropic regions with controlled cooling can be used to template meso-scale NP structures. This process can also be reversible, thus after the initial cooling from the isotropic to nematic phase, on re-heating to the isotropic phase again, the NPs can once again form a homogeneous dispersion in the isotropic phase.

This process of NP self-assembly which has been termed 'phase transition templating' relies on this partial miscibility of the NPs between the nematic and isotropic phases, culminating in the coexistence of a NP rich isotropic phase and NP poor nematic phase. This phase separation process has been predicted theoretically for spherical NPs dispersed into an NLC using a mean-field approach by Osipov and Gorkunov [123]. The molecular theory predicts some interesting effects depending on the interactions between the NPs and the LC molecules as well as the NP concentration.

They found that the NP rich isotropic and NP poor nematic phase coexistence can only exists above a certain threshold NP concentration and the temperature range over which this coexistence can occur can be very large, even as large as the temperature of the nematic phase itself in some circumstances. It was also found, that above another threshold NP concentration, the system will undergo a transition directly into this phase separated state as the temperature is decreased, but below the threshold concentration, the system will first transition into a homogeneous nematic phase before transitioning into the coexisting state. This type of behaviour was also verified experimentally by the same authors and others for two different systems of NPs dispersed into LCs, an LC polymer and also a low molecular weight LCs [124].

The 'phase transition templating' process for self-assembling NPs is essentially a way of exploiting this phase separation phenomenon to create mesoscale assemblies of NPs. Several groups have been able to do this using a range of different NPs with varying surface functionalisations. Early work by Milette et al. used GNPs with an alkyl thiol monolayer coating or alkyl thiol

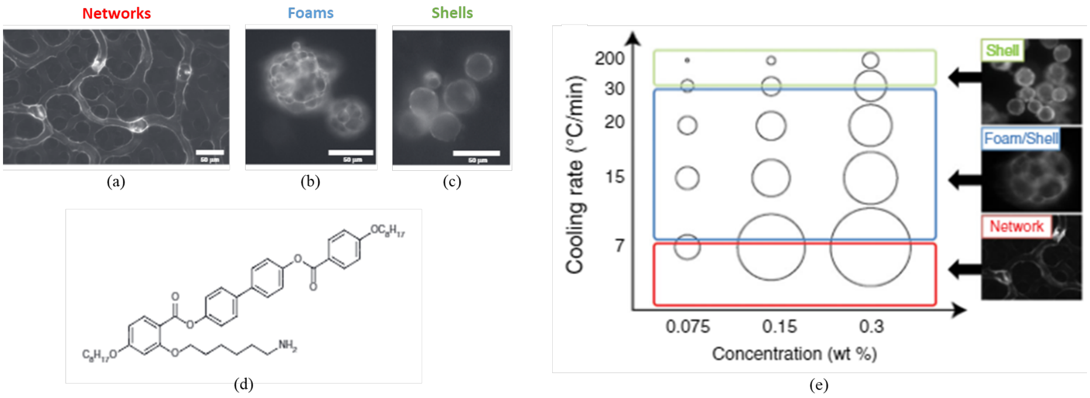

Figure 1.16: Isotropic to nematic phase transition driven QD self-assembly into a) 'tubular' networks, b) 'foams' and c) 'shells' using side-on mesogen functionalised QD, with d) the chemical structure of the laterally linked mesogen. e) shows the cooling rate and QD concentration dependence of the structure formation. Taken from [126].

and end-on mesogenic group mixed monolayer dispersed into either 5CB or 8CB [125]. They were able to reversibly form long-range NP networks by transitioning from the homogeneous isotropic phase to the nematic phase and found that depending on the cooling rate, they could control the length-scale and density of the network formation.

More recent work on this topic has involved the use of QDs with side-on mesogenic [73]and promesogenic [74] surface functionalisations. With this type of side-on mesogenic surface functionalisation (see figure 1.16(d)), it has been shown that not only can long-range networks be formed, but a variety of other structures can also be formed by controlling both the QD concentration and the cooling rate from the isotropic to the nematic phase (see figure 1.16(e)) [126].

Interestingly, the different structures formed, which consisted of networks, foams and shells shown in figures 1.16(a), 1.16(b) and 1.16(c) respectively, were hollow as a result of the type of surface functionalisation used. The formation of these hollow micro structures was attributed to a second stage of nematic nucleation within the remaining QD rich isotropic regions of the LC. This has been verified theoretically with a free-energy model for the case of hollow NP shell formation[127]. Non-mesogenic alkyl chain surface functionalisation has also been shown to exhibit this type of phase transition driven self-assembly, forming long-range QD networks in 5CB, albeit with slightly different characteristics as a result [128]. It appears from their fluorescence microscopy images that the QD networks formed, were solid rather than the hollow tubular worm like networks formed with the side-on mesogenic functionalisation.

1.3.5 Direction of the Current Work

In this work, a comparison of the effects of two different types of surface functionalisation is made for NLC nanocomposites. Specifically the surface functionalisations used are side-on mesogenic and non-mesogenic alkyl chains. The NP of choice is a CdSe QD, the reason for choosing QDs is primarily due to their photoluminescence, which enables easy imaging of the self-assembled structures formed. Additionally, QDs, unlike some types of NPs, do not posses any other intrinsic properties that can influence the properties of the LC, as ferroelectric NPs do for example. This means that the effect of the NP core composition has on the nanocomposite properties and NP self-assembly can essentially be neglected, and solely the effects of surface functionalisation and NP size can be studied.

For the first time, a direct comparison of the effect these two types of surface fictionalisations have on the nanocomposite properties, such as the phase behaviour, LC order and related physical properties is performed. These effects and modifications to the nanocomposite properties are intrinsically linked to the phase transition driven QD self-assembly and thus the interplay between the two is also studied here. The results of this work can therefore be used to guide not only future work on QD-LC nanocomposites, but also for work done on all types of LC nanocomposites where the surface functionalisation of the nanomaterial is used to tune the behaviour of the nanocomposite.

The first results chapter of this thesis covers in detail, the application of dielectric spectroscopy to characterise LC materials and LC nanocomposites. The effects of the LC test cells on the measurements were studied and subsequently accounted for in the experimental design and data analysis methods. To do so, an equivalent circuit approach was developed and used; whereby the dielectric spectroscopy data can be retrospectively corrected enabling more accurate determination of LCs and LC nanocomposites physical properties.

The second results chapter focuses on understanding the phase behaviour of the LC nanocomposites as well as the phase transition driven self-assembly of the QDs within the LC host. The influence that the different types of surface functionalisation have on the order of the LC nanocomposites is determined and related to both the phase behaviour and QD self-assembly.

The final results chapter of this thesis aims to understand how the surface functionalisation affects the alignment of the LC nanocomposites as well as the effects on the dielectric and elastic properties determined through the use of dielectric spectroscopy. To do so, the methods developed for the analysis of LC dielectric spectroscopy data covered in the first results chapter have been employed.

Chapter 2

Experimental Methods

2.1 Introduction

In this chapter, the experimental methods and characterisation techniques used are discussed. The chapter is split into three sections: device fabrication, sample preparation, and characterisation techniques. Firstly the details of the techniques and procedures used for the fabrication of the LC devices used in this work are covered in detail; secondly, the sample preparation methods used are described; and finally, each of the characterisation techniques used are discussed. A more detailed and specific description of how some of these techniques (such as dielectric spectroscopy) were used, how the measurements were performed and how to interpret the data as well as the details of the analysis methods will be covered in subsequent chapters.

2.2 Device Fabrication

LC devices such as the one shown in figure 2.1, are typically constructed using two adjacent, conductive glass substrates, separated by a distance in the range of one to several hundred μm, but most frequently just several μm. A thin ($\sim 70nm$) layer of indium tin oxide (ITO) coating on the glass substrates provides the conductive coating enabling the application of electric fields across the LC sample, which is capillary filled between the two glass substrates. In certain circumstances it is necessary to use a specific electrode pattern which is produced from the uniformly coated ITO glass using a photolithography process with an acid etch.

In order to uniformly align the LC without using external fields, the ITO coated glass substrates are coated with an alignment layer (AL). The most commonly used AL materials are polymeric materials, which are spin coated in a suitable solvent and then baked onto the ITO coated glass substrates to form a thin film. Alternative methods of LC alignment also include the use of surface relief gratings. By using different AL materials and preparation techniques, it is possible to achieve uniform alignment with homeotropic or planar anchoring of the LC. After all AL treatment has been completed, the cell is constructed using either spacer beads or spacer film to separate the glass substrates by the desired distance and secured in position using either thermally or UV cured glue. Each step of this process is discussed in further detail in chronological order within this section.

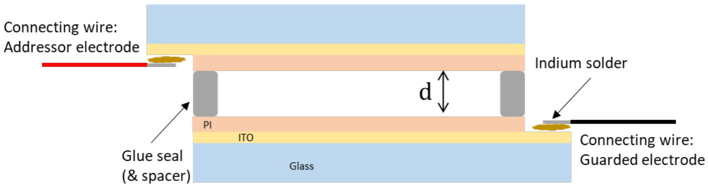

Figure 2.1: Schematic of a typical LC device constructed from staggered ITO coated glass substrates with an AL deposited on each substrate and connecting wires soldered to the ITO electrodes using indium.

2.2.1 Substrate Preparation

Prior to commencing any lithography processing, AL deposition or cell construction (in the case of non aligned cells) it is necessary to cut the glass to the appropriate sized substrates followed by thorough cleaning of the substrates to avoid contamination in the processing steps or of the sample with dust, grease or any other unwanted contaminants. The glass is first scored (on one or both sides depending upon the situation) by using a diamond or hardened steel tipped scribe and breaking along the length of the score. After removal of any glass fragments from the cut edges, the substrates are placed in a Polytetrafluoroethylene (PTFE) substrate holder inside an appropriately sized glass beaker to undergo the four step cleaning process:

1. 1 part Decon 90 (D90) surface active cleaning agent to 9 parts De-Ionized (DI) water - 30 minute ultrasonication.

2. DI water - 30 minute ultrasonication.

3. Methanol - 30 minute ultrasonication.

4. Isopropyl alcohol (IPA) - 30 minute ultrasonication.

It should be noted that it is necessary to ensure there is no D90 residue on the substrates or in the beaker between steps one and two by rinsing thoroughly with DI water and all subsequent steps should only be initiated once substrates and beaker are completely solvent free from the previous step. Once the four step cleaning process is complete and all remaining solvent residue has evaporated, the substrates undergo (ITO side up) a 15 minute UV-Ozone exposure.

2.2.2 Spin Coating

Once thoroughly cleaned, the substrates are ready for the next step of the device fabrication process. This may be either the photolithography step or AL deposition, both of which require spin coating of polymeric materials in order to produce a uniform film thickness. The polymeric material is typically dissolved in a solvent (usually in monomer form) to give a polymer solution of sufficiently low viscosity to spread over the entire substrate to give the desired film thickness, which is given by [129, 130]:

$$h_{film} =\propto \frac{\kappa_p^{\beta}\eta^{\gamma}(T)}{\omega^{\alpha}}, \tag{2.1}$$

where κ_p is the concentration of the polymer in the solvent, η is the temperature dependant viscosity of the polymer solution and ω is the spin rate. The exponents, α, β and γ are dependant upon the type of polymer solution and substrate combination. Thus, h_{film} can be controlled by varying either C or ω whilst maintaining a constant temperature. Other external factors may also play a role in determining h_{film} such as humidity, which may affect α, β or γ .

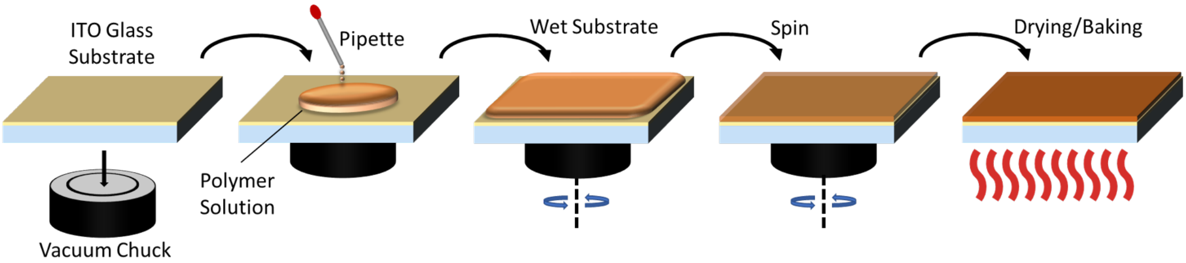

Figure 2.2: Schematic diagram of spin coating process showing deposition of polymer solution onto ITO substrate, followed by wetting of the substrate, spinning and finally drying/baking of the substrate to evaporate excess solvent and adhere the film to the substrate (in the some cases, for instance PI films, this may also act as a polymerisation/imidization step).

When spin coating, the substrate is first positioned centrally on the chuck and secured using a vacuum. The polymer solution should then be deposited onto the substrate surface ensuring complete wetting. The substrate is then spun at an initially low rate (typically 500rpm) before ramping up to the desired spin speed (typically several thousand rpm). The duration of spinning is typically around a minute, but can vary, depending on the material and conditions. A schematic representation of this process can be seen in figure 2.2.

2.2.3 Electrode Patterning

Depending on the type of device, it is sometimes necessary for the electrodes to be patterned. For instance, if the LC cell is to be used for taking sensitive dielectric measurements, a guarded electrode design as shown in figure 2.3(a) should be used [131]. In this case, one of the substrates is coated in unpatterned ITO, whilst the guarded electrode pattern on the adjacent substrate, consists of a circular 'active' electrode area of ITO that is separated from the 'guarding' electrode by a thin gap ($\sim 10\mu m$) where the ITO has been removed. The 'active' area of the electrode is where the voltage across the two substrates is applied, whilst the 'guarding' electrode is connected to ground. This is done to improve the homogeneity of the applied electric field across the sample, minimising the edge effects and stray capacitances at the perimeter of the 'active' electrode. Other electrode patterns may also be required such as interdigitated electrodes as shown on figure 2.3(b) for in-plane switching (IPS) devices or making in-plane conductivity measurement for example.

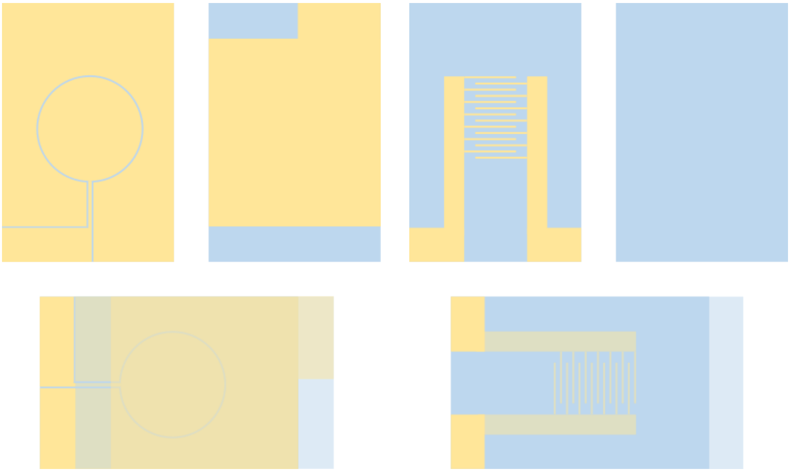
(a) (b)

Figure 2.3: Schematic of a) guard ring and b) interdigitated electrode patterns. The yellow and blue shaded areas represent regions of ITO and no ITO respectively. The arrangement of the individual plates an the top is shown at the bottom.

There are two approaches to performing photolithography depending on the type of photoresist used, which are positive and negative tone photoresists. A positive tone photoresist is a polymer which is weakened by exposure to light and thus becomes more soluble in a specific solvent known as the 'developer'. A negative tone photoresist works in the opposite way: on exposure to light, the polymer is strengthened through inter-chain cross-linking and thus becomes less soluble in the developer. Throughout this work, the positive tone photoresist Shipley 1813 was used. Exposure to light of the photoresist can be achieved in either one of two ways, masked, or maskless lithography. The former utilises a chrome photomask where the desired electrode pattern is present as regions of chrome on a glass plate through which high intensity light is shone and the latter uses a laser with a small spot size to selectively expose regions of the photoresist and is thus also known as direct write lithography (DWL).

Each of these methods has their own advantages and limitations, masked is generally faster than maskless lithography and is therefore used for high volume production of patterned electrodes, but is, however, limited to the pattern on the chrome photomask. On the other hand, maskless photolithography is generally slower, but does not require a pre-made photomask to enable selective exposure; instead, a pulsed small spot laser is raster scanned across the substrate, enabling a variety of features and patterns to be produced. This capability therefore makes maskless DWL well suited for prototyping of electrode patterns and the subsequent production of chrome photo-masks for higher volume electrode patterning, as has been previously done in the Soft Matter Physics group at the University of Leeds.

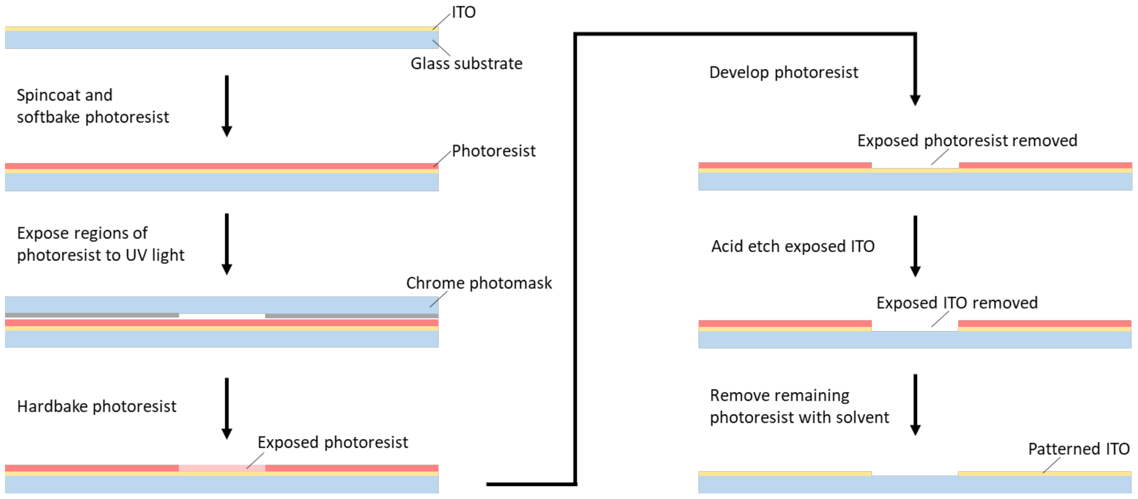

Figure 2.4: Schematic diagram showing the step by step process of photolithography using a positive tone photoresist to create patterned ITO electrodes

The step by step masked photolithography process using a positive tone photoresist can be seen in figure 2.4. The first step of the process is to spin coat a layer of photoresist that is dissolved in a solvent on to the ITO glass. The substrate is then placed in an oven or on a hotplate to 'soft bake' the photoresist, evaporating any remaining solvent. The photoresist coated substrate is then exposed to high intensity UV light through the chrome photo-mask that imparts the desired pattern onto the photoresist. The areas of the photoresist which are exposed to the UV light (i.e. the areas of the photo mask which are not covered in any chrome), are chemically modified, enabling the photoresist to be readily dissolved by the developer. By submersing the substrates into the developer for the correct duration of time, only the exposed areas of photoresist are removed to reveal the ITO in the desired pattern. The substrate is then quenched in deionised water immediately after removal from the developer solution to prevent over development. The substrates are then placed back into the oven or onto the hotplate to 'hard bake' the remaining regions of photoresist before the acid etching step. The substrates are then submersed into an acid solution (typically hydrochloric and/or nitric acid mixed with deionised water) to etch away the exposed areas of ITO.

The duration of etching is critical, since not enough time in the acid bath results in incomplete removal of ITO in the regions where it should be removed (areas where photoresist has been removed), creating short circuits. Too long in the acid bath results in the removal of ITO in the regions where it should not be removed (areas underneath the remaining photoresist) and therefore changing the dimensions of the features. Similar to the development step, the substrates are quenched in deionised water immediately after etching to stop any excess etching. The final step in the lithography process is the removal of the remaining photoresist by using a suitable solvent capable of dissolving the unexposed regions of the photoresist, such as acetone. This leaves the glass substrate with a patterned ITO coating on its surface, ready to be used for the remainder of the device fabrication process following another repetition of the cleaning process outlined in Section 2.2.1.

2.2.4 Alignment

Alignment of LCs within devices can be achieved through the application of external fields, however, for most applications, LC alignment without the application of external fields is required. To do this, anchoring of the LC at the substrate surfaces is employed. The alignment direction can be split into two categories, either parallel to the surface normal known as homeotropic (HT) or perpendicular to the surface normal known as planar homogeneous (PH) anchoring.

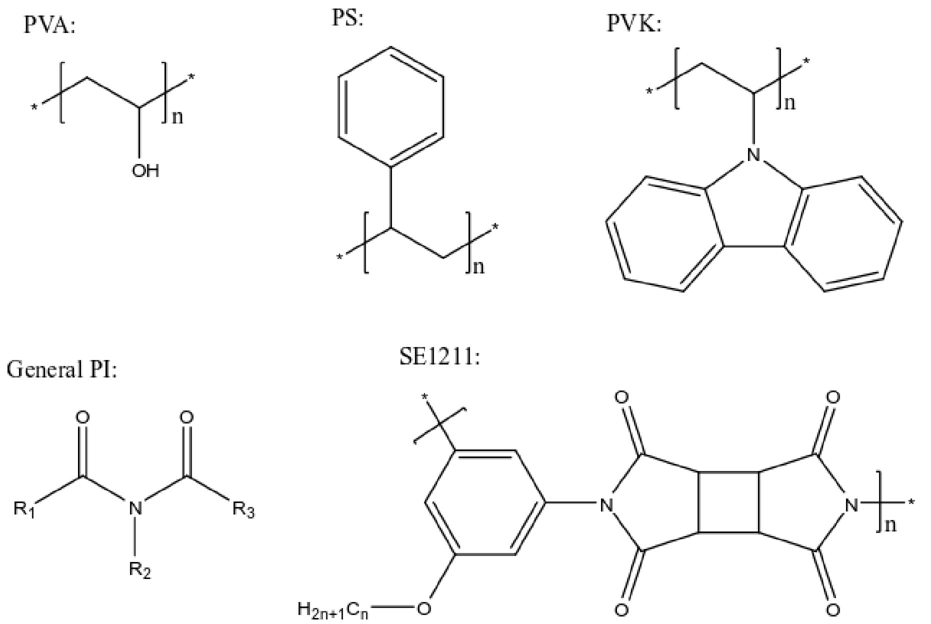

Figure 2.5: Chemical structures of some polymeric alignment materials. Top left to right: Polyvinyl alcohol (PVA), Polystyrene (PS) and Polyvinylcarbazole (PVK). Bottom left to right: general polyimide (PI) structure and structure of Nissan Chemicals PI SE1211.

In reality, true HT or PH anchoring is not always achieved. The director may reside at some angle away from either the surface normal in the case of HT anchoring or the surface plane in the case of PH anchoring. This angle is known as the surface pretilt θ_p which is typically $\sim 2^\circ$ for PH alignment, but depends on both the AL and LC material used.

The most common method of LC alignment through anchoring at the substrate surface is achieved by coating the substrates in a thin film of a certain type of polymeric material that interacts strongly with the LC molecules causing them to preferentially lie along a given direction. These polymeric films are typically $\lesssim 100nm$ thick and are formed by dissolving the polymer either in its monomer or polymer form into a suitable solvent, then filtered to remove any large particulates and subsequently spin coated onto the substrate surface (following the procedure outlined in 2.2.2. Once the substrates have been coated in the polymer solution, they are baked to remove the excess solvent and to also polymerise the film in the case of spin coating in monomer form. Historically, polymers such as polyvinylalcohol (PVA) have been used as alignment materials, however, it is now common to use polyimides which have been developed for use in LC displays due to their high heat-resistance and chemical stability. The chemical structures of some of these materials can be seen in figure 2.5.

Uniform PH alignment using this technique is generally achieved by rubbing the polymeric film after it has been baked. The rubbing machine consists of a vacuum table on which the substrates

Material	Alignment Type	Rubbing Orientation	θ_p
PVA	PH	Parallel	$0°$
PS	PH	Perpendicular	N/A
PVK	PH	Perpendicular	N/A
PI SE1211	HT	N/A	$90°$
PI SE3510	PH	Parallel	$\sim 7 - 8°$
PI SE130	PH	Parallel	$\sim 2°$

Table 2.1: Alignment characteristics of some polymeric alignment materials. Alignment type refers to either PH or HT anchoring. Rubbing orientation refers to the orientation of the easy axis of alignment relative to the rubbing direction in the plane of the substrate for the case of rubbed PH alignment materials. θ_p refers to the pretilt angle measured from the surface plane.

are secured, which is then moved back and forth under a rotating microfiber cloth covered roller (figure 2.6). An important parameter in the quality of LC alignment and anchoring strength is the rubbing strength L, defined as:

$$L = Nl\left(1 + \frac{2\pi r\omega}{60\nu}\right), \tag{2.2}$$

where N is the number of times the substrates passes the roller, l is the contact length between the roller and the substrate, r is the roller radius, ω is the rotation rate of the roller measured in revolutions per minute (r.p.m.) and ν is the speed at which the substrate passes the roller. The height of the roller can be manually adjusted (using a set of grub screws), thus enabling control of l , N and ν are controlled using a program written in python, whilst r and ω are fixed, enabling complete control over L.

The easy axis of alignment (direction in which **n** preferentially lies), is most commonly along the direction of rubbing, which is the case for PVA and most PH PIs. It is thought that the rubbing of the polymer surface orients the polymer chains forming an ordered surface which can interact anisotropically with the LC on a molecular level [132]. The purely physical mechanism of LC alignment due to 'micro-groove' formation relies only on the interaction of LC molecules with themselves and not with the AL itself. Evidence of LC alignment within micro-grooves has been shown with grooved ITO formed using atomic force microscopy nanolithography, therefore removing any additional contribution from intermolecular interactions between polymer chains and the LC at the AL surface [133]. The same group have also shown LC alignment using periodic grating structures formed from both polymeric materials and ITO [134].

The contribution from molecular interactions between aligned polymer chains (and their sub-

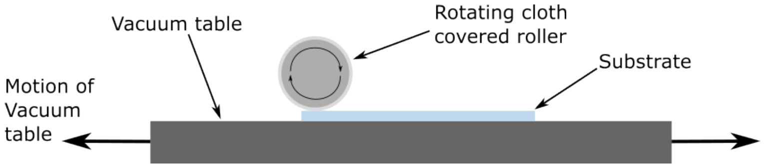

Figure 2.6: Side on view of the rubbing machine used to rub PI ALs.

stituents), however, is now considered as the dominating mechanism due to a number of studies indicating that molecular orientation at the surface of polymer thin films indeed stems from mechanical rubbing [135], resulting in the anisotropic molecular interactions causing LC alignment [136][137]. Other polymeric AL materials such as polystyrene (PS) and polyvinylcarbazole (PVK), which have phenyl rings situated as side groups off the main polymer chain (figure 2.5), have been shown to exhibit an easy axis which lies orthogonal to the direction of rubbing [138][139][140].

2.2.5 Cell Construction

Spacing of the two glass substrates to form LC test cells, is controlled by either polymer spacer film or spacer beads. The choice between the two depends on the requirements of the application and the ease of construction. Spacer film is generally best suited to single cell fabrication, whereas the use of spacer beads is generally best suited to the bulk cell fabrication process, however, can still be used for single cells. When using spacer film, two strips of spacer film are cut, UV glue is deposited on either side of the substrate which is used to secure the spacer film strips in position, as shown in figure 2.7(a). A second layer of UV glue is then deposited on top of the spacer film which then adheres to the opposing substrate when sandwiched together and the glue is cured in a UV curer. The duration of curing depends on the UV glue being used, but is typically around 30 minutes. When the substrates have been sandwiched together, they are held in position using bulldog clips whilst the glue is curing.

If spacer beads are used, they must be evenly distributed onto one of the substrates. This is done by using gravitational deposition as shown in figure 2.7(c). To ensure uniform spacing and to limit their effect of the spacer beads on the characterisation of the LC devices, the number density of spacer beads on the substrate needs to be controlled. In order to do so, the size of the deposition chamber and spacer beads must be considered. The mass of beads m_b, required to give a number density of beads, n in a chamber of horizontal cross-sectional area, A is defined as:

$$m_b = \frac{4\pi}{3} A n \rho r^3, \tag{2.3}$$

where ρ is the mass density of the material the beads are made from and r is the average radius of the spacer beads. One of the substrates from each of the pair (e.g. the lower substrate) are first loaded into the deposition chamber through a door at the front. The required mass of spacer beads is then measured out and loaded into the port on the right hand side of the deposition chamber that can be seen in figure 2.7(c). The beads are then dispersed into atmosphere within the box using compressed air and then allowed to settle for at least 30 minutes.

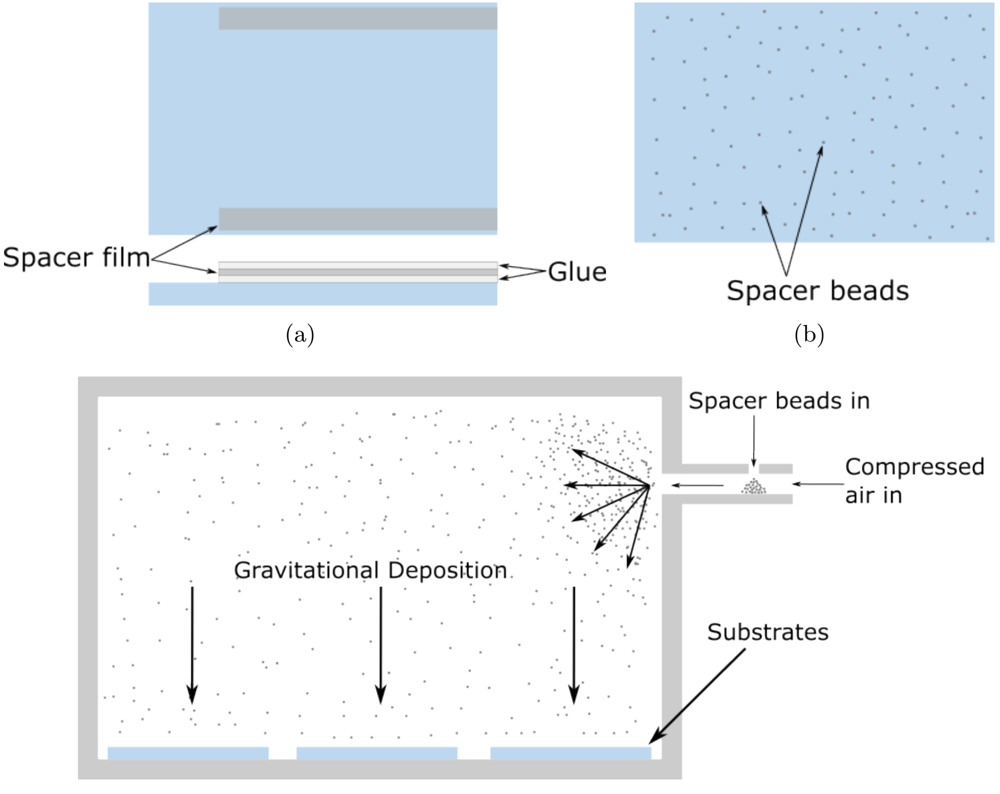

(a) (b)

(c)

Figure 2.7: Methods of spacing substrates when constructing LC devices, a) using polymer spacer film and b) using spacer beads. c) method of gravitational depositing of spacer beads onto glass substrates in a deposition chamber.

The two substrates are then glued together, which can be done in one of two ways. Either the opposing (top) substrate (without spacer beads) has a glue pattern deposited onto its (AL) surface before being lowered down onto the bottom substrate, or the top substrate can be positioned on the bottom substrate and a glue seal can be applied from the outside. Typically thermal glue is best suited to the former of these options and can be cured on a hotplate, whilst UV glue is best suited to the latter. If the glue is deposited onto the substrate rather than applied from the outside after sandwiching, the glue deposition machine can be used as shown in figure 2.8(a). This is particularly useful for the bulk cell fabrication process, where the pattern of a 3x4 cell array must be deposited onto the substrate. The typical glue pattern deposited onto a GR substrate for a single cell is shown in figure 2.8(b).

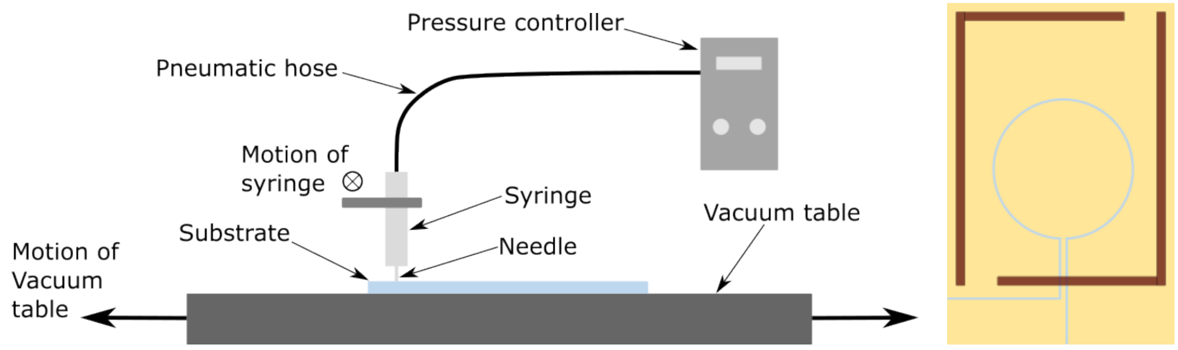

(a) (b)

Figure 2.8: a) Side-on view of the glue deposition machine used to deposit thermal glue onto substrates. b) Typical thermal glue pattern deposited onto a GR substrate with two gaps left at either end for capillary filling of LC.

Once the glue has been deposited, the substrates are then sandwiched together, with the substrate that has spacer beads deposited onto it on the bottom and the substrate with the glue pattern brought in to contact from above to ensure the spacer beads remain on the substrate surface. The substrates are then temporarily held together using bulldog clips before being vacuum bagged. Once vacuum bagged, the glue can be cured, when using thermal glue, this is done with the sandwiched substrates on a hotplate whilst being pressed with weights. The baking temperature and duration are specific for the thermal glue being used, but typically around $160°C$ for two hours. The vacuum bagging and pressing is done to ensure the most uniform cell gaps possible. For bulk cell fabrication, once the glue has been cured, the sandwiched substrates must be separated into individual constructed cells. This is done by scoring both substrates using a diamond scribe breaking along the length of the scores.

2.3 Materials and Sample Preparation

2.3.1 Materials

The LC host used for the formation of the LC nanocomposites was the nematic mixture MLC6204-000 synthesised and provided by Merck KGaA, Darmstadt, Germany. The reason for choosing this mixture was due to it's highly positive $\Delta\epsilon$ making it suitable for use in ZBD and other LCDs. Additionally, the use of a mixture such as MLC6204 with low molecular fluorescence enables more effective FM to be performed on the QD-LC nanocomposites to image the QDs within the LC rather than the LC itself. The main disadvantage to using a mixture such as MLC6204 is that the exact molecular structure of the compounds and ratio of compounds within the mixture is proprietary.

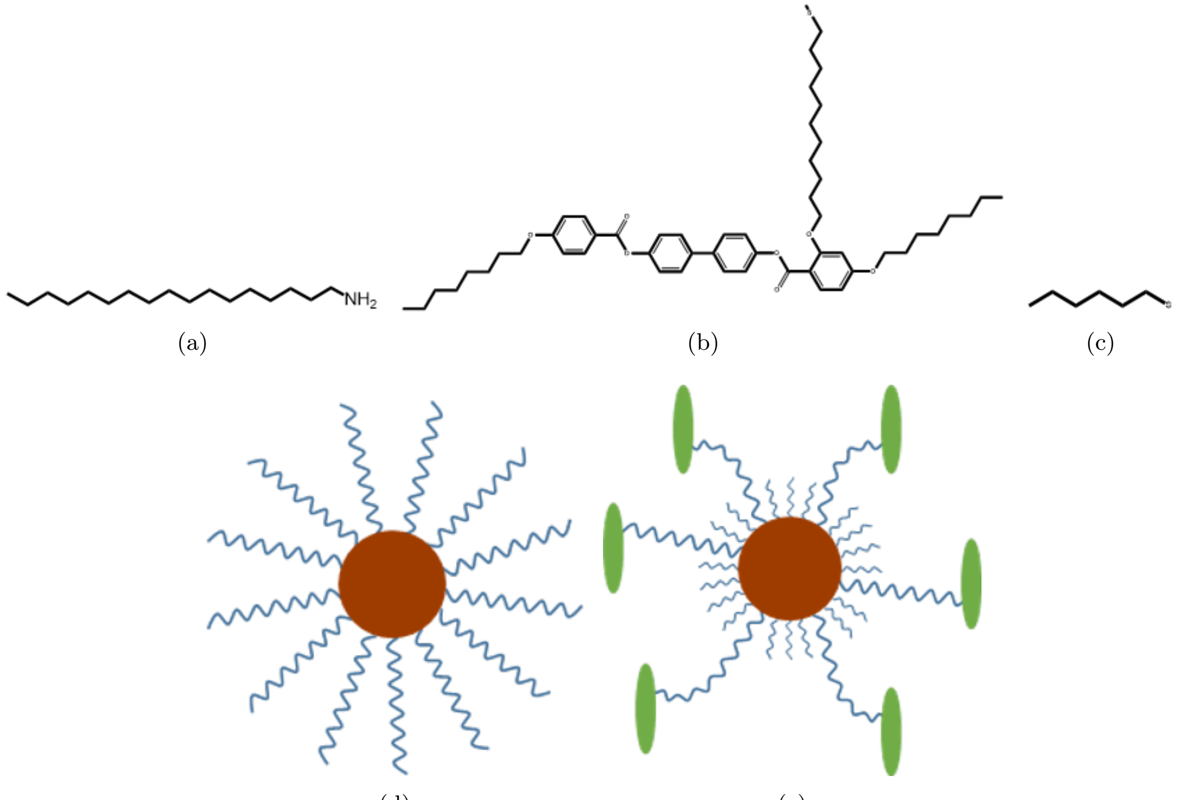

(a) (b) (c)

(d) (e)

Figure 2.9: Chemical structures of the organic surface functionalisation used on the CdSe QDs. a) ODA chains, b) the mesogenic group used on the LC QDs with the flexible alkyl linker and c) the hexanethiol co-ligands on the LC QDs. d) and e) show a cartoon style schematic of the ODA and LC QDs respectively.

All of the QDs used in this work consisted of a cadmium selenide (CdSe) core and an organic surface functionalisation. Two types of surface functionalisation were used, a commercially available non-mesogenic alykyl chain and a custom mesogenic surface functionalisation. The non-mesogenic surface functionalisation can be seen in figure 2.9(a) consisted of a monolayer of octadecylamine (ODA) chains and were purchased from MKNano (division of MK Impex Corp.); the QD with this surface functionalisation from herein will be referred to as ODAQD. The mesogenic surface functionalisation consisted of a mesogenic group that was connected to the QD surface in a side-on orientation via a flexible alky linker as shown in figure 2.9(b) and a haxanethiol co-ligand (figure 2.9(c))in an approximately 2:3 ratio were sythesised and kindly provided by Haifa Ojaym and Georg Mehl (University of Hull, UK); from herein, these QD will be referred to as LCQD. The core size of the LCQD was $\sim 2.6nm$ and two core sizes of the ODAQD were purchased and used in this work, $\sim 2.6nm$ and $\sim 6.5nm$ with the smaller core sized used as a direct comparison to the LCQD and the larger core size to compare the effect of core size with the same ODA functionalisation.

For the study of dielectric spectroscopy in LC devices, an isotropic dielectric liquid, trans-1-n-propyl4-(40-ethylphenyl) cyclohexane (PCH32) also provided by Merck KGaA, Darmstadt, Germany with a similar structure to the common CB LCs was used in addition to the LC mixture MLC6204. The molecular structure of PCH32 can be seen in figure 2.10(a). The organic salt used to dope this material with was tetra butyl ammonium tetra phenyl borate (TBATPB) with the chemical structure shown in figure 2.10(b).

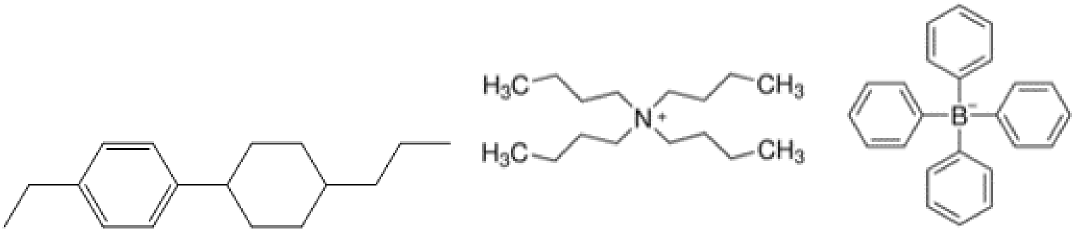

(a) (b)

Figure 2.10: Chemical structures of a) the isotropic dielectric liquid PCH32 and b) the organic salt TBATPB used in the study of dielectric spectroscopy of LC devices.

2.3.2 Nanocomposite Preparation

The LC nanocomposites used in this work were all prepared following the same process. Firstly the dry QD were dissolved into a common solvent, in which the host LC material is also soluble, in this case toluene was used. The dry QD were weighed out using a mass balance and the correct quantity of solvent then added to the dry QDs to create a mixture of the desired QD concentration. The QD-solvent mixture was then vortex mixed and sonicated to ensure all QD aggregates have been broken up and the QD were fully dissolved in the solvent. Once complete dissolution of the QD was achieved and a stable solution had been formed, this was then mixed with the host LC at a known quantity, again, measured out using a mass balance. The host LC used was the highly$\Delta\epsilon$ nematic mixture MLC6204-000 (Merck KGaA, Darmstadt, Germany).

The QD-solvent-LC mixture was vortex mixed and sonicated to ensure the LC and QD were fully dissolved before the solvent was then evaporated at elevated temperatures above the T_{NI}

of the pure host LC. To ensure complete evaporation of the solvent, mass constancy was checked repeatedly following heating under vacuum. Once complete solvent evaporation was achieved, the remaining QD-LC dispersion was sonicated at elevated temperatures above T_{NI} to ensure homogeneous QD dispersion within the final QD-LC nanocomposite. The same method was also used to dope the isotropic liquid PCH32 with the organic salt TBATPB by replacing the QD with the salt and using acetone as the common solvent to dissolve both the salt and the host dielectric liquid.

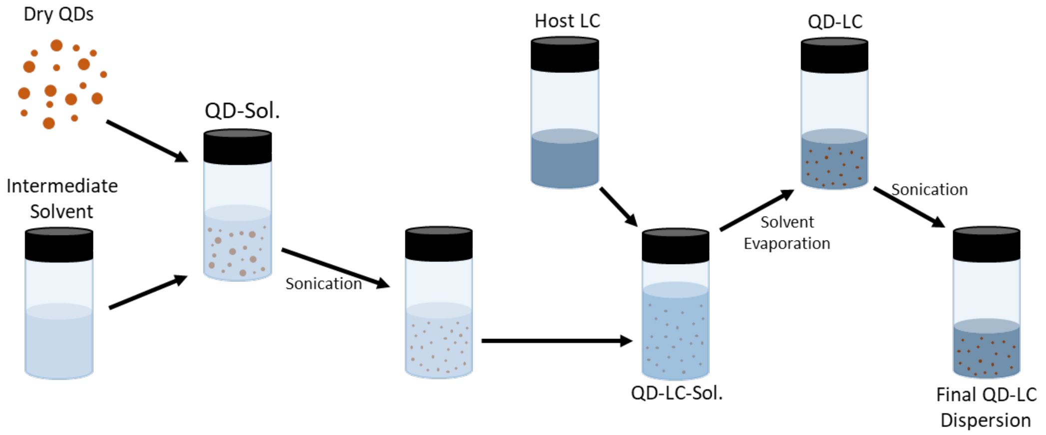

Figure 2.11: Schematic of the QD-LC nanocomposite preparation procedure.

The final QD-LC nanocomposite was kept in the isotropic phase following the final sonication prior to performing any kind of characterisation. The nanocomposites were then capillary filled into LC test cells in the isotropic phase for optical microscopy and dielectric characterisation. The samples were then cooled as required into the nematic phase at a controlled rate on a Linkam LTS120 water cooled Peltier hot stage using a T95-PE controller unless stated otherwise. For all other forms of characterisation, such as differential scanning calorimetry (DSC) and refractometry, the nanocomposites were also kept in the isotropic phase prior to performing measurements and temperature control was provided by the equipment rather than an external hot stage.

2.4 Characterisation Techniques

2.4.1 UV-Vis Spectroscopy

UV-Vis spectroscopy in both reflection and transmission mode have been used in this work. Specifically, UV-Vis reflection mode spectroscopy has been used to measure the cell gaps of the LC devices prior to filling as well as to measure thin film thicknesses (e.g. ALs). UV-Vis transmission mode spectroscopy has been used to measure the absorption spectra of the LCs and QDs used in this work.

2.4.1.1 Reflection Mode Spectroscopy

Reflection mode spectroscopy is used to measure the spacing between the substrates in LC test cells, also known as the cell gap. The microscope used to do so is setup in reflection mode and is focused on either the glue seal, spacer beads or spacer film. A bright and dark field is then taken using a mirror and black background in place of the cell respectively.

The reflection spectra from the cell is then recorded and used to calculate the cell gap d. The reflection spectra typically consists of a number of minima and maxima (see figure 2.12(a))which correspond to the wavelengths that destructively and constructively interfere when reflected from each substrate(see figure 2.12(b)). This happens due to the size of the cell gap relative to the wavelength of light; when the wavelength of light is equal to a half integer of d, the reflected rays from each substrate interfere constructively.

To calculate d from the reflection spectra, the number of maxima in the visible range from $450 - 700nm$ should be counted and the distance between the first and last maxima recorded. The following formula is then used [141]:

$$d = \frac{\lambda_1 \lambda_2 m}{2(\lambda_2 - \lambda_1)}, \tag{2.4}$$

where λ_1 is the wavelength of the first peak, λ_2 is the wavelength of the last peak and m is the number of peaks.

In addition to using reflection mode spectroscopy to measure the cell gap of LC devices, UV-Vis reflection spectroscopy can also be used to measure thin film thicknesses, for instance to measure the thickness of the PI thin film ALs. In order to do this, the PI coated ITO glass substrates were illuminated by a white light source on a microscope in transmission mode and the resulting transmission spectra recorded in the same way as when measuring cell gaps. To calculate the film thickness h_{film}, however, the wavelength of the peak position λ in the reflection spectra can be used in the following equation provided that $n_{air} < n_{film} < n_{ITO}$ [142]:

$$h_{film} = \frac{m\lambda}{2n_{film}Cos\theta}, \tag{2.5}$$

where $m = 1$ and θ is the angle of incidence of the light on the film to the surface normal, which was assumed to be 0° when measured on a microscope in reflection mode.

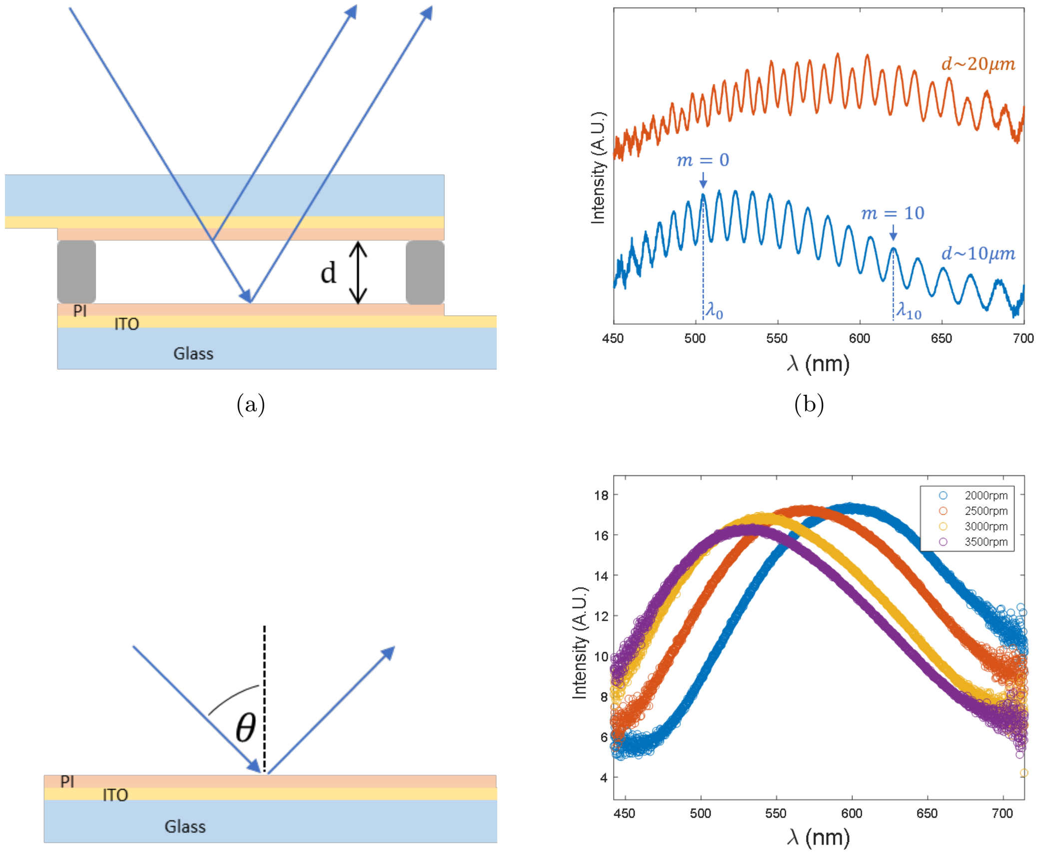

(a) (b)

(c) (d)

Figure 2.12: a) Interference of light reflected from inner interface between either substrates when performing LC cell gap measurements using UV-Vis reflection spectroscopy. b) Typical reflection spectra from nominally $10\mu m$ thick (blue) and $20\mu m$ thick LC cells showing multiple maxima from constructive interference in the range $450-700nm$. c) UV-Vis reflection spectra measurements of PI thin film on ITO substrate and d) shows the typical reflection spectra from the same PI material of different thicknesses, achieved by spin coating at different maximum spin speeds.

2.4.1.2 Transmission Mode and Absorption Spectroscopy

Absorption spectra measurements were taken by comparing the transmission spectrum of a reference sample and that of the material of interest. For measuring the absorption spectra of

LC dopants, the transmission spectrum of the reference sample is taken which is that of the pure host solvent used to disperse the dopant in (see figure 2.13). The transmittance through a sample is defined as:

$$T(\lambda) = \frac{I(\lambda)}{I_0(\lambda)} \tag{2.6}$$

where $I_0(\lambda)$is the wavelength dependant intensity of the transmitted spectrum for the reference sample and $I(\lambda)$ is the wavelength dependant intensity of the transmitted spectrum for the sample. The absorbance A of the sample is related to the transmittance and is defined as:

$$A(\lambda) = -log_{10}(T) = log_{10}\left(\frac{I_0(\lambda)}{I(\lambda)}\right). \tag{2.7}$$

To relate the absorbance to the concentration of dopant in the solution, the Beer-Lambert law can be used [143][144]:

$$A(\lambda) = log_{10}\left(\frac{I_0(\lambda)}{I(\lambda)}\right) = \xi(\lambda)cl, \tag{2.8}$$

where ξ is the molar attenuation coefficient, c is the molar concentration and l is the optical path length.

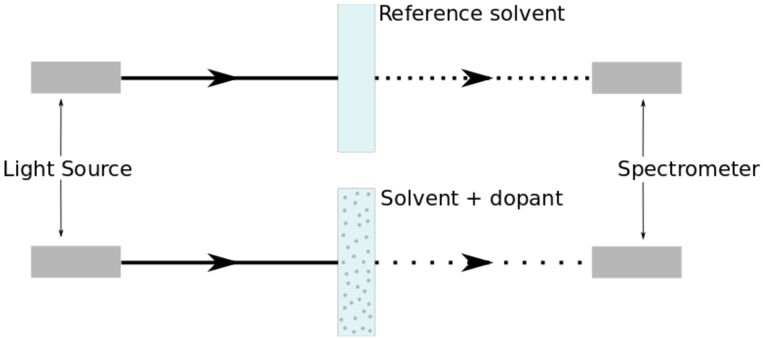

Figure 2.13: Method of UV-Vis absorption spectroscopy for determining the absorption spectra of LC dopants such as QDs.

2.4.2 Surface Profilometry

In addition to using UV-Vis reflection spectroscopy to measure the thickness of PI thin film ALs, surface profilometry was also used. The Bruker DektakXT stylus profilometer was used to map the surface of the PI thin film ALs on ITO glass substrates, capable of measuring a minimum step height of $< 10nm$ and a maximum step height of up to $1mm$ [145]. The process works by dragging a small rounded tip on a cantilever in one direction across the substrate. This process can be repeated several time to build up a 3D map of the surface topography.

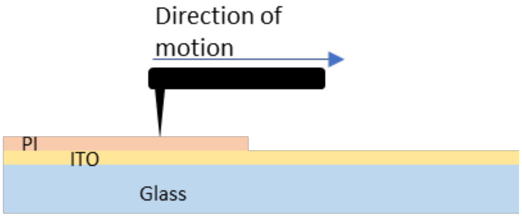

Figure 2.14: Schematic of surface profilometry on PI thin film ALs on ITO glass substrates using a stylus profilometer.

The resolution in the xy plane is determined by the tip size, which can be changed between either a $0.2\mu m$ or a $2\mu m$ radius tip depending on the measurements to be performed. The force applied by the tip on the substrate can also be controlled between $0.1mg$ and $15mg$. The PI thin films were prepared on the ITO glass substrates by spin coating and baking as per the procedure outlined in Sections 2.2.2 and 2.2.4. To measure the film thickness, part of the film was removed using a scalpel and to create a step-like structure from the PI to the ITO surface the stylus tip was dragged across as shown in figure 2.14.

2.4.3 Fluorescence Spectroscopy

Fluorescence spectroscopy measurements were performed using an Edinburgh instruments FLS1000-DD-stm spectrometer to find the fluorescence spectra of the pure LC host, QDs and the QD-LC nanocomposites. To illuminate the sample, the FLS1000-DD-stm uses a 450W xenon arc lamp, which provides an optimal spectral range of $250nm \lesssim \lambda \gtrsim 1000nm$ [146]. In the FLS1000, a double grating monochromator is used to select the wavelength range of light used to illuminate the sample and similarly, to select the wavelength range that is emitted by the sample to be measured by the photomultiplier (PMT) emission detector, which is capable of single photon counting. A spectral resolution of $0.01nm$ with an accuracy of $\pm 0.2nm$ is achievable using the double grating monochromators for both the excitation and emission, and by using the continuously adjustable slits at the entrance and exit of the two monochromators, a spectral band pass of up to 30nm can be achieved. In addition to the PMT emission detector, the FLS1000 also has a photodetector angled to measure the transmission within the sample chamber, enabling simultaneous UV-Vis transmission and absorption spectroscopy measurements to be performed using this equipment.

To perform fluorescence spectroscopy measurements on a liquid sample contained in a quartz cuvette, the cuvette is placed in a temperature controlled cuvette holder in the main sample chamber, where the excitation light is shone into the cuvette, exciting the fluorophores which then relax and fluoresce, emitting light of a longer wavelength which is collected at 90° to the direction of excitation light so as to avoid interference from any transmitted excitation light as can be seen in figure 2.15(a). For smaller sample volumes, a micro-cuvette was used to perform measurements on the liquid samples as shown in figure 2.15(b).

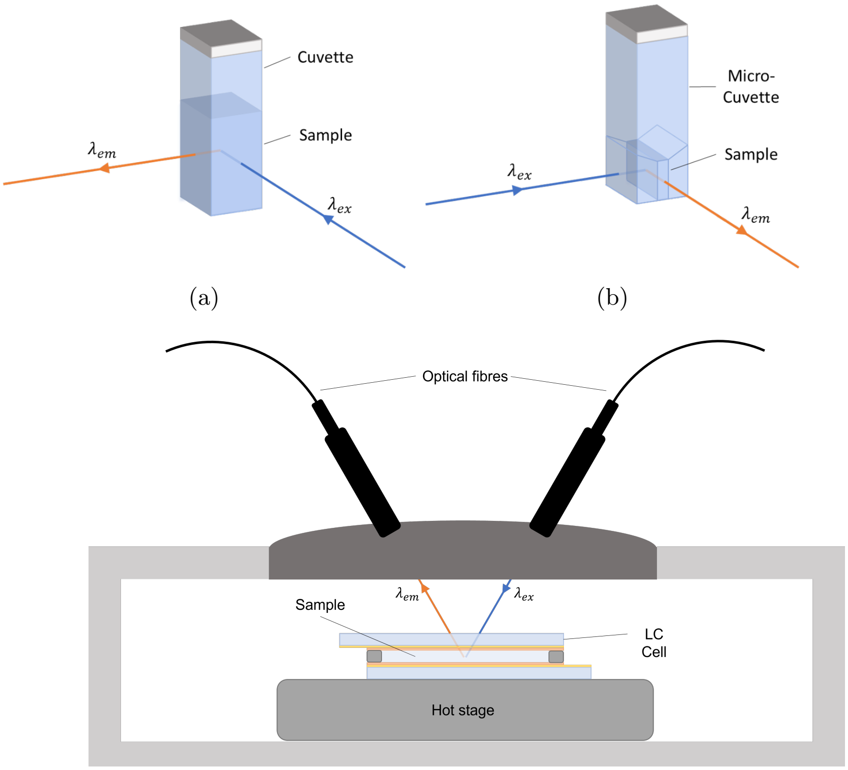

(a) (b)

(c)

Figure 2.15: Schematic diagrams showing the setups used for fluorescence spectrometry with the orientation of excitation (λ_{ex}) and emission (λ_{em}) light paths used in the fluorescence spectroscopy measurements. a) Liquid sample in quartz cuvette and b) liquid sample in quartz micro-cuvette for smaller sample volumes, note that both cuvettes were held in a temperature controlled cuvette holder within the sample chamber of the FLS1000 fluorescence spectrometer. c) liquid sample in LC cell mounted on Linkam hot stage with optical fibre attachments for the excitation and emission light to be taken from and returned to the FLS1000.

It should be noted that when dispersing/dissolving a fluorophore into a host solvent at too high concentrations, the intensity of fluorescence emission can be reduced due to the inner filter effect. This is where fluorophores closer to the excitation light source will absorb/scatter the excitation light, thus stopping fluorophores in the centre of the sample cuvette from recieving as high intensity excitation. This creates a reduction in the fluorescence emission intensity collected as it is the fluorophores in the centre of the sample cuvette which predominantly contribute to the fluorescence emission that is able to be collected by the detector due to geometric constraints.

Typically, solutions with a QD concentration of $\gtrsim 0.1wt\%$ can lead to the inner effect. In addition to the inner filter affect just described, which is known as the primary inner filter effect, if the excitation and emission wavelengths of the fluorophore significantly overlap, it is possible for fluorescence emission to be reabsorbed by the sample and thus reduce the intensity of fluorescence emission collected by the detector, which is known as the secondary inner filter effect. With regards to the inner filter effect, note the orientation of the micro-cuvette shown in figure 2.15(b), where it can be seen the long axis of the liquid sample volume is oriented in the direction of the emission light to maximise emission intensity collected by the detector.

To perform fluorescence measurements on samples filled into LC test cells, a 'fibre launcher' provided by Edinburgh Instruments was used. This consisted of a set of optical fibres which were fitted in place of the sample cuvette holder to collect and redirect excitation light from the sample chamber to an external Linkam hot stage on which the sample cell was mounted as in figure 2.15(c). Fluorescence emission from the sample cell was then collected by another optical fibre and directed back into the main sample chamber to the emission detector. The fluorescence emission spectra can be corrected for instrumentation effects and artifacts by using an excitation reference detector (positioned before the sample), to which some of the excitation light is directed by a beam splitter. Depending on the sample setup, whether using sample cuvette within the sample chamber or if using a sample cell mounted on an external hot stage, the type of spectral correction applied is different and was therefore changed within the Edinburgh Instruments Fluoracle software to apply the appropriate spectral correction.

2.4.4 Differential Scanning Calorimetry

Differential Scanning Calorimetry (DSC) is an experimental technique that is used to identify phase transitions within a material by measuring the heat flow in/out of the sample as a function of temperature. A known mass of the sample is stored in a hermetically sealed aluminium pan that is placed in the measurement chamber next to a reference sample that, in this case, is an empty (air filled) but otherwise identical pan. The temperature of the measurement chamber is either increased or decreased at a constant controlled rate and the heat flow in or out of the two samples is measured using two individual thermocouples.

The difference in the heat flow between the sample and reference pan can then be deduced which corresponds to the heat flow in/out of the sample material [147]. The isobaric specific heat capacity of a material C_P is defined as the amount of energy required to raise the temperature of the material by a unit temperature and is related to the enthalpy H by:

$$C_P = \left(\frac{\partial H}{\partial T} \right) \bigg|_P . \tag{2.9}$$

When performing DSC, however, it is more appropriate to relate C_P to the measured heat flow q and controlled temperature gradient dT/dt:

$$C_P = q \bigg/ \frac{dT}{dt}, \tag{2.10}$$

where $q = dH/dt$. By plotting the trace of either q or C_P against T it is possible to see at what temperatures thermodynamic phase transitions take place. In the case of LC materials, this can show the nematic - isotropic transition, crystallisation and glass transitions (depending on cooling rate). All DSC measurements were performed on the TA instruments Q20, using a cooling rate of $10°C/min$.

2.4.5 Microscopy

2.4.5.1 Polarising Optical Microscopy

The most commonly used experimental technique for the characterisation of LC devices is polarising optical microscopy (POM), which is particularly useful when studying LC phases as it enables significant insight into the LC alignment and director orientation. POM can be performed in either a reflection or transmission mode microscope setup. When using a transmission mode setup, a (linear) polariser and analyser are positioned either side of the birefringent sample, which is positioned on a rotation stage to allow for the sample to be rotated with repsect to the fixed orientation of the polariser and analyser as shown in figure 2.16.

Both the first polariser in the optical path, and the second (termed the analyser) can be rotated to be aligned parallel or perpendicular (crossed) to one another, allowing or preventing light from passing through the analyser in the absence of a sample between the two (2.17(a)). Consider a slab of birefringent material between the polarisers. If its optic axis is not parallel to either polariser, then the incident light experiences a retardation. This results in some degree of polarisation modulation, such as conversion of the initial polarised light to elliptical polarisation, thus some light is transmitted through the analyser. When linearly polarised light passes through the birefringent material at some angle relative to the optic axis, the light is split into two components, one parallel to n_e and one parallel to n_o, the extraordinary (E-ray) and ordinary (O-ray) rays respectively as shown in 2.17(b). When these two rays are recombined, the net polarisation is rotated relative to the linear polarisation which entered the birefringent slab and thus a component of this light is then able to pass through the analyser which is oriented at 90° to the polariser.

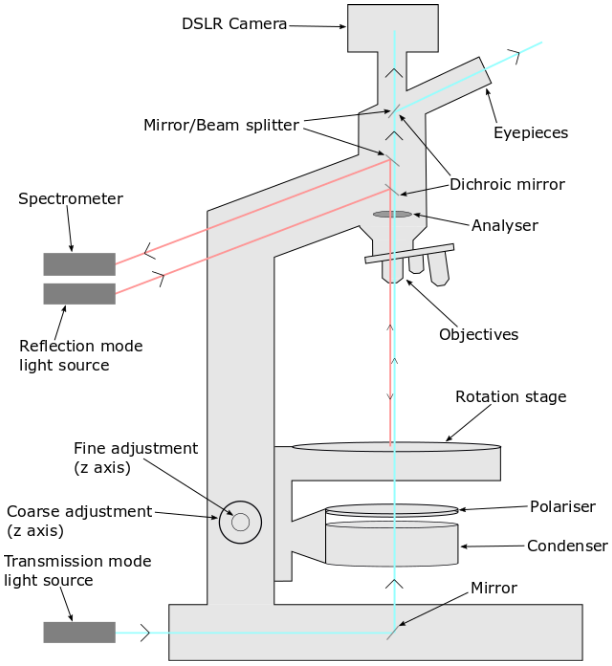

Figure 2.16: Schematic diagram showing the microscope set up used for both POM and FM. The light path when set up for POM is shown by the blue lines and the light path when set up for FM is shown by the red lines.

The wavelength of light transmitted is also dependant upon the birefringence and thickness of the material; hence by using a white light source, and with knowledge of the sample thickness, it is possible to calculate the birefringence (or vice versa). LC samples/devices can be mounted on a hot stage which is positioned on the rotation stage so that the sample can be heated/cooled between the different phases whilst being viewed between crossed polarisers. The magnification can be altered by using different microscope objectives which in this work was primarily a x10 objective, but x5, x20, x50 and x100 objectives were also used depending on the scale of magnification required. The microscope predominantly used in this work was the Leica DM2700, other Leica microscope models were also used but the majority of microscopy was performed on this setup.

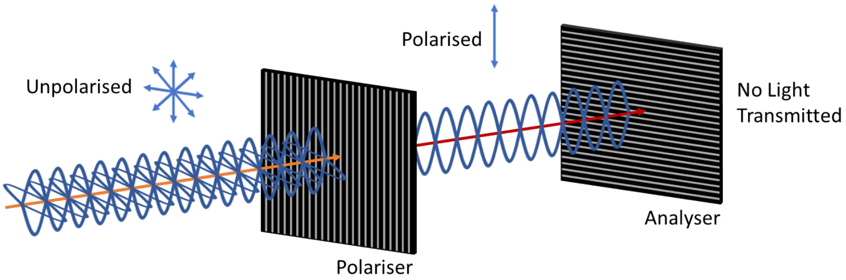

(a)

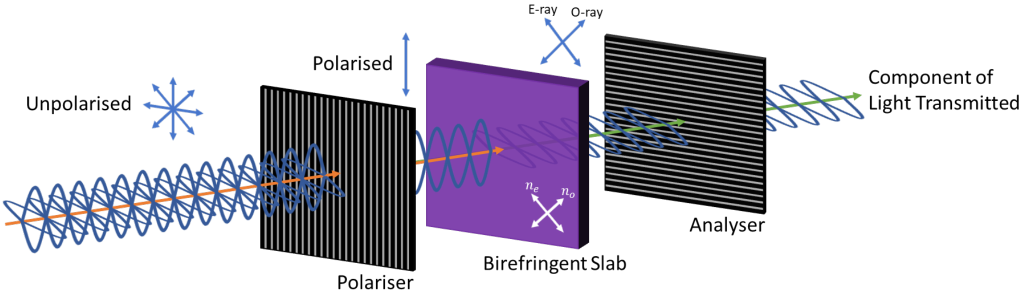

(b)

Figure 2.17: Schematic diagrams illustrating the operating principle of POM. a) crossed polariser and analyser with no birefringent material between the two transmitting no light and b) crossed polariser and analyser with a slab of birefringent material positioned between the two which transmits a component of the light after being retarded by the birefringent slab.

2.4.5.2 Fluorescence Microscopy

In addition to POM, Fluorescence microscopy (FM) was also used extensively in this work to study the QD-LC nanocomposites. FM provides a useful tool to examine the formation of QD micro-structures within the QD-LC nanocomposites. The basic principle of FM relies on illuminating a fluorophore with either a laser or a broad band UV-Vis light source. The fluorophore is excited by this light and when it relaxes, emits light of a longer wavelength, that can than be collected and used to create an image of either individual, or composite super structure the fluorophores. This can be achieved with a reflection microscope setup as shown in figure 2.16.

If using a broad band UV-Vis light source, the excitation light passes through a dichroic mirror and set of filters are used to split the light by its wavelength, transmitting longer wavelengths whilst shorter wavelengths are reflected. The red lines in figure 2.16 show the path the light takes from the light source to the sample that receives only shorter wavelengths and then re-emits longer wavelengths that pass through the dichroic mirror and can be directed to the spectrometer and/or eyepieces/camera depending on microscope setup. If a laser is used as the excitation light source, a similar method is used but rather than splitting the excitation light into shorter and longer wavelengths using a dichroic mirror and filters, only the light emitted and reflected by the sample needs to be filtered to only collect the light that has been emitted by the fluorophore, and not any of the excitation light that may have been reflected/scattered by the sample. Similarly to POM, the a Leica DM2700 was also used for FM, however, in some cases, for higher resolution and/or to excite QDs with different excitation wavelengths, a Zeiss LSM880 + Airyscan Upright Confocal Microscope was used.

2.4.6 Dielectric Spectroscopy

2.4.6.1 Fundamental Theory

The dielectric and conductive properties of a material are measured using Impedance/Dielectric spectroscopy. An alternating electric field is applied across a parallel plate capacitor, which is capillary filled with the LC sample and the frequency dependant impedance measured. Complex impedance is analogous to resistance: it has the same Ohm-like relation to the voltage and current. The difference, however, is that resistance is a measure of the opposition to the flow of direct current (dc) whereas impedance is a measure of the opposition to the flow of an alternating current. If a sinusoidal voltage is applied across the sample, then the resulting current will also be sinusoidal, but with a phase difference between the two:

$$V(\omega) = V_0 e^{j\omega t} \tag{2.11a}$$

$$I(\omega) = I_0 e^{j\omega t - \phi} \tag{2.11b}$$

where ϕ is the phase angle between the applied voltage and resulting current. The impedance is therefore defined by:

$$Z^* = \frac{V}{I} = \frac{V_0 e^{j(\omega t)}}{I_0 e^{j(\omega t - \phi)}} = |Z|e^{j\phi}, \tag{2.12}$$

where $|Z| = \frac{V_0}{I_0}$ is the magnitude of the impedance. Using Euler's formula, impedance may also be represented in the complex form:

$$Z^* = |Z|e^{j\phi} = Z' + jZ'', \tag{2.13}$$

where Z' and Z'' are the real (resistance) and imaginary (reactance) components of the impedance,

$|Z|$ is the magnitude of the impedance and ϕ is the phase angle between the applied voltage and the measured current, which is related to the impedance by:

$$\tan\phi = \frac{Z''}{Z'}. \tag{2.14}$$

When describing dielectric materials, it is more conventional to use the complex capacitance C^* which is related Z^* by:

$$C^* = \frac{1}{j\omega Z^*}, \tag{2.15}$$

that again, can be written in the form:

$$C^* = C' + jC'' = |C|e^{j\delta} \tag{2.16}$$

where C' is the real component and C'' is the imaginary component of capacitance. However, all of the quantities discussed so far depend on the sample dimensions and thus it is necessary to relate these to geometrically independent quantities that describe the properties of the material, such as the permittivity and conductivity. In frequency domain dielectric measurements, the permittivity is defined in the same (frequency dependant) complex form as the impedance and capacitance:

$$\epsilon^*(\omega) = \epsilon'(\omega) + j\epsilon''(\omega) = |\epsilon|e^{j\delta}, \tag{2.17}$$

where ϵ' & ϵ'' are the real and imaginary components of the complex permittivity respectively (real permittivity and dielectric loss) and δ is the loss angle. Again, the loss tangent can be related to the real and imaginary parts of the permittivity as well as capacitance:

$$\tan\delta = \frac{\epsilon''}{\epsilon'} = \frac{C''}{C'} = \frac{1}{tan\phi} \tag{2.18}$$

For a uniform parallel plate capacitor without edge effects, the capacitance and permittivity are related through the active electrode area A and the sample thickness d:

$$C = \frac{\epsilon_0\epsilon_r A}{d} \tag{2.19}$$

where ϵ_0 is the vacuum permittivity and ϵ_r is the relative permittivity of the sample. In the case of an empty (air filled capacitor) it is assumed that $\epsilon_r = 1$ and so the capacitance of the empty cell is:

$$C_0 = \frac{\epsilon_0 A}{d} \tag{2.20}$$

Provided that the empty and filled capacitor dimensions are the same, the frequency dependent permittivity of a material can be calculated through the ratio of the filled and empty cell capacitance:

$$\epsilon = \frac{C}{C_0} \tag{2.21}$$

The frequency dependent complex permittivity can also be directly related to the impedance through the angular frequency and C_0:

$$\epsilon^*(\omega) = \frac{1}{j\omega C_0 Z^*(\omega)}. \tag{2.22}$$

By expressing both $\epsilon^*(\omega)$ and $Z^*(\omega)$ in complex form and rearranging equation 2.22 it is possible to find expressions for the real permittivity and dielectric loss in terms of the real and imaginary components of the impedance:

$$\epsilon' = \frac{-Z''}{\omega C_0 |Z|^2} \tag{2.23a}$$

$$\epsilon'' = \frac{Z'}{\omega C_0 |Z|^2}. \tag{2.23b}$$

It can be seen from equation 2.23a, that the real part of the permittivity is proportional to the reactance and equation 2.23b shows that the dielectric loss is proportional to the resistance. Physically, this is because ϵ' is a measure of how well a material can store electrical energy, i.e. the reactance $Z'' = -\frac{1}{\omega C}$, whilst ϵ'' on the other hand, describes how 'lossy' the material is, i.e. how much energy is dissipated due to the flow of current which results from the alternating field and is therefore proportional to the resistance Z'. To give a measure of a material's geometrically independent resistance to the flow of charge, the resistivity is used:

$$\rho = \frac{RA}{d}, \tag{2.24}$$

where R is the resistance of the sample, A and d are the active electrode area and sample thickness respectively. The inverse of the resistivity is the conductivity, which can be defined in terms of the conductance $G = \frac{1}{R}$, the inverse of resistance:

$$\sigma = \frac{1}{\rho} = \frac{Gd}{A}. \tag{2.25}$$

Analogously to the permittivity, the conductivity may be expressed in a frequency dependent complex form and is related to the complex permittivity:

$$\sigma^*(\omega) = \sigma'(\omega) + j\sigma''(\omega) = j\omega\epsilon_0\epsilon^*(\omega). \tag{2.26}$$

Writing $\epsilon^*(\omega)$ in complex form, the real and imaginary parts of σ^* can be found:

$$\sigma'(\omega) = \omega\epsilon_0\epsilon''(\omega) \tag{2.27a}$$

$$\sigma''(\omega) = \omega\epsilon_0\epsilon'(\omega) \tag{2.27b}$$

In the case where there is no contribution to ϵ' (from 'bound' charges) the d.c. conductivity can be attained from equation 2.27b:

$$\sigma_0 = \epsilon''(\omega)\epsilon_0\omega \tag{2.28}$$

2.4.6.2 Practical Implementation

Dielectric spectroscopy measurements were performed using either an Agilent E4980A or a Novocontrol Alpha-A analyser depending on the range of frequencies and voltages to be applied. The Agilent E4980A was used to apply a frequency range of $20Hz - 2MHz$ at voltages of $0.05V_{rms} - 20V_{rms}$ to the LC test cells. The Novocontrol Alpha-A was used to apply a broader frequency range of $0.1mHz - 10MHz$ but at lower voltages of $0.1V_{rms} - 1V_{rms}$. In all cases, the LC test cells were mounted on a Linkam hot stage for temperature control.

To electrically connect the LC test cells to the dielectric spectrometers, three 30cm long wires with diameters of $0.25mm$ were soldered using indium to the exposed ITO of the three electrodes on the glass substrates (figure 2.18(b)). These wires were then fed out of the holes in the Linkam hot stage housing to connect to the dielectric spectrometer. The wires soldered to the active and addressor electrodes were connected to two coaxial BNC cables coming from the dielectric spectrometer with kelvin clips and the wire soldered to the guarding/ground electrode was connected to the ground of the dielectric spectrometer, which can be seen in the photographs shown in figures 2.18(d) and 2.18(e) for the Agilent and Novocontrol dielectric spectrometers respectively.

To measure the dielectric properties of the PI thin film ALs, the films were prepared on a GR substrate as described in subsections 2.2.2 and 2.2.4 which then had a layer of conductive polymer (PEDOT:PSS) spun down to act as the addressor electrode directly in contact with the PI film. To connect the wires, a conductive epoxy was used to bond the wire to the PEDOT film as can be seen in figure 2.18(c). A more comprehensive discussion of how all dielectric measurements were performed, as well as how to interpret and analyse the data is given in Chapter 3.

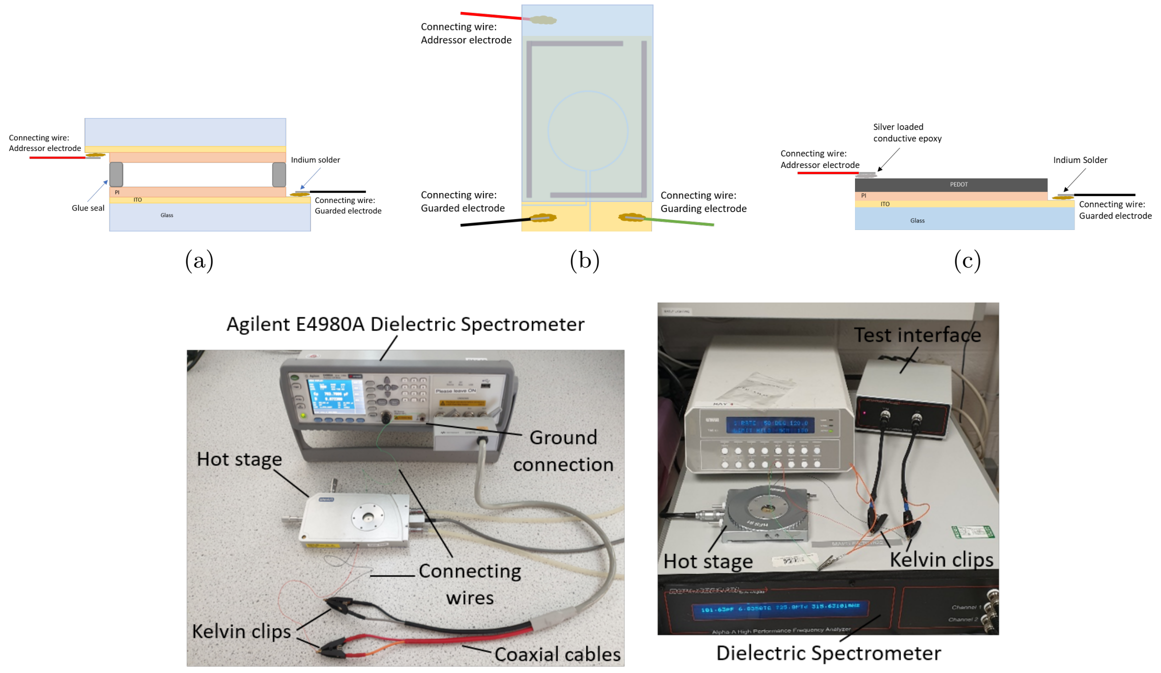

(a) (b) (c)

(d) (e)

Figure 2.18: Schematic diagrams showing how electrical connections between the GR LC tests cells and the dielectric spectrometers shown with a) side on view and b) top down view. c) the method used for measuring the dielectric properties of the PI thin films.

2.4.7 Refractometry

Refractive index measurements of the pure LC and the QD-LC nanocomposites were performed using an Abbé refractometer to find both the ordinary (n_o) and extraordinary (n_e) refractive indices, as well as the isotropic refractive index (n_{iso}). An Abbé refractometer consists of two prisms of high refractive index (higher than the refractive index of the liquid to be measured), between which the liquid sample to be measured is placed. In the case of LC materials, the LC must be aligned between the prisms either in HT or PH alignment. To achieve the HT alignment, a monolayer coating of Cetyltrimethyl ammonium bromide (CTAB) was used and to achieve PH alignment, a thin film of PVA was coated onto the prisms and rubbed perpendicular to the direction of propagation of light into the prisms.

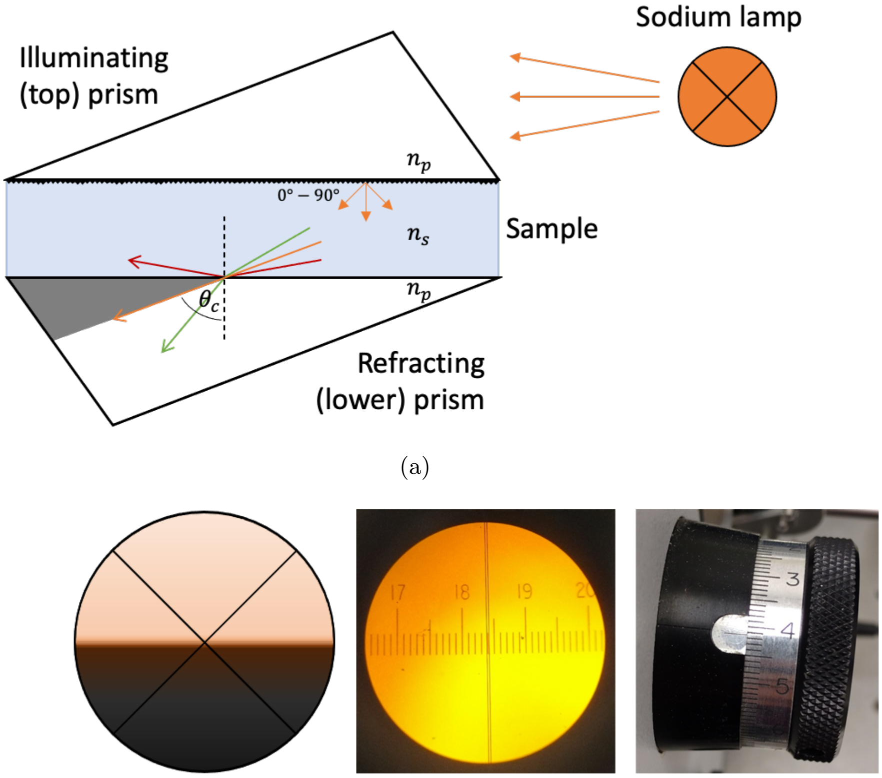

(a)

(b) (c) (d)

Figure 2.19: a) Schematic representation of an Abbé refractometer operating principal. b) dark line from total internal reflection when viewed through the eyepiece and positioned correctly on cross-hairs. c) angle scale when viewed through the second eyepiece. d) Vernier scale used to find second and third decimal places of angle of total internal reflection.

To illuminate the sample, monochromatic light produced by a sodium lamp emitting at $589nm$ was used. The light is passed through the top prism, where it is refracted towards the sample, the surface of this prism is rough and thus scatters the light at the interface between the sample and the prism, ensuring that light passes into the sample at all angles ($0° - 90°$ relative to the prism surface normal). The light is refracted as it passes into the sample and propagates towards the lower prism. Once the light has passed through the sample to the lower prism, depending on the angle of incidence at the interface, some of the light is transmitted and refracted by the lower prism and some is reflected as is shown in 2.19(a).

Light incident on the lower prism at a glancing angle is refracted at the critical angle θ_c, which is the angle measured when using the Abbe refractometer. At $\theta < \theta_c$, light is transmitted and refracted by the lower prism, whereas at $\theta > \theta_c$, light is totally internally reflected and thus appears as a dark band when viewed through the eyepiece (figure 2.19(b)). To measure θ_c, a rotatable mirror reflects the refracted light into a telescope and by orienting the mirror such that the top of the dark band is positioned on the cross-hairs as in figure 2.19(b). The angle of the mirror and therefore θ_c is then measured using a telescopic vernier. The vernier scale (figure 2.19(d)) is adjusted such that the scale shown in figure 2.19(c) lies with the two long vertical lines are either side of the single decimal place scale division marker. θ_c measured to the first decimal place is then read from the scale shown in figure 2.19(c) followed by the second and third decimal places read from the vernier scale shown in figure 2.19(d).

In the case of a birefringent sample such as LCs, the light is split into two linear polarisation states, one of which experiences n_e and the other experiences n_o. When measuring the two values of θ_c for a birefringent material, a linear polariser can be used to make the dark region corresponding to the totally internally reflected light experiencing n_o clearer by blocking out the light polarised at 90° which has experienced n_e and thus has been transmitted and refracted through the lower prism. The value of the refractive indices of the sample can then be calculated by using:

$$n_s = n_p sin\theta_c, \tag{2.29}$$

where n_s is the refractive index of the sample and n_p is the refractive index of the prism. Since the refractive index of the prism changes with temperature, it is necessary to account for this and therefore use the Abbe scale conversion charts to convert the measured θ_c to n_s.

2.4.8 Pretilt Measurements

Measurements of the pretilt θ_p of the pure LC and QD-LC nanocomposites in LC test cells were performed using a modified crystal rotation method capable of measuring pretilt angles anywhere between 0 and 90° [148]. The LC test cell is positioned between a crossed polariser and analyser with the optic axis (rubbing direction in a PH cell) of the LC oriented at 45° to to the polariser and analyser. The transmittance as a function of the rotation angle of the cell β is measured using a photodiode as the cell is rotated. The positions of the minima and maxima in the measured transmittance can be used to calculate θ_p which is measured as the angle of the

LC from the plane of the substrates. A schematic diagram of the experimental setup is shown in figure 2.20.

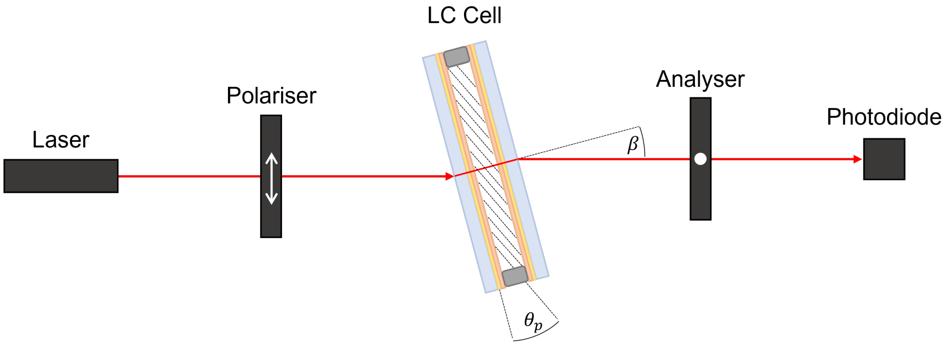

Figure 2.20: Schematic of LC pretilt measurement with LC test cell positioned between crossed polariser and analyser with the optic axis oriented at 45°. the dashed lines within the LC test cell represent the orientation of the director and the dashed lines outside of the cell represent the axes normal to and in the plane of the substrates.

The transmittance as a function of θ_p and β can be modeled using equation 2.30 [148]:

$$T = \frac{1}{2} sin^2 \left[\frac{\pi d}{\lambda} f(\theta_p, \beta) \right] \tag{2.30a}$$

$$f(\theta_p, \beta) = \frac{1}{c^2}(a^2 - b^2) sin(\theta_p) cos(\theta_p) sin(\beta) + \frac{1}{c}\sqrt{\left(1 - \frac{a^2b^2}{c^2} sin^2(\beta)\right)} - \frac{1}{b}\sqrt{1 - b^2 sin^2(\beta)} \tag{2.30b}$$

$$c^2 = a^2 cos^2(\theta_p) + b^2 sin^2(\theta_p) \tag{2.30c}$$

where $a = \frac{1}{n_e}$ and $b = \frac{1}{n_o}$, the values used for n_e and n_o are those found for the pure LC and QD-LC nanocomposites measured at the same temperature as the pretilt measurement as described in the previous section 2.4.7. For a cell with a known cell gap d and light with wavelength λ, the positions of the maxima and minima in the measured transmittance can be modeled by tuning the values of θ_p. For the measurements performed in this work, a red $\lambda = 633nm$ laser was used and the LC test cells rotated through $-40° \leq \beta \geq 40°$.

2.4.9 Light Scattering

Light Scattering (LS) techniques utilise the scattering of electromagnetic radiation from matter specifically in the visible wavelength range. Other scattering techniques may utilise different wavelength ranges such as x rays, the choice of wavelength length range and hence the scattering technique used depends upon the length scale and order within a system one intends to probe.

The general principles of LS are, however, valid for these other types of scattering techniques. When light interacts with matter, it may be scattered elastically or in-elastically; in the case of elastic scattering of visible light from particles much smaller than the wavelength of light ($\lesssim 0.1\lambda$), isotropic scattering is observed and thus the Rayleigh scattering regime is applicable [149]. For particles of larger sizes or for shorter wavelengths ($\gtrsim 0.1\lambda$), the Rayleigh scattering model breaks down due to anisotropic scattering, at which point, Mie theory better describes the intensity of the scattered radiation and it's angular dependence. The simpler case of Rayleigh scattering is first discussed here. In a Cartesian coordinate system, linearly polarised light (electric field oscillating in the x-direction) propagating along the z-direction can be described in both space and time by:

$$E(z,t) = E_0 cos\Bigg(2\pi\big(\nu t - \frac{z}{\lambda}\big)\Bigg), \tag{2.31}$$

where E_0 is the amplitude, ν is the frequency and λ is the wavelength of the wave in a vacuum - both the speed and wavelength will be attenuated by a factor equal to the inverse of the refractive index of the medium through which the light is propagating. Consider the interaction of this light with a particle located at the origin, the electrons in the particle oscillate with the electric field, inducing a dipole moment, P, which takes the form:

$$P = \alpha E = E_0 cos\Bigg(2\pi\nu t\Bigg), \tag{2.32}$$

where α is the polarisability of the particle and c is the speed of light in a vacuum. An oscillating dipole emits light in all directions due to the acceleration of the charged particles, thus the scattered light at a point r from the particle is proportional to the second derivative with time of the induced polarisation of the particle [150]:

$$E_s = \frac{1}{c}\frac{1}{r}\frac{d^2P}{dt^2}\bigg|_{t'-\frac{r}{c}} = -\frac{4\pi^2}{\lambda^2 r}\alpha E_0 cos\Bigg(2\pi\nu\big(t - \frac{r}{c}\big)\Bigg). \tag{2.33}$$

The intensity of the wave scattered from the particle is proportional to the mean-square average of the field, which if multiplied by the number of scatterers N, the familiar λ^{-4} dependence of Rayleigh scattering is obtained:

$$I_s = \frac{16\pi^4 N\alpha^2 I_0}{\lambda^4 r^2}, \tag{2.34}$$

where I_0 is the intensity of the incident light.

A generalised LS setup is depicted in figure 2.21, where a monochromatic, coherent light source such as a laser is used to shine light through the sample. Provided the sample is a disordered system, the light is scattered in all directions, producing what is known as a speckle pattern which consists of bright and dark regions resulting from the constructive and destructive interference of the scattered light respectively. The speckle pattern will appear to 'blink'/'flicker' as a result of thermal or other types of motion within the sample. Before reaching the sample, however, the incident light first passes through a polariser and then a beam splitter, enabling polarisation control and a direct measurement of the incident light intensity by the first detector. The detector arm consists of an analyser, an optical-fibre and a second detector is positioned at an angle θ to the z-axis (in the y-z plane for 2d LS). An optical fibre is used to in order to collect light from a specific region of the speckle pattern to send to the detector [151], normally an avalanche photo-diode [152].

The incident and scattered light can be described by their wavevectors, $\vec{q_i}$ and $\vec{q_s}$, respectively. In the Rayleigh scattering regime, these wavevectors are of the same magnitude, $|\vec{q_i}| = |\vec{q_s}| = \frac{2\pi n}{\lambda}$ where n is the refractive index of the sample and λ is the vaccuum wavelength of both the incident and scattered light. Thus the only difference between the incident and scattered wavevectors is their direction, meaning the we can define the scattering vector as the difference between the two:

$$q \equiv \vec{q_i} - \vec{q_s} = 2|\vec{q_i}|sin\left(\frac{\theta}{2}\right) = \frac{4\pi n}{\lambda}sin\left(\frac{\theta}{2}\right) \tag{2.35}$$

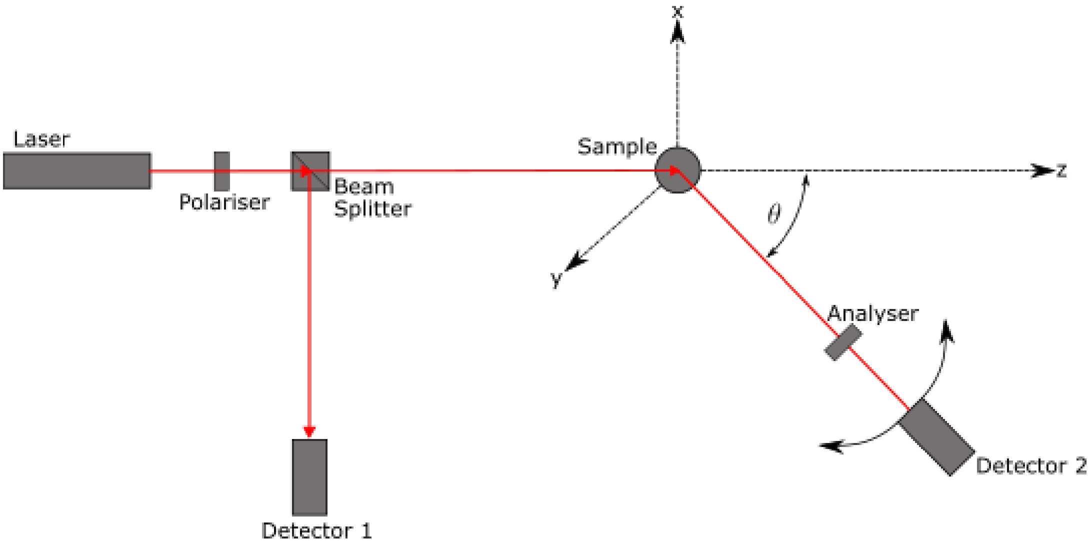

Figure 2.21: Schematic of a general light scattering setup that could be used for both static and dynamic light scattering experiments.

2.4.9.1 Static Light Scattering

In static light scattering (SLS), the angular dependence of the time-averaged scattered intensity of light shone through a sample of particles dispersed in a solvent is used to determine the particle sizes. As mentioned earlier, in order for an angular dependence of scattering intensity to manifest, the particle size must be large enough in comparison to the wavelength of incident light ($\gtrsim 0.1\lambda$). In this case, the angular dependence resulting from the geometry of the particle is described by the form factor:

$$P(q) \equiv \frac{I(q)}{I(0)}, \tag{2.36}$$

where $I(q)$ is the scattered intensity at wave vector q and $I(0)$ is the scattered intensity when $q =$ 0 - i.e. when the detector is positioned at $\theta = 0$ (see figure 2.21) . Equation 2.36 can be visualised by plotting $P(q)$ against q where $P(q)$ will drop drop-off with increasing q less substantially than for larger particles. To accurately determine $P(q)$ experimentally,it is necessary to account for the angular dependence arising from the experimental setup as well as the solvent used to disperse the particles in. In order to do so, the excess Rayleigh ratio is used:

$$\Delta R(q) = \frac{I_s(q) - I_{solv}(q)}{I_{ref}(q)} \left(\frac{n_s}{n_{ref}} \right)^2 R_{ref} \tag{2.37}$$

where I_s(q) is the scattered intensity from the sample, $I_{solv}(q)$ is the scattered intensity from the pure solvent, I_{ref} is the scattered intensity from a reference sample, n_s and n_{ref} are the refractive indices of the sample and reference sample respectively and R_{ref} is the Rayleigh ratio of the reference sample. Note that the reference quantities can be taken from literature but must be for the same temperature and incident wavelength as the measured values. Additionally, all intensity values can be normalised with respect to the incident laser intensity [153]. Plotting the result of equation 2.37 against q, it is possible to ascertain any changes in the particle sizes for instance due to aggregation at higher concentrations etc.

2.4.9.2 Dynamic Light Scattering

Dynamic light scattering (DLS) utilises the intensity fluctuations with time of a small 'bright' region of the speckle pattern, often, this is done by using a fibre optic to collect the light to send to the detector. These intensity fluctuations result from the Brownian motion of the individual particles in the sample. The light scattered from each particle interferes with itself either constructively or destructively depending upon the path difference created by the particles motion and thus fluctuates in time. The rate at which the light intensity fluctuates is related to the timescale of the diffusive motion of the particles which is dependant upon their size. The scattered light intensity is monitored in time using a photon correlation spectrometer, enabling the intensity correlation function to be measured:

$$g_2(\tau) = \frac{< I(t)I(t+\tau) >}{< I(t) >^2}, \tag{2.38}$$

where t is a an instantaneous point in time (often $t = 0$), τ is the lag time (length of time after time t) and $<>$ denotes an average over time. The intensity is first recorded at time, t and subsequently at intervals, τ after t; generally ranging from $\tau \approx ns - s$ over which time g_2 undergoes an exponential decay. The intensity auto correlation function is related to the field auto correlation function through the Siegert relation:

$$g_2(\tau) = 1 + \sigma[g_1(\tau)]^2 \tag{2.39}$$

where σ is an empirically determined parameter dependant upon the experimental setup which can be found from the intercept of a $g_2(\tau) - 1$ against τ plot and $g_1(\tau)$ is the field correlation function:

$$g_1(\tau) = \frac{< E(t)E^*(t+\tau) >}{< E(t)E^*(t) >}. \tag{2.40}$$

$g_1(\tau)$ will also undergo an exponential decay with respect to τ; for a monomodal and monodisperse particle population this decay can be described by a single exponential for either the field or intensity correlation function:

$$g_1(\tau) = e^{-\Gamma\tau}, \tag{2.41a}$$

$$g_2(\tau) = A + Be^{-2\Gamma\tau}, \tag{2.41b}$$

where $A \approx 1$ and $B \approx \sigma$ through the Siegert relation (equation 2.39 and Γ is the decay rate which holds the information about the size of the particles hydrodynamic radius, which can be determined from the scattering vector and the Stoke's-Einstein equation:

$$D = \frac{\Gamma}{q^2} = \frac{K_B T}{6\pi\eta R_h}, \tag{2.42}$$

where K_B is Boltzmann's constant, T is the temperature of the sample, η is the solvent viscosity at temperature, T and R_h is the hydrodynamic radius. It is often necessary, however, to fit DLS data from a polydisperse or multimodal particle population i.e. the particles in the solution are of a range of sizes centred around an average particle size or are of multiple different sizes or even both. In which case, a single exponential is no longer sufficient to describe the shape of the correlation functions and more complex fitting functions are required. One such method commonly used to describe a polydisperse sample is to use a cumulant analysis where a Taylor expansion around a central average decay rate is performed:

$$g_1(\tau) = e^{-\bar{\Gamma}\tau}\left[1 + \frac{\mu_2\tau^2}{2!} - \frac{\mu_3\tau^3}{3!}\right], \tag{2.43a}$$

$$g_2(\tau) = A + Be^{-2\bar{\Gamma}\tau}\left[1 + \frac{\mu_2\tau^2}{2!} - \frac{\mu_3\tau^3}{3!}\right], \tag{2.43b}$$

where A and B are fitting parameters and μ_i are the moments of the distribution, with $\mu_1 = 0$ by the definition of $\bar{\Gamma}$, whilst μ_2 and μ_3 are the variance and skew of the decay rate distribution respectively:

$$\mu_i = \int_0^\infty (\Gamma - \bar{\Gamma})G(\bar{\Gamma})d\Gamma, \tag{2.43c}$$

$\bar{\Gamma}$ is the average decay rate defined as a function of the decay rate distribution, $G(\Gamma)$:

$$\bar{\Gamma} = \int_0^\infty \Gamma G(\Gamma)d\Gamma. \tag{2.43d}$$

This distribution can be used to find the average hydrodynamic radius from equation 2.42, whilst the polydispersity index (PDI) can be obtained through the second moment of the distribution:

$$PDI = \sqrt{\frac{\mu_2}{\bar{\Gamma}^2}} \tag{2.43e}$$

Fitting equations 2.43a or 2.43b can be done with a least squares fitting routine to obtain values for A, B, μ_i and $\bar{\Gamma}$. In the case of multimodal distributions, the cumulant method is inadequate since it only allows a single average decay rate value to be determined. In order to determine a number of decay rates resulting from multimodal particle size distribution, another alternative method could be to used, for instance, a bimodal distribution:

$$g_1(\tau) = \alpha e^{-\Gamma_1\tau} + (1-\alpha)e^{-\Gamma_2\tau}, \tag{2.44}$$

where Γ_i is the decay rate corresponding to the i^{th} particle size and α is the fraction of intensity scattered by particle 1. This method is rather limited however, since it is assumed the i^{th} particle distribution is monodisperse which may not be the case. To analysing DLS data from polydisperse multimodal particle distributions more complex methods must be employed to find the true decay rate distribution such as performing a regularised inverse Laplace transform on $g_1(\tau)$:

$$g_1(\tau) = \mathcal{L}\big[G(\Gamma)\big] = \int_0^{\infty} e^{-\Gamma\tau} G(\Gamma) d\Gamma, \tag{2.45a}$$

$$\Rightarrow G(\Gamma) = \mathcal{L}^{-1}\big[g_1(\tau)\big]. \tag{2.45b}$$

There are some important considerations to be taken when using the inverse Laplace transform in this manner; since the problem is ill-posed, great care must be taken to ensure the $G(\Gamma)$ result attained is physically reasonable and even then, this does not mean the result truly represents the particle size distribution. As a result, a number of regularisation methods have been developed in order to perform the inverse Laplace transform and converge on a valid and physically appropriate solution. Such methods include Provencher's 'CONTIN', a constrained regularisation algorithm written in FORTRAN for inverting noisy multi exponential data satisfied by a linear integral equation such as equation 2.45a [154][155]. Since the development of 'CONTIN', its widespread use has lead others to write their own versions of the program in other computing languages based on Provencher's algorithm. One such function called 'rilt' (regularised inverse Laplace transform) has been written in Matlab by Marino [156]. An alternative method to performing an inverse Laplace transform to determine the decay rate distribution from a polydisperse and/or multi-modal particle population, one could use a stretched and/or a sum of stretched exponentials: noisy

$$g_1(\tau) = \sum_{i=1}^{n} A_i e^{-(\Gamma_i \tau)^{\beta_i}}, \tag{2.46}$$

where A_i is the intensity contribution, Γ_i is the average decay rate and $0 \leq \beta_i \leq 1$ is the stretching parameter for the i^{th} particle size. Equation 2.46 can equally be used to model $g_2(\tau) - 1$ data. There are some limitations associated with using 2.46 to fit experimental DLS data; the particle size distribution is assumed to be symmetrical about the average decay rate for each particle size and information regarding the polydispersity of the contained within the stretching parameter, unlike inn the cumulant method, cannot easily be converted into a numerical value for the polydispersity index.

2.5 Summary

In this chapter, the basic principles of all experimental methods and techniques used in this thesis have been covered. The first section explained the method of fabricating the LC devices used to characterise the samples, the second section described how the samples were prepared and the third section explained how each of the characterisation techniques work at a fundamental level. A more detailed description of how some of these techniques were implemented and how the data collected was processed/analysed can be found in later chapters.

Chapter 3

Dielectric Spectroscopy for the Determination of Permittivities and Elastic Constants of LCs and LC Nanocomposites

3.1 Introduction

The fundamentals of dielectric materials and the general experimental technique of dielectric spectroscopy were introduced in sections 1.1.4 and 2.4.6. This chapter will focus on the application of dielectric spectroscopy for the characterisation of NLCs and LC nanocomposites. Most dielectric studies of LCs and LC nanocomposites are only performed using narrow frequency ranges, typically around the kHz region to determine the static permittivities and elastic constants [48, 50, 71, 82, 157, 158]. There have, however, been several studies which focus on the dielectric behaviour and effect of ionic impurities in the LC at lower frequencies (mainly in the Hz range) [159, 160, 161]. To describe the dielectric behaviour including the influence of ions and the formation of electrical double layers at these frequency ranges, equivalent circuit analysis techniques can be used [162, 163, 164]. Here, a much wider frequency range of mHz - MHz is studied, within which, the effects of ionic impurities and the formation of electrical double layers causing electrode polarisation (EP) are present, in conjunction with the influence of the LC test cell.

Since NLCs are anisotropic dielectric liquids, it is necessary to align uniformly the LC when performing dielectric spectroscopy to measure the dielectric properties either parallel ($\epsilon_{\|}$) or perpendicular ($\epsilon_{\perp}$) to $\mathbf{n}$. To do this, dielectric spectroscopy must be performed using specially designed/constructed LC test cells (refer to 1.1.6.1 and 2.2). It is also possible to use such uniformly aligned cells to determine the elastic properties of the LC by measuring the dielectric properties as a function of the applied voltage, hence measuring whilst the LC is undergoing a Fréedericksz transition (refer to section 1.1.6.2 of chapter 1). Thus, to accurately determine these properties, it is necessary to understand how the LC test cell, as well as interactions between the LC and the test cell affect the dielectric spectroscopy measurements. This of course introduces the added complexity of how the thin film PI ALs used to align the LC affect the measurements being taken.

To develop a more holistic understanding of this, the contributions to the complete complex dielectric spectra of the individual components which comprise the LC test cell and LC sample were studied. The dielectric frequency response of empty LC test cells were measured, as well as the thin film PI ALs used to make the cells. Specifically, the PIs SE130 and SE1211 (Nissan Chemicals) were used as the PH and HT ALs, as in the rest of the work performed (the cells were constructed as described in the previous chapter, section 2.2). Test cells without ALs (NAL cells) were also used. These cells and their specifications are listed in table 3.1.

To simply matters, the isotropic liquid PCH32 was used in place of the NLC to fill the test cells. The molecular structure of PCH32 is similar to that of common CB NLCs (see figure 2.10(a)), but instead of the rigid biphenyl core, PCH32 has a single phenyl group connected to a cyclohexane, which reduces the rigidity in the core of the molecule, thus preventing the formation of LC phases. The absence of macroscopic anisotropy, enabled the effects of the LC test cell across a range of temperatures to be studied without having to consider the effects of alignment, applied voltage and director reorientation on the resulting dielectric spectra of the filled cells. Equivalent circuit analysis of the dielectric spectroscopy data was then performed and the methodology used is presented here. This includes the contributions of individual circuit components/elements to the dielectric spectra, as well as how to combine them to model more complex spectra, such as that found from dielectric liquids in LC test cells.

Following this, dielectric spectroscopy measurements of the high $\Delta\epsilon$ NLC MLC6204 were performed in $5\mu m$ and $20\mu m$ PH and HT cells for comparison. The measurement methods to accurately determine the dielectric properties of NLCs is covered, in particular, the method required to accurately measure $\epsilon(V)$ curves of NLCs and the considerations that must be made when performing such measurements are discussed. The effects of alignment layers on these measurements were studied and an equivalent circuit approach was developed and used to correct the $\epsilon(V)$ curves prior to fitting in order to more accurately determine the elastic and dielectric properties of the LC. The fitting routine used was specifically developed to further improve the accuracy of elastic constant and permittivity measurements for high $\Delta\epsilon$ NLC such as MLC6204.

3.2 Dielectric Spectroscopy Measurements in LC Devices

3.2.1 Measurement Procedure

Once the LC test cells had been constructed and their cell gaps measured, dielectric spectroscopy measurements of the empty cells were then measured across a frequency range of 100mHz-10MHz at a voltage of $1V_{rms}$. Measurements were taken on cooling at $30°C$ intervals from $120°C$ to $30°C$ for the NAL cells and from $150°C$ to $30°C$ for the SE1211 cells. A cooling rate of $10°C/min$ was used, with a temperature stabilisation time of 1 minute prior to performing the measurement once the desired temperature had been reached. The cells were held at their first measurement temperature of $120°C$ for 5 minutes prior to performing any measurements, to ensure that moisture was evaporated from the cells. Connection of the cells to the dielectric spectrometer, is made through $\approx 0.1\Omega$ $30cm$ long copper wires, soldered to the ITO electrodes via gold plated Kelvin clips. This allowed the cells to be placed on a Linkam hotstage for temperature control (as described in 2.4.6).

Following the empty cell measurements, dielectric spectroscopy measurements of the filled cells were then performed across a frequency range of 10mHz-10MHz at three temperatures on cooling of 75, 50 and $25°C/min$. A temperature stabilisation time of three minutes was used at each temperature prior to performing the measurements. All spectra were collected using a logarithmic frequency scale as this provides the best balance between time spent performing the measurements and collecting enough data to resolve the processes that take place across the full frequency ranges. It should be noted that the cooling rates and temperature stabilisation times can and should be chosen appropriately for the material being measured. When using LC materials, it is necessary cool through the isotropic-nematic transition at a slow enough rate to ensure good alignment is achieved in the nematic phase. Additionally, since the anisotropic properties of LCs are dependent on their alignment and temperature dependent orientational order, a longer temperature stabilisation time is typically required compared to measurements of an isotropic material, where alignment and orientational order effects can be neglected. The nuances of specific types of LC dielectric spectroscopy measurements are discussed in further detail later in this chapter.

Table 3.1: Cells of $5\mu m$ nominal thickness used for studying the effects of the LC test cell on dielectric spectroscopy measurements.

Cell	AL	Filling Mixture	$d(\mu m)$
5NAL-1	None	PCH32	5.61 ± 0.06
5NAL-2	None	0.1%TBATPB-PCH32	5.59 ± 0.04
5SE1211-1	PI SE1211	PCH32	5.28 ± 0.08
5SE1211-2	PI SE1211	0.1%TBATPB-PCH32	5.2 ± 0.1

3.2.2 Dielectric Spectra of Empty LC Test Cells

As previously discussed in section 2.4.6, when performing dielectric spectroscopy, the resulting current response across the LC test cell is measured whilst a sinusoidal voltage is applied across the cell. This enables the complex impedance or complex capacitance to be calculated (see equations 2.12 and 2.15). It is common for the frequency dependent complex impedance to be used to display the behaviour of predominantly dissipative/conductive materials, for instance highly ionic solutions. However, since here, the materials are weakly conductive dielectric liquids, it is more appropriate to represent the spectroscopy data in the form of the frequency dependent complex capacitance. This is particularly true if one wishes to display the data on a Cole-Cole plot, in which the imaginary component of the frequency dependent complex quantity is plotted against the real component [23]. For example, if the data is displayed in its complex impedance form when there is very little conduction, it becomes difficult to distinguish different features on the Cole-Cole plot and vice versa if the data is displayed in its complex capacitance form when there is very little capacitive behaviour, then again, the Cole-Cole plot becomes difficult to distinguish different features. Thus, all results here are displayed as the frequency dependent complex capacitance and on Cole-Cole plots.

The frequency dependent complex capacitance of the empty 5NAL-1 and 5SE1211-1 cells are shown in figure 3.1. The frequency dependent complex capacitance of the 5NAL-2 and 5SE1211-

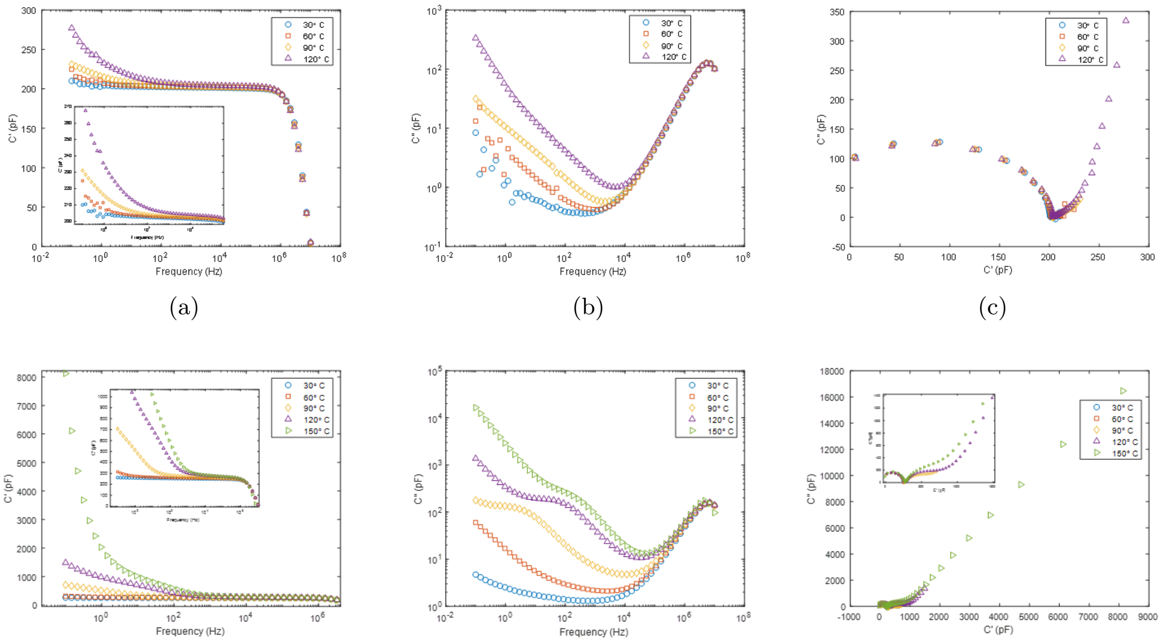

(a) (b) (c)

(d) (e) (f)

Figure 3.1: Complex capacitance spectra of empty LC test cells. a) real capacitance against frequency, b) imaginary capacitance against frequency and c) Cole-Cole capacitance plot of $5\mu m$an empty NAL cell. d) real capacitance against frequency, e) imaginary capacitance against frequency and f) Cole-Cole capacitance plot of $5\mu m$an empty HT SE1211 cell.

2 cells are not shown here, but display the same behaviour as the 5NAL-1 and 5SE1211-1 cells, albeit with slightly different absolute values of C' and C" which arises from the different cell gaps between the cells. The behaviour of these cells is typical of any properly constructed LC test cell with a guarded electrode design. Thus, any differences in behaviour, such as the absolute values of C' or C" and/or changes in the frequency at which spectral features are seen then only arise from differences in cell gap and AL material and film thickness.

All empty cell spectra show three distinct features (figures 3.1(a) and 3.1(d)); the low frequency region, which shows an 'upturn' in C' as the frequency decreases; the intermediate frequency range which shows a plateua in C'; and a high frequency region which shows a 'roll off' as the frequency is increased from this platuea in C'. The low frequency 'upturn' can be attributed to electrode polarisation (EP) effects, which occur at low frequencies when ions in the device (glass/ITO in NAL cells and glass/ITO/PI for AL cells) migrate towards the electrodes and form a capacitive double layer, thus creating the increase in C'. As the frequency is increased, the EP effects subside and the value of C' approaches a plateau, this generally lies in the kHz frequency region. It is in this kHz plateau region that the value of the empty cell capacitance

C_0 is taken. At higher frequencies, this plateua of C' can be seen to 'roll-off', this is due to the series resistance of the electrodes and connecting wires.

Comparing the NAL and SE1211 cells, the addition of the PI thin film ALs significantly increases the low frequency EP, which is to be expected as the thin films which are directly in contact with the ITO electrode contain considerably more ionic impurities than the glass/ITO alone. The magnitude of the EP effect increases with increasing temperature in both the NAL and SE1211 cells, as expected. An additional loss peak in C" is present in the SE1211 cells at temperatures of $90°C$ and above, which shifts to higher frequencies as the temperature further increases. This loss peak corresponds to a process that takes place either within the PI thin film ALs. Taking the frequencies of these peak positions and plotting natural log of their corresponding timescale against 1/T shows Arrhenius-like behaviour, which suggests that this process is likely not ionic but rather a glassy relaxation process of the PI.

3.2.3 Dielectric Spectra of Isotropic Dielectric Liquids in LC Test Cells

The frequency dependent complex capacitance spectra of both NAL and SE1211 cells filled with PCH32 and 0.1wt%TBATPB-PCH32 can be seen in figures 3.2 and 3.3 respectively. Compared to the empty cell measurements, more significant EP effects are seen in the filled cells, with the most prominent EP arising in the cells filled with the salt doped mixture, as one would expected (figures 3.3(a) and 3.3(d)). Interestingly, the addition of ALs reduces the absolute magnitude of the EP when filled with either the pure PCH32 (figures 3.1(a) and 3.1(d)) or the salt doped PCH32 (figures 3.3(a) and 3.3(d)). Present at slightly higher frequencies than the EP effects in all filled cells are loss peaks in C" ($\sim 10Hz$ at $25°C$), which are not present in the empty cells. Unlike the loss peaks seen in the SE1211 empty cells (figure 3.1(e)), the loss peaks in the filled cells occur at much lower temperatures and do not show Arrhenius-like behaviour. It is therefore thought that these peaks correspond to ionic effects. A slight broadening of these peaks can also be seen due to the addition of the TBATPB salt to PCH32. The introduction of different ionic species which have different mobilities to the ionic species present in the pure PCH32, could cause this broadening, thus strengthening the conclusion that these peaks arise from ionic impurities.

In the AL cells, however, the $\sim 10Hz$ peak is much more prominent, both in the cells filled with the PCH32 (figure 3.2(e)) and in the cells filled with 0.1%TBATPB-PCH32 (figure 3.3(e)).

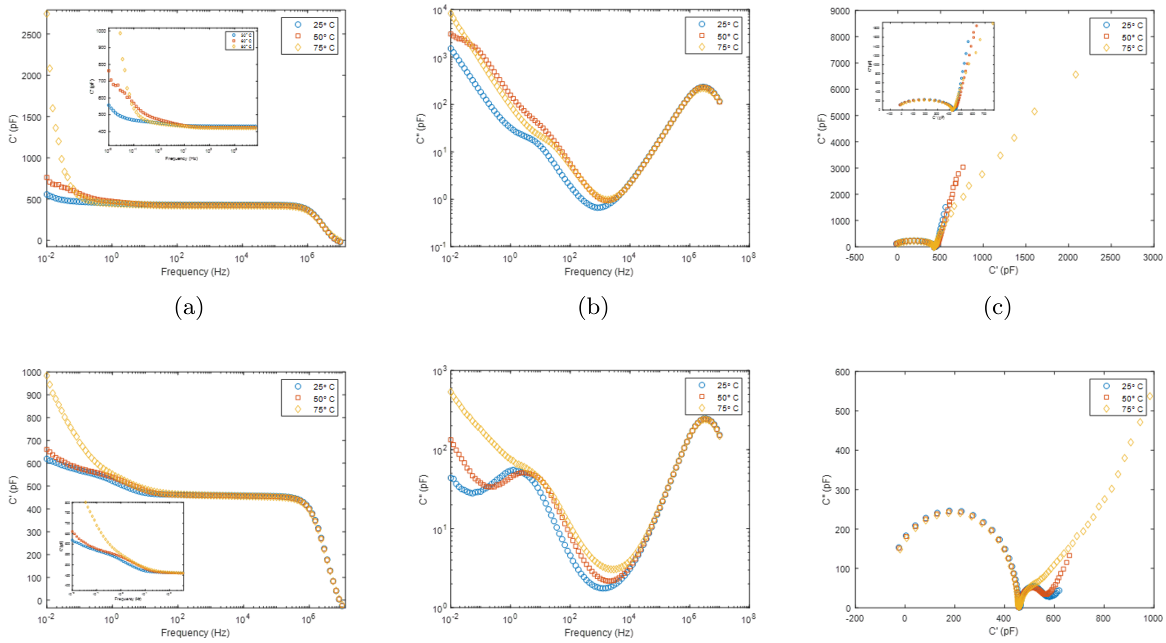

(a) (b) (c)

(d) (e) (f)

Figure 3.2: Complex capacitance spectra of PCH32 filled LC test cells. a) real capacitance against frequency, b) imaginary capacitance against frequency and c) Cole-Cole capacitance plot of 5μm NAL cell. d) real capacitance against frequency, e) imaginary capacitance against frequency and f) Cole-Cole capacitance plot of 5μm HT SE1211 cell.

This reduction in the magnitude of EP seen in C' and relative increase in the strength of the loss process attributed to Maxwell-Wagner polarisation [165, 166, 167] within the AL cells can be ascribed to the 'blocking effect' of the PI thin film ALs on the ITO electrodes. Films of dielectric materials have been used to coat electrodes in dielectric spectroscopy experiments as a means to reduce the ionic conductivity and EP in highly conductive electrolytes [168]. The implementation of blocking electrodes has been claimed to reveal hidden structural relaxation processes [169]. This has, however, been contested and the revealing of hidden loss peaks was attributed to ionic processes [170], as is thought to be happening here.

Thus, the loss peak seen in the case of the NAL cells can be attributed to EP and in the case of the SE1211 cells, these loss peaks can be attributed to Maxwell-Wagner interfacial polarisation (IP) at the interface between the dielectric liquid and the PI ALs. These two types of polarisation can be distinguished through the frequencies at which features are see in the C' and C" spectra [171]. The frequency of the loss peak in C" due to EP corresponds to the frequency at which the minimum in the second derivative of C' is found and the the frequency of the loss peak due to Maxwell-Wagner IP corresponds to the frequency of the inflection point in C’. Figure 3.4 shows the formation of an electrical double layer at low frequencies with (figure 3.4(b)) and without (figure 3.4(c)) ALs. It is clear that the addition of the ALs acts to block the double layer from forming in such close proximity to the ITO electrodes and therefore reduces the magnitude of the upturn in C’ and the C” at frequencies below the loss peak. An increase in the concentration of ionic impurities leads to both an increase in the magnitude of the upturn seen in C’ and C” below the loss peak and also the frequency at which the double layer formation begins to take place, since there will be more ions in the vicinity of the electrode or AL interface.

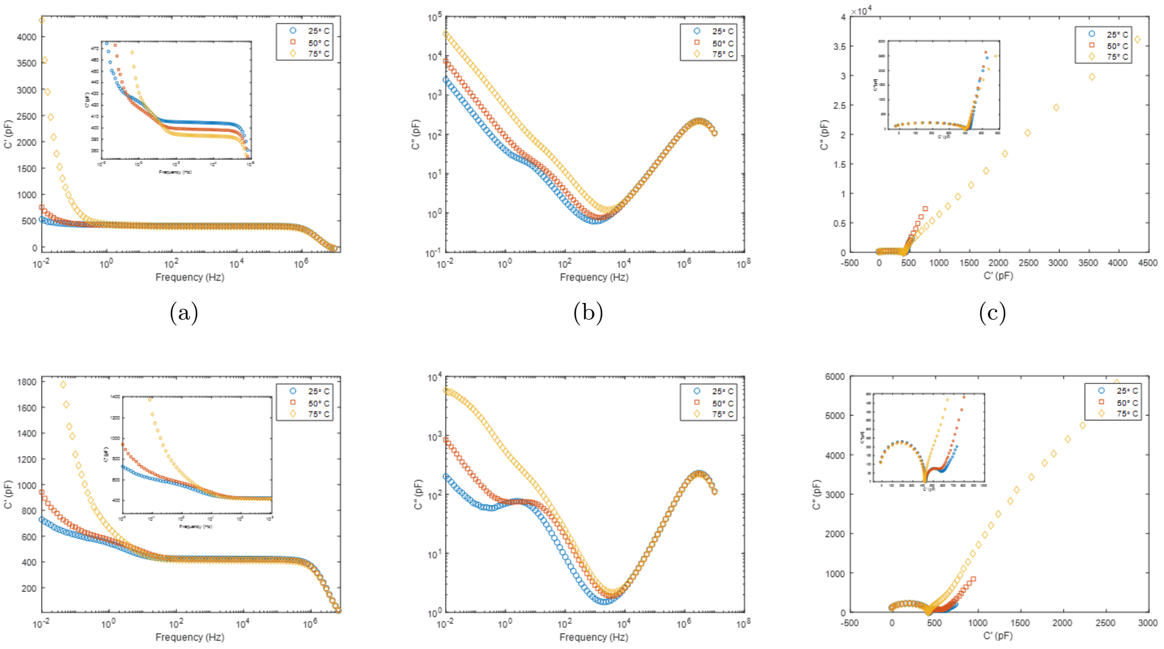

(a) (b) (c)

(d) (e) (f)

Figure 3.3: Complex capacitance spectra of 0.1wt%TBATPB-PCH32 filled LC test cells. a) real capacitance against frequency, b) imaginary capacitance against frequency and c) Cole-Cole capacitance plot of 5μm NAL cell. d) real capacitance against frequency, e) imaginary capacitance against frequency and f) Cole-Cole capacitance plot of 5μm HT SE1211 cell.

Similarly to the empty cell measurements, in the high frequency region, the C’ roll-off due to the electrode resistance can be seen. However, for the same cell, which is now filled with a dielectric liquid of a higher permittivity than the air the empty cell was filled with, this roll-off now comes in at lower frequencies. This is due to the increase in the capacitance which results from filling the cell, thus, for the same electrode resistance, the characteristic relaxation time increases. It is therefore important to consider the effect of both EP at low frequencies and electrode resistance at high frequencies when designing and constructing LC test cells in order to perform accurate permittivity measurements. If the electrode resistance is too high for a material with a high ion content and/or measurements at high temperatures, where EP effects come in at higher frequencies, the plateau region in C' from which ϵ is taken may exist over only a very small frequency range, or not at all, making interpretation of the data considerably more difficult.

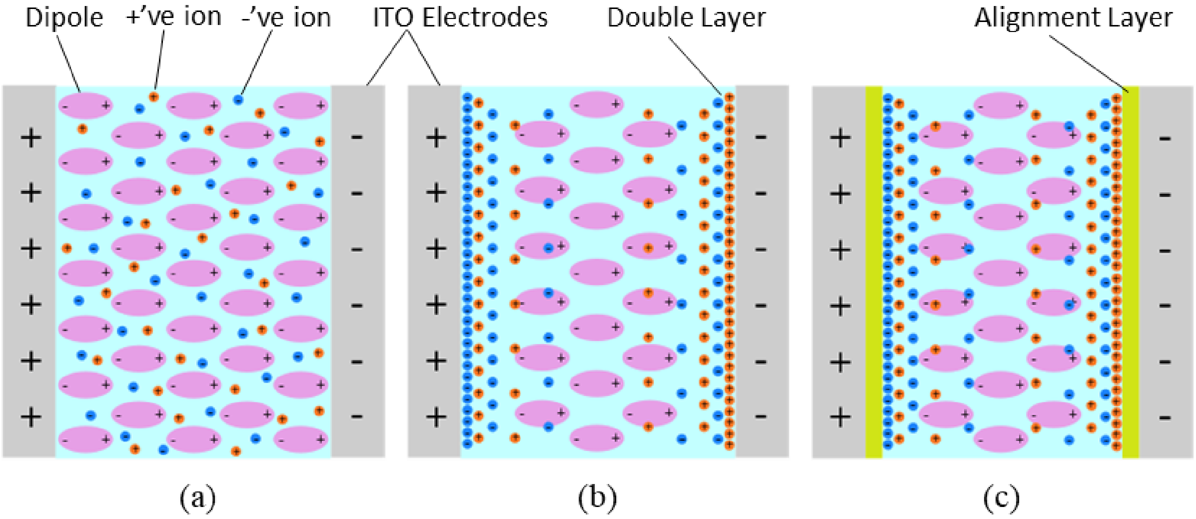

Figure 3.4: Schematic representations of ionic impurities within dielectric liquid under an applied field of a) sufficiently high frequency so as to prevent the formation of electrical double layers at the interface with the electrodes, b) sufficiently low frequency such that ions can migrate to the electrode interfaces to form an electrical double layer creating electrode polarisation c) of sufficiently low frequency such that ions can migrate to the AL interfaces to form an electrical double layer creating Maxwell-Wagner interfacial polarisation.

3.3 Modelling Dielectric Spectra

To model complex dielectric spectra, two approaches can be used, both of which are covered here. The first of which is the use of dielectric permittivity models, such as the Debye model or the Havriliak-Negami model which were briefly introduced in 1.1.4.2. The second of which is the use of equivalent circuit models covered in detail in the following sections. The method of using each of these approaches is discussed and examples of the resulting dielectric spectra are shown. In the case of equivalent circuit modelling, the basic circuit components are first introduced, followed by an explanation of the process of constructing more complex circuit models. Additional circuit components are also introduced and their implications for modelling more complex features within the dielectric spectra are explored.

3.3.1 Dielectric Permittivity Models

The Debye model (equation 1.29a) can be used to describe a Debye type relaxation process in the complex permittivity spectra. A Debye type relaxation consists of a relaxation process with a single well defined characteristic timescale τ_c and is typical of dipolar relaxation in a dielectric material as discussed in 1.1.4.2. In reality, the relaxation processes seen in dielectric materials do not necessarily follow this Debye-like behaviour, but often show broadening of the relaxation process due to a distribution of characteristic relaxation timescales rather than a single well defined relaxation timescale. To account for this broadening, the Cole-Cole model can be used if the broadening of the relaxation process is symmetric around the peak, i.e. if the different characteristic relaxation timescales are evenly distributed above and below the mean timescale [23].

If the broadening is asymmetric, i.e. if the different characteristic relaxation timescales are not evenly distributed above and below the mean timescale, but are weighted either above or below the mean timescale then the Cole-Davidson model can be used [24]. The Havriliak-Negami model (equation 1.30a) provides a generalisation of these cases, enabling either symmetric or asymmetric broadening of the relaxation process to be modelled by using appropriate values for α and β [25]. Figure 3.5 shows the frequency dependence ϵ^* for a single a single relaxation as modeled by the Havriliak-Negami model in these different circumstances.

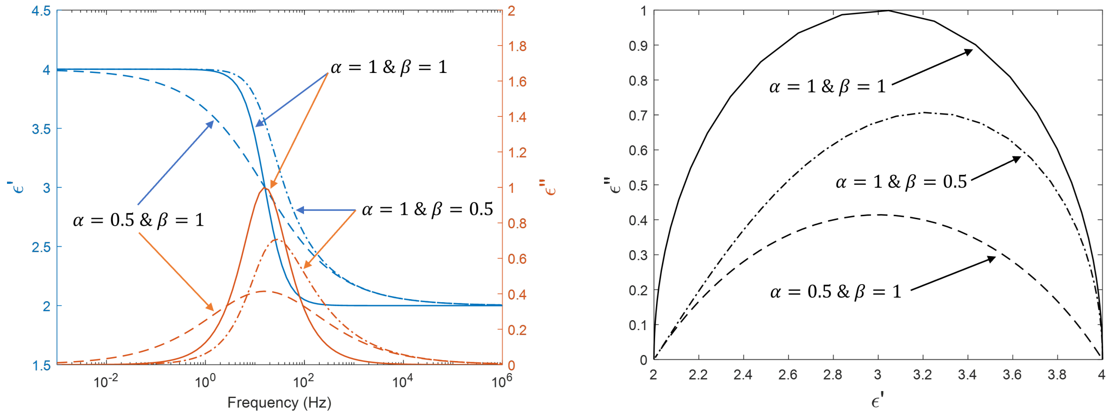

(a) (b)

Figure 3.5: a) real and imaginary permittivity against frequency, b) Cole-Cole permittivity plot of Havriliak-Negami model for a relaxation process with $\tau_c = 0.01s$, $\epsilon_s = 4$ and $\epsilon_{inf} = 2$ for $\alpha = 1$ and $\beta = 1$ corresponding to a Debye type relaxation (solid lines), $\alpha = 0.5$ and $\beta = 1$ corresponding to a Cole-Cole type relaxation with symmetric broadening of the relaxation process (dashed lines) and $\alpha = 1$ and $\beta = 0.5$ corresponding to a Cole-Davidson type relaxation with asymmetric broadening of the relaxation process (dashed dotted lines).

3.3.2 Equivalent Circuit Models

3.3.2.1 Fundamental Circuit Components

Equivalent circuits are built up from individual circuit elements/components, the three most fundamental and commonly used are the 'ideal' capacitor (C), resistor (R) and inductor (L), the symbols for which are shown in figures 3.6(a), 3.6(d) and 3.6(g). Each of these components contributes to the total complex impedance and complex capacitance with a different frequency dependence, hence combinations of these components can be used to model the overall frequency dependence of real dielectric spectra. The complex impedance and complex capacitance dependence for each of these components are displayed in table 3.2.

Table 3.2: Equivalent circuit components complex impedance and capacitance.

Component	Impedance	Capacitance
Capacitor	$Z_C^* = \frac{1}{j\omega C}$	$C_C^* = C$
Resistor	$Z_R^* = R$	$C_R^* = \frac{1}{j\omega R}$
Inductor	$Z_L^* = j\omega C$	$C_L^* = -\frac{1}{\omega^2 L}$
Constant Phase Element	$Z_{CPE}^* = \frac{1}{(j\omega)^n Q}$	$C_{CPE}^* = (j\omega)^{n-1} Q$

The frequency dependent complex capacitance for each of the components are shown in figures 3.6(b), 3.6(e) and 3.6(h) as well as their corresponding Cole-Cole capacitance plots which are shown in 3.6(c), 3.6(f) and 3.6(i) for a capacitor, resistor and inductor respectively. The capacitance, resistance and inductance values used here have been chosen to represent the values typically seen in LC dielectric spectroscopy measurements. As can be seen, the 'ideal' capacitor shows a constant non-zero C', independent of frequency and a zero C" across all frequencies. The 'ideal' resistor on the other hand shows a non-zero C" with a negative logarithmic frequency dependence and a zero C' across all frequencies. Inductors, similarly to capacitors show a non-zero C' and a zero C" across all frequencies, however, C' shows a strong frequency dependence which corresponds to an increasing reactance with increasing frequency.

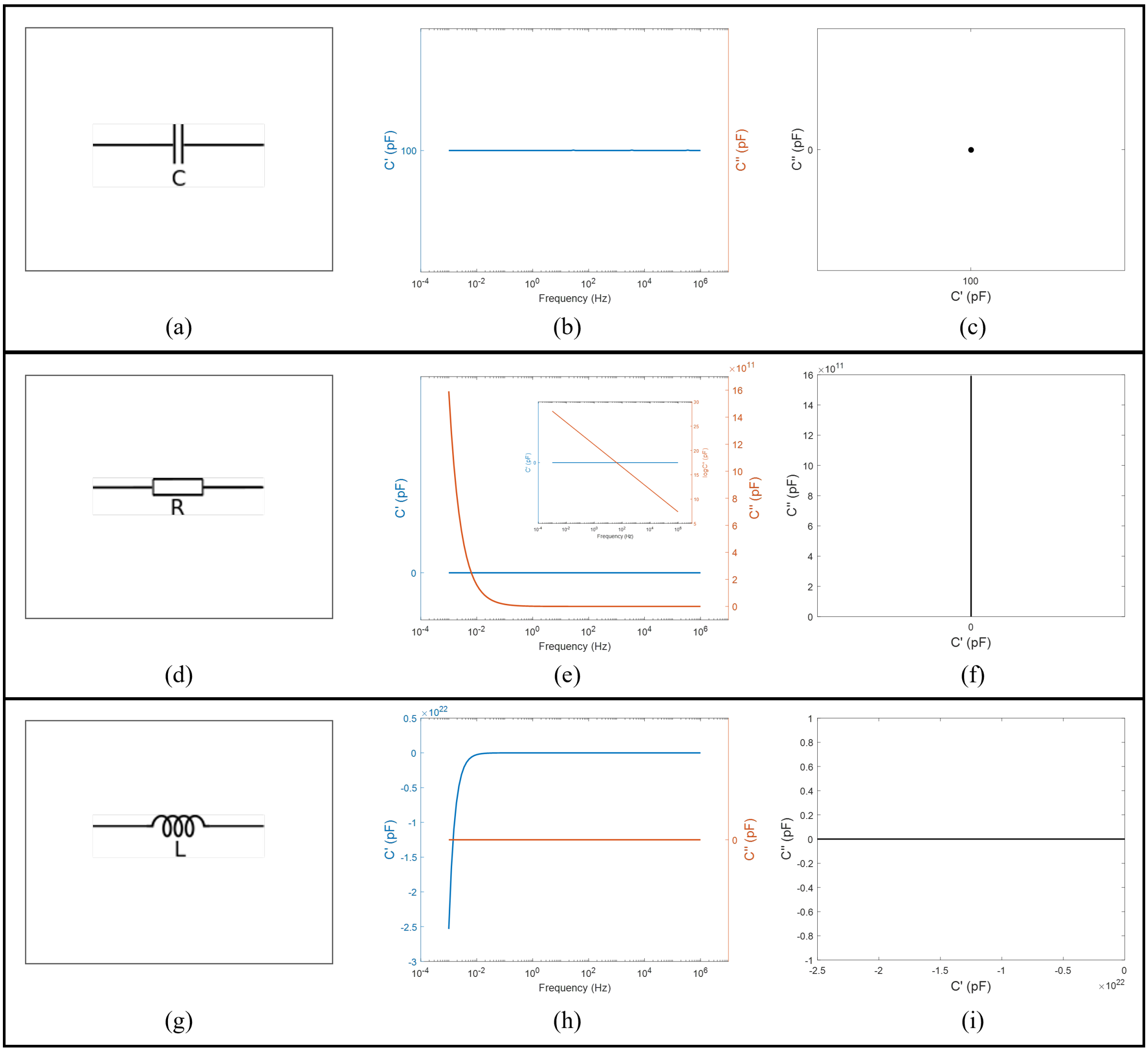

Figure 3.6: The three basic equivalent circuit components. a) Ideal Capacitor of $100pF$ with corresponding b) frequency dependent complex capacitance and c) Cole-Cole plot. d) Resistor of 100Ω with corresponding e) frequency dependent complex capacitance and f) Cole-Cole plot. g) Inductor of $1\mu H$ with corresponding b) frequency dependent complex capacitance and c) Cole-Cole plot.

3.3.2.2 Circuit Construction

Equivalent circuits are constructed by combining the individual circuit components that are shown in figure 3.6. To calculate the total complex impedance and/or complex capacitance of the circuits, the complex impedance of the individual components are summed together. The way in which the individual complex impedances or capacitances are summed together depends on whether the components are in series or parallel, the correct method of addition for each of these cases is summarised in table 3.3. A set of simple equivalent circuits and their corresponding frequency dependent complex capacitances and Cole-Cole capacitance plots are shown in figure 3.7.

Table 3.3: Method of summation of n individual components in series or parallel to find the total complex impedance or capacitance.

Combination	Total Impedance	Total Capacitance
Series	$Z_T^* = \sum_{i=1}^{n} Z_i^*$	$\frac{1}{C_T^*} = \sum_{i=1}^{n} \frac{1}{C_i^*}$
Parallel	$\frac{1}{Z_T^*} = \sum_{i=1}^{n} \frac{1}{Z_i^*}$	$C_T^* = \sum_{i=1}^{n} C_i^*$

The first circuit (figure 3.7(a)) shows a series RC combination which creates a 'roll-off' in C'. For a series RC circuit, the time constant is defined as $\tau_c = RC$, which is related to the frequency through $f = \frac{1}{2\pi\tau}$ where $2\pi\tau$ is the angular frequency. The 'roll-off' shown here at $f_c = 15.9MHz$ or $\tau_c = 10ns$ corresponds to a capacitor with capacitance of $C = 100pF$ and resistor of $R = 100\Omega$, which are of the same order of magnitude as the values of the LC layer capacitance and series electrode resistance of the LC test cells used in this work. Hence the 'roll-off' seen in this equivalent circuit model appears at approximately the same frequency as that seen in the dielectric spectra of the LC test cells already shown in section 3.2.3 (figures 3.2(a), 3.3(a), 3.2(d) and 3.3(d)). The second circuit (figure 3.7(d)) shows a parallel RC combination, also known as a 'lossy' capacitor. This combination is used to describe the behaviour of real capacitors which exhibit some loss, albeit small, as real dielectric materials do not behave purely capacitively. The losses which arise from current flow through the dielectric material are modelled by the resistor in parallel with the 'ideal' capacitor. The frequency dependent complex capacitance of this circuit, which can be seen in 3.7(e) shows a non-zero frequency independent C' and frequency dependent non-zero C" as expected from the combination of each of the individual components behaviour (figures 3.6(b) and 3.6(d)).

To combine components to form more complex circuits comprised of numerous series and parallel component combinations, it is necessary to group components when calculating the total impedance or capacitance. Components can be split into series and parallel groups, the total complex impedance or capacitance of each of the groups should be calculated prior to calculating the total complex impedance or capacitance of the circuit by summing the impedances or capacitances of the component groups. For instance, to calculate the circuit shown in figure 3.7(g), the impedance/capacitance of the R_1C_1 series combination is first calculated which is then added to the impedance/capacitance of the C in parallel. Looking at the frequency dependent complex capacitance (figure 3.7(h)) and Cole-Cole plot (figure 3.7(i)) produced by this circuit, the familiar Debye relaxation can be seen with the same $\tau_c = 0.01s$ as the Debye relaxation modelled by equation 1.29a shown in 3.5. To model a non-Debye type relaxation similarly to the Havriliak-Negami equation, one can continually add RC combinations in parallel with the R_1C_1 combination, each with a different τ_c. This can be done to account for both symmetric and asymmetric broadening of the relaxation. For the step in C' to reduce to a non-zero value, at frequencies above τ_c an additional resistor in series with the Debye circuit can be added. In this case, C' will fall from a value of $C + C_1$ to C, thus for the values used here, C_T will fall from a value of $200pF$ to $100pF$.

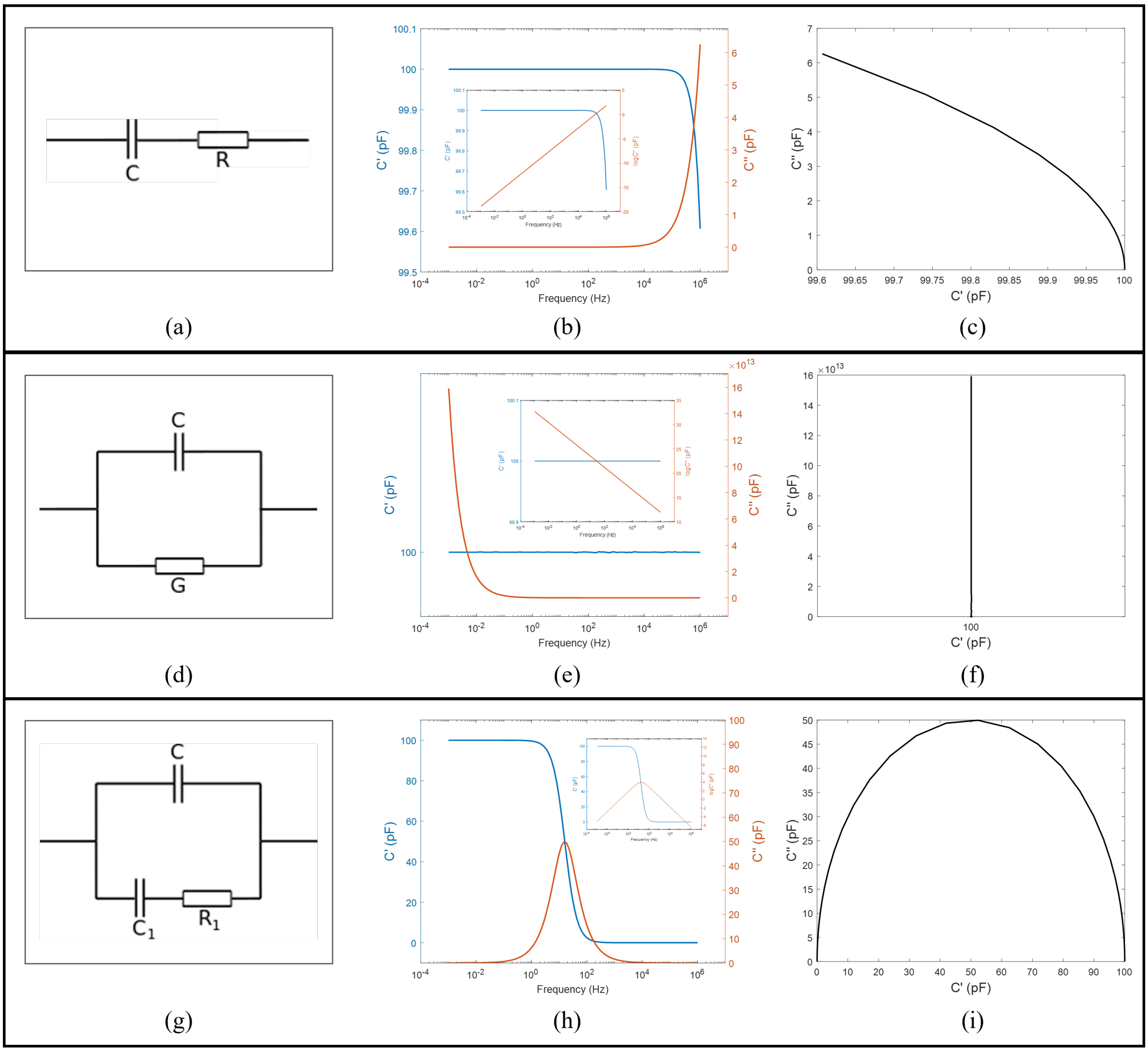

(a) (b) (c)

(d) (e) (f)

(g) (h) (i)

Figure 3.7: Construction of basic equivalent circuits, a) series RC with corresponding b) frequency dependent complex capacitance and c) Cole-Cole plot. d) parallel RC or 'lossy' capacitor with corresponding e) frequency dependent complex capacitance and f) Cole-Cole plot. g) Debye circuit with corresponding h) frequency dependent complex capacitance and i) Cole-Cole plot. $C = 100pF$, $R = 100\Omega$, $G = 1nS$, $R_1 = 100M\Omega$ and $C_1 = 100pF$.

3.3.2.3 Additional Circuit Components

In addition to the three most basic circuit components of a capacitor, resistor and inductor, one can use more complex circuit components to adjust the frequency behaviour of equivalent circuits. One of the most versatile and useful of such components is the constant phase element (CPE) as shown in figure 3.8(a). A CPE can be used to describe the behaviour electrical double layers which form at the interface between dielectric liquids and the electrodes or other dielectric material interfaces [172, 173]. The complex impedance and complex capacitance for a CPE is shown in table 3.2.

Depending on the value of n used, a CPE can behave as an ideal capacitor ($n = 1$ and $\phi = -90°$), as an ideal resistor ($n = 0$ and $\phi = 0°$) or as a component with properties somewhere between the two ($0 < n < 1$) [174]. A CPE can also behave as a Warburg element ($n = 0.5$ and $\phi = 45°$), which is another type of circuit element with a constant phase angle [175]. The behaviour of a CPE in each of these cases is shown in figures 3.8(b) and 3.8(c). The absence of C" in the case of $n = 1$ when the CPE is behaving as an ideal capacitor and the zero C' in the $n = 0$ case when the CPE is behaving as an ideal resistor. When used in an equivalent circuit of a 'lossy' capacitor and an equivalent series resistance (figure 3.8(d)), the familiar shape of the frequency dependent complex capacitance which is seen from LC test cells is produced (figure 3.8(e)). Changes to the Q and n values of the CPE can be used to tune the shape of the C' and C" curves to give the same shapes as those seen in real dielectric spectroscopy data from LC test cells.

It should be noted that although the CPE is used to describe the formation of electrical double layers, which primarily takes place at low frequencies (upturn in C'), effects are also seen at higher frequencies. For instance, by lowering the value of n, the shape of C" around the frequencies of the C" minima is changed, as well as changes to the plateau of C' across the same frequency range. These effects on the shape of C' and C" are though to arise due to the structure of the ITO electrodes which are not flat surfaces, but a fractal 'cityscape-like' structure into which the PI or dielectric liquid intermingles, forming a complex interface between the two. Thus, the behaviour of the double layer does not follow that of an ideal capacitor, but instead displays more complex behaviour that is described more accurately by the CPE.

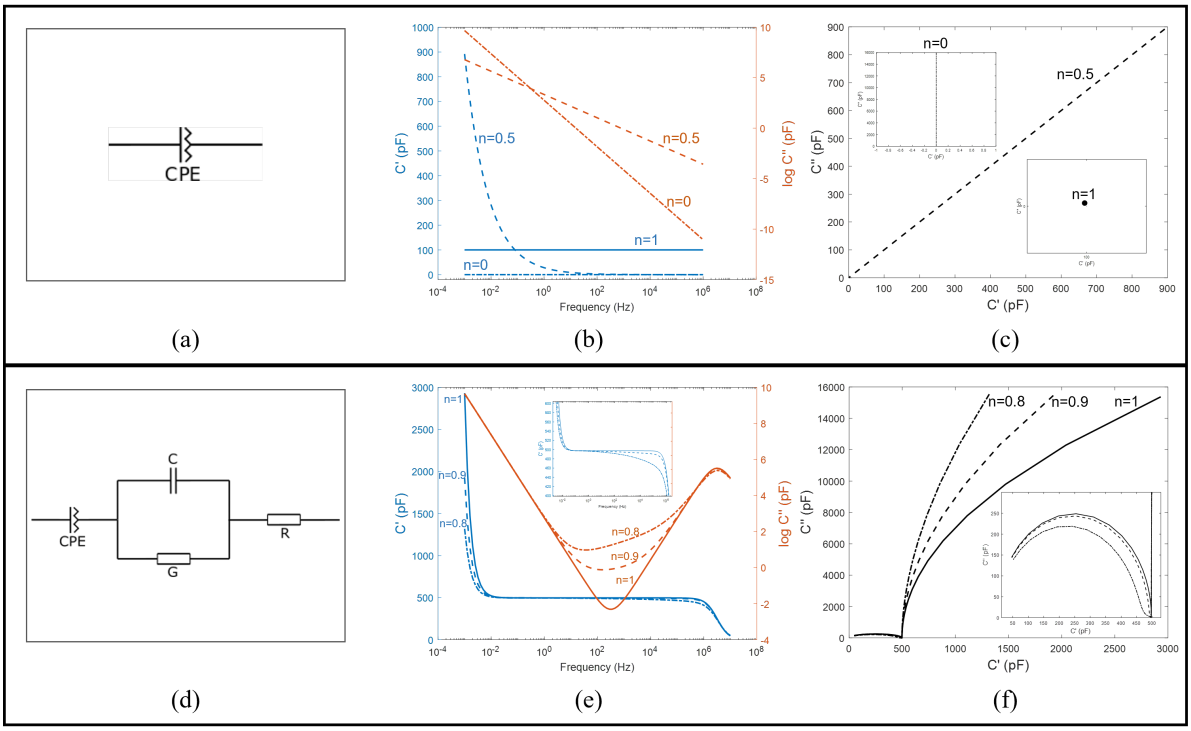

(a) (b) (c)

(d) (e) (f)

Figure 3.8: Additional circuit component a) constant phase element (CPE) with corresponding b) frequency dependent complex capacitance and c) Cole-Cole plot for $Q = 100pF$ and $n = 1$ (solid lines), $n = 0.5$ (dashed lines), $n = 0$ (dot dashed lines). d) equivalent circuit example of a CPE in series with a 'lossy' capacitor and series resistance with corresponding e) frequency dependent complex capacitance and f) Cole-Cole plot for $C = 500pF$, $G = 0.1nS$, $R = 100\Omega$, $Q = 100nF$ and $n = 1$ (solid lines), $n = 0.9$ (dashed lines), $n = 0.8$ (dot dashed lines).

3.3.2.4 Model of Dielectric Liquid Spectra

To describe the full frequency dependent dielectric spectra of dielectric liquid filled LC test cells, an equivalent circuit model comprised of a combination of the aforementioned equivalent circuits shown in figures 3.7(g) and 3.8(d). The resulting circuit can be seen in figure 3.9(a). Where C_{LC} and G_{LC} are the capacitance and conductance of the LC test cell filled with the dielectric liquid sample respectively, CPE_{dl} is the 'non-ideal' capacitance of the electrical double layer and R_E is the equivalent series resistance of the electrodes and connecting wires. C_i and R_i are the series RCs which forms the Debye circuit with C_{LC} and creates the relaxation process associated with the ions in the dielectric liquid. Here, $i = 2$, which means that there is a total of two series RCs in parallel with C_{LC}, thus broadening the relaxation process. The complex capacitance of both pure PCH32 filled NAL cells (figures 3.9(b) and 3.9(c)) and 0.1%TBATPB-PCH32 filled NAL cells (figures 3.9(d) and 3.9(e)) is described well by this equivalent circuit model across the full frequency range measured (10mHz - 10MHz).

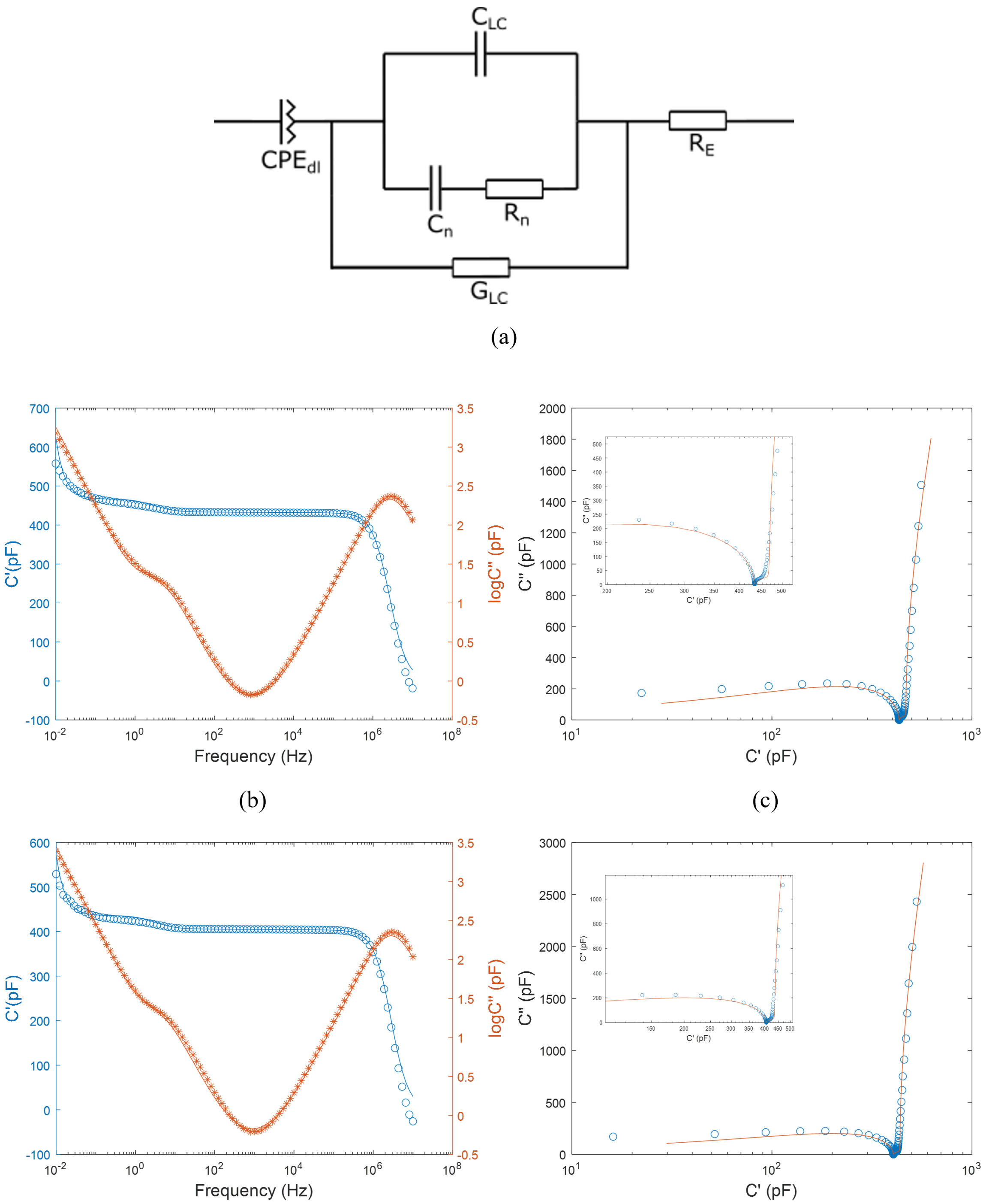

(a)

(b) (c)

(d) (e)

Figure 3.9: a) Equivalent circuit model of dielectric liquid filled NAL cells. Note that the resistor in parallel has been labelled G_{LC} as it corresponds to the conductance of the LC. b) frequency dependent complex capacitance and c) Cole-Cole plot of PCH32 filled NAL cell. d) frequency dependent complex capacitance and e) Cole-Cole plot of 0.1%TBATPB-PCH32 filled NAL cell. The measured C' and C" is shown by the open circles and the solid lines show the C' and C" as calculated using the equivalent circuit model.

The component values used in this equivalent circuit modelling of PCH32 and 0.1%TBATPB-PCH32 in NAL cells are shown in table 3.4. Using the empty cell capacitance (equation 2.21) to calculate the relative permittivity, gave $\epsilon' = 2.2$ for both samples. The conductivity, calculated from G_{LC} using the cell gap and active electrode area in equation 2.25 increased by a factor of ~ 1.5 by doping the PCH32 with 0.1wt% TBATPB salt. EP effects were also enhanced, as expected. The magnitude of the double layer capacitance Q_{dl} increased by a factor of ~ 2.5 and n of the CPE was reduced from 0.98 to 0.95. This change in the CPE_{dl} values suggests that the magnitude of the electrical double layer capacitance increased due to the higher ion content, and the decrease in n indicates more resistive behaviour of the electrical double layer, due to an increased charge transfer at the electrodes.

Table 3.4: Component values from equivalent circuit modelling in figure 3.9.

$C_{LC}(pF)$	$G_{LC}(pS)$	$C_1(pF)$	$R_1(G\Omega)$	$C_2(pF)$	$R_2(G\Omega)$	$Q_{dl}(nF)$	n	$R_E(\Omega)$
444	122	20	4	14	2	20	0.98	140
410	180	14	6	16	2	50	0.95	140

The low frequency ionic relaxation process modelled by the R_iC_i combinations showed a shift to slightly lower frequencies/longer timescales. The pure PCH32 gave timescales of $\tau_1 = 0.080s$ and $\tau_2 = 0.028s$, corresponding to $f_1 = 2.0Hz$ and $f_2 = 5.7Hz$, whereas the 0.1%TBATPB-PCH32 gave timescales of $\tau_1 = 0.084s$ and $\tau_2 = 0.032s$, corresponding to $f_1 = 1.9Hz$ and $f_2 = 4.9Hz$. This shift in timescales resulted from the additional ionic impurities added to the PCH32 with lower mobilities than the ionic species present in just the pure PCH32. The cell gap of the samples can also have an impact on the timescale of this ionic relaxation process, but the small difference in cell gap between these samples (equivalent within error), was considered to have negligible effect.

3.4 Interpretation and Analysis of LC Dielectric Data

So far, only the dielectric spectra of weakly conductive isotropic dielectric liquids has been discussed with detailed consideration of the effects that the LC test cells have on the measured spectra. In this section, the dielectric spectra of NLCs such as the highly positive $\Delta\epsilon$ mixture MLC6204 is analysed.

Firstly, the measurement and interpretation of the frequency dependent complex permittivity and the impact the LC test cells used have on the measurements are covered. Following this, the methodology used to perform accurate LC permittivity measurements whilst considering the effects of the LC test cell on the measurement is explained. The correction techniques used to account for the LC test cell effects, in particular that of the ALs using an equivalent circuit approach are then presented. And finally, the fitting routines used to analyse the LC permittivity-voltage data are explained.

3.4.1 Frequency Dependent Complex Permittivity

Dielectric measurements were performed in PH (PI SE130 ALs) and HT (PI SE1211 ALs) GR LC test cells of nominally $5\mu m$ and $20\mu m$ spacings at $0.1Vrms$ to find $\epsilon_{||}$ and $\epsilon_{\perp}$. Figures 3.10(a) and 3.10(b) show the frequency dependent complex permittivity from the $5\mu m$ and $20\mu m$ cells respectively. The permittivities were then calculated using the empty cell capacitance method (section 2.4.6). The ALs in all cells are of approximately the same thickness ($\sim 100nm$ on each substrate) and thus the difference in behaviour between the $5\mu m$ and $20\mu m$ cells is due to the difference in cell gap only.

The ionic relaxation process in the $20\mu m$ cells is significantly stronger but comes in at lower frequencies as expected and due to the lower capacitance in the $20\mu m$ cells, the 'roll-off' in ϵ' due to the series electrode resistance comes in at higher frequencies, thus creating a larger ϵ' plateau region from which the true LC ϵ' can be measured. One should also note, however, the difference in ϵ' plateau values between the $5\mu m$ and $20\mu m$ cells. The $5\mu m$ HT cell shows significantly lower $\epsilon'_{||}$ values than the $20\mu m$ HT cell.

This difference in the measured values of $\epsilon'_{||}$ arises due to the effects of the thin film PI ALs on the electrode surfaces. The PI ALs have a considerably lower ϵ' than the LC, particularly in the HT case, which means that the measured ϵ' of the AL and LC series combination is significantly lower than the true ϵ' of the LC. This effect is not seen as considerably in the PH cell case since ϵ' of the AL and the LC $\epsilon'_{\perp}$ are of a similar magnitude, and in the case of the isotropic dielectric liquid used earlier in this chapter, this effect is almost non existent since the ϵ' of PCH32 and the ALs were approximately the same. Thus, it can be seen for high permittivity LCs such as MLC6204 where $\epsilon'_{LC} >> \epsilon_{AL}$, the effect of ALs must be accounted for in order to perform accurate permittivity measurements, particularly so if thin LC test cells and/or thick ALs are used. The methods used to do this are covered in detail in the following sections.

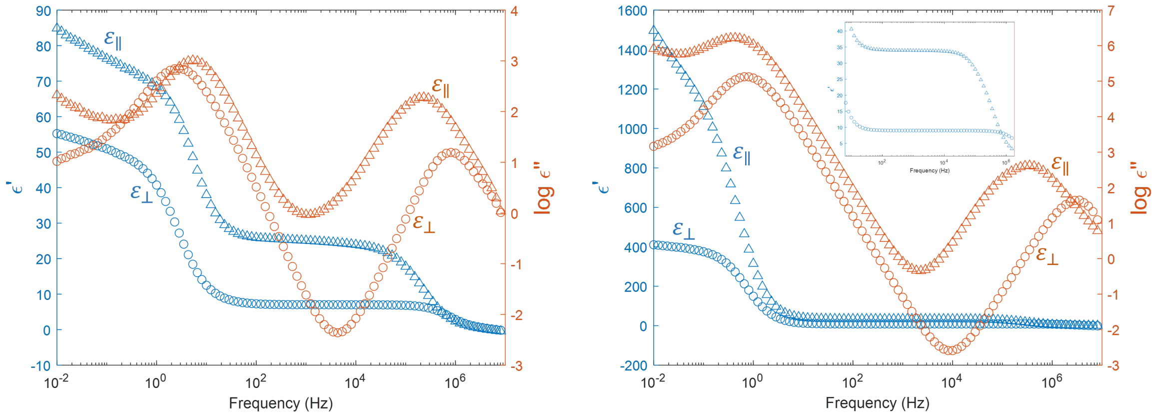

(a) (b)

Figure 3.10: Frequency dependent complex permittivity of MLC6204 in the nematic phase at $25°C$ in nominally a) $5\mu m$ and b) $20\mu m$ PH (circles) and HT (triangles) cells at $0.1Vrms$.

3.4.2 Permittivity-Voltage Measurements

Permittivities can also be used to determine the elastic constants of LCs. To do so, the Fréedericksz transition in homogeneously aligned cells is used (see section 1.1.6 of chapter 1). In the previous section, a voltage of just $V_{app} = 0.1V_{rms}$ was used to measure both $\epsilon_{\perp}$ or $\epsilon_{\parallel}$ in PH or HT cells which caused no director reorientation, since $V_{app} << V_{th}$. For an LC with $\Delta\epsilon > 0$, one may use just a PH cell to find $\epsilon_{\perp}$ and $\epsilon_{\parallel}$ or in the case of an LC with $\Delta\epsilon < 0$, one may instead use just an HT cell by applying a range of voltages to induce the Fréedericksz transition and measure $\epsilon(V)$ in the process. Linear fitting of the measured $\epsilon(V)$ curve can be used to find the elastic constants K_{11} and K_{33}. It is here, when performing $\epsilon(V)$ curve fitting, that correction due to the effect of the ALs becomes ever more important, as not only is the absolute value of the permittivity affected by the ALs, but there is a voltage dropped across the ALs and thus the true voltage that is applied across the LC layer is actually lower than the voltage applied across the cell.

When performing $\epsilon(V)$ measurements, not only must an appropriate frequency be chosen to measure at (as discussed in the previous section), it is also necessary to allow enough time following the application of each voltage for the director reorientation to take place and the new director profile through the cell to stabilise. This can be seen in the capacitance $C(t)$ or permittivity $\epsilon(t)$ against time curves at a particular applied voltage V_{app} and frequency f_{app}. The curves show an initially sharp increase which decays towards a plateau as $t \to \infty$. The longest stabilisation times are at/around V_{th} and thus it is at these voltages one must take most care to ensure a long enough stabilisation time is used. This is particularly true for fitting the curves, since this is the region of the $\epsilon(V)$ curve which holds the information required to find K_{11} and K_{33}.

Figure 3.11(a) shows the stabilisation time around V_{th} for MLC6204 which is the longest for the $0.5V$ measurements as this is the closest voltage to V_{th} for MLC6204. It should be noted, however, that the voltages shown here are the voltages applied across the entire cell and not the voltage across the LC film only, and is therefore only representative of nominally $20\mu m$ thick cells with $\sim 100nm$ ALs. The impact of the stabilisation time on the $\epsilon(V)$ can be seen in figure 3.11(b), which clearly shows that not allowing enough time for the director to stabilise at $V \gtrsim V_{th}$ results in larger value of V_{th} and therefore also K_{11} as $K_{11} \propto V_{th}$. At $V < V_{th}$, the shorter stabilisation time has less of an impact as minimal director reorientation takes place, however, this is dependent upon the degree of pretilt in the cell, which will be discussed further in the following sections 3.4.4. As $V >> V_{th}$, the impact of the shorter stabilisation time also begins to minimise.

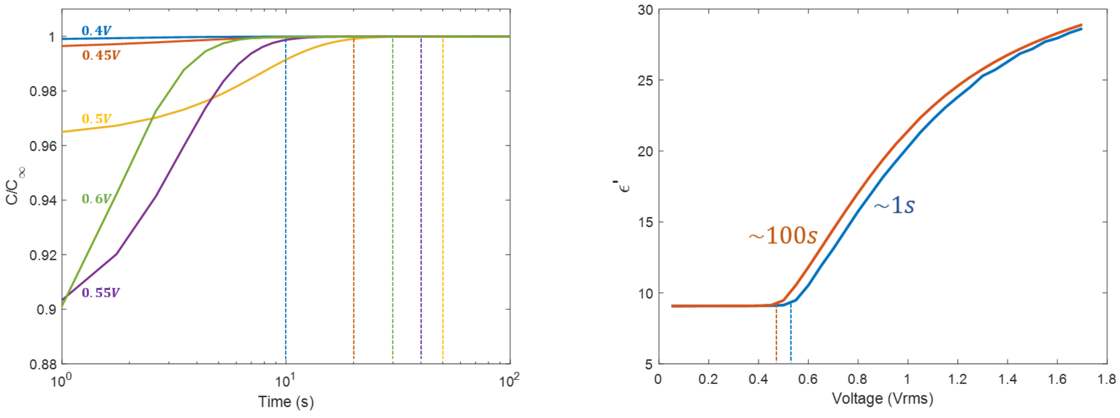

(a) (b)

Figure 3.11: MLC6204 in a $20\mu m$ PH cell with $\sim 100nm$ thick ALs a) capacitance against time at 10kHz for different applied voltages around V_{th}, the capacitance is normalised relative to the capacitance as $t \rightarrow \infty$ for each voltage and the dotted lines show the minimum required stabilisation time for each voltage. b) difference in $\epsilon(V)$ curves for $\sim 1s$ and $\sim 100s$ stabilisation times at 10kHz, the dotted lines show the apparent V_{th} for each stabilisation time.

3.4.3 Alignment Layer Correction

It is possible to correct the total measured permittivity of the LC test cell (permittivity of ALs and LC) to find the true permittivity of the LC by using an equivalent circuit model. The thin film ALs on each electrode surface act as two additional capacitors in series with the air gap in an empty cell (figure 3.12(a)) or in series with the LC film in a filled cell (figure 3.12(b)). By calculating the total capacitance of the cell from these equivalent circuit models, the following equation for the total measured permittivity can be found using the dimensions of the cell:

$$\epsilon_T = \frac{\epsilon_{LC}\epsilon_{AL}(h_{LC} + 2h_{AL})}{h_{LC}\epsilon_{AL} + 2h_{AL}\epsilon_{LC}}, \tag{3.1a}$$

where h_{AL} is the AL film thickness (on each substrate), ϵ_{AL} is the permittivity of the AL material, $d = h_{LC}$ is the thickness of the LC film and ϵ_{LC} is the true permittivity of the LC. In the case of the permittivity of the LC being calculated from the filled to empty cell capacitance ratio, the total measured permittivity takes on a modified form:

$$\epsilon_T = \frac{\epsilon_{LC}(2h_{AL} + h_{LC}\epsilon_{AL})}{2h_{AL}\epsilon_{LC} + h_{LC}\epsilon_{AL}}. \tag{3.1b}$$

It should be noted, that the thickness of the air gap in the empty cell and the thickness of the LC film in the filled cell are assumed to be the same. Thus, to account for the effect of the ALs, the AL film thickness and permittivity need to be known in conjunction with the cell gap and is therefore measured as part of the cell construction process. It is also assumed that the measured cell gap is the spacing between the two AL surfaces in the cell and not the distance between two ITO electrode surfaces, and thus the cell gap and LC film thickness are the same ($d = h_{LC}$).

One can see the AL effect on the total measured permittivity modelled using equation 3.1b in figures 3.12(c) and 3.12(d) for AL thicknesses of $50nm$ and $100nm$ respectively. The thicker AL reduces the total measured permittivity relative to the true LC permittivity much more significantly than the thinner AL. The effect is also much more pronounced in thinner cells and as the difference in LC permittivity and AL permittivity increases. Thus, to minimise this effect, especially if one were to neglect it in permittivity measurements, using thinner ALs with thicker cell gaps would be preferable. However, even in $20\mu m$ cells with only $50nm$ thick ALs, the effect remains pronounced at high permittivities and thus, for high permittivity LCs AL correction should be performed routinely for accurate permittivity measurements.

As mentioned briefly in the previous section, not only do the ALs affect the total measured permittivity of the cell, but there is also a voltage drop across them which reduces the true voltage applied across the LC film. Thus, in permittivity-voltage measurements of high ϵ and

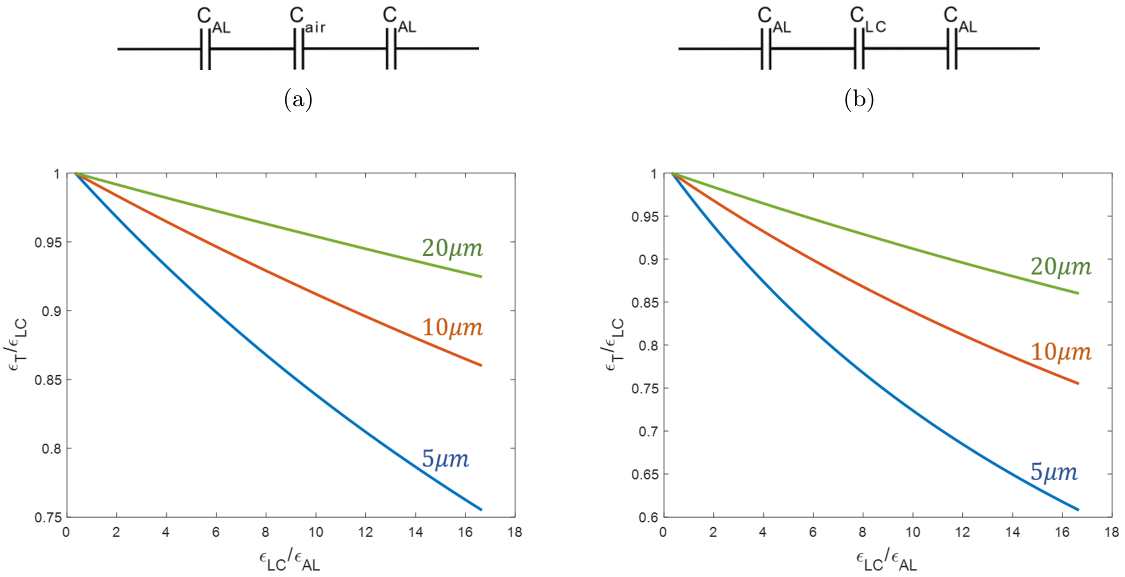

(a)

(b)

(c)

(d)

Figure 3.12: Equivalent series capacitance circuits of a) empty and b) filled cells with ALs used to model the effect of the ALs on the total measured permittivity as a function of the ratio between the LC permittivity and the AL permittivity for AL thicknesses of c) $h_{AL} = 50nm$ and d) $h_{AL} = 100nm$ for cell gaps of $d = 5\mu m$, $d = 10\mu m$ and $d = 20\mu m$. Here, the AL permittivity was fixed at the typical values for PI ALs of $\epsilon_{AL} = 3$ and the permittivity of the LC was changed from ϵ_{LC} to $\epsilon_{LC} = 50$.

$\Delta\epsilon$ materials, a correction should also be applied to the applied voltage in order to find the true voltage applied across the LC film. Since the total charge on each of the capacitors in series is the same, one can apply Kirchhoff's voltage law to find the true voltage applied across the LC film:

$$V_{LC} = \frac{V_{app}}{1 + \frac{2h_{AL}\epsilon_{LC}}{h_{LC}\epsilon_{LC}}}, \tag{3.2a}$$

where V_{app} is the voltage applied across the entire LC test cell. However, one must first know the true permittivity of the LC to correct the applied voltage. Thus, rearranging equation 3.1b for the permittivity of the LC gives:

$$\epsilon_{LC} = \frac{\epsilon_T \epsilon_{AL} h_{LC}}{2h_{AL} + \epsilon_{AL} h_{LC} - 2\epsilon_T \epsilon_{AL}} \tag{3.2b}$$

To correct the measured $\epsilon(V)$ curves, equations 3.2a and 3.2b are applied to the data. To exemplify the magnitude of this effect, the $\epsilon(V)$ curve of an MLC6204 filled $20\mu m$ cell at $25°C$ has been corrected for both $100nm$ and $200nm$ thick ALs, the results of which are shown in figure 3.13. Even in $20\mu m$ cells, the combined effect of the ALs on the permittivity and the voltage significantly alters the $\epsilon(V)$ curves, particularly at higher applied voltages where LC reorientation has taken place. V_{th} and the gradient of the $\epsilon(V)$ curve just above V_{th} are altered which means the values of K_{11} and K_{33} attained from fitting are also altered by the ALs. Additionally, at $V >> V_{th}$, the magnitude of ϵ and the gradient of $\epsilon(V)$ are reduced by the ALs which also significantly affects the values of both $\epsilon_{\parallel}$ and $\Delta\epsilon$. At lower voltages ($V << V_{th}$), where $\epsilon_{\perp}$ is measured, the absolute value of the ϵ is less significantly affected but is still reduced by the ALs since $\epsilon_{LC} > \epsilon_{AL}$. These implications for fitting of the $\epsilon(V)$ curves are discussed in more detail in the following section where the $\epsilon(V)$ curve fitting methods are discussed.

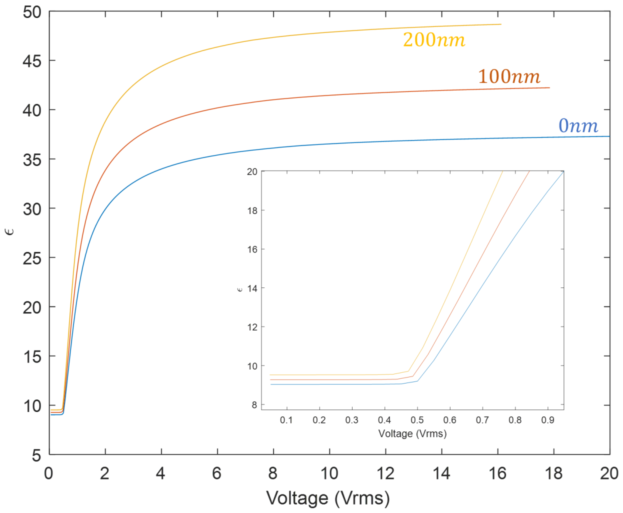

Figure 3.13: $\epsilon(V)$ curves of MLC6204 in a $20\mu m$ PH LC test cell at $25°C$ before AL correction (blue line) and after correcting for $100nm$ (orange line) or $200nm$ (yellow line) thick ALs.

3.4.4 Permittivity-Voltage Curve Fitting

As already mentioned in the previous sections, the $\epsilon(V)$ curves can be fitted to find $\epsilon_{\perp}$, $\epsilon_{\parallel}$, $\Delta\epsilon$, V_{th}, K_{11}, and K_{33}. Thus, measurement and fitting of the $\epsilon(V)$ curves is a useful way to find the dielectric and elastic properties of LCs. Hence, in this section, the methods for analysing $\epsilon(V)$ curves through different fitting routines are explored and a new methodology to do so correctly for high $\Delta\epsilon$ LCs is proposed and the reasons for doing so are explained.

3.4.4.1 Linear Permittivity-Voltage Fitting

The simplest method of $\epsilon(V)$ fitting uses a set of three linear fits to appropriate regions of the $\epsilon(V)$ curve. In the low voltage region at $V < V_{th}$ (figure 3.14(a)) a linear fit (equation 3.3a) is used to find $\epsilon_{\perp}$ from the intercept with the y-axis. In the high voltage region at $V >> V_{th}$ one can see $\epsilon(V)$ becomes asymptotic; it is the value of this asymptote that gives $\epsilon_{\parallel}$. By re-plotting the $\epsilon(V)$ curve against the inverse voltage, another single linear fit (equation 3.3c) can be used to find the value of the asymptote and hence $\epsilon_{\|}$ provided certain conditions are met [176]. An inverse voltage extrapolation is performed from the high voltage linear region of the $\epsilon(1/V)$ curve (figure 3.14(b)) to find the y-axis intercept which gives $\epsilon_{\|}$.

$$\epsilon = m_{\perp} V + \epsilon_{\perp} \tag{3.3a}$$

$$\epsilon = m_s V + c \tag{3.3b}$$

$$\epsilon = m_{\|} \frac{1}{V} + \epsilon_{\|} \tag{3.3c}$$

The electric Fréedericksz transition occurs when **E** is applied perpendicular to **n** for a homogeneously aligned nematic with $\Delta\epsilon > 0$. Hence, in a cell with zero surface pretilt, to find the discontinuity at V_{th}, the intersection between the $V < V_{th}$ fit (which will have a gradient of $m_{\perp} = 0$) and the $V > V_{th}$ fit (given by equation 3.4a) is sufficient to accurately determine V_{th}. It should be noted that the $V > V_{th}$ fitting region is of great importance, in some cases, the linear region only extends for a small voltage range above V_{th}.[177, 178]. Thus, if the curve is fit to either too high or too low voltages, the calculated value of V_{th} could be higher/lower than the true value. If the field is not applied perpendicular to **n**, as is the case in a cell with non-zero pretilt, then there is no discontinuity at V_{th}. This means that the linear fitting around V_{th} becomes more erroneous. If the $V < V_{th}$ fit is performed up to too high voltages, nearing V_{th}, then the calculated value of V_{th} will be higher than the true value. The complications added by non-zero pretilt and alternative fitting routines that can be used to negate its effect are discussed in further detail in the following section.

Once V_{th} has been found, K_{11} can be calculated using equation 3.4b, following this, K_{33} can then be calculated using equation 3.4c [30, 179].

$$V_{th} = \frac{\epsilon_{\perp} - c}{m_s - m_{\perp}} \tag{3.4a}$$

$$K_{11} = \epsilon_0 \Delta\epsilon \left(\frac{V_{th}}{\pi} \right)^2 \tag{3.4b}$$

$$K_{33} = K_{11} \left(\frac{2\Delta\epsilon}{V_{th} m_s} - \frac{\Delta\epsilon}{\epsilon_{\perp}} \right) \tag{3.4c}$$

It is therefore clear that using this type of fitting routine without performing the appropriate AL corrections to the $\epsilon(V)$ curves will lead to significant inaccuracies in the values attained, particularlyK_{33} and $\epsilon_{||}$ which rely on accurate determination of the $\epsilon(V)$ gradient in the $V > V_{th}$ and $V >> V_{th}$ regions, respectively.

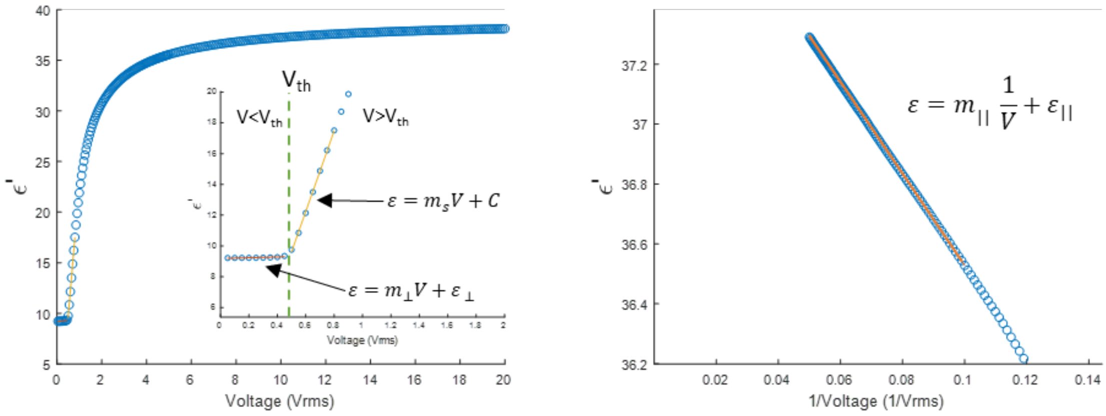

(a) (b)

Figure 3.14: Linear fitting of $\epsilon(V)$ curves a) around V_{th} showing the $V < V_{th}$ fit as well as the fit of the slope at $V > V_{th}$ and b) an infinite voltage extrapolation at $V >> V_{th}$.

3.4.4.2 Welford and Sambles Approach

To model the $\epsilon(V)$ curves continuously from low to high voltages, including the effect of a non-zero pretilt on the curves, the approach developed by Welford and Sambles (WS) can be used [29]. The permittivity of the LC is calculated from director profile through the cell (figure 1.8(b)) using the values of $\epsilon_{||}$ and $\epsilon_{\perp}$ as a function of the voltage applied across the LC. By doing so, the $\epsilon(V)$ curve can be modelled continuously over the range of voltages applied rather than approximating regions of the curve to be linear. Additionally, this approach, since it accounts for the pretilt of the LC, can be used to more accurately determine the permittivities and elastic constants of LCs. To show the effect of changes in pretilt, the WS approach has been used to calculate the $\epsilon(V)$ curves for a high $\Delta\epsilon$ NLC with varying degrees of pretilt.

As can be seen from figure 3.15, an increase in pretilt results in higher ϵ values at $V < V_{th}$ and a loss of the discontinuity in $\epsilon(V)$ at V_{th}. The increase in ϵ values at $V < V_{th}$ arises due to added contribution of $\epsilon_{||}$ to the total ϵ as the electric field is no longer applied perpendicular to $\mathbf{n}$ but at some angle $< 90°$. This also means that some director reorientation begins at $V < V_{th}$ hence the loss of the discontinuity in $\epsilon(V)$ at V_{th}. It is possible to correct the ϵ values at $V < V_{th}$ to find a more accurate value for $\epsilon_{\perp}$ without using the WS approach, but only if the pretilt in the

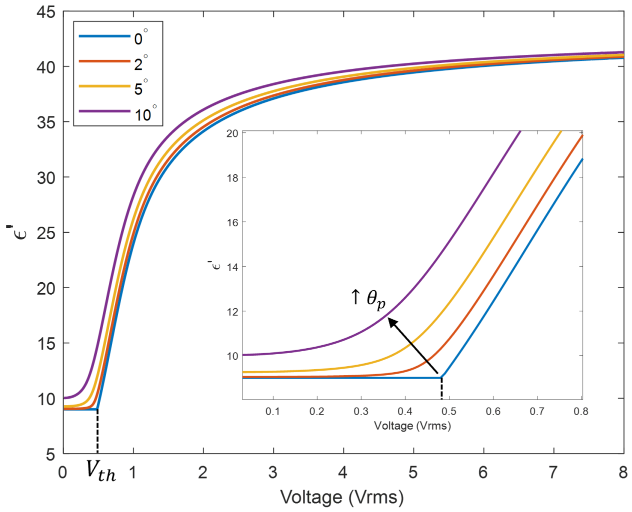

Figure 3.15: Model of the $\epsilon(V)$ curves for a high $\Delta\epsilon$ NLC using values of $K_{11} = 7pN$, $K_{33} = 11pN$, $\epsilon_{\|} = 43$ and $\epsilon_{\perp} = 9$, showing the effect of increased pretilt $\theta_p = 0°$ (blue), $\theta_p = 2°$ (orange), $\theta_p = 5°$ (yellow) and $\theta_p = 10°$ (purple) using the Welford and Sambles approach.

cell is measured directly. The total permittivity ϵ for a uniform director profile (antiparallel cell with no field applied) including the contribution of $\epsilon_{\|}$ and $\epsilon_{\perp}$ is given by:

$$\epsilon = \epsilon_{\perp} cos^2\theta_p + \epsilon_{\|} sin^2\theta_p \tag{3.5}$$

where θ_p is the pretilt angle measured between the director and the plane of the substrate. The value of $\epsilon_{\|}$ should first be found using an infinite voltage extrapolation which can then be plugged into equation 3.5 and rearranged for $\epsilon_{\perp}$ with the measured pretilt and the total permittivity at $V < V_{th}$.

If the pretilt is unknown, then the WS approach can be applied to the measured $\epsilon(V)$ curves with θ_p as a fitting parameter, whereby the rate of change of the $\epsilon(V)$ curve gradient around V_{th} can be used to infer the value of θ_p. However, in fitting the $\epsilon(V)$ curves for $\epsilon_{\|}$, $\epsilon_{\perp}$, K_{11}, K_{33} and θ_p using the WS approach across the full voltage range, inaccuracies in each of the fitted parameters can be produced. Evidence of this can be seen in the WS fits shown in figures 3.16(a) and 3.16(b), as well as the fitting results and goodness of fit measures shown in tables 3.5 and 3.6, where the fitted curve shows significant deviations from the measured $\epsilon(V)$ data. In an attempt to improve the quality of the fit, particularly in the $V >> V_{th}$ region, $\epsilon_{\|}$was fixed to the value found from the $1/V$ extrapolation using equation 3.3c on region three of the $\epsilon(V)$ curve. This still did not, however, provide a satisfactory fit across the entire $\epsilon(V)$ curve.

By fixing $\epsilon_{||}$, the error of the fit in region one was reduced, but in region two and three, it was increased.

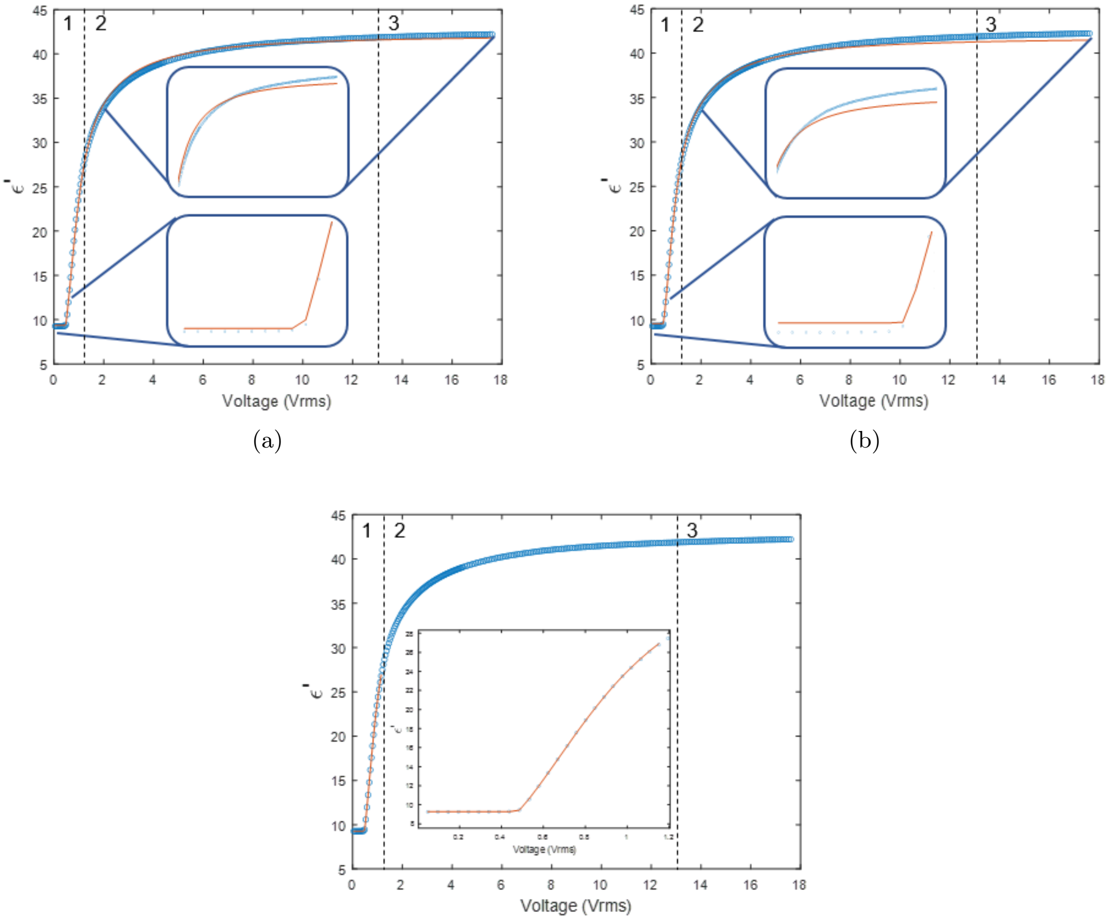

(a)

(b)

(c)

Figure 3.16: WS fitting of MLC6204 eps(V) curves at 25°C across the full voltage range with a) $\epsilon_{||}$, $\epsilon_{\perp}$, K_{11}, K_{33} and θ_p all as fitting parameters; b) with $\epsilon_{||}$ fixed to the value found from the infinite voltage extrapolation and c) a voltage range limited ($V \lesssim 2.5V_{th}$) WS fit with $\epsilon_{||}$ fixed to the value found from the infinite voltage extrapolation but $\epsilon_{\perp}$, K_{11}, K_{33} and θ_p all as fitting parameters. The curves are divided into three regions, the first of which is the $V < 2.5V_{th}$ region, the second is the transition region ad the third is the $1/V$ extrapolation region.

These problems in fitting with the WS approach are less of an issue with lower $\Delta\epsilon$ LCs but more so with higher $\Delta\epsilon$ LCs such as MLC6204 as used here. Due to the shape of the $\epsilon(V)$ curves in regions two and three for high $\Delta\epsilon$ LCs, the quality of the fit is significantly reduced compared to that of lower $\Delta\epsilon$ LCs. Ignoring this results in inaccurate values of K_{11}, K_{33}, $\epsilon_{||}$, and $\epsilon_{\perp}$ being determined from the fits. Thus, to negate these issues for high $\Delta\epsilon$ materials and more accurately determine K_{11}, K_{33}, $\epsilon_{||}$, and $\epsilon_{\perp}$, it is first necessary to achieve a satisfactory fit of the $\epsilon(V)$ curves at high V (in region three) to find $\epsilon_{||}$ and then subsequently around V_{th} (in region one) to find K_{11}, K_{33}, and $\epsilon_{\perp}$.

Firstly, to accurately determine $\epsilon_{\|}$, an infinite voltage extrapolation within regions three of the $\epsilon(V)$ curve is used. Then, by fixing $\epsilon_{\|}$ to the value found from the infinite voltage extrapolation, a voltage limited WS fit can be applied to region one of the $\epsilon(V)$ curve, where $V \lesssim 2.5V_{th}$. This enables a satisfactory fit to be applied to find $\epsilon_{\perp}$, K_{11}, K_{33} and θ_p, as shown in figure 3.16(c) and table 3.6. The error in the WS fit in region one of the $\epsilon(V)$ curve is significantly reduced by limiting the voltage range to be fit and fixing $\epsilon_{\|}$ to the value found from the $1/V$ extrapolation fit in region three which also gave a significantly lower χ^2 value. Using this fitting routine following the correction of the measured $\epsilon(V)$ curves enables one to accurately determine $\epsilon_{\|}$, $\epsilon_{\perp}$, K_{11} and K_{33} of high $\Delta\epsilon$ LCs whilst accounting for the pretilt.

Table 3.5: $\epsilon(V)$ fitting results for a) WS fitting across the entire voltage range with $\epsilon_{\|}$, $\epsilon_{\perp}$, K_{11}, K_{33} and θ_p all as fitting parameters; b) WS fitting across the entire voltage range with $\epsilon_{\|}$ fixed at the value found from the $1/V$ extrapolation and c) the voltage range limited ($V \lesssim 2.5V_{th}$) WS fitting with $\epsilon_{\|}$ fixed at the value found from the $1/V$ extrapolation. The insets in a) and b) show the fits around V_{th} in region 1 and the fits in regions 2 and 3 enlarged. The inset in c) shows the fit in region 1 enlarged.

Fit	$K_{11}(pN)$	$K_{33}(pN)$	$\epsilon_{\|}$	$\epsilon_{\perp}$	θ_p
a	7.2	14.1	43.7	9.3	0.1
b	7.6	11.3	43.2	9.5	0.1
c	7.2	11.6	43.2	9.3	0.1

Table 3.6: $\epsilon(V)$ 'goodness-of-fit' χ^2 values by region of the curve for a) WS fitting across the entire voltage range with $\epsilon_{\|}$, $\epsilon_{\perp}$, K_{11}, K_{33} and θ_p all as fitting parameters; b) WS fitting across the entire voltage range with $\epsilon_{\|}$ fixed at the value found from the $1/V$ extrapolation and c) the voltage range limited ($V \lesssim 2.5V_{th}$) WS fitting with $\epsilon_{\|}$ fixed at the value found from the $1/V$ extrapolation.

Fit	Region 1	Region 2	Region 3
a	0.098	0.40	0.16
b	0.084	0.54	0.58
c	0.0016	-	6.1×10^{-7}

3.4.4.3 AL Effect on Fitting Results

Following the fitting routine outlined in the previous section, for the high $\Delta\epsilon$ LC MLC6204 in $20\mu m$ PH cells, the magnitude of the effect of the AL thickness on the values of the elastic constants and permittivities can be found. Figure 3.17(a) shows that when correcting for thicker ALs, the value of K_{11} increases as h_{AL} increases, but K_{33} decreases. At $h_{AL} = 100nm$, the value of K_{11} is $\sim$ 10% larger than at $h_{AL} = 0nm$, whereas K_{33} is $\sim$ 4% lower than the value at $h_{AL} = 0nm$. The effect on $\epsilon_{\|}$, is the most significant of the permittivities, since the ratio $\epsilon_{\|}/\epsilon_{AL}$ is the largest. $\epsilon_{\|}$ at $h_{AL} = 100nm \sim 1.1$ times the value found at $h_{AL} = 0nm$.

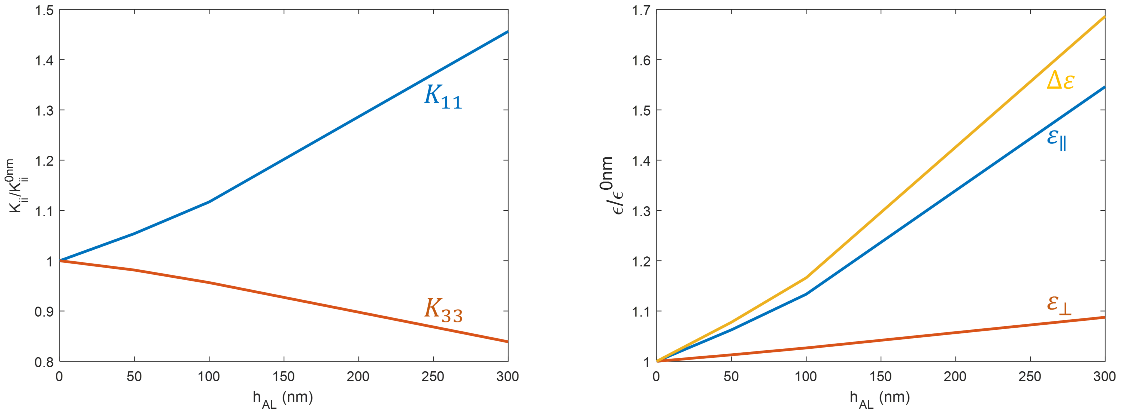

(a) (b)

Figure 3.17: Effect of AL thickness on MLC6204 $\epsilon(V)$ curve fitting results for a) elastic constants K_{11} (blue line) and K_{33} as well as b) permittivities $\epsilon_{\perp}$ (orange line), $\epsilon_{\|}$ (blue line) and $\Delta\epsilon$ (yellow line). All curves were fit using the WS model with $\theta_p = 2°$ and $\epsilon_{\|}$ found from the infinite voltage extrapolation for each AL thickness. Both the elastic constants and permittivity values have been normalised to the values found from fitting at $h_{AL} = 0nm$.

It is therefore evident, that by not correcting the $\epsilon(V)$ curves prior to performing fitting, inaccuracies in the values of the elastic constants and permittivities are created. The results here are for a $20\mu m$ cell and it should be noted that if a lower cell gap was used, the effect of the ALs on the $\epsilon(V)$ curve would be more pronounced and therefore fitting of the curves would return more inaccurate values for the elastic constants and permittivities, especially so if thicker ALs are used.

3.5 Summary

In this chapter, the practicalities of performing dielectric measurements and the determination of elastic constants of LCs in the LC test cells have been covered. The effects of the LC test cells themselves were first investigated using the isotropic dielectric liquid PCH32. LC test cells with and without PI ALs were used and the effects of ionic impurities at low frequencies were explored. It was found that the addition of PI thin film ALs increased the magnitude of EP at low frequencies in empty cells, but reduced the magnitude of the EP at low frequencies by acting as a blocking layer which separated the charged double layer from the electrode surface.

Consequently, the loss process associated with the ionic impurities forming the double layer was affected and rather than resulting from EP, was produced by Maxwell-Wagner IP at the AL surfaces. By doping of the PCH32 with 0.1wt% of the organic salt TBATPB, it was confirmed that these processes could be attributed to ionic impurities. Thus, it is necessary to take into consideration the effects of ionic impurities when dielectric spectroscopy measurements within LC test cells.

An equivalent circuit approach was used to model the complex capacitance spectra of PCH32 and 0.1%TBATPB-PCH32 in LC test cells across a frequency range of mHz to MHz. The circuit components required to assemble the equivalent circuits used to model the spectra attained from dielectric liquids in LC test cells were introduced. An equivalent circuit model was developed to accurately model the dielectric data and the effects of ionic impurities. An increase in the conductivity and changes to the low frequency ionic loss process were found as a result of organic salt TBATPB doping of the isotropic liquid PCH32. The differences in the EP effects due to the additional ionic impurities in the TBATPB doped PCH32 were accounted for by modifications to the values of Q_{dl} and n in the CPE used to model these effects. The use of a CPE in the equivalent circuit model enabled the middle frequency range to be modelled effectively, including the shape of the minima in the C" curves and the slightly sloped plateau in C' over the same frequency range.

In addition to the effects of the ALs at low frequencies, the AL effects at higher frequencies when performing $\epsilon(V)$ measurements were also investigated using an equivalent circuit approach. It was shown that for high ϵ materials with low ϵ ALs, the total measured ϵ is significantly lower than the true ϵ of the material. Furthermore, the voltage dropped across the ALs when performing $\epsilon(V)$ measurements in conjunction with the altered absolute value of ϵ significantly alters the $\epsilon(V)$ curves, which has major implications for the determination of the physical proprieties of the LC.

By applying a suitable equivalent circuit model to correct the $\epsilon(V)$ curves, the elastic constants K_{11} and K_{33}, as well as the permittivities $\epsilon_{\|}$ and $\epsilon_{\perp}$ could be determined more accurately. A new fitting routine was also proposed to do this, whereby an infinite voltage extrapolation was performed on the corrected $\epsilon(V)$ to find $\epsilon_{\|}$ which was then used as a fixed value to perform a WS fit at lower voltages around V_{th}, which accounted for the effects of non-zero pretilt in the cells. Using this fitting routine, the magnitude of the effect of the ALs on the fitting results for

K_{11}, K_{33}, $\epsilon_{\|}$, $\epsilon_{\perp}$ and $\Delta\epsilon$ was shown. This method of analysis was therefore developed to more accurately determine K_{11}, K_{33}, $\epsilon_{\|}$, $\epsilon_{\perp}$ for LC materials with a high $\Delta\epsilon$ and is later employed in chapter 5 to investigate the effects of surface functionalisation on the dielectric and elastic properties of LC nanocomposites.

Chapter 4

QD-LC Nanocomposite Phase Behaviour, Order and QD Self-Assembly

4.1 Introduction

This chapter is the first to concentrate on the properties of the QD-LC nanocomposites. The role of surface functionalisation within LC nanocomposites is investigated in order to understand how the use of mesogenic and non-mesogenic surface functionalisation is used to control both the nanocomposite properties and subsequently the self-assembly of nanomaterials. The fluorescence properties of the QDs and the QD-LC nanocomposites are first determined so that fluorescence microscopy can be properly utilised to study the QD self-assembly within the nanocomposites. The effect of the CdSe QD surface functionalisation on the nematic-isotropic phase transition is studied using a combination of polarising optical microscopy (POM) and differential scanning calorimetry (DSC). These effects are then related to the different types of QD micro-structures that are self-assembled through the isotropic-nematic transition.

The QD-LC nanocomposites used in this chapter were prepared according to the procedure outlined in chapter 2 section 2.3.2. A total of three different CdSe QDs were used, with two different types of surface functionalisation, one of which was mesogenic and the other non-mesogenic. The CdSe QDs with non-mesogenic octadecylamine (ODA) ligands (chemical structure shown in figure 4.1(a)) are referred to as ODAQDs. The expected anchoring of the ODAQDs can be seen in the schematic cartoon shown in figure 4.1(b)). The mesogen functionalised CdSe QDs with mesogenic ligands connected to the QD surface via a flexible alkyl linker and hexanethiol co-ligands (chemical structures shown in figure 4.1(c) and 4.1(d)) are referred to as LCQDs. A schematic cartoon of their structure and the expected alignment of the mesogenic groups with the host LC in the nanocomposites can be seen in figure 4.1(e).

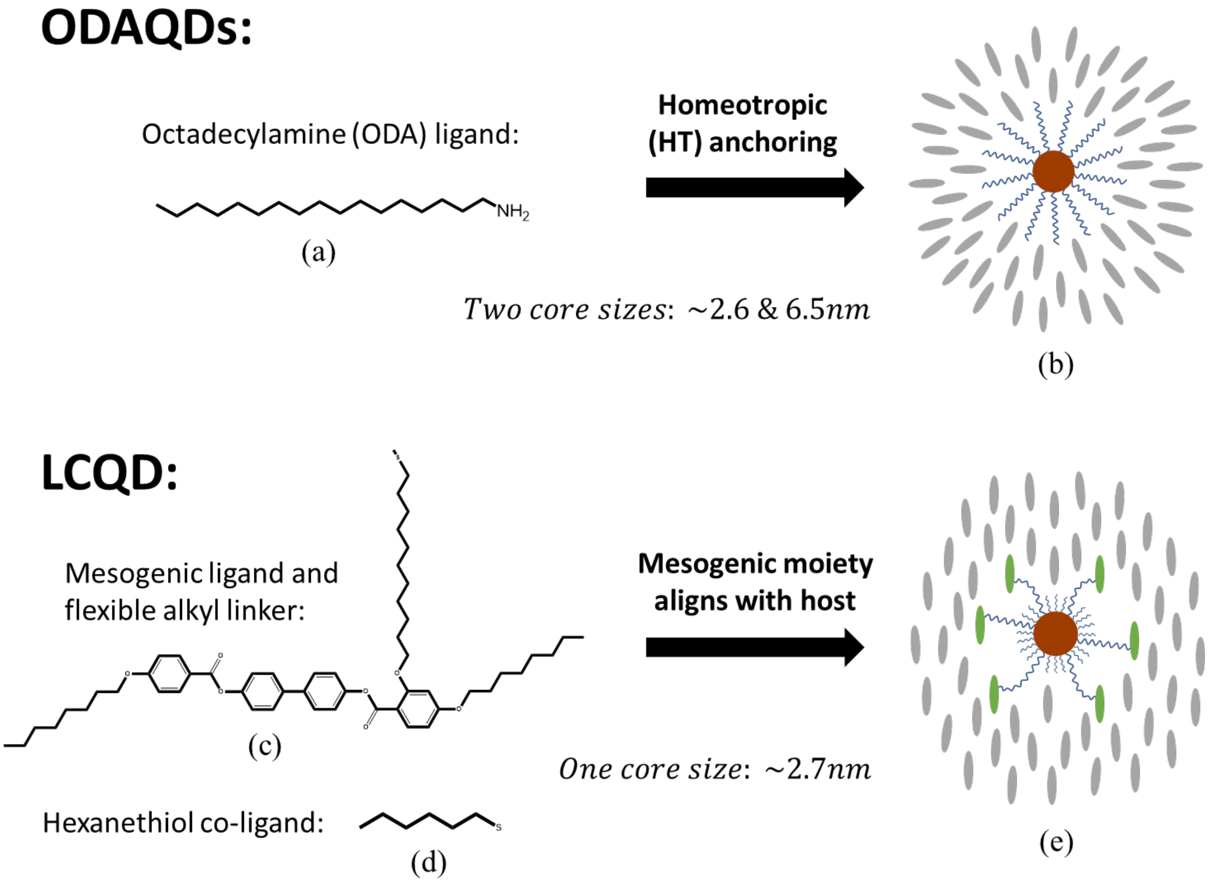

Figure 4.1: Chemical structures of CdSe QD surface functional groups and schematic cartoons of the expected anchoring/alignment of the LC host in the QD-LC nanocomposites. a) ODAQDs with b) expected anchoring of the host and c) mesogenic ligand, d) Hexanethiol co-ligand of LCQD with e) expected alignment of the host NLC and mesogenic ligands at the QD surface.

4.2 Fluorescence Properties

The fluorescence properties of the LCQD and ODAQDs were measured according to the procedures outlined in chapter 2 section 2.4.3. The fluorescence properties were measured both in solution in toluene and in the host LC MLC6204. Figure 4.2(a) shows a comparison of the fluorescence spectra from the different QDs in toluene at room temperature.

Both of the ODAQDs clearly show a singular sharp main band edge emission peak. The different wavelength of these peaks correspond to the different QD core sizes, the smaller ODAQD has a main band edge emission peak at $\lambda_{em} \approx 530nm$ when excited at $\lambda_{ex} = 320nm$ and is therefore referred to as ODA$_{530}$QD. Whereas the larger ODAQD has a main band edge emission peak at $\lambda_{em} \approx 650nm$ when excited at $\lambda_{ex} = 610nm$ and is therefore referred to as ODA$_{650}$QD. The LCQD, however, shows a main edge emission peak at $\lambda_{em} \approx 537nm$ and another broader emission peak at longer wavelengths with a peak at $\sim 745nm$ when excited at $\lambda_{ex} = 400nm$. This longer wavelength emission peak corresponds to emission via surface deep trap states which exist on the QD surface due to structural imperfections of the core.

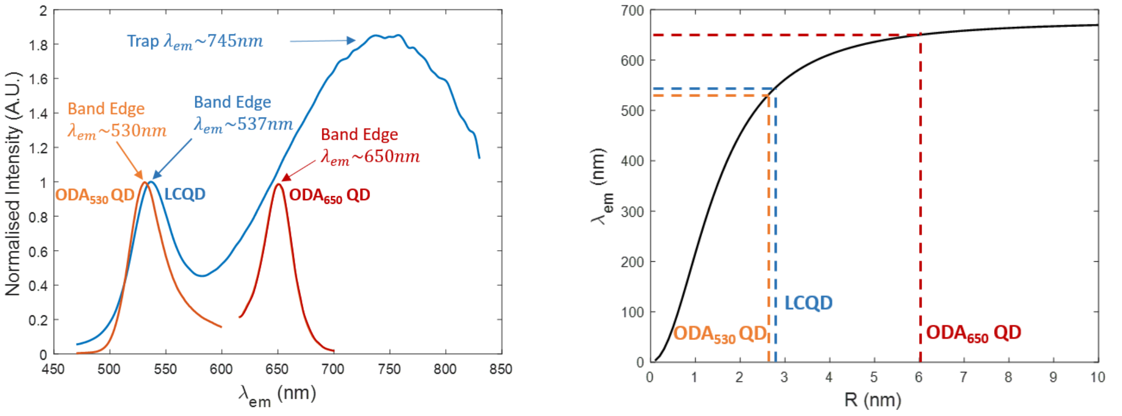

Figure 4.2: a) Fluorescence emission spectra of LCQD excited at $\lambda_{ex} = 400nm$ (blue), ODA$_{530}$QD excited at $\lambda_{ex} = 320nm$ (orange) and ODA$_{650}$QD excited at $\lambda_{ex} = 610nm$ (red) in toluene at room temperature. b) size dependence of the peak emission wavelength of CdSe QDs according to the Brus model (equation 1.56) using $E_g^{Bulk} = 1.84eV$, $m_e = 0.13m_0$, $m_h = 0.3m_0$ and $\epsilon = 9.56$.

The full absorbance, fluorescence excitation and emission spectra for the LCQD, ODA$_{530}$QD and ODA$_{650}$QD in toluene are shown in figures A.1(a), A.1(b) and A.1(c) respectively. The full emission maps of the LCQD and ODA$_{650}$QD in toluene are also shown in figures A.2 and A.3 respectively. The fluorescence properties of the host LC MLC6204 are shown in figures A.1(d) and A.4. Full emission maps as a function of excitation wavelength of the LCQD both in toluene and as a a nanocomposite in MLC6204 can also be seen in figuresA.2 and A.5 respectively, showing the effect of the dispersing into the host LC MLC6204. For comparison, an emission map of the ODA$_{650}$QD in toluene can also be seen in figure A.3.

Figure 4.3 illustrates the difference between band edge emission and trap emission via surface trap states which have an energy level somewhere between the conduction and valence band, hence the longer wavelength of emission when electrons relax back to the valence band from the conduction band via these trap states. The intensity of trap emission relative to the band edge emission is dependent upon the density of surface deep trap states which is influenced by QD size, surface functionalisation and the surrounding solvent the QDs are dispersed into [180]. It has been shown that QDs with smaller core sizes exhibit higher intensity trap emission due to the higher density of surface trap states which arise due to the increased surface to volume ratio of the smaller QDs [181].

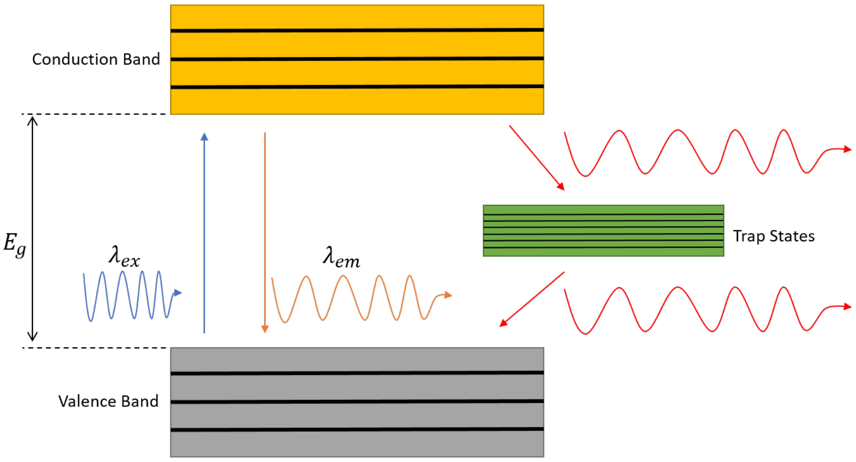

Figure 4.3: Schematic diagram of QD band edge emission and QD trap emission.

Certain types of ligands are known to increase the density of surface deep trap states and therefore increase the intensity of trap emission whilst quenching band edge emission. Such molecules include thiols, which have been used to tune the trap emission intensity through a ligand exchange process with amine ligands [182]. This effect arises due to the increased quantum yield, which results from the attachment of amine groups to the QD surface that bind to the Cadmium atoms and form a donor/acceptor bond. This eliminates electron relaxation via the surface deep trap states [183, 184]. Hence, the difference in relative trap emission intensity between the LC QD and ODAQD seen here. The LCQD has a significant number of hexanethiol groups attached the QD surface, whereas the ODA QD has none, thus reducing the density of surface deep trap states. Additionally, a comparison between the LCQD before (hexane thiol only) and after ligand exchange (hexane thiol and mesogenic groups with alkyl amine linker) shows a further increase in the relative intensity of the trap emission for the QD with only hexanethiol surface functionalisation.

The wavelength of the main band edge emission of QDs can be modelled using the Brus equation (equation 1.56) and is shown in figure 4.2(b) for CdSe QDs. The peak wavelength of the band edge emission from the LCQD, therefore corresponds to an average core radius of $\sim 2.7nm$. As for the ODAQDs, the ODA$_{530}$QD emission corresponds to an average core radius of $\sim 2.6nm$, comparable to that of the LCQD. The larger ODA$_{650}$QD emission corresponds to a core of $\sim 6.5nm$ radius, significantly larger than both.

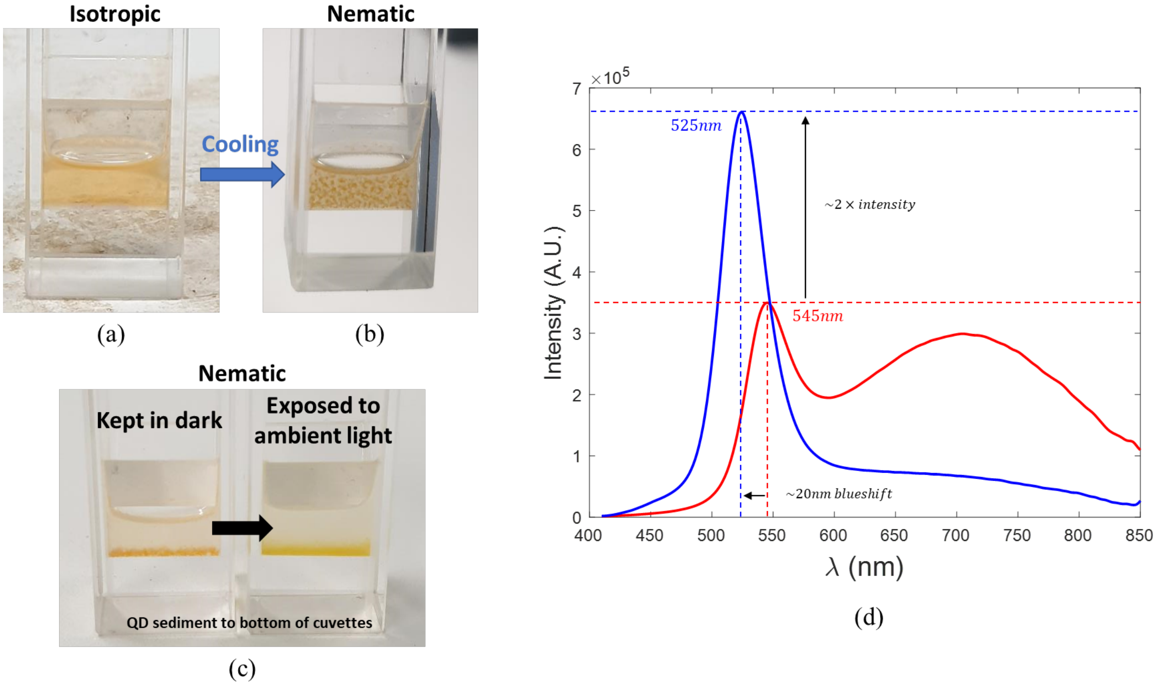

Figure 4.4: $0.43wt\%$LCQD nanocomposite a) well dispersed in the isotropic phase and b) after cooling into the nematic phase where regions of high QD concentration can be seen. c) Sedimentation of the QDs to the bottom of the cuvette and also the change in colour from being exposed to ambient light for several days. d) The fluorescence emission spectra of the $0.4wt\%$LCQD nanocomposite in the nematic phase, before (red line) and after (blue line) exposure to ambient light for several days.

When dispersed into the LC at high enough concentrations, the LCQD showed a slight red shift of the main band edge emission peak from $\lambda = 537nm$ in toluene to $\lambda = 545nm$ when cooled into the nematic phase as shown in figures 4.4(b) and 4.4(d). This red shift of the fluorescence peak from the high concentration LCQD nanocomposites in the nematic phase is thought to arise as a result of Forster resonance energy transfer (FRET) between closely packed QDs [185]. After cooling into the nematic phase, the initially well dispersed QDs separate into regions of high QD concentration with close QD packing and regions of lower QD concentration where the QD are better dispersed and thus not packed as closely. In the regions with close QD packing, resonant energy transfer from smaller to larger QD takes place thus quenching the fluorescence emission of the smaller dots whilst enhancing the fluorescence emission of the larger dots, which results in a red shift of the overall main band edge emission peak from the full QD population

[186, 187, 188].

The fluorescence properties of the LCQD in the nanocomposite were also affected by exposure to ambient light. Figure 4.4(c) shows the visual difference between the $0.4wt\%$LCQD nanocomposite following prolonged exposure to ambient light. The main band edge emission peak of the LCQD in MLC6204 was blue shifted and the intensity enhanced, whereas the trap emission was also quenched, as shown in figure 4.4(d). Thus, when performing FM on the nanocomposites, the fluorescence wavelength can change depending on the degree of exposure the sample has already had and so variation in the colour of the QD in the FM images varies slightly.

The underlying cause of this change to the LCQD fluorescence spectra is thought to arise from a photoetching process. Exposure of QDs to light under certain conditions has been previously been used to control the fluorescence wavelength of QDs through a reduction in their size by etching material away from the surface of the QDs, thereby reducing their size and subsequently the wavelength of their fluorescence emission [189]. The extent to which this effect takes place and hence the reduction of the QD core size and subsequent degree to which the fluorescence is blue shifted depends on both the irradiation wavelength and exposure time [190]. The photoetching of the LCQD seen here, is thought to not only reduce the effective core size of the QDs, but also reduce the density of surface trap states. This can be seen from the fluorescence spectra in figure 4.4(d), which shows a significant reduction in the intensity of the trap emission whilst simultaneously increasing the intensity of the main band edge emission by approximately 2 times.

The range of QD concentrations of the ODA_{530}QD nanocomposites from low to high QD concentrations under white light can be seen in figure 4.5. The top of the image shows the nanocomposites in the isotropic phase immediately following the final sonication step of the nanocomposite preparation process and the bottom image shows the same samples once cooled into the nematic phase. Only the ODA_{530}QD nanocomposites are shown here, but these samples are also representative of the appearance of the LCQD and ODA_{650}QD nanocomposites across comparable concentration ranges, showing a similar colour gradient with increasing QD concentration. The appearance of the LCQD nanocomposites were very similar to the ODA_{530}QD nanocomposites, whereas ODA_{650}QD nanocomposites showed a dark red/brown colour due to their larger core size.

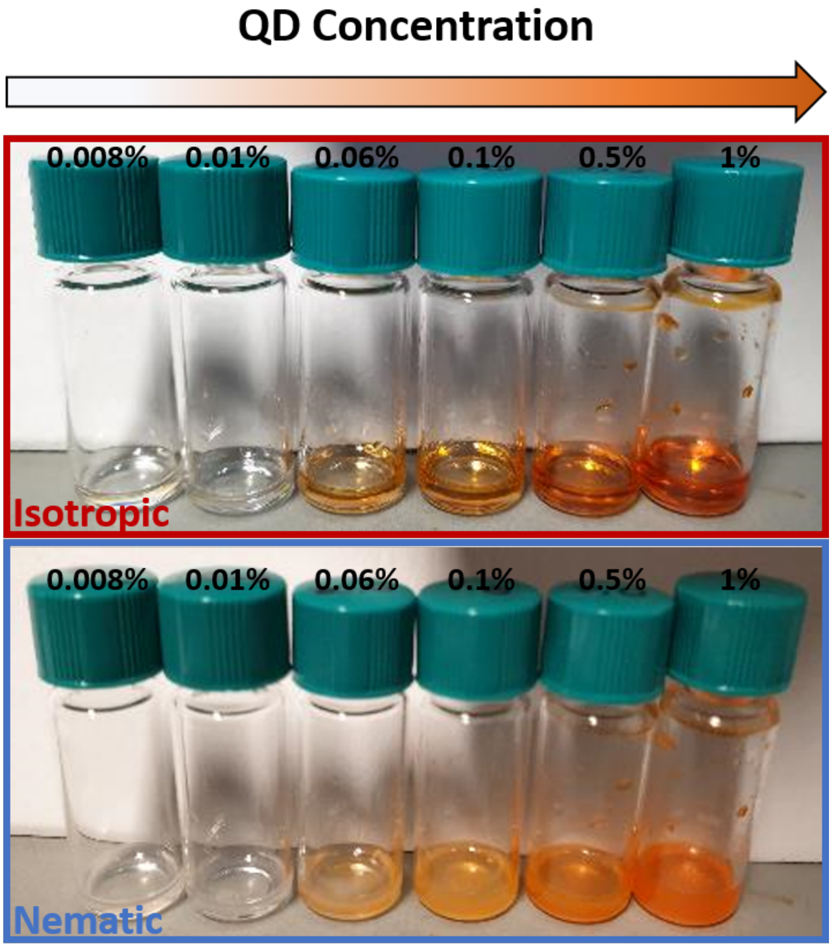

Figure 4.5: Concentration range of $ODA_{530}QD$ nanocomposites in MLC6204 in the isotropic phase (top - red) following sonication and after cooling into the nematic phase (bottom - blue).

4.3 Nematic-Isotropic Phase Transitions

The phase behaviour, in particular, the nematic-isotropic phase transition of the QD-LC nanocomposites was studied using both DSC and POM. It should be noted, that all of the POM phase transition temperature measurements presented here were performed using PH cells. The nematic-isotropic phase transition temperature (T_{NI}) was measured for the LCQD, $ODA_{530}QD$ and $ODA_{650}QD$ nanocomposites as a function of QD concentration. The enthalpies (ΔH) of the phase transitions are also measured. Firstly, the measured DSC curves of the different DSC curves are presented, followed by a description of the analysis methods used to find the T_{NI} and ΔH values. A comparison of the phase behaviour between the different QDs is then made and related to the effect of the surface functionalisation.

4.3.1 DSC Traces

DSC traces of the isotropic-nematic transition were taken on cooling at 10°C and are shown for the LCQD in figure 4.6(a), for the ODA$_{530}$QD in figure 4.6(b) and for the ODA$_{650}$QD in figure 4.6(c). No visible change to the transition peaks was seen as a result of doping with the LCQD, even up to concentrations of 1wt%. Both ODAQDs on the other hand show both a significant reduction in the temperature at which the transition takes place, thus reducing T_{NI}, but also a significant softening of the transition indicated by the 'flattening' and 'broadening' of the peaks. which becomes more prominent at higher QD concentrations.

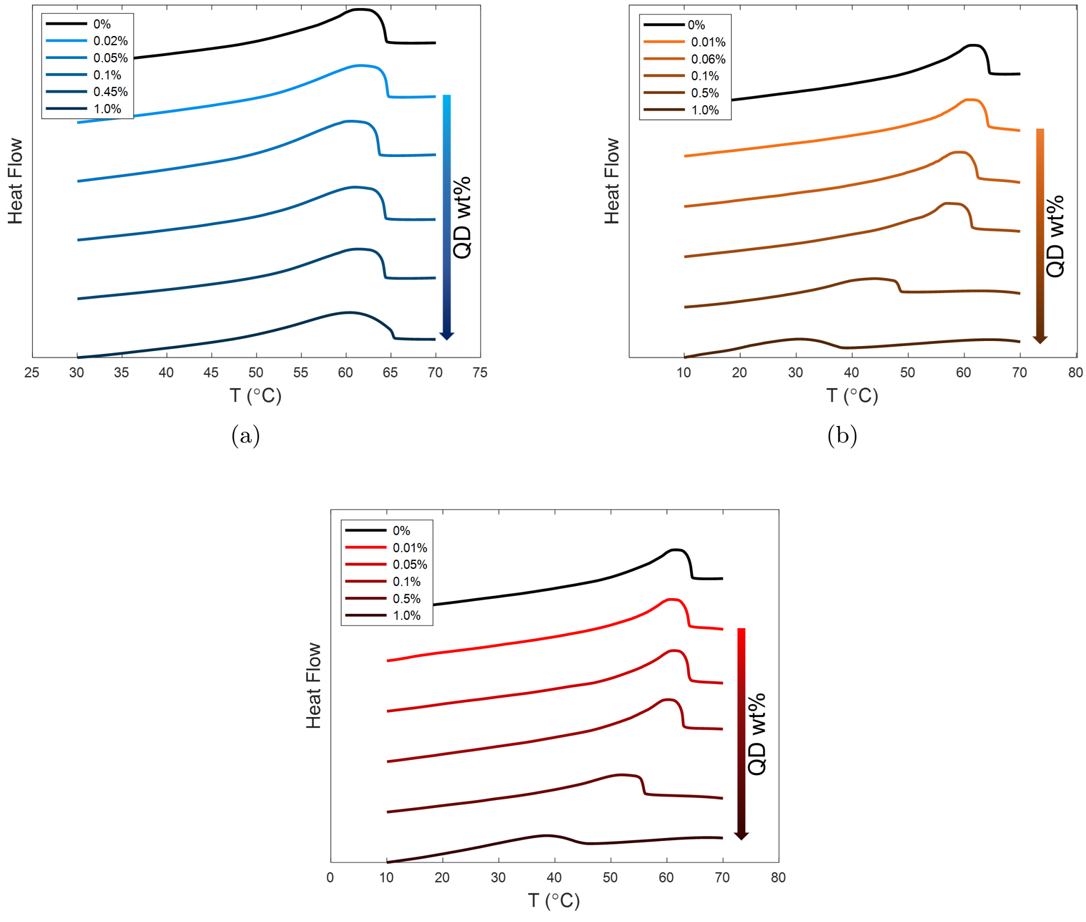

(a)

(b)

(c)

Figure 4.6: DSC traces on cooling from the isotropic to nematic phase at 10°C of a) LCQD, b) ODA$_{530}$QD and c) ODA$_{650}$QD nanocomposites in MLC6204 at increasing concentrations.

4.3.2 DSC Trace Analysis

The T_{NI} of the nanocomposites were taken as the onset of the DSC peak on cooling by applying two linear fits and finding their point of intersection as shown in figure 4.7(a). One of the fits was applied to the baseline above the transition, and the other was applied to the approximately linear region of the peak at temperatures just below the onset of the transition. These two linear fits were extrapolated to find their point of intersection (black circle in figure 4.7(a)), which was taken as the value for T_{NI}. To find the nematic-isotropic phase transition enthalpies (ΔH), the area under the transition peaks of the DSC curves on cooling in figures 4.6(a), 4.6(b) and 4.6(c) were calculated. To do so, the gradient of the curves in the isotropic phase just above T_{NI} was extrapolated to meet the curve below the transition to account for the sloping baseline. The area enclosed by this extrapolation and the DSC curve at the transition peak, which is shown as the shaded region in figure 4.7(b) was taken as the value for ΔH. The region of the curve in the isotropic phase just above T_{NI} was used to perform the linear fit for the extrapolation and was also used in the fitting to find T_{NI}.

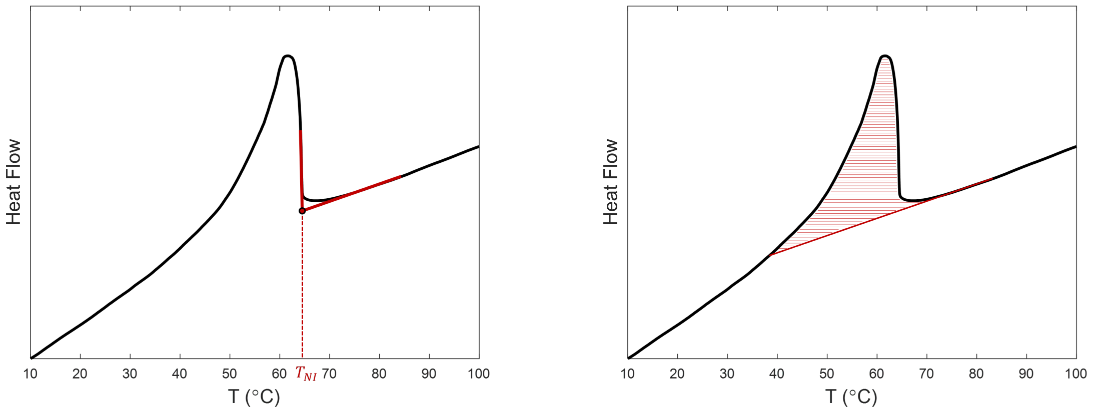

(a)

(b)

Figure 4.7: Examples of DSC heat flow fitting to find a) T_{NI} shown by the black circle at the intersection points between the two linear extrapolations and b) ΔH which is found from the area under the transition peak shown by the shaded region. The curves shown here are for pure MLC6204 on cooling at $10°C$.

4.3.3 Transition Temperatures and Enthalpies

The T_{NI} results of the DSC curve fitting are compared for all of the QD types as a function of their concentration in figure 4.8(a). The LCQD does not change T_{NI} within error for any of the concentrations measured, thus indicating that the side on mesogenic moieties attached to the QD surface are not disrupting the order of the host LC. Both ODAQDs, however, do significantly reduce T_{NI}, and more so with the smaller QD size for the same concentration. This suggests the ODA ligands, do significantly disrupt the director of the host LC, reducing the overall order in the nanocomposite.

For the DSC T_{NI} measurements, a single linear fit was applied for each QD, for which the y-intercept $T_0 = 64.8°C$ is the T_{NI} of the pure LC host MLC6204. The gradients of the fits were found to be $-0.3 \pm 0.6°C/wt\%$, $-27 \pm 2°C/wt\%$ and $-18 \pm 1°C/wt\%$ for the LCQD, ODA$_{530}$QD and ODA$_{650}$QD respectively. The difference in gradients between the two ODAQD sizes could be a result of the different volume fraction of the QDs. The smaller QDs have a larger surface to volume ratio than the larger QDs and for the same mass of QD added to the LC, there is a larger number density of QD, and thus a higher volume fraction of QD, which therefore more significantly disrupts the director of the host LC.

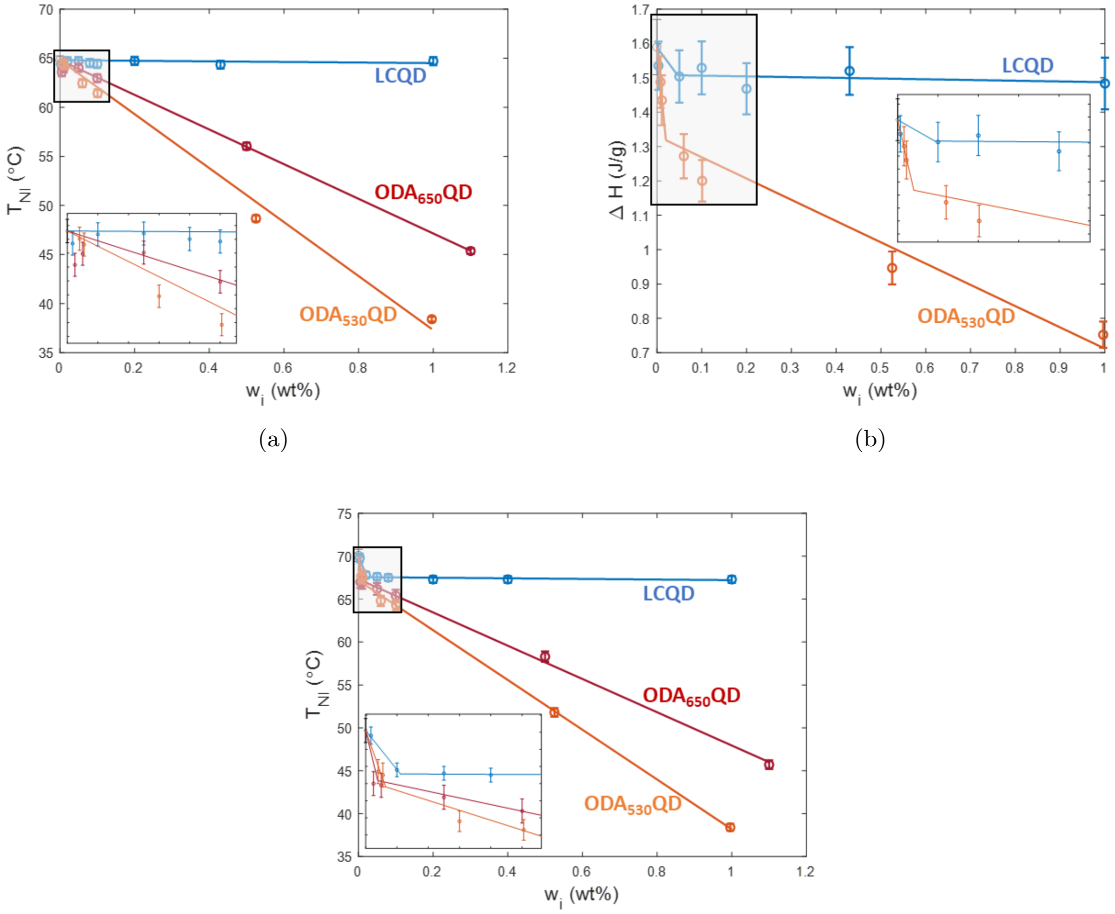

(a)

(b)

(c)

Figure 4.8: a) Nanocomposite T_{NI} measured at the onset of the exothermic peak in the DSC trace measured on cooling at $10°C$ from the isotropic to nematic phase and b) the corresponding enthalpy of the phase transition measured as the area under the same peaks. c) shows the phase transition temperatures measured in $20\mu m$ PH cells using POM on cooling at $1°C/min$. The maximum error in the DSC T_{NI} measurements was $\pm 0.4°C$ and in the POM measurements it was $\pm 0.7°C$.

The T_{NI} of the nanocomposites measured using POM in $20\mu m$ PH cells can be seen in figure 4.8(c), which, unlike the measurements performed using DSC, shows an initial steep decrease in T_{NI} at low QD concentrations, which then becomes less steep at higher concentrations. It is thought that the two approximately linear regions are not seen in the DSC T_{NI} measurements, potentially because of the faster cooling rate used than in the POM measurements. This type of behaviour is seen for each of the QD types, albeit with different gradients in the different regions which occur at different QD concentrations. The two regions, which can be approximated as linear has been previously been predicted theoretically by Osipov and Gorkunov [123], and also shown experimentally in nanocomposites of NPs in both low molecular weight LC and polymeric LCs [124]. The proposed, qualitative phase diagrams for this type of behaviour of the LCQD and ODAQD nanocomposites are shown in figures 4.9(a) and 4.9(b) respectively.

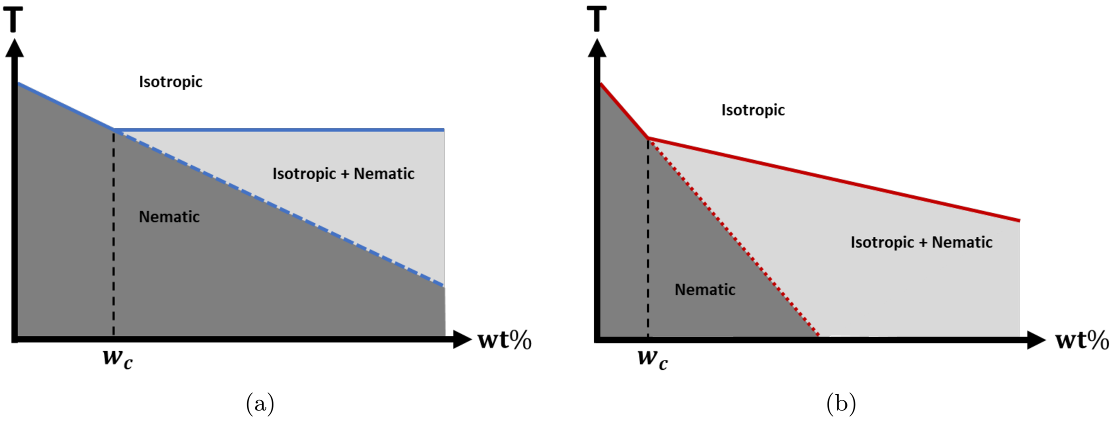

(a) (b)

Figure 4.9: Proposed phase diagrams of a)LCQD and b) ODAQD nanocomposites.

This two region type of behaviour corresponds to the point at which phase coexistence of a QD rich (high QD concentration) isotropic phase and QD poor (low QD concentration) nematic phase can exist. At QD concentrations below this critical concentration w_c, as the temperature is decreased, the nanocomposite transitions directly from the isotropic to the nematic phase. It is in this first low QD concentration region in which T_{NI} steeply decreases as the QD concentration increases. Above w_c, the nanocomposites first transition into the phase coexistence region before transitioning into the wholly nematic state. As the temperature is decreased through the phase coexistence region, the volume of isotropic phase decreases, whilst the volume of nematic phase increases until the entire nanocomposite is nematic.

Rough estimates of the temperature range over which the phase coexistence region extends can be made through studying the samples on cooling using a combination of POM and FM. It was found for both the LCQD and ODAQDs, that the range temperature range over which the isotropic and nematic phase coexists, increases with increasing QD concentration as predicted by Osipov and Gorkunov [123]. In the case of the LCQD nanocomposites at a QD concentration of $1wt\%$, the isotropic and nematic phase coexistence was seen up to $10°C$ below the initial T_{NI}. In the case of the ODAQDs, however, this temperature range was found to extend significantly further. The ODA$_{530}$QD nanocomposites showed evidence of phase coexistence at temperatures over $20°C$ below the initial T_{NI}. This is to be expected though, since the increase in QD concentration within the remaining isotropic regions, further decreases T_{NI}, therefore preventing the isotropic to nematic transition within these regions.

Interestingly, the LCQD nanocomposite shows the steep decrease in T_{NI} at low QD concentrations, but then at higher concentrations above w_c, similarly to the DSC T_{NI} does not decrease with increasing concentration. Both ODAQDs in the higher concentration also gave the same gradient past w_c as the DSC within error. These gradients found in the high concentration region of the POM measurements were $0.1 \pm 0.5°C/wt\%$, $-26 \pm 4°C/wt\%$, $-17 \pm 1°C/wt\%$ for the LCQD, ODA$_{530}$QD and ODA$_{650}$QD respectively. The critical concentrations found from the linear fitting are summarised in table 4.1. The critical volume fractions (ϕ_c) were estimated from w_c through the core sizes of the different QDs calculated from their fluorescence using the Brus equation and assuming that the mass of the QD and surface groups is approximately just the mass of the QD core since the mass density of the ligands are negligible compared to the mass density of the QD cores. As expected, the LCQD nanocomposites showed the highest values of both w_c and ϕ_c due to the mesogenic surface functionalisation. The ODA$_{530}$QD showed significantly higher critical values of w_c and ϕ_c than the ODA$_{650}$QD, thus suggesting there is some kind of intrinsic size dependence of the QD miscibility. A comparison of these ϕ_c estimates to the theoretically predicted values by Osipov and Gorkunov reveals that the values measured here are significantly lower. It is likely that this is due to the choice of interaction parameters used in the model.

Table 4.1: Critical QD concentrations from two region linear fitting of POM T_{NI} measurements of QD-LC nanocomposites.

QD Type	$w_c(wt\%)$	$\phi_c(v\%)$
LCQD	0.022 ± 0.008	~ 0.372
ODA$_{530}$QD	0.013 ± 0.001	~ 0.043
ODA$_{650}$QD	0.008 ± 0.001	~ 0.006

The nematic-isotropic phase transition enthalpies (ΔH) found from the area under the DSC curve transition peaks are plotted in figure 4.8(b). The same type of two region behaviour seen in the POM T_{NI} measurements was revealed. The critical concentrations found from linear fitting of these two regions are not equivalent to those found from the fitting of the POM T_{NI} measurements, but do show the same trend between the different surface fictionalisations. The mesogenic surface functionalisation significantly increases the critical QD concentration by approximately ten times when calculated from the ϕ_c values.

4.4 Refractive Indices and Order Parameters

The phase behaviour of the QD-LC nanocomposites, which was shown in section 4.3, was found to depend on the type of QD surface functionalisation. This dependence of the phase behaviour is thought to arise from the disruption of the host LC director, where, the mesogenic surface functionalisation of the LCQD causes minimal disruption to the director, but the alkyl chain functionalisation of the ODAQDs, causes significant disruption to the director due to HT anchoring of the host at the QD surface. This disruption of the host director is manifested as a reduction in S and T_{NI}. Thus, in order to quantify the level of distortion created by the QDs as a result of their different surface functionalisation, the order parameter of the QD-LC nanocomposites was determined. To do so, the refractive indices of the nanocomposites were first measured using an Abbe refractometer according to the method outlined in chapter 2 section 2.4.7.

The refractive indices were then fit using equation 1.39 on a Haller plot of $log\left(\frac{n_e^2-n_o^2}{n^2-1}\right)$ against the reduced temperature $(1-\frac{T}{T^*})$. T^* is the temperature at which $S=0$ following an extrapolation of S to $T>T_{NI}$ which is $1-2$°C above T_{NI} for a typical NLC. Thus, in order to properly perform a Haller fit of the refractive index data, T^* should be included as a fitting parameter in equation 1.39, whereby the correct choice of T^* would minimise the error of the fit for a given value of β and $\frac{\Delta\alpha}{\bar{\alpha}}$. Here, however, defining T^* for the QD-LC nanocomposites is difficult, since, particularly in the case of the ODAQD nanocomposites at higher QD concentrations, the nematic-isotropic transition is softened. Thus, to perform the Haller fitting, the T_{NI} found from the refractive index measurements was used as the value for T^*. The T_{NI} value was defined as the point at which splitting of the unpolarised n_{iso} line into the polarised n_e and n_o lines was seen through the refractometer.

The refractive indices of the pure MLC6204 were first fit to find the value of $\frac{\Delta\alpha}{\bar{\alpha}} = 0.46 \pm 0.01$. This was then fixed in all subsequent Haller fitting of the nanocomposites, as it was assumed that the isotropic QDs do not have a measurable effect on the molecular polarisability of the LC. Once the Haller fitting had been performed for each of the nanocomposites, S was calculated from equation 1.4 by raising the reduced temperature to the exponent β found from the fitting, again using $T^* = T_{NI}$. The quality of (all) the Haller fits, measured by the R^2 value can be found in table 4.2, and the resulting β values with associated standard error can be seen in table 4.3. The error in S was calculated from error propagation of equation 1.4.

4.4.1 LCQD Nanocomposites

The refractive indices, Haller plots and resulting order parameter for the LCQD nanocomposites at $0wt\%$, $0.1wt\%$ and $1wt\%$ QD concentrations are compared in figures 4.10(a), 4.10(b) and 4.10(c) respectively. Unexpectedly, a reduction in S was found from the addition of the LCQDs, with increasing concentration. The error in S increased with decreasing T from, $\Delta S \approx 0.07\%$ at $T/T_{NI} \approx 0.99$ to $\Delta S = 0.3\%$ at $T/T_{NI} = 0.82$. The reduction in S though, was more significant than the random error across the entire nematic range, hence, it was due to a systematic error in the measurement. A manifestation of alignment effects between the prisms in the Abbé refractometer were to blame.

The LCQD nanocomposites were found to give poor HT alignment, with significant regions of the sample in PH alignment in HT cells, particularly so when using CTAB AL's as done for the pure LC and ODAQD nanocomposites. Hence, PH alignment using PVA ALs on the Abbe prisms was used for the LCQD nanocomposites. This gave good PH alignment between the prisms, but with some level of pretilt, which increases with increased QD concentration. Thus, the values of n_e were reduced slightly in the LCQD nanocomposites when compared to the pure LC (figure 4.10(a)), due to a contribution from n_o. The $1wt\%$ nanocomposite showed a $\sim 0.02\%$ average increase across the nematic range, with the increase becoming more significant approaching T_{NI}. Interestingly, the gradient of $n_e(T)$ for the $1wt\%$ LCQD nanocomposite differed significantly from the gradient of the pure LC. At $T/T_{NI} < 0.96$, n_e of the LCQD nanocomposite was increased, but at $T/T_{NI} > 0.96$, n_e was decreased compared to n_e of the pure LC.

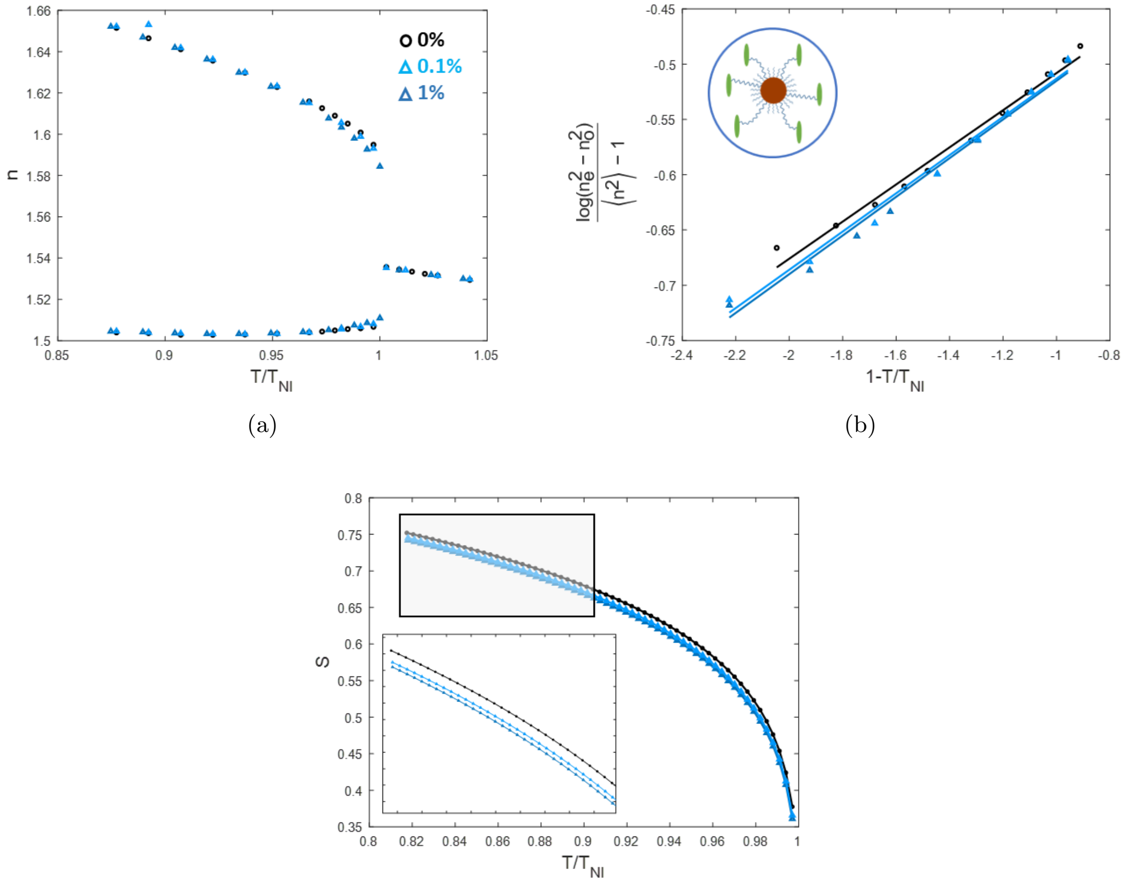

(a)

(b)

(c)

Figure 4.10: a) Refractive Indices, b) Haller Plots and c) order parameter of LCQD nanocomposites at $0wt\%$ (black circles), $0.1wt\%$ (light blue triangles) and $1wt\%$ (dark blue triangles) QD concentrations in the host LC MLC6204. Error bars have not been included on these plots as they are of the same size or smaller than the data points, all values of n are within ± 0.001.

4.4.2 ODAQD Nanocomposites

The ODA_{530}QD nanocomposites showed a significant reduction in S with increasing QD concentration, as was expected from the T_{NI} decrease with increasing QD concentration. Isotropic and nematic phase coexistence could clearly be seen, as there was not a well defined splitting of the n_{iso} line into the n_e and n_o lines as the temperature was decreased. Instead, the n_e and n_o lines appeared whilst the n_{iso} line remained over a large temperature range. This effect became more pronounced at higher QD concentrations and the temperature range over which this phase coexistence could be seen became larger. It should be noted, that in this phase coexistence temperature region, n_{iso} has not been plotted in figure 4.11(a). The increase in gradient of the Haller plots (figure 4.11(b)) can clearly be seen, which results in the increased β values from fitting, which subsequently reduce the calculated values of S in figure 4.11(c).

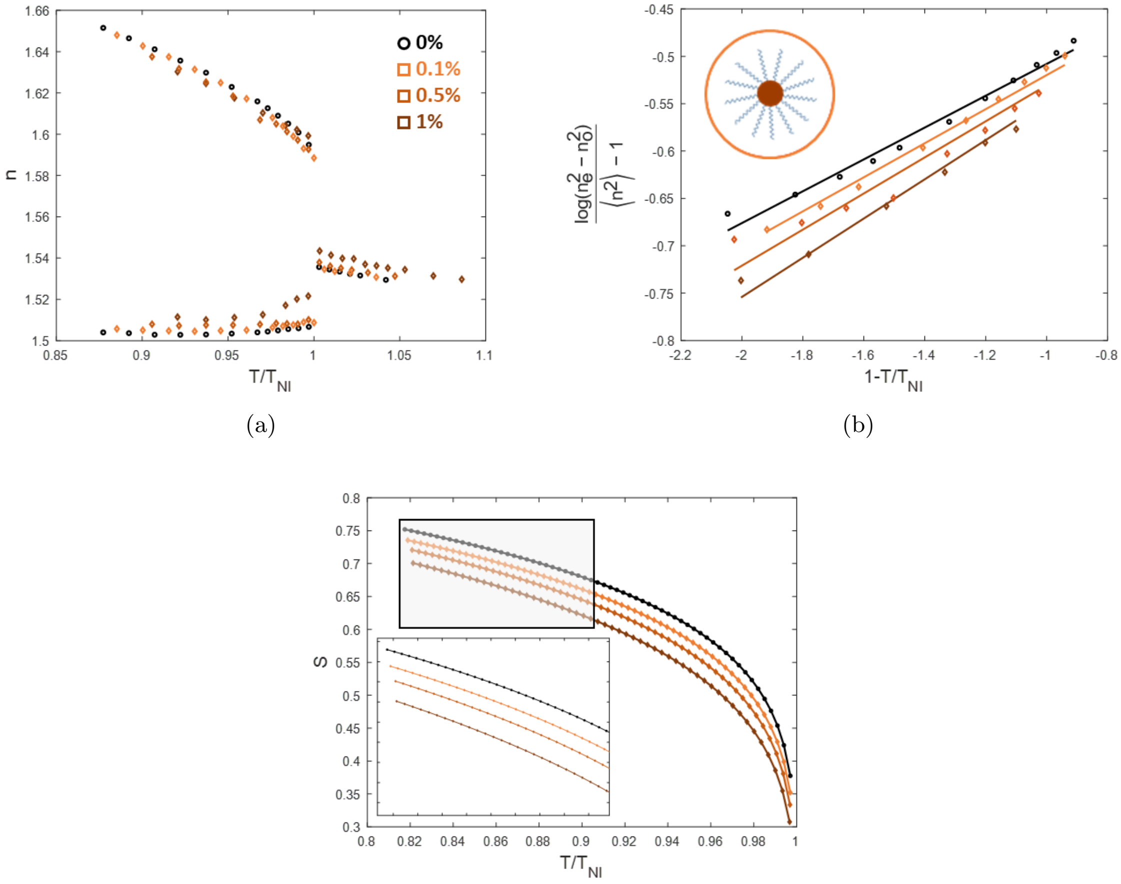

(a)

(b)

(c)

Figure 4.11: a) Refractive Indices, b) Haller Plots and c) order parameter of ODA$_{530}$QD nanocomposites at $0wt\%$ (black circles), $0.1wt\%$ (light orange squares), $0.5wt\%$ (mid orange squares) and $1wt\%$ (dark blue squares) QD concentrations in the host LC MLC6204. Error bars have not been included on these plots as they are of the same size or smaller than the data points.

The ODA$_{650}$QD nanocomposites also show a reduction in S as one would expect from the reduced T_{NI}. Unlike the ODA$_{530}$QD nanocomposites, however, a linear reduction in S at a given T/T_{NI} with increasing QD concentration is not seen. The $0.1wt\%$ QD concentration nanocomposite shows a much less significant reduction in S than expected, which could be due to an error in the concentration of QD in the nanocomposite. At high QD concentrations ($1wt\%$) in both the ODA$_{530}$QD and ODA$_{650}$QD nanocomposites, an increase of n_{iso} is seen. It is thought this is due to segregation of the QDs to the prism surfaces as has been seen in cells both with and without ALs. The reason this has primarily affected the $1wt\%$ nanocomposites rather than the lower concentrations is because the refractive index measurements for these samples was taken on heating rather than cooling, thus the QD migration was able to take place following the first transition from the isotropic to nematic phase. As a result, it is possible that the order of these nanocomposites may be even lower than was measured as there are less QDs in the bulk when the refractive index measurements were performed.

Both the ODAQD nanocomposites showed a significantly larger error in S as a result of the increased standard error in β from Haller fitting. The largest error was found for the $1wt\%$ ODA$_{650}$QD nanocomposite of $\Delta S \approx 0.1\%$ at $T/T_{NI} \approx 0.82$, which fell to $\Delta S = 0.3\%$ at $T/T_{NI} = 0.99$. The $0.5wt\%$ ODA$_{530}$QD nanocomposite showed the largest error out of the three ODA$_{530}$QD concentrations measured, with $\Delta S \approx 0.8\%$ at $T/T_{NI} \approx 0.82$, which fell to $\Delta S = 0.2\%$ at $T/T_{NI} = 0.99$. In all cases though, the reduction in S was more significant than the error. Therefore, in the absence of the alignment effects present in the LCQD nanocomposites, this reduction could be entirely attributed to the disordering effect of the ODAQDs.

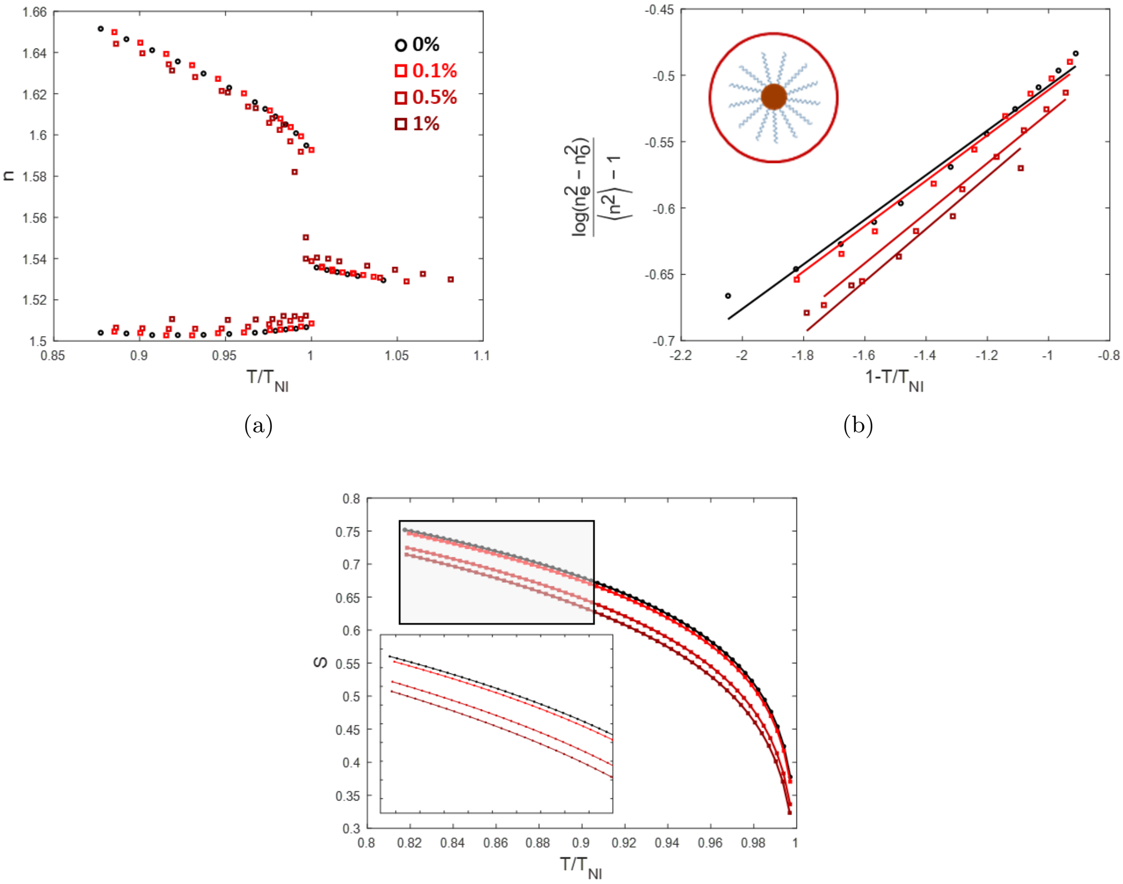

(a) (b)

(c)

Figure 4.12: a) Refractive Indices, b) Haller Plots and c) order parameter of ODA$_{650}$QD nanocomposites at $0wt\%$ (black circles), $0.1wt\%$ (light red squares), $0.5wt\%$ (mid red squares) and $1wt\%$ (dark red squares) QD concentrations in the host LC MLC6204. Error bars have not been included on these plots as they are of the same size or smaller than the data points.

4.4.3 Comparison of QD Nanocomposites

To compare the effect of the different surface functionalisation directly, figures 4.13(a), 4.13(b) and 4.13(c) show the refractive indices, Haller plots and order parameter respectively for the $1wt\%$ LCQD, ODA$_{530}$QD and ODA$_{650}$QD on the same plots. A comparison of the β values from the Haller fitting for all of the nanocomposites is shown in table 4.3. Larger values of β correspond to a lower S.

It can be seen that the ODA$_{530}$QD has the most significant impact on S, creating an approximately 8.5% reduction at a concentration of $1wt\%$. The ODA$_{650}$QD caused an approximately 6.3% reduction in S at $1wt\%$, whilst the LCQD created only a slight reduction of 1.3% at $1wt\%$ which can be attributed to the increased pretilt from the LCQD. The ODA$_{530}$QD therefore clearly creates the most significant disruption to the director of the host LC, followed by the ODA$_{650}$QD. This is in agreement with the T_{NI} measurements, which shows the most significant reduction from the addition of the ODA$_{530}$QD, followed by the ODA$_{650}$QD. Similarly to the reduction in T_{NI}, the difference between the two ODAQDs may be due to the smaller QD having a higher number density and volume fraction in the host LC for the same weight concentration as the larger QD.

Table 4.2: R^2 values from Haller fitting of refractive indices for the different QD-LC nanocomposites with $\frac{\Delta\alpha}{\bar{\alpha}} = 0.46 \pm 0.01$ found from the fitting of pure MLC6204, which also gave $\beta = 0.168 \pm 0.007$, with $R^2 = 0.984$ (for comparison).

	LCQD	ODA$_{530}$QD	ODA$_{650}$QD
$0.1wt\%$	0.987	0.993	0.987
$0.5wt\%$	-	0.924	0.985
$1wt\%$	0.986	0.980	0.988

Table 4.3: β values and corresponding standard error from Haller fitting of refractive indices for the different QD-LC nanocomposites with $\frac{\Delta\alpha}{\bar{\alpha}} = 0.46 \pm 0.01$ found from the fitting of pure MLC6204, which also gave $\beta = 0.168 \pm 0.007$, with $R^2 = 0.984$ (for comparison).

	LCQD	ODA$_{530}$QD	ODA$_{650}$QD
$0.1wt\%$	0.173 ± 0.007	0.180 ± 0.006	0.171 ± 0.007
$0.5wt\%$	-	0.19 ± 0.2	0.189 ± 0.008
$1wt\%$	0.175 ± 0.007	0.21 ± 0.01	0.20 ± 0.02

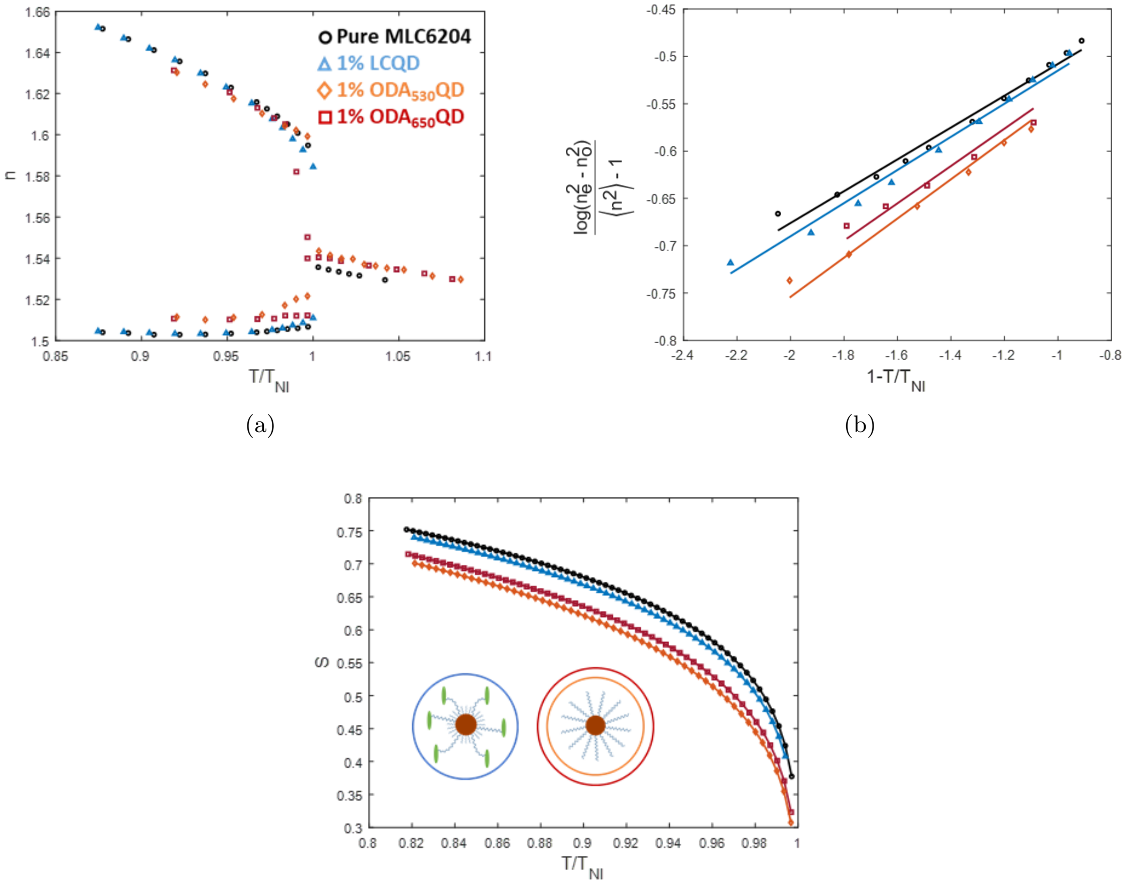

(a)

(b)

(c)

Figure 4.13: a) Refractive indices, b) Haller plots and c) order parameters of the different QD-LC nanocomposites at $1wt\%$ LCQD (blue triangles), ODA$_{530}QD$ (orange diamonds) and ODA$_{650}$QD (red squares). Error bars have not been included on these plots as they are of the same size or smaller than the data points.

4.5 Phase Transition Driven QD Self-Assembly

As already discussed in chapter 1 section 1.3.4, the isotropic-nematic phase transition can be used to self-assemble QD micro structures in QD-LC nanocomposites. A range of structures can be formed depending on the QD concentration and cooling rate used [126]. This type of particle self-assembly relies upon the coexistence of the nematic and isotropic phase as the concentration of particles in the anisotropic fluid is increased beyond a threshold concentration. Depending on the type of surface functionalisation used, different structures can be formed. In the case of a side-on mesogenic surface functionalisation, it has been shown that QD shells, foams and hollow tubular worm-like networks can be formed [73, 126].

To further understand the role of surface functionalisation in phase transition driven self-assembly, the formation of tubular worm-like QD networks within the LC matrix are studied.

The structure and self-assembly mechanism of these structures formed from either mesogen functionalised LCQD or non-mesogen functionalised ODAQDs (of two different sizes) are investigated. To do so, the nanocomposites were studied in PH cells, as were used to perform the POM transition temperature measurements in section 4.3.3. The effect of the surface functionalisation on the order of the LC nanocomposites, investigated in the previous section 4.4, is also related to the QD self-assembly and used to explain the difference in formation mechanisms.

4.5.1 Tubular QD Network Formation

4.5.1.1 Structure Formation Mechanism

In the case of the LCQD nanocomposites, if cooled at an appropriate rate from the isotropic to nematic phase, worm-like tubular networks are self-assembled. In order for this to take place, the nanocomposite is first prepared according to the procedure outlined in chapter 2 section 2.3.2. An initially homogeneous QD dispersion in the isotropic phase of the nanocomposite is formed (enlarged region of figure 4.14(a)). On cooling this homogeneous dispersion, nematic nucleation begins to take place as the nanocomposite is cooled below T_{NI}. Provided there is a high enough QD concentration in the nanocomposite, the system phase separates into a coexistence of both isotropic and nematic phase.

At this point, QD migration from the nematic phase into the remaining regions of isotropic phase takes place, producing a higher QD concentration in the isotropic phase than the nematic phase (enlarged region of figure 4.14(d)). The nematic regions continue to grow, whilst the isotropic regions shrink, until the majority of the nanocomposite is nematic with some isotropic strands remaining (figure 4.14(e)). It is at this point in the cooling process, that a second stage of nematic nucleation takes place within the remaining isotropic strands, forming tube-like isotropic strands with a nematic core (enlarged region of figure 4.14(f)). Following this, the outer diameter of the isotropic tubes remains constant, while the inner core of nematic phase grows outwards, narrowing the walls of the isotropic tubular strand, whilst QD migration continues into the the isotropic regions (enlarged region of figure 4.14(e)). Eventually, the inner nematic core expands until there is no longer any isotropic phase remaining and the entire nanocomposite is in the nematic phase with the tubular QD networks locked in position (figure 4.14(h)). As this is taking place, the isotropic strands are also shrinking along their length, back towards what become the nodes which connect the tubules.

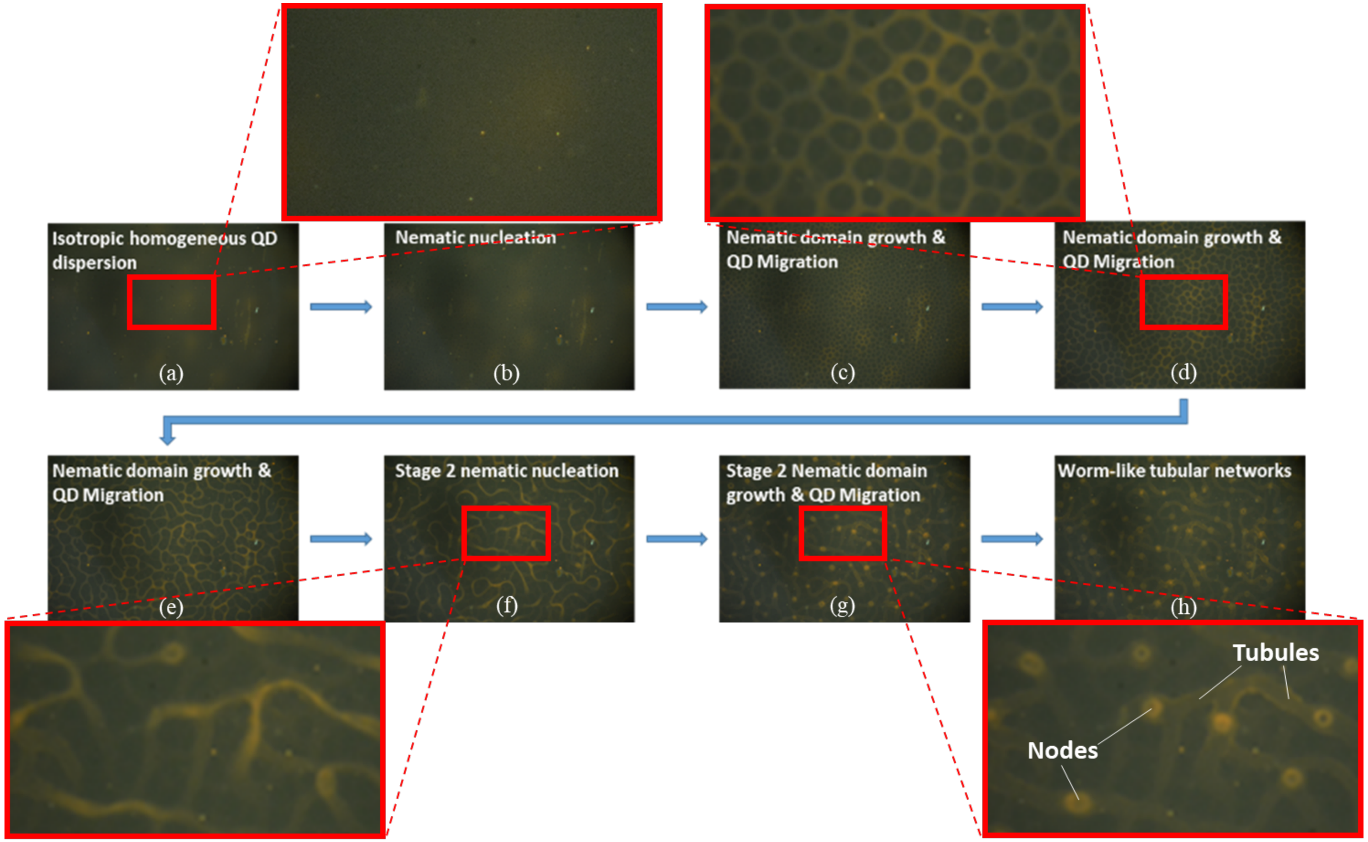

Figure 4.14: FM photographs on cooling a 0.4$wt\%$ LCQD nanocomposite at 10°C/min from a) the initially homogeneously dispersed isotropic nanocomposite to b) the first stage of nematic nucleation, followed by c), d) and e) nematic domain growth and QD migration before f) the second stage of nematic nucleation, g) second stage of nematic domain growth and QD migration to finally h) the fully formed worm-like tubular QD networks formed.

Evidence of the QD migration into the remaining isotropic regions on cooling once nematic nucleation has taken place can be seen in figures 4.15(a) and 4.15(b), which show the POM and FM photographs of the same region of the sample respectively. The dark non birefringent regions in figure 4.15(a) can be confirmed to be isotropic and not homeotropic since a PH cell was used and it is known that the LCQD nanocomposites retain planar alignment in PH cells, evidence of this is also shown and discussed in Chapter 5. Additional evidence that the non-birefringent regions must be isotropic and not homeotropic can be found by performing dielectric spectroscopy measurements to find the temperature dependent permittivity across the nematic-isotropic phase transition. The results of these measurements, which prove this is the case can also be seen in Chapter 5.

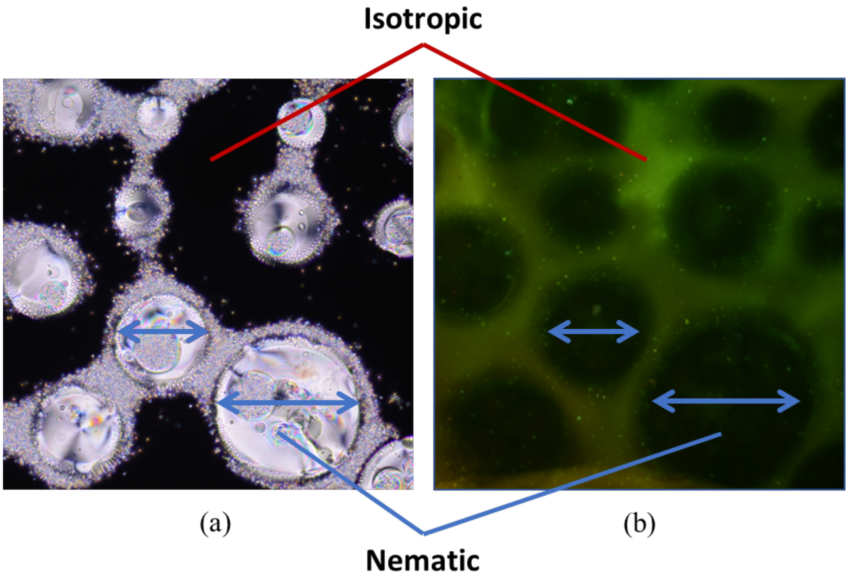

Figure 4.15: a) POM photograph and b) corresponding FM photograph at the first stage of nematic nucleation and growth, showing the QD rich isotropic regions and QD poor nematic regions. The red arrows indicate the consitency in the size of the nematic regions in the POM photographs and the QD rich regions in the FM photographs.

Depending on the QD concentration in the nanocomposite, QD micro-structure formation may not occur. Figure 4.16(a) shows a $0.08wt\%$ LCQD nanocomposite in the nematic phase following cooling from the isotropic phase at a rate of $1°C/min$. At this concentration, no network formation is seen. However, at the same cooling rate, if the QD concentration is increased to $\gtrsim 0.1wt\%$, observable QD network formation takes place, as shown in figure 4.16(b). Thus it appears there is a threshold concentration for this type of LCQD at $\sim 0.1wt\%$ at which network formation is able to take place.

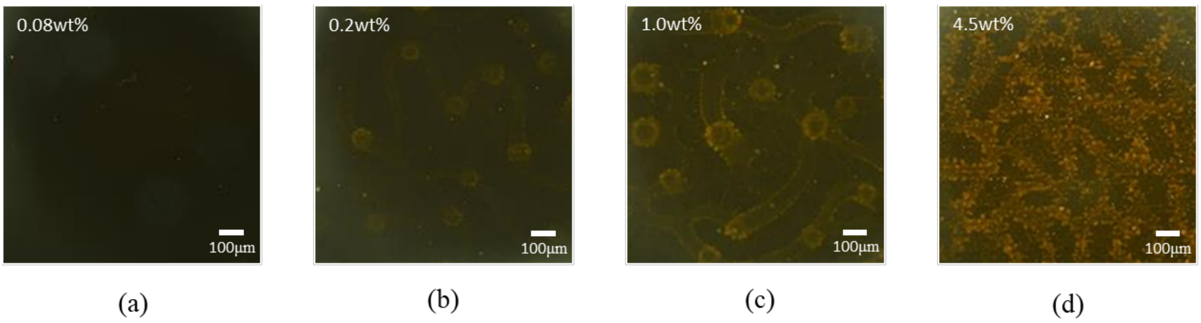

(a) (b) (c) (d)

Figure 4.16: FM photographs showing the concentration dependence of worm-like tubular QD network formation in LCQD nanocomposites cooled at $1°C/min$. a) $0.08wt\%$, b) $0.2wt\%$, c) $1wt\%$, d) $4.5wt\%$.

Interestingly, this is significantly larger (almost five times larger), than the w_c found from the T_{NI} measurements as a function of QD concentration in the LCQD nanocomposites. It is possible that although the phase coexistence does take place when cooling from the isotropic phase at concentrations between $w_c = 0.022wt\%$ and $0.1wt\%$, but the difference in concentration between the isotropic and nematic phase is not significant enough to be visible. This may arise due to the phase coexistence region only existing over such a small temperature range that there is not enough time when constantly cooling for significant QD migration to take place. Thus, in this concentration range, it could be possible to enable QD structure formation by holding the temperature in the phase coexistence region just below T_{NI} for a period of time before continuing to cool to fully nematic. However, it is likely this will have an impact on the structure of the networks formed, or even form a different structure.

4.5.1.2 Structure Scale Control

It is possible to control the scale of the QD networks by altering the cooling rate. Figure 4.17(a)-(c) shows the difference in the size of the tubular QD networks when cooled at $1°C/min$ and $10°C/min$. The faster the nanocomposite is cooled from the isotropic phase, the smaller the diameter of the tubular networks. The outer diameter of the micro-tubules depends on the cooling rate up to the point at which the second stage of nematic nucleation takes place. Cooling at a faster rate from the isotropic phase into and through the phase coexistence region, results in isotropic strands of a smaller diameter by the time stage two nematic nucleation takes place. Once stage two nematic nucleation has begun, the outer diameter is fixed and the inner diameter of nematic phase expands, narrowing the walls of the micro-tubules.

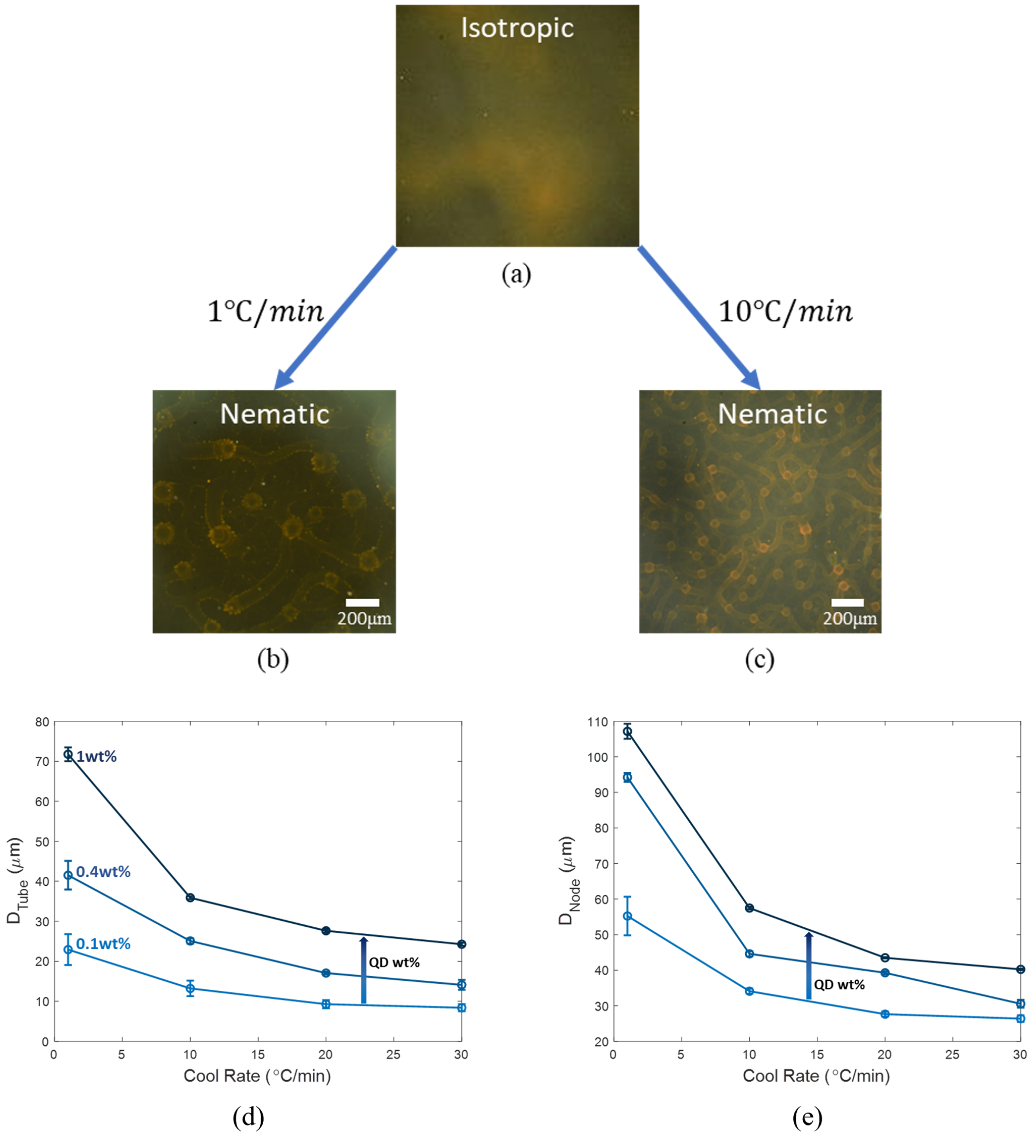

Figure 4.17: FM photographs showing the cooling rate dependence on the length scale of the worm-like tubular QD networks from a) the initially homogeneous isotropic LCQD nanocomposite to b) fully nematic cooled at $1°C/min$ or c) fully nematic cooled at $10°C/min$. Average outer diameter of self-assembled LCQD d) tubules and e) nodes against cooling rate for QD concentrations of $1wt\%$ (dark blue), $0.4wt\%$ (mid blue) and $0.1wt\%$ (light blue). solid lines are a guide for the eye.

Figures 4.17(d) and 4.17(e) show the average outer diameters of the tubules and nodes respectively. The average outer diameter of the tubules and nodes were calculated from many measurements measurements taken from multiple different tubules and nodes throughout the samples with their corresponding standard error. Although there is a significant amount of variation in the sizes for a given concentration and cooling rate, it can clearly be seen that the outer diameter of both the tubules and nodes decreases with both increasing cooling rate and deceasing QD concentration in the nanocomposite. The nodes are also of a significantly larger size than the tubules. It is thought that the nodes are larger than the tubules due to the shrinking of several isotropic strands back towards the point at which the node is formed, hence the outer diameter of the nodes becomes enlarged compared to the tubules. The reason for the concentration dependence, however, is not entirely clear.

The cooling rate dependence found here does not entirely agree with previous work using QD-LC nanocomposites with a similar side-on mesogenic surface functionalisation in 5CB, where using cooling rates between 7 and $30°C/min$ formed a 'foam' rather than a 'network' as has been found here for approximately the QD same concentrations [126]. It should be noted though, that the structure formation shown here has been performed in $20\mu m$ cells and thus the nanocomposite has been confined to a film. This could be a possibility as to why at the same cooling rates and QD concentrations, 'networks' have been formed here rather than 'foams'. Additionally, the different host LC may have also played a role, since the LC mixture used here, MLC6204, even as a pure LC without QD doping, has somewhat of a phase coexistence region where isotropic and nematic phase can coexists.

4.5.2 Surface Functionalisation Effect on Network Formation

So far, only the micro-structures formed by cooling LCQD nanocomposites from the isotropic to the nematic phase at different cooling rates and QD concentrations have been discussed. The ODAQD nanocomposites can also form worm-like networks when cooled at the appropriate rate from the isotropic to nematic phase. However, the surface functionalisation affects this formation process, and rather than hollow tubules being formed, solid networks are formed. Figure 4.18(a), 4.18(b) and 4.18(c) show the difference between the networks formed in LCQD, $ODA_{530}QD$ and $ODA_{650}QD$ nanocomposites.

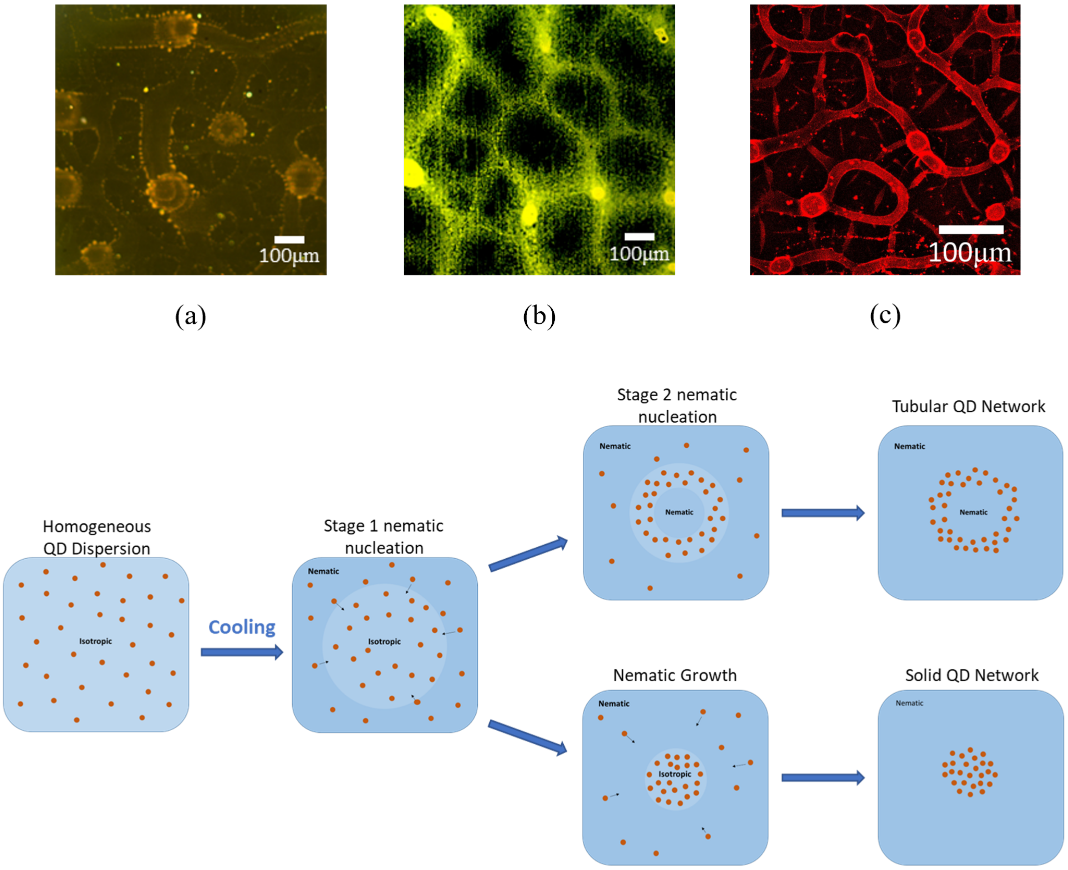

(a) (b) (c)

(d)

Figure 4.18: QD networks formed by cooling $1wt\%$ a) LCQD, b) ODA$_{530}$QD and c) ODA$_{650}$QD nanocomposites at $1°C/min$ with the corresponding schematic of the different structure formation mechanisms.

The ODAQD, unlike the LCQD nanocomposites show a continually decreasing T_{NI} with increasing QD concentration due to the distrotion created by the QD surface functionalisation, as discussed earlier in this chapter in sections 4.3 and 4.4. This difference in phase behaviour of the ODAQD nanocomposites prevents the second stage of nematic nucleation from taking place, which is responsible for the hollow tubular QD network formation as shown schematically in figure 4.18(d).

AS QD migration to the remaining isotropic strands following the first stage of nematic nucleation in the ODAQD nanocomposites, the increased concentration of QD in the isotropic phase further reduces the T_{NI} of the nanocomposite in this region. Hence, as the overall temperature of the nanocomposite continues to cool, and the isotropic strands shrink, the temperature within them never drops below T_{NI} as a result of the increased QD concentration, thus preventing the second stage of nematic nucleation. This results in the solid worm-like QD networks seen in figures 4.18(b) and 4.18(c). It could still be possible to form hollow QD structures in nanocomposites of the ODAQDs at sufficiently low cooling rates and QD concentrations. This may enable the second stage of nematic nucleation to take place still if the increase in concentration of QD in the isotropic regions is not significant enough to prevent the temperature in these regions from dropping below T_{NI}.

4.6 Summary

In this chapter, the phase behaviour, order and QD self-assembly in QD-LC nanocomposites using QDs with different types of surface functionalisation were investigated. QD-LC nanocomposites with a side-on mesogenic surface functionalisation or an ODA alkyl chain surface functionalisation were compared across a range of QD concentrations in the host LC mixture MLC6204. It was hypothesised that the flexible alkly linker used to connect the mesogenic moiety to the QD surface of the LCQD would enable the mesogen to orient with the director of the LC host in the nanocomposites. The alkyl chain of the ODAQDs, however, which are known to induce HT anchoring were hypothesised to distort the director of the LC host in the nanocomposites.

The investigation into the phase behaviour of the QD-LC nanocomposites discussed in section 4.3 of this chapter revealed significant differences between the different QDs. A decreasing T_{NI} with increasing QD concentration was found across the full concentration range measured (up to $1wt\%$) in the nanocomposites made with both sizes of the ODAQDs, the LCQD nanocomposites, however, did not. Instead, the LCQD nanocomposites showed an initial steep reduction of T_{NI} with increasing QD concentration when measured using POM, as did the ODAQD nanocomposites, but above a threshold concentration, showed no further decrease of T_{NI} as the QD concentration was increased. The T_{NI} of the ODAQD nanocomposites above the threshold QD concentration continued to decrease as the QD concentration was further increased, but at a slower rate. This difference in the phase behaviour between the nanocomposites implies that the LCQD does not cause any disturbance to the director of the host LC, whereas the ODAQDs do.

Further investigation into the effects of the different surface functionalisation types were then carried out to quantify the extent to which the LCQD and ODAQDs distort the director by measuring the order parameters of the nanocomposites. To do so, the refractive indices of the nanocomposites were measured directly using an Abbe refractometer. Using the Haller method, the refractive index data was fit to find the β exponents which were then used to calculate S from equation 1.4 for each of the nanocomposites.S decreased with increasing QD concentration in both of the ODAQD nanocomposites, but more so for the smaller ODA$_{530}$QD than the larger ODA$_{650}$QD. These results agreed well with the trends found for the phase behaviour of these nanocomposites, which showed the most significant reduction of T_{NI} in the ODA$_{530}$QD nanocomposites. The LCQD nanocomposites, however, showed a slight but unexpected reduction in S. Nonetheless, the LCQD nanocomposites showed the highest S out of all of the nanocomposites as expected, when considering the LCQD had the least impact on the nematic-isotropic phase transition.

In the final part of this chapter, the phase transition driven QD self-assembly in the nanocomposites was studied. It has previously been shown that a variety of different QD micro-structures can be formed on cooling through the isotropic-nematic phase transition using side-on mesogen functionalised QDs. Here, further understanding the self-assembly mechanism and characteristics of QD network formation was the primary focus. The influence of cooling rate and QD concentration on QD network formation were investigated. Higher QD concentrations and slower cooling rates led to the formation of larger diameter QD networks, whilst lower QD concentrations and faster cooling rates led to the formation of smaller diameter QD networks.

Tubular QD network formation was found in the LCQD nanocomposites at faster cooling rates than previously shown. It has been hypothesised that this was possibly due to the use of a LC mixture as the host, which shows somewhat of a phase coexistence region even in the pure LC as opposed to using a pure compound such as 5CB which shows minimal isotropic and nematic phase coexistence. Additionally, the nanocomposites were confined within $20\mu m$ cells, which may have also led to the formation of networks at faster cooling rates than expected.

The surface functionalisation effects on the nanocomposite ordering and phase behaviour were then related to the QD micro-structure formation. It was shown that using the disordering ODAQDs at high ($1wt\%$) concentrations significantly altered the network formation process, leading to the self-assembly of solid QD networks rather than the hollow tubular QD networks seen at the same cooling rates and concentrations in the LCQD nanocomposites. In both cases, the phase transition driven self-assembly relies on the phase coexistence of QD rich isotropic and QD poor nematic regions in the QD-LC nanocomposites which occurs above a threshold QD concentration on cooling from the initially homogeneous isotropic phase. However, the disordering affect of the ODAQDs means that during the phase coexistence, the QD migration into the isotropic regions results in a reduction of the local T_{NI} in these regions, which continues to decrease as the QD concentration increases. As a result, the second stage of nematic nucleation within the isotropic regions responsible for the formation of hollow structures is prevented. Thus, it is proposed that in addition to using different QD concentrations and cooling rates to control the outer diameter of the structures, by using a combination of disordering and order preserving QD surface functionalisation, the inner diameter of hollow structures could also be controlled.

Chapter 5

QD-LC Nanocomposite Alignment, Dielectric and Elastic Properties

5.1 Introduction

It has already been shown in Chapter 4, that using a side-on mesogenic QD surface functionalisation leads to the preservation of order within the QD-LC nanocomposite when compared to the pure LC host and therefore, does not significantly alter the nematic-isotropic phase transition. Conversely, it was shown that alkyl chain functionalisation such as that of the ODAQDs, has a significant impact on the order within the QD-LC nanocomposites and thus also the nematic-isotropic phase transition as well. These order preserving and disordering QDs when used in QD-LC nanocomposites, therefore not only showed considerably different phase behaviour, but also showed interesting effects on the phase transition driven QD self-assembly. LC doping with nanomaterials has previously been shown to produce a variety of alignment effects and alter the electro-optic, dielectric and elastic proprieties as discussed in section 1.3.3 of chapter 1. This chapter therefore investigates the effects of QD surface functionalisation on both the alignment and director profile of the QD-LC nanocomposites in LC devices, as well as the dielectric and elastic properties.

POM textures of the different QD-LC nanocomposites and the director profiles in the nanocomposites responsible for the textures found across a range of QD concentrations are presented. Pretilt measurements of the nanocomposites in aligned cells were performed to provide quantitative evidence of the alignment within the cells. Dielectric spectroscopy measurements of the nanocomposites were performed, including the permittivity-voltage curves, which were then analysed according to the process outlined in chapter 3 section 3.4. The elastic constant, permittivity and pretilt results are presented for the different QD-LC nanocomposites and the implications of the different types of surface functionalisation discussed.

5.2 Textures and Alignment

POM was used to study the alignment of the different QD-LC nanocomposites between untreated glass substrates and also in aligned cells. The QD-LC nanocomposites were capillary filled between the glass substrates or into the aligned cells in the isotropic phase following heated sonication to ensure good QD dispersion following the procedure outlined in chapter 2 section 2.3.2. The samples were then cooled from the isotropic phase into the nematic phase at a controlled rate (typically $1°C/min$ unless stated otherwise). The relevant textures formed in the nematic phase of the nanocomnposites are presented in this section with the corresponding director profiles.

5.2.1 Untreated Glass

Between untreated glass slides, the pure LC host MLC6204 produced good HT alignment, which was confirmed by rotating the sample between crossed polarisers in the nematic phase as shown in figure 5.1(a) and 5.1(b). The LCQD nanocomposites at low concentrations, also produced HT alignment, which is shown in figure 5.1(c) for the $0.05wt\%$ nanocomposite. As the LCQD concentration was increased, however, regions of planar alignment appeared, but with the majority of the sample remaining HT as can be seen in with the $0.4wt\%$ sample shown in figure 5.1(d).

On doping with the ODA$_{530}$QD, depending on the concentration, areas of both HT and planar alignment were seen. At lower concentrations, HT alignment was induced, but unlike the pure LC host, some birefringent spots were also seen, as shown in the $0.06wt\%$ sample in figure 5.1(e). As the concentration of the ODA$_{530}$QD was increased, HT alignment was lost and planar alignment was instead seen at a concentration of $0.05wt\%$, shown in figure 5.1(f). Further increasing the concentration to $0.1wt\%$ and $1wt\%$ again produced HT alignment as shown in figures 5.1(g) and 5.1(h), however, more birefringent spots of a larger size were formed around the QD clusters.

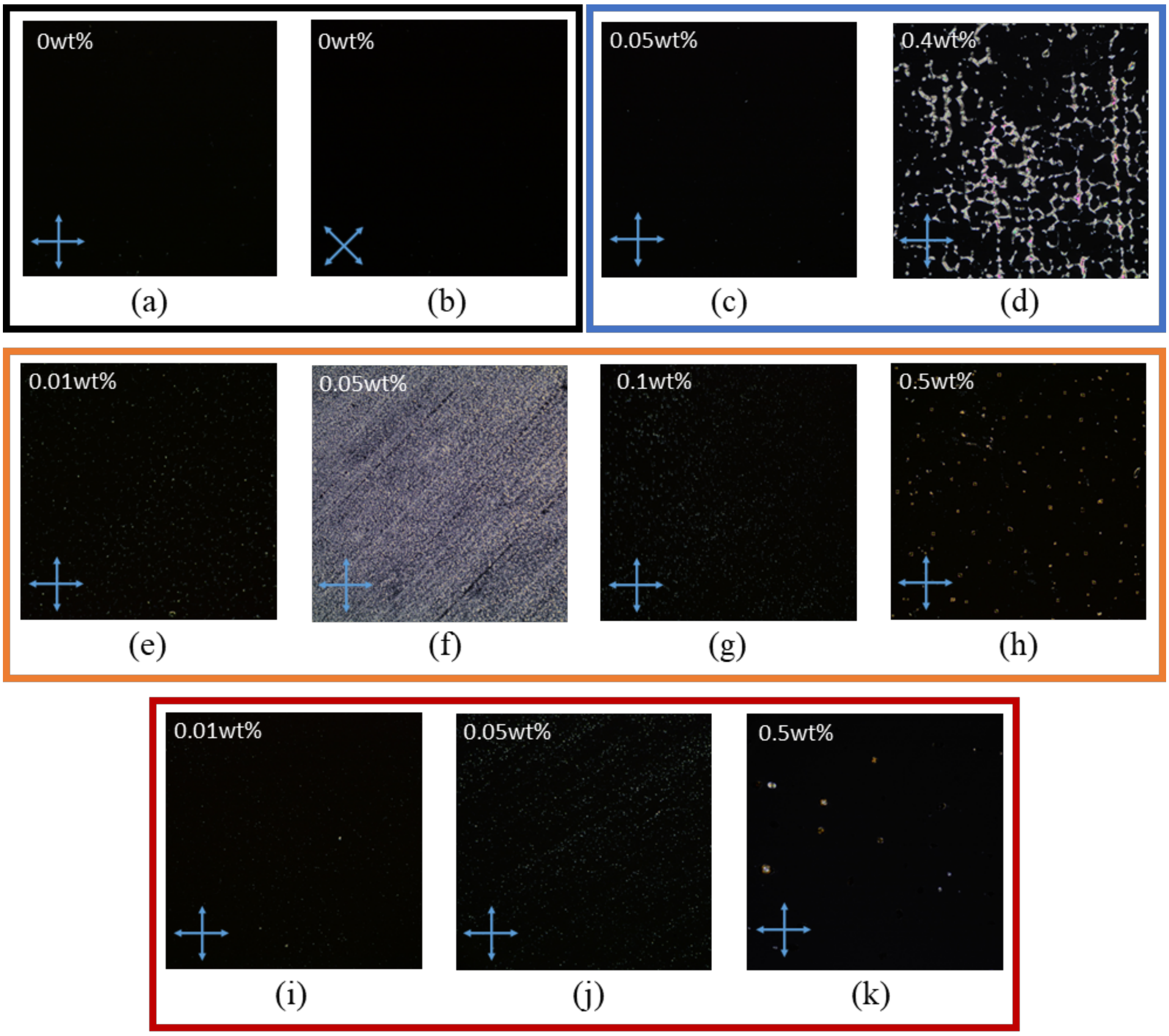

Figure 5.1: POM textures between crossed polariser and analyser of pure LC MLC6204 and QD-LC nanocomposites between untreated glass slides. a) Pure LC and b) when rotated 45° relative to polarisers showing HT alignment. LCQD nanocomposites at concentrations of c) $0.05wt\%$ showing good HT alignment and b) $0.4wt\%$ showing a mixture of HT alignment and birefringent strings of planar alignment. ODA$_{530}$QD nanocomposites at concentrations of e) $0.01wt\%$ showing HT alignment with some birefringent spots, f) $0.05wt\%$ showing random planar alignment, g) $0.1wt\%$ showing HT alignment with some birefringent spots and h) $0.5wt\%$ showing HT alignment with larger birefringent spots around QD clusters. ODA$_{650}$QD nanocomposites at i) $0.01wt\%$ showing HT alignment, j) $0.05wt\%$ showing mainly HT alignment but with some birefringent spots and k) $0.5wt\%$ showing HT alignment with birefringent spots around QD clusters.

The ODA$_{650}$QD showed similar behaviour as the ODA$_{530}$QD. At low and high concentrations, good HT alignment was produced, but with some birefringent spots, as shown in the 0.01$wt\%$ and 0.5$wt\%$ samples in figures 5.1(i) and 5.1(k) respectively. At intermediate concentrations of 0.05$wt\%$, predominantly HT alignment was still seen, but with a much higher density of birefringent spots displaying planar alignment.

It is thought that at low ODAQD concentrations, the alignment is controlled by the weak HT anchoring of the untreated glass substrates, but as the QD concentration is increased, QD clustering and aggregation begins to disturb the HT alignment, forming planar aligned regions which appear as the birefringent spots. At high enough QD concentrations though, a sufficient quantity of QD migrate to the substrate surface, forming a layer of QD which create HT alignment. The LCQD, however, at these concentrations promotes planar anchoring when at the interface with the substrate.

5.2.2 Cells with Alignment Layers

POM textures of the different QD-LC nanocomposites were studied in 20μm PH cells at a range of different concentrations. The textures formed by the LCQD nanocomposites for concentrations of 0.08$wt\%$ - 4.5$wt\%$ can be seen in figure 5.2. Across the full concentration range, good PH alignment was retained; this was confirmed by rotating the samples through 45° between cross polarisers to show clear bright and dark states. This remained the case, even at the highest concentration of 4.5$wt\%$, where the QD micro-structure formation changed considerably from the hollow tubular networks seen at lower concentrations. One feature to note, however, is the increasing density of birefringent 'strings' that formed with increasing QD concentration. This has been reported previously in other NP-LC nanocomposites, but using other non mesogenic surface functionalisation [65, 66, 102].

Contrarily, both of the ODAQDs caused significant alignment changes when filled into 20μm PH cells. The smaller ODA$_{530}$QD at higher concentrations of 0.5 and 1$wt\%$ created complete HT alignment, as can be seen in figures 5.3(h)-(m). The highest concentration of 1$wt\%$ showed a very high density of birefringent 'strings', likely due to the network formation seen at this concentration. Interestingly, at the intermediate concentrations of 0.5$wt\%$ and 0.1$wt\%$, no QD micro-structure formation was seen, whereas at the lower concentration of 0.06$wt\%$ QD cluster formation was seen. At the lower ODA$_{530}$QD concentrations of 0.06$wt\%$ and 0.1$wt\%$, PH alignment was retained, but with a significant number of birefringent 'strings' present.

The larger ODA$_{650}$QD nanocomposites in $20\mu m$ PH cells showed a number of interesting features across the range of QD concentrations used. Even at the lowest concentration of $0.05wt\%$ shown in figure 5.4(a) and (b), significant alignment effects were created. Many birefringent 'strings' can be seen in the dark states of figures 5.4(a),(c),(e) and (g) as well as changing birefringence colours throughout the samples in the bright states 5.4(b),(d),(f) and (h). The changing birefringence colours in the bright state become more evident at higher QD concentrations. At the lower two concentrations of $0.05wt\%$ and $0.1wt\%$, QD cluster formation took place and at higher concentrations of $0.5wt\%$ and $1.0wt\%$ network formation was seen. At these higher concentrations, where QD network formation took place, regions of HT formed at the location of the QD networks. Evidence for HT alignment rather than isotropic in these regions is provided later in this chapter (section 5.3.3).

An interesting temperature dependent alignment effect was also seen with the larger ODA$_{650}$QD nanocomposites in PH cells, where on reheating through the nematic phase, HT domains centered at the site of QD clusters/networks begin to grow. Figure 5.5(a) shows this process taking place in the $0.1wt\%$ ODA$_{650}$ nanocomposite on heating through the nematic phase. The nanocomposite was first cooled at $1°C/min$ from the isotropic phase into the nematic phase to form the solid QD clusters. Surrounding the QD clusters at $20°C$, changing birefringence colours can be seen moving radially away from the QD clusters. On subsequent heating, these birefringence colours begin to change as one would expect from the reduced birefringence resulting from the temperature induced reduction in S. As heating continues, HT regions situated at the location of these QD clusters appear, still with the changing birefringence colours radiating away from the QD cluster as shown in figure 5.5(c). With continued heating, the HT regions continue to grow until a complete HT alignment transition is seen several $°C$ below the T_{NI} of the nanocomposite.

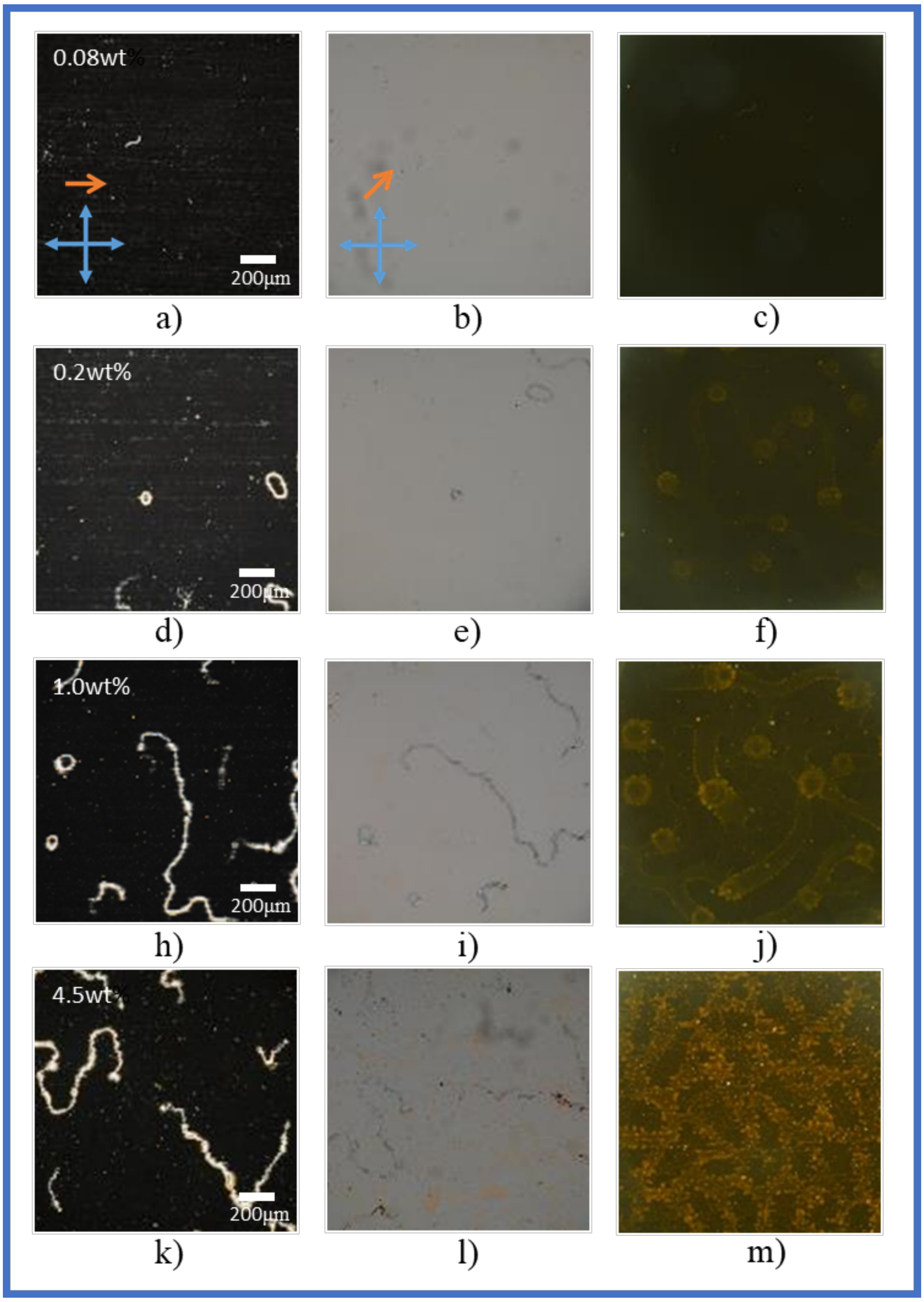

Figure 5.2: POM textures of LCQD nanocomposites in $20\mu m$ PH cells at concentrations of a)-c) $0.08wt\%$, d)-f) $0.2wt\%$, h)-j) $1.0wt\%$, k)-m) $4.5wt\%$ in the nematic phase following cooling from the isotropic phase at $1°C/min$. a), d), h) and k) show samples oriented with rubbing direction aligned with polariser/analyser. b), e), i) and l) show samples oriented with rubbing direction 45° to the polariser/analyser. c), f), j) and m) show the corresponding FM images of the QD micro-structures.

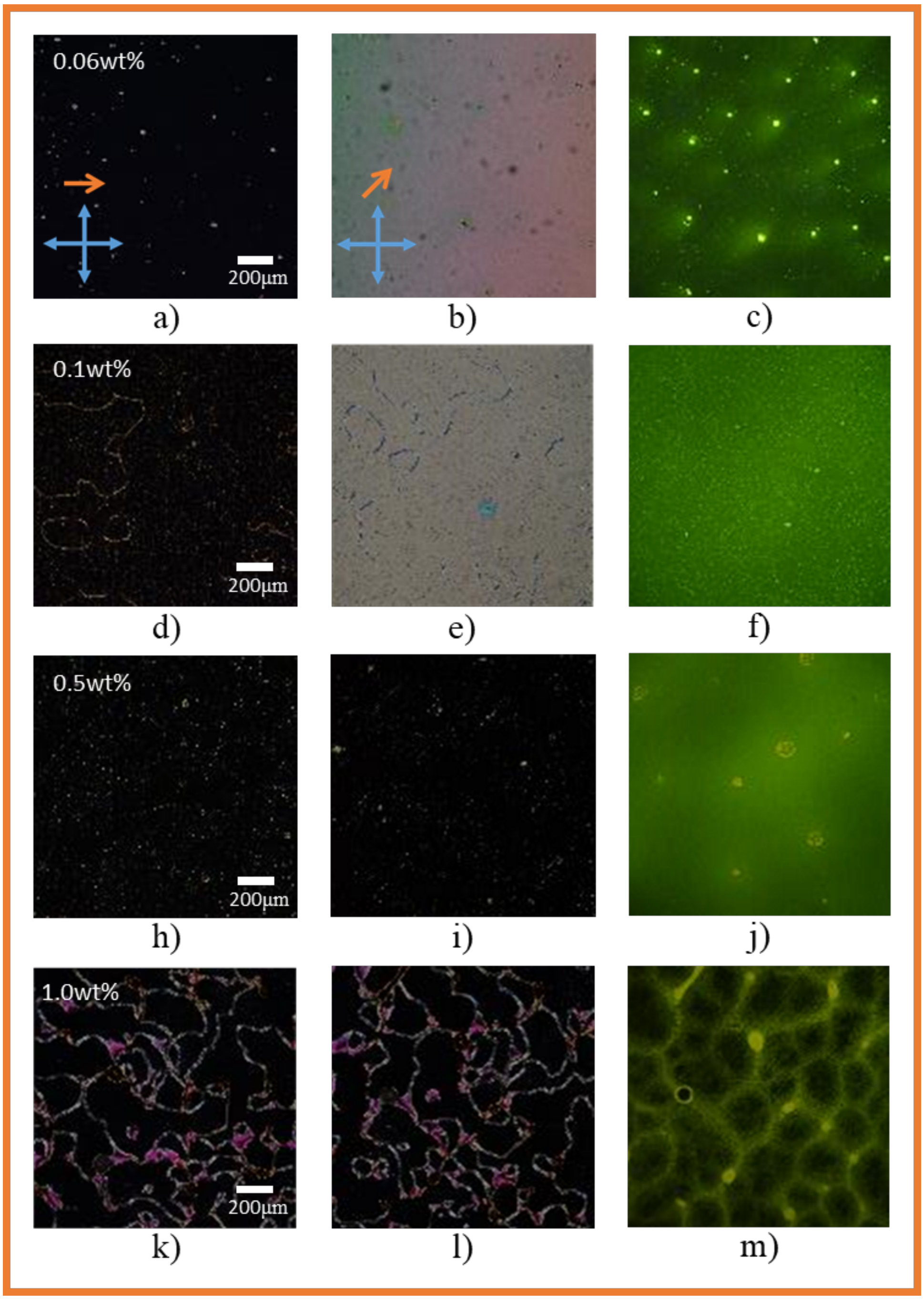

Figure 5.3: POM textures of ODA$_{530}$QD nanocomposites in 20μm PH cells at concentrations of a)-c) 0.06$wt\%$, d)-f) 0.1$wt\%$, h)-j) 0.5$wt\%$, k)-m) 1.0$wt\%$ in the nematic phase following cooling from the isotropic phase at 1°. a), d), h) and k) show samples oriented with rubbing direction aligned with polariser/analyser. b), e), i) and l) show samples oriented with rubbing direction 45° to the polariser/analyser. c), f), j) and m) show the corresponding FM images.

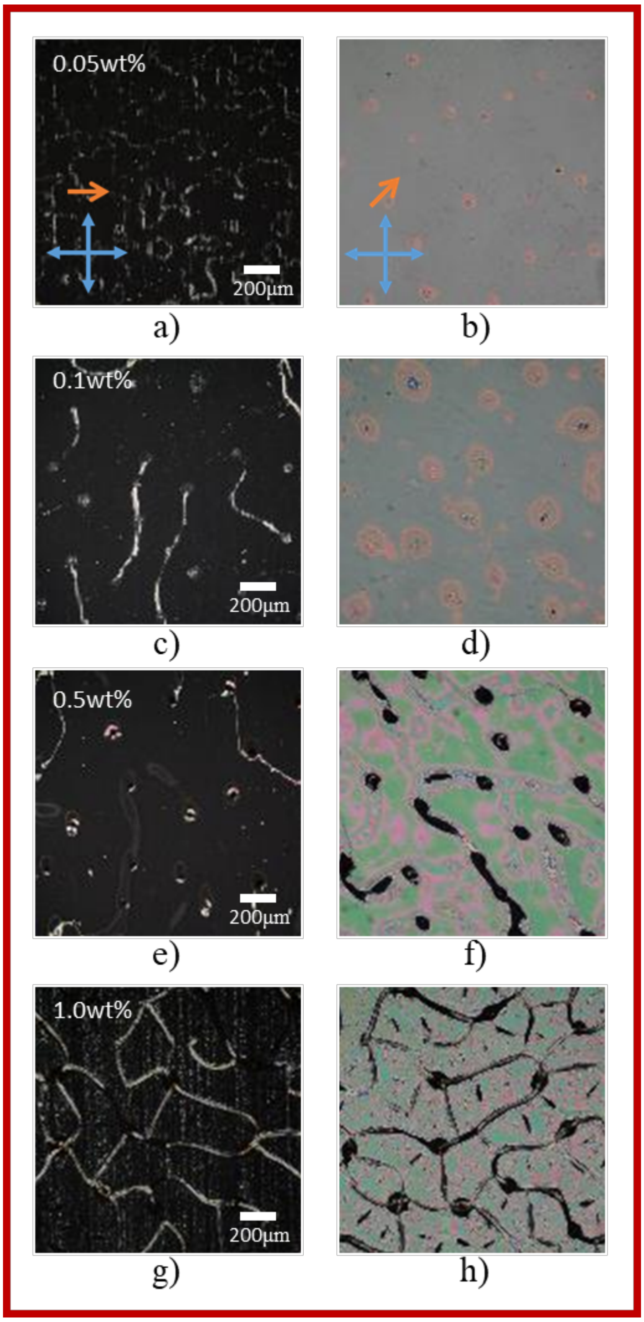

Figure 5.4: POM textures of ODA$_{650}$QD nanocomposites in 20μm PH cells at concentrations of a)-c) 0.05$wt\%$, d)-f) 0.1$wt\%$, h)-j) 0.5$wt\%$, k)-m) 1.0$wt\%$ in the nematic phase following cooling from the isotropic phase at 1°. a), d), h) and k) show samples oriented with rubbing direction aligned with polariser/analyser. b), e), i) and l) show samples oriented with rubbing direction 45° to the polariser/analyser.

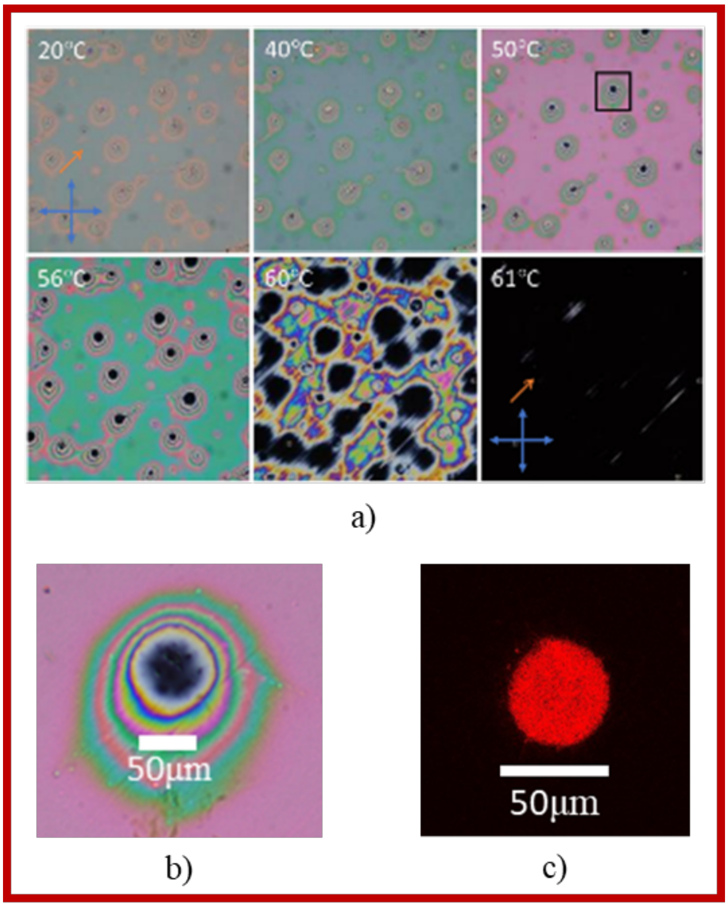

Figure 5.5: $ODA_{650}QD$ nanocomposites a) showing HT alignment transition on heating through the nematic phase ($T_{NI} = 65.4°C$) on cooling from the isotropic phase at $1°C/min$) with b) showing the HT region forming surrounded by changing birefringence colours resulting from the director profile changing from HT to PH when moving radially away from the centre of the c) QD cluster shown imaged using FM.

5.2.3 Director Profiles

The proposed director profiles that correspond to the POM textures produced by the LCQD nanocomposites in aligned cells are shown in figure 5.6. The director profile produced in PH cells, which gave good PH alignment (figure 5.6(a) and (b)) can be seen in the schematic of figure 5.6, where a hollow QD structure is shown in the middle of the cell. It is thought that there is a combination of these structures both in the middle of the cell and at the surface, which results in an increase of the pretilt but does not affect the orientation of the director in the plane of the substrate, i.e. the director remains aligned with the rubbing direction. It is also possible that the networks form with some of the hollow micro-structures in contact with both substrate surfaces when the lateral size of the structures, as measured in chapter 4 section 4.5.1 are considered, since these can be larger than the gap between the substrates.

At the same QD concentration of $1wt\%$, however, the LCQD nanocomposites do not show good HT alignment when filled into $20\mu m$ HT cells and cooled into the nematic phase at $1°C/min$ (figure 5.6(d)), hollow tubular QD networks (figure 5.6(d)). Again, similarly to the PH cell case, it is thought that the hollow QD micro-structures form both in the bulk as well as at the surfaces. The proposed director profile in and around a hollow QD micro-structure which has formed at the substrate surface is shown in figure 5.6. Surrounding the hollow QD micro-structure, the LC takes on HT alignment due to the anchoring of the ALs, but within the micro-structure and in the region below it, the QD takes on a planar orientation. This can clearly be seen when comparing figures 5.6(d) and (e) which shows the planar regions in the areas with bright, highly luminescent QD networks and HT regions in the areas with lower fluorescence luminescence indicating there are not QD networks in these regions. This mixture of HT and PH alignment results in a set of defects surrounding the hollow QD micro-structure, a pair of $-\frac{1}{2}$ defects and a $+\frac{1}{2}$ defect shown by the red and blue circles in figure 5.6(f). In the case that the QD micro-structure formed such that it was in contact with both substrates which could also be the case here, the pair of $-\frac{1}{2}$ defects either side of the hollow QD micro-structure would remain, and the $+\frac{1}{2}$defect would be lost.

The ODAQD nanocomposites at higher concentrations in PH cells showed either fully HT alignment with some birefringent 'strings' in the case of the ODA_{530}QD (figures 5.7(a) and (b)) or planar with regions of HT (figures 5.7(d) and (e)) in the case of the ODA_{650}QD. When full HT alignment was created in the PH cells, a high enough quantity of the ODA_{530}QD

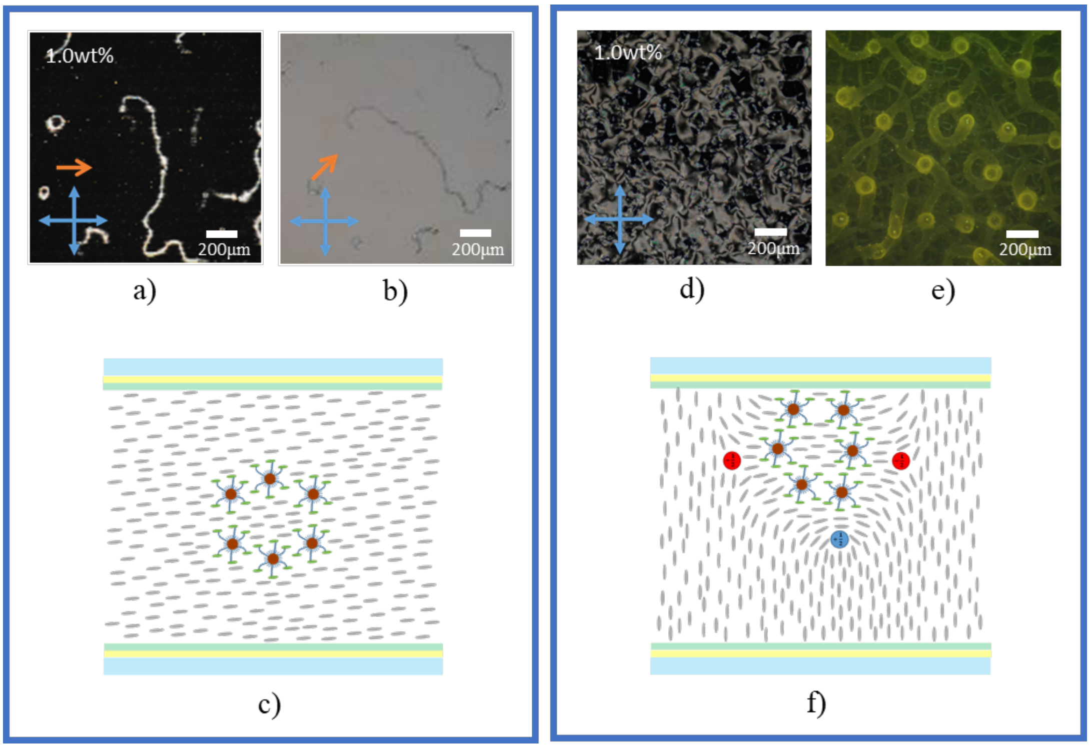

Figure 5.6: POM textures of high concentration $1wt\%$ LCQD nanocomposite in a $20\mu m$ PH cell with a) rubbing direction oriented a) parallel and b) 45° to polariser/analyse as well as in d) a $20\mu m$ HT cell with e) FM photograph of QD network. The proposed director profiles which correspond to the POM textures are shown schematically in c) for the PH cells and f) for the HT cells.

migrated to the substrate surfaces to form a layer of QD which covered the ALs and thus produced complete HT alignment. This was only seen high enough QD concentrations, as at lower concentrations, not enough QD are able to cover the AL sufficiently to prevent the PH anchoring being more energetically favourable. To form the mixture of HT and planar anchoring seen with the $ODA_{650}QD$ nanocomposites in the PH cells, the solid QD micro-structures form a region of HT alignment as shown in figure 5.7(f) for the case of a QD micro-structure formed in the middle of the cell. Similarly to the formation of the hollow micro-structures in the LCQD case, the solid micro-structures of $ODA_{650}QD$ could also form at a surface or extending between the two surfaces. In the latter case, due to the solid micro-structure, the non-birefringent region would be exhibited due to a lack of LC rather than HT alignment of the LC.

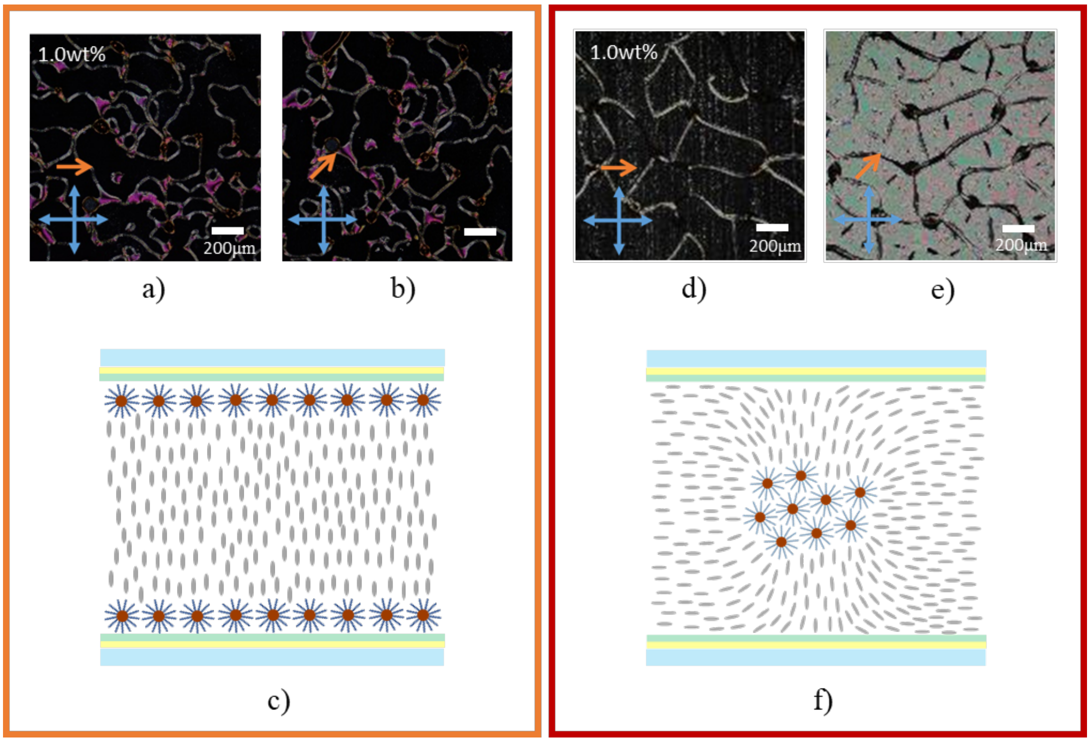

Figure 5.7: POM textures of high concentration $1wt\%$ ODA$_{530}$QD nanocomposite in $20\mu m$ PH cell with rubbing direction oriented a) parallel and b) 45° to the polariser/analyser with c) the proposed director profile. As well as $1wt\%$ ODA$_{650}$QD nanocomposite in $20\mu m$ PH cell with rubbing direction oriented d) parallel and e) 45° to the polariser/analyser with f) the proposed director profile.

5.2.4 Pretilt Measurements

To definitively determine the effects of the different surface functionalisation on the QD-LC nanocomposite alignment in the PH cells, pretilt measurements were performed on the pure LC MLC6204, as well as $0.5wt\%$ LCQD and $0.5wt\%$ ODA$_{530}$QD nanocomposites as described in section 2.4.8. To do so, an adapted crystal rotation method was used [148], whereby a $\sim 50\mu m$ PH cell filled with either the pure LC or QD-LC nanocomposites, was rotated between crossed polarisers and the resulting transmission intensity against cell angle measured. Note, the use of nominally $50\mu m$ thick cells for pretilt measurements as $20\mu m$ thick cells typically did not give a strong enough signal for accurate measurements.

Examples of the intensity against cell angle measurements for the different nanocomposites are shown in figure 5.8, where the different pretilt in each of the samples results in the shifting of the symmetry angle. Several measurements of each sample were taken from angles ±40° either side of the cell normal and curves of the transmitted intensity calculated to model the transmission data using equation 2.30. Average pretilt values of $\theta_p \sim 2°$ for the pure LC, $\theta_p \sim 10°$ for the LCQD nanocomposite and $\theta_p \sim 89°$ for the ODA$_{530}$QD nanocomposite were found. These values confirm that the LCQD does create an increase in the pretilt when compared to the pure LC, and the ODA$_{530}$QD at high concentrations creates complete HT alignment by segregation of a high enough quantity of QD to the substrate surfaces.

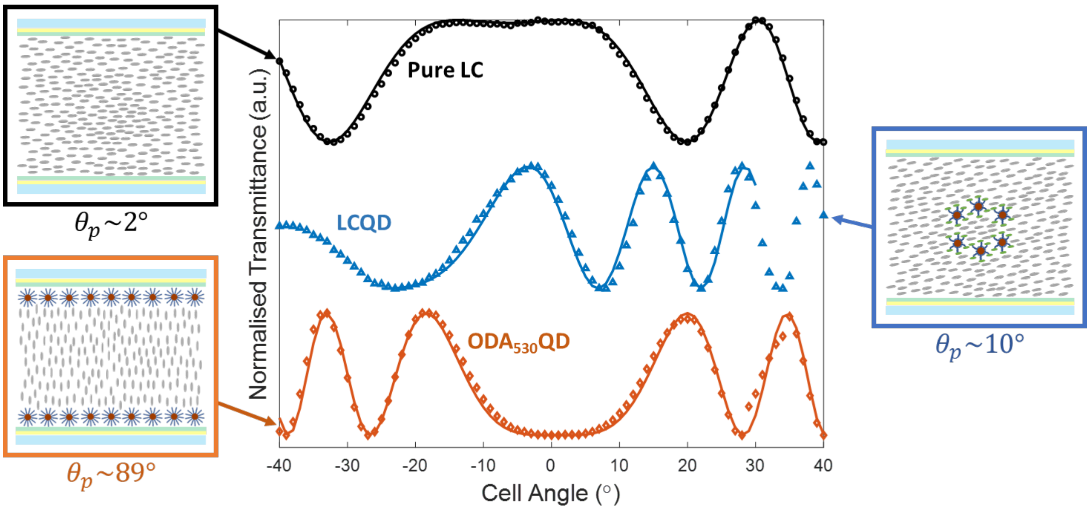

Figure 5.8: Pretilt measurement examples of pure MLC6204 (black circles), 0.5wt%LCQD nanocomposite (blue triangles) and 0.5wt%ODA$_{530}$QD nanocomposite (orange diamonds) in 50μm PH cells, with the corresponding calculated pretilt curves plotted as the solid lines of the same colour for each of the samples.

5.3 Dielectric Spectroscopy

Dielectric spectroscopy measurements of the QD-LC nanocomposites were performed to determine how the different surface functionalisation affects the dielectric and elastic properties of the nanocomposites. The frequency response of the real and imaginary permittivities both parallel and perpendicular to the director were measured. To do so, the permittivities were calculated from the empty cell capacitance as described in chapter 2 section 2.4.6. The frequency response of the QD-LC nanocomposites were then used to determine the appropriate frequency at which to perform $\epsilon(V)$ measurements according to the procedures discussed in chapter 3 section 3.4. The $\epsilon(V)$ curves were then measured using an appropriate stabilisation time (see chapter 3 section 3.4.2) and then corrected for the effect of the ALs (see chapter 3 section 3.4.3). Following this, the corrected $\epsilon(V)$ were then analysed using a combination of linear and WS fitting (see chapter 3 section 3.4.4) to find values for $\epsilon_\perp$, $\epsilon_\|$, K_{11}, K_{33} and θ_p. The results of which are compared later in this section and discussed with regards to the effect of the different surface functionalisation used.

5.3.1 Frequency Response

The frequency response of $\epsilon'_{\perp}$ and $\epsilon''_{\perp}$ are shown in figures 5.9(a) and 5.9(c) respectively. The frequency response of $\epsilon'_{||}$ and $\epsilon''_{||}$ are shown in figures 5.9(b) and 5.9(d) respectively. The values for $\epsilon_{\perp}$ were taken at $0.05V_{rms}$ and the values for $\epsilon_{||}$ were taken at $20V_{rms}$. It should be noted that an AL correction has not been applied here as it is not necessary to do so at this point to find the information required from the frequency response. It can clearly be seen that the frequency response of the LCQD nanocomposite is similar to that of the pure LC, the difference in the position of the ϵ'' minima are only a result of different electrode and connecting wire resistances.

The ODA_{530}QD nanocomposite on the other hand, shows a considerable change in behaviour. The magnitude of the loss is greater and IP effects at the AL interface come in at much higher frequencies than both the pure LC and the LCQD nanocomposites. As a result, there is no obvious plateau in the ϵ' frequency response of the ODA_{530}QD nanocomposites at which to take the permittivity measurements, thus making accurate $\epsilon(V)$ measurements more difficult compared to the pure LC and LCQD nanocomposites. The ODA_{650}QD nanocomposite shows behaviour somewhere between the LCQD nanocomposite and the ODA_{530}QD nanocomposite, with a greater magnitude of loss than the pure LC and LCQD nanocomposite as well as IP effects coming in at slightly higher frequencies. There is, however, still a well defined plateau in both $\epsilon'_{\perp}$ and $\epsilon'_{||}$ over a wide frequency range, making ϵ' measurements at a specific frequency convenient and reliable. The frequency dependent $\epsilon_{\perp}$ and $\epsilon_{||}$ across a range of temperatures can be seen for the pure LC as well as each of the nanocomposites in figures B.1, B.2, B.3 and B.4.

It should also be noted that the ODA_{530}QD nanocomposite, although initially the sample had good PH alignment (see figures 5.3(d) and 5.3(e)), it was found that after applying electric fields at such low frequencies in the isotropic phase, but after cooling back into the nematic phase, the alignment was no longer PH, but was instead HT. The low frequency fields caused a significant enough quantity of the QD to migrate to the AL interface, thus causing HT alignment to be induced, similarly to what was seen in the ODA_{530}QD sample at higher concentrations of 0.5 and $1wt\%$ without application of any electric fields (see figures 5.3(h), 5.3(i) and 5.3(h), 5.3(i)).

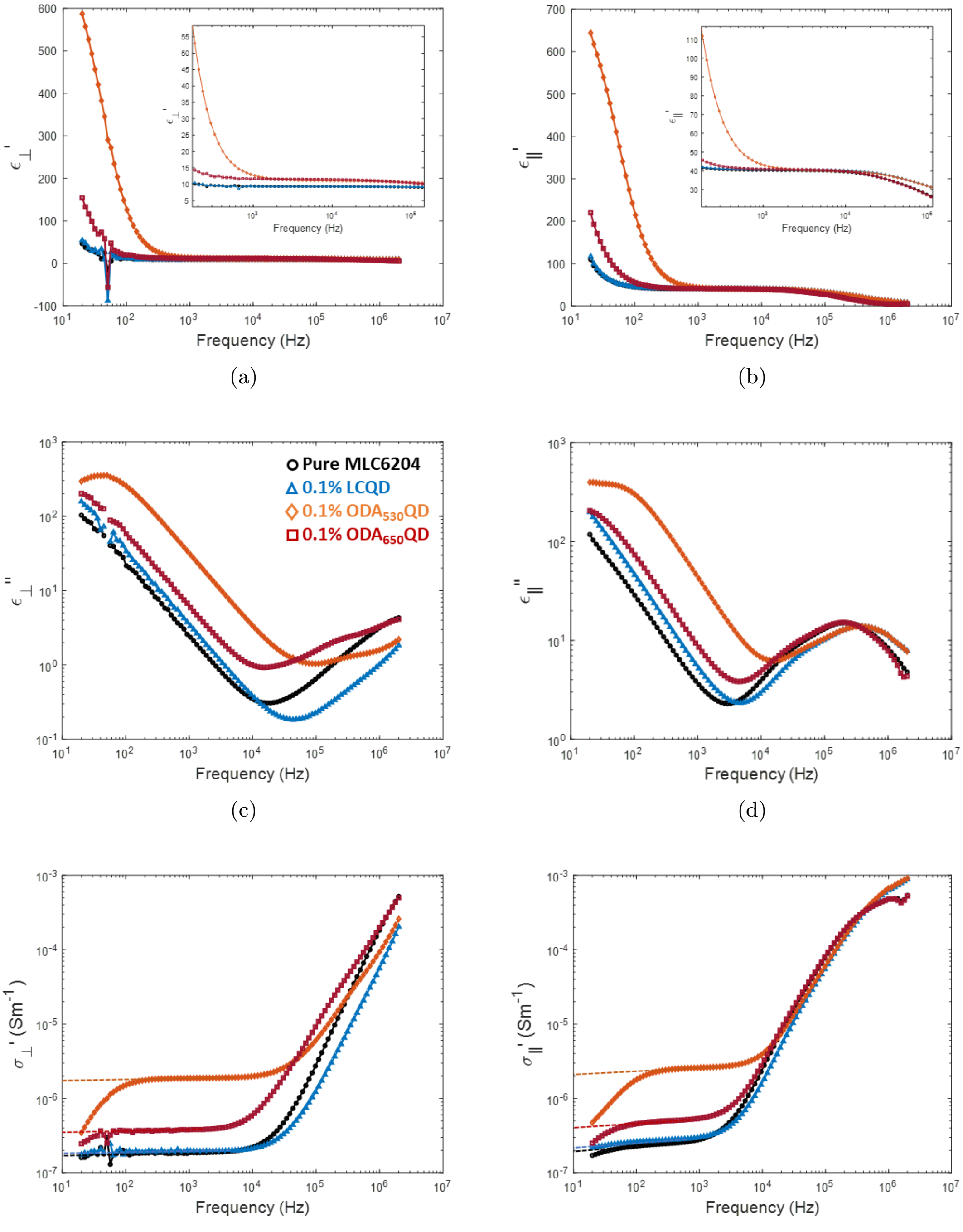

(a) (b)

(c) (d)

(e) (f)

Figure 5.9: Dielectric spectroscopy frequency response of QD-LC nanocomposites at $20°C$. Real permittivity a) perpendicular and b) parallel to the director, imaginary permittivity c) perpendicular and d) parallel to the director, real conductivity e) perpendicular and f) parallel to the director. The dashed line on the conductivity plots show the plateau at which the conductivity is measured. Pure MLC6204 (black circles), $0.1wt\%$LCQD nanocomposite (blue triangles), $1wt\%$ODA$_{530}$QD nanocomposite (orange diamonds). $\epsilon_\perp$, $\sigma_\perp$ measured at $V = 0.05V_{rms}$ and $\epsilon_\parallel$, $\sigma_\parallel$ measured at $V = 20V_{rms}$ in a $20\mu m$ PH cell.

A similar effect was also seen in the ODA$_{650}$QD nanocomposites, albeit only at the higher concentrations of 0.5 and $1wt\%$, however, the $0.1wt\%$ sample did not shown this effect. Following the application of low frequency fields which induced HT alignment, the samples were re-heated to isotropic in order to check if this process is reversible. It was found that even after heating to isotropic and holding overnight, on subsequent cooling, HT alignment was again produced, indicating the QD are trapped at the AL interface, as was found for the higher concentration samples which produced HT alignment on first cooling without any electric fields applied.

The conductivity of the $0.1wt\%$LCQD nanocomposite at $20°C$ was comparable to the pure LC, both perpendicular and parallel to $\mathbf{n}$, as can be seen from figures 5.9(e) and 5.9(f) respectively. At higher temperatures in the nematic phase approaching T_{NI}, however, the LCQD nanocomposite was found to show lower conductivity than the pure LC. Both the $0.1wt\%$ ODA$_{530}$QD and ODA$_{650}$QD showed higher conductivity perpendicular and parallel to $\mathbf{n}$ but much more significantly with the smaller ODA$_{530}$QD. Interestingly, this conductivity increase showed the opposite temperature dependence in the ODA$_{530}$QD nanocomposite, the conductivity relative to that of the pure LC increased with increasing temperature, but the ODA$_{650}$QD remained roughly constant with temperature.

It is well known that doping LCs with additives can increase the concentration of ionic impurities and thus increase the conductivity. However, it has also been shown that doping LCs with certain types of nanomaterials can have the opposite effect, and reduce the concentration of ionic impurities through 'ion trapping' [95, 191]. Ions in the LC can adsorb onto the surface of the nanomaterial, effectively reducing the concentration of ions available for conduction, thus reducing the ionic conductivity since this depends on the concentration and mobility of the ions in the LC. Ion 'trapping' by nanomaterials dispersed in the LC, has been shown to depend on the type of nanomaterial, i.e. the material the NP core is made from, the concentration and purity of the NPs in the host LC. Ion 'releasing' by nanomaterials whereby desorption of ions from the NP surface into the LC also takes place, thus depending on the conditions just mentioned, three different regimes are possible; net ion 'trapping' (conductivity reduction), net ion 'releasing' (conductivity increase) or an 'equilibrium' between the two (conductivity unchanged compared to pure the LC) [192, 193].

From the results shown here, it is clear that both the type of surface functionalisation and QD size impact the ion adsorption and desorption rate. Hence at a temperature of $20°C$ with $0.1wt\%$

concentration of QD, the LCQD nanocomposite falls into the 'equilibrium' regime, where the rate of ion adsorption and desorption is approximately the same, since the conductivity compared to the pure LC is unchanged. The ODA_{530} and ODA_{650}QD nanocomposites, however, both fall into the net ion 'releasing' regime, where more ionic impurities are introduced to the LC, and thus, the conductivity is increased. Interestingly, both the LCQD and ODA_{530}QD both show a temperature dependence, but of the opposite sense. The LCQD nanocomposite moves into the ion 'trapping' regime as temperature is increased, whereas the ODA_{530}QD nanocomposite moves further into the ion 'releasing' regime, which suggests a strong dependence on the type of surface functionalisation used, since the two QDs are of comparable core size. This kind of temperature dependence of the ion 'trapping' and ion 'releasing', has previously been simulated for different NP types and concentrations [194]. The difference in the conductivity of the two ODAQD nanocomposites also suggests a strong dependence on the QD core size. It is possible that at lower QD concentrations, the LCQD nanocomposite could move into the ion 'trapping' regime and the ODAQD move towards the 'equilibrium' regime.

5.3.2 Permittivity-Voltage Curves

A comparison of the $\epsilon(V)$ curves measured at $25°C$ and after AL correction for the different QD-LC nanocomposites is shown in figure 5.10(a). The inset shows an expanded view of the WS fitting around V_{th} shown by the low V shaded region. The high V shaded region of figure 5.10(a) shows the voltage range over which the $1/V$ extrapolations were performed, which can be seen in figure 5.10(b). A significant increase in the pretilt can be seen by the less well defined V_{th} and increased value of $\epsilon_\perp$ at $V < V_{th}$ in the $\epsilon(V)$ curves for the QD-LC nanocomposites compared to the pure LC. WS fitting of the data should enable the change in pretilt resulting from the QD at the AL surface to be accounted for. It should be noted though, that these measurements were performed at the same absolute temperature and not the same reduced temperature. Hence, the difference between the high V values of the pure LC and the LCQD nanocomposite for example, is predominantly due to this difference in the reduced temperatures since the LCQD nanocomposites showed a reduction in T_{NI} when measured in $20\mu m$ PH cells (see chapter 4 section 4.3).

The $1/V$ plots at high V reveal that the ODA_{650}QD nanocomposite has a significantly different gradient in this region than the pure LC and the other nanocomposites. Therefore, even though the absolute value at the maximum applied voltage of $20V_{rms}$ is higher than the LCQD nanocomposite, this difference in gradient means the LCQD still has a higher $\epsilon_{\|}$. This difference in gradient arises due to the alignment effect of the ODA$_{650}$QD, whereby, more of the LC reorients at lower V than the LCQD nanocomposite or pure LC, but as V is further increased, the disordering effect of the QD dominates over the induced HT alignment. The $\epsilon(V)$ curves for the pure LC, $1wt\%$LCQD, $0.1wt\%$ODA$_{530}$QD and $0.1wt\%$ODA$_{650}$QD across their nematic temperature ranges can be seen in the appendix, in figures C.1, C.2, C.3 and C.4 respectively. The linear and WS fitting of these curves across the nematic temperature range is also shown in the same figures and the results of which are presented and discussed in the following sections.

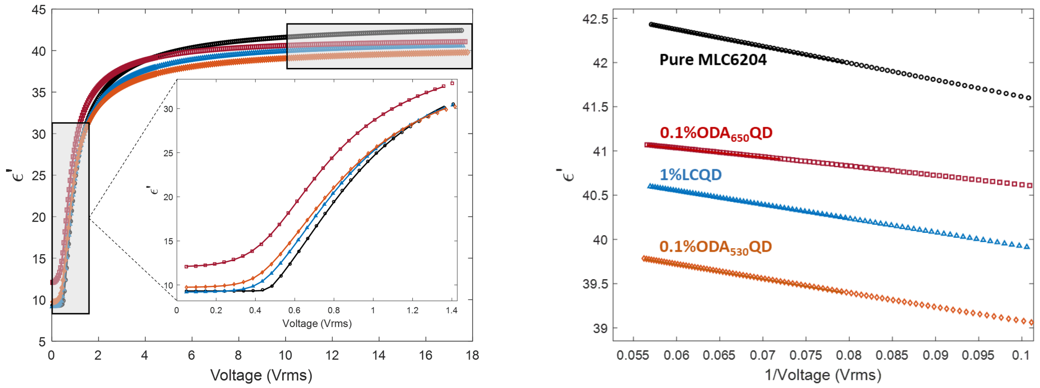

(a) (b)

Figure 5.10: $\epsilon(V)$ curve comparison at $25°C$ between the different QD-LC nanocomposites with inset of a) showing the WS fitting around V_{th} (shaded region at low V) and b) $1/V$ extrapolation (of shaded region at high Vin a)). Pure MLC6204 $\approx 0.87T_{NI}$ (black), $1wt\%$LCQD $\approx 0.87T_{NI}$ (blue), $0.1wt\%$ODA$_{530}$QD $\approx 0.89T_{NI}$ (orange) and $0.1wt\%$ODA$_{650}$QD $\approx 0.88T_{NI}$ (red) nanocomposites in MLC6204.

5.3.3 Permittivities

The effect of the different surface functionalisation in the QD-LC nanocomposites is evident in the $\epsilon(T)$ curves. Figure 5.11(a) shows $\epsilon_{\perp}$, $\epsilon_{\|}$ and ϵ_{iso} against reduced temperature for the pure LC MLC6204, $1wt\%$LCQD, $0.1wt\%$ODA$_{530}$QD and $0.1wt\%$ODA$_{650}$QD nanocomposites, whilst 5.11(b) shows the values of $\Delta\epsilon$ for the same samples. The $\epsilon_{\perp}$ values here were taken as the ϵ value at $0.05V_{rms}$ and the $\epsilon_{\|}$ values were calculated from the $1/V$ extrapolation to infinite V. By measuring the $\epsilon(V)$ curves of the pure LC in several nominally $20\mu m$ thick PH cells and then fitting each of the curves to find the average ϵ values, the standard error associated with these values could also be calculated. The average relative errors found across the $\epsilon_{\|}$ measurements was 1.1% and the maximum error found in the $\epsilon_{\perp}$ measurements (taken at $0.05V_{rms}$) was 1.4%. Error bars have not been plotted in figures 5.11(a) and 5.11(b) to keep the plots readable.

Figure 5.11(c) shows the concentration dependence LCQD nanocomposites permittivities as a function of concentration at $25°C$. Across the entire concentration range measured, no change to any of the permittivities can be seen within error, regardless of network formation. The LCQD nanocomposite, even at a QD concentration of $1wt\%$ shows within error the same ϵ values as the pure LC, whilst both the ODAQD nanocomposites show a significant reduction in $\epsilon_{||}$. This can be attributed to the reduction in S due to the disordering nature of the ODAQDs since $\epsilon \propto S$. This result agrees well with the order parameters in chapter 4 section 4.4, which showed that both the ODAQDs reduce S with increasing QD concentration. Thus, it is expected that $\epsilon_{||}$ of the ODAQD nanocomposites should show a reduction when calculated from a $1/V$ extrapolation, as the effects of the LC alignment is removed.

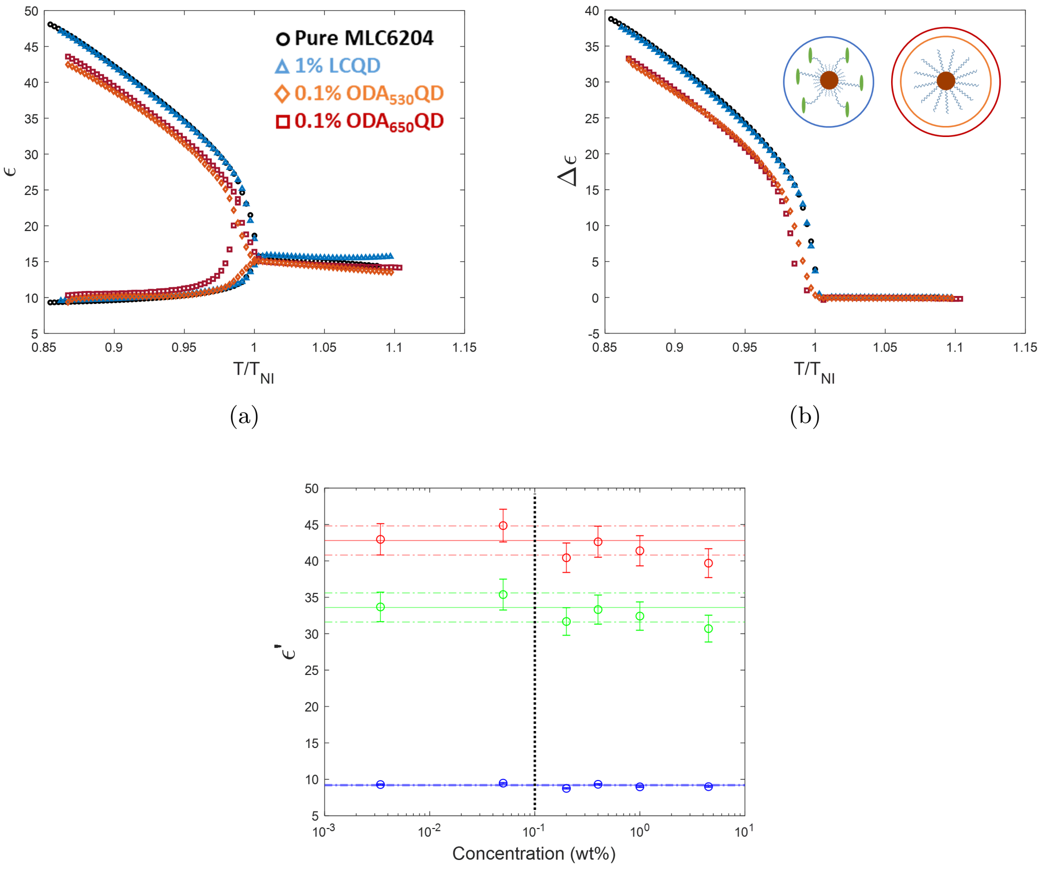

(a)

(b)

(c)

Figure 5.11: Permittivities of the different QD-LC nanocomposites, a) $\epsilon_{||}$ and $\epsilon_{\perp}$, b) $\Delta\epsilon$ against reduced temperature. Pure MLC6204 (black), $1wt\%$LCQD (blue), $0.1wt\%$ODA$_{530}$QD (orange) and $0.1wt\%$ODA$_{650}$QD (red) nanocomposites in MLC6204. c) shows $\epsilon_{parallel}$ (red), $\epsilon_{\perp}$ (blue) and $\Delta\epsilon$ (green) as a function of LCQD concentration at $25°C$, the black dashed line indicates the concentration threshold above which network formation takes place.

Assuming that the addition of these QDs to the LC does not inherently affect the molecular dipole moment of the LC regardless of the type of surface functionalisation used, the difference in $\Delta\epsilon$ of the pure LC and the QD-LC nanocomposites can be written from equation 1.34c as:

$$\Delta\epsilon_{LC} - \Delta\epsilon_{QDLC} = \frac{NhF}{\epsilon_0}\big(\Delta\alpha_{LC}S_{LC} - \Delta\alpha_{QDLC}S_{QDLC}\big), \tag{5.1a}$$

where $\Delta\alpha_{LC}$ and $\Delta\alpha_{QDLC}$ are the polarisability anisotropies of the pure LC and QD-LC nanocomposites respectively, whilst S_{LC} and S_{QDLC} are the order parameters of the pure LC and QD-LC nanocomposites respectively. In the case that the addition of QD to the LC also does not affect the polarisability, then equation 5.1a can be reduced to:

$$\Delta\epsilon_{LC} - \Delta\epsilon_{QDLC} = \frac{NhF\Delta\alpha_{LC}}{\epsilon_0}\big(S_{LC} - S_{QDLC}\big). \tag{5.1b}$$

As can be seen from equation 5.1b, the only variable which affects $\Delta\epsilon$ of the QD-LC nanocomposites is the change in order which is directly affected by the effect of the surtface functionalisation on the host LC. It is therefore concluded, that the change in permittvities seen from dielectric spectroscopy measurements on the pure LC and the ODAQD nanocomposites arises from the affect of the alkyl chain surface functionalisation on the order of the host LC. An interesting feature to point out in the $\epsilon(T)$ curve of the $0.1wt\%$ODA$_{650}$QD nanocomposite curve, is the increase of $\epsilon_\perp$ at temperatures just below T_{NI}. $\epsilon_\perp$ starts to increase several $°C$ below T_{NI} until the value reaches the same as $\epsilon_\parallel$, at which point, both decrease with increasing temperature until T_{NI} is reached. This result confirms the HT alignment transition shown in the POM photographs of figure 5.5 is definitely an alignment transition and not a transition to the isotropic phase.

5.3.4 Elastic Constants, Vth and Pretilt

The WS fitting results of the $\epsilon(V)$ curves around V_{th} for the pure LC MLC6204 and the LCQD nanocomposites at a range of QD concentrations of 0.2, 1 and $4.5wt\%$, as well as the $0.1wt\%$ODA$_{530}$QD and $0.1wt\%$ODA$_{650}$QD nanocomposites in MLC6204 are presented and discussed in this section. A comparison of the LCQD nanocomposites' K_{11}, K_{33}, V_{th} and θ_p values across the nematic temperature range are shown in figures 5.12(a), 5.12(b), 5.12(c) and 5.12(d) respectively. K_{11} and K_{33} of the LCQD nanocomposites as a function of QD concentration at a temperature of $25°C$ can also be seen in figure 5.12(e).

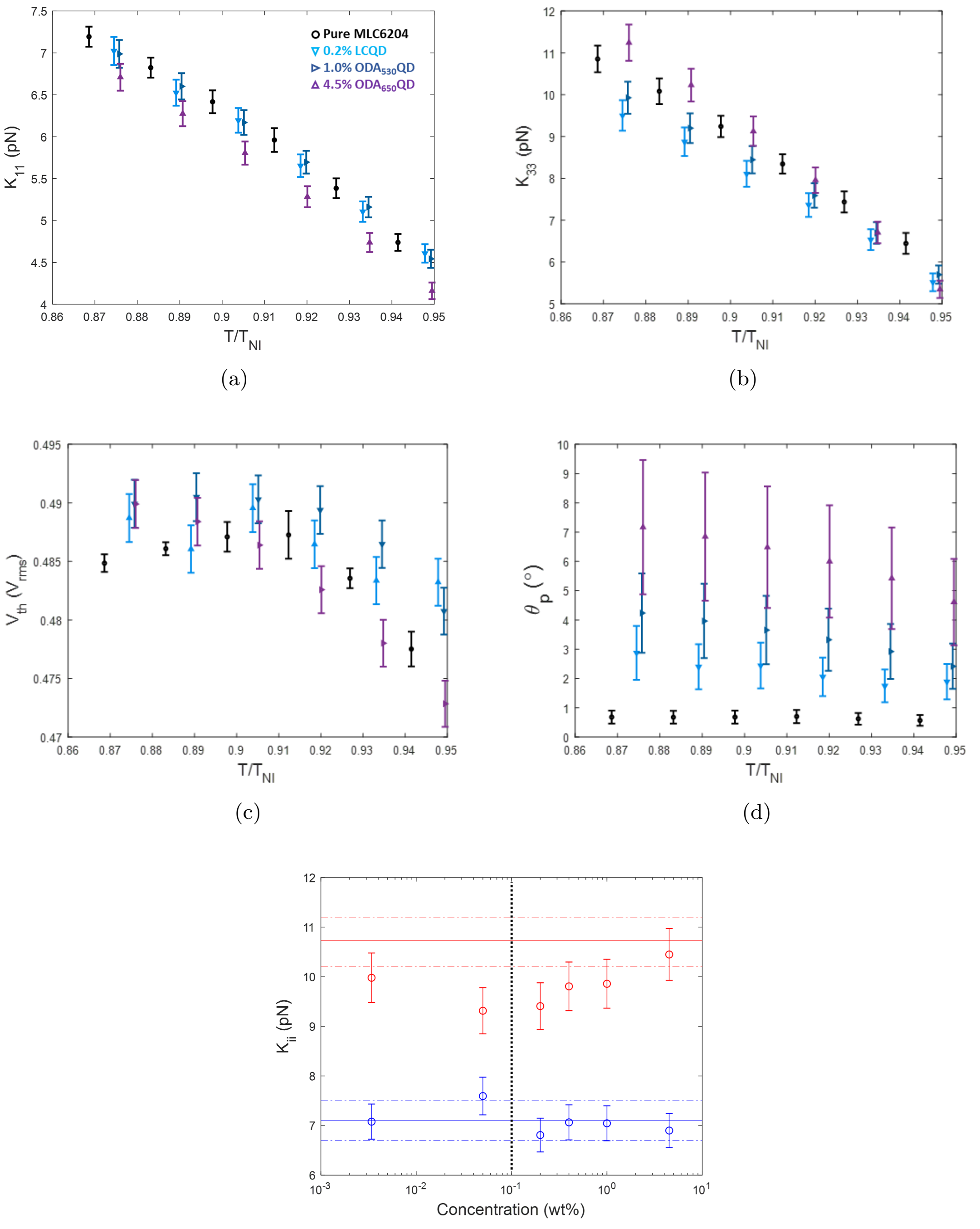

(a)

(b)

(c)

(d)

(e)

Figure 5.12: Elastic constants a) K_{11} and b) K_{33} as well as c) threshold voltage and d) pretilt of LCQD nanocomposites at different QD concentrations found from WS fitting of the $\epsilon(V)$ curves against reduced temperature. Pure MLC6204 (black), $0.2wt\%$LCQD (light blue downwards triangle), $1wt\%$LCQD (dark blue sideways triangles) and $4.5wt\%$LCQD (purple upwards triangle) nanocomposites in MLC6204. e) shows the LCQD nanocomposites concentration dependence of K_{11} (blue) and K_{33} (red) at $25°C$.

K_{11}, K_{33} and V_{th} results of the LCQD nanocomposites within error, are unchanged compared to the pure LC, as one would expected, since both the S measurements and the ϵ measurements confirm the order preserving nature of the LCQD. Hence if S is unchanged, then K_{ii} should remain unchanged, since $K_{ii} \propto S$. θ_p of the LCQD nanocomposite, however, shows a significant (approximately five times average) increase compared to the pure LC. Although the absolute values of θ_p found from $\epsilon(V)$ fitting don't fully agree with the results found from directly measuring θ_p using the modified crystal rotation method in section 5.2.4, the relative increase (compared to the pure LC), due to the LCQD is approximately the same (approximately five times) for the $1wt\%$ nanocomposite. The $\epsilon(V)$ fitting of the pure MLC6204 at R.T. gave a value of $\theta_p \approx 0.7°$ whereas the direct measurement gave $\theta_p \approx 2°$. The reason for the discrepancy is not clear, but $\epsilon(V)$ WS fitting consistently gave lower θ_p values than the direct measurement using the modified crystal rotation method. It is possible, that the difference in these results could be due to the difference in cell gaps used for the dielectric spectroscopy and pretilt measurements of $20\mu m$ and $50\mu m$ respectively.

Figures 5.13(a), 5.13(b), 5.13(c) and 5.13(d) show K_{11}, K_{33}, V_{th} and θ_p as a function of T/T_{NI} respectively. Similarly to the ϵ values discussed in the previous section, the errors here have been calculated from multiple measurements of the pure LC in several nominally $20\mu m$ PH test cells. The average and maximum relative errors for K_{11} were found to be 2.0% and 2.4% respectively, whilst for K_{33} they were found to be 3.1% and 3.8%. For V_{th} these were found to be 0.2% and 0.4%, whilst for θ_p the average and maximum were found to be 32%, and 41%. The error bars in the figures 5.13(a), 5.13(b), 5.13(c) and 5.13(d) for the pure LC are the standard errors calculated from the $\epsilon(V)$ fitting results of several cells, whilst the error bars for the QD-LC nanocomposites have been calculated from the maximum relative errors for each of the parameters, K_{11}, K_{33}, V_{th} and θ_p.

Both of the ODAQD nanocomposites show somewhat peculiar elastic constant results. The ODA_{530}QD nanocomposite shows similar K_{11} values at lower T, but as T is increased, the values do not decrease with the expected gradient of the pure MLC6204 and LCQD nanocomposites. The K_{33} values of this nanocomposite also show an unexpected gradient with T, but at lower T, the values are larger than expected and as T is increased, the K_{33} values approach those of the pure LC. The ODA_{650}QD nanocomposite shows a large and unexpected increase in K_{11} compared to the pure LC. The K_{33} results, however, are significantly lower than the pure LC in the case of the ODA$_{650}$QD nanocomposite, more in line with the effect one would expect from a disordering QD.

The V_{th} values of the LCQD nanocomposite, are approximately the same within error and follow the same temperature dependence as the pure LC. The ODA$_{530}$QD, however, although has similar V_{th} values shows a very different temperature dependence to the pure LC and LCQD nanocomposite. The change in temperature dependence of K_{11} and K_{33} of the ODA$_{530}$QD nanocomposites are therefore thought to stem from the increased IP effects seen in the frequency response of ϵ which depend on both T and V, thus making accurate $\epsilon(V)$ measurements and subsequently finding accurate elastic constant values particularly difficult.

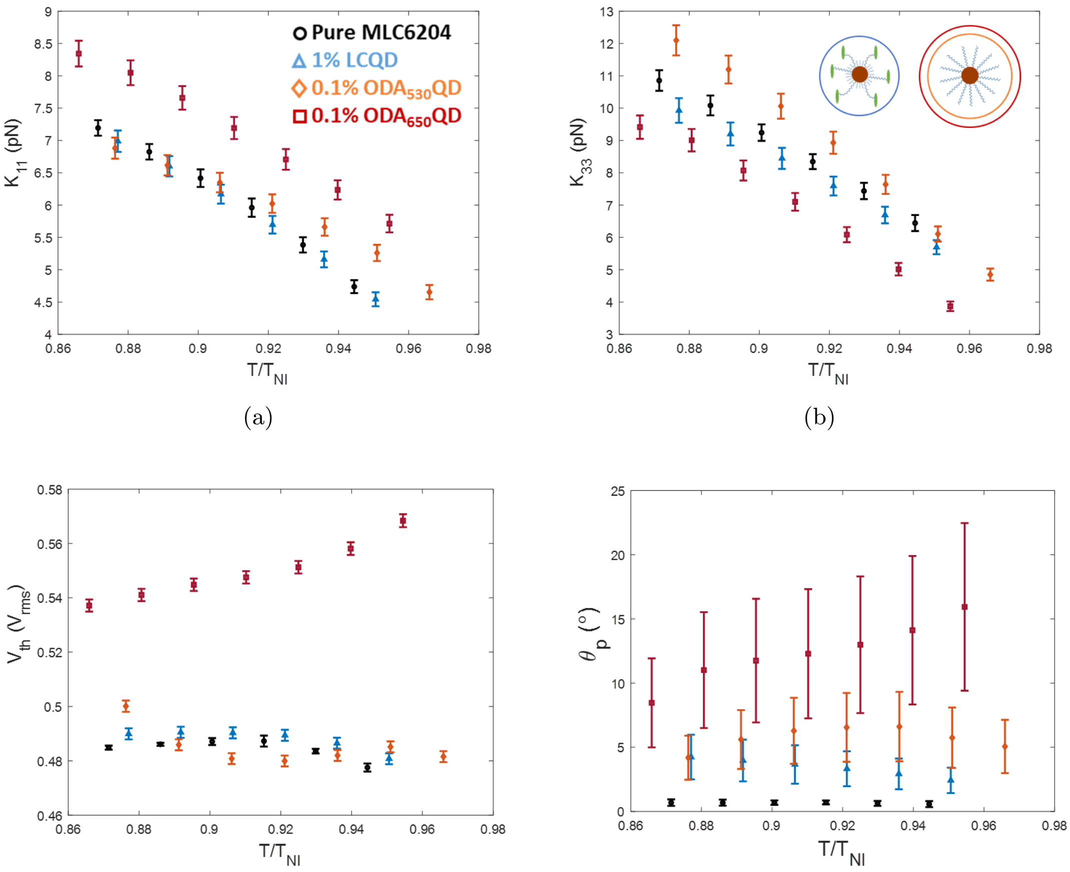

(a)

(b)

(c)

(d)

Figure 5.13: Elastic constants a) K_{11} and b) K_{33} as well as c) threshold voltage and d) pretilt of the different QD-LC nanocomposites found from WS fitting of the $\epsilon(V)$ curves against reduced temperature. Pure MLC6204 (black), 1wt%LCQD (blue), 0.1wt%ODA$_{530}$QD (orange) and 0.1wt%ODA$_{650}$QD (red) nanocomposites in MLC6204.

Table 5.1: Comparison of θ_p values from WS fitting of the $\epsilon(V)$ curves in $20\mu m$ cells and direct measurement using the crystal rotation method in $50\mu m$ cells (at room temperature).

Sample	$\epsilon(V)$ WS Fitting (°)	Measured (°)
Pure MLC6204	0.3	2
$0.5wt\%$ LCQD	-	10
$1wt\%$ LCQD	4	-
$0.1wt\%$ $ODA_{530}QD$	5	-
$1wt\%$ $ODA_{530}QD$	-	89
$0.1wt\%$ $ODA_{650}QD$	10	-

The θ_p values in figure 5.13(d) show the largest increase from the $ODA_{650}QD$ nanocomposite compared to the pure LC, followed by the $ODA_{530}QD$ nanocomposite and then the LCQD nanocomposite. The $ODA_{650}QD$ nanocomposite also gave the highest V_{th} values from WS fitting, hence the unexpectedly large K_{11} values, but lower K_{33} values. Interestingly, the $ODA_{650}QD$ nanocomposite actually gave the lowest V_{th} and K_{11} from linear fitting indicating the large effect of the increased pretilt on the results. The effect of pretilt on the interpretation of the $\epsilon(V)$ curves can evidently lead to significant discrepancies in the values of V_{th} and therefore elastic constants. Thus, the unexpectedly large values of K_{11} are believed to be erroneous in this case. A comparison of the θ_p values found from WS fitting of the $\epsilon(V)$ curves and the direct measurements of the different nanocomposites can be seen in table 5.1.

It has been previously been shown by Urbanski et. al. that in the case of NPs residing at the AL interface, can cause change to the anchoring energy and initial pretilt angle of the LC [104]. They identified three alignment regimes that can take place in NP-LC nanocomposites; 'no surface interaction', 'strong interaction' or 'slight interaction'. In the case of 'no surface' interactions, NPs reside in the bulk and so no consideration of the effects on the anchoring of the LC need to be made and therefore, even the simplest linear fitting regime is suitable, provided strong anchoring of the AL and low pretilt angles ($\theta_p < 2°$). 'Strong interaction' corresponds to such a high quantity of NPs residing at the surface that the PH anchoring of the AL is completely overcome by the NPs, and thus full HT alignment of the LC takes place. This typically happens with alkyl chain functionalised NPs or QDs at high concentrations, as was shown earlier in this chapter, section 5.2. In the intermediate case of 'slight interactions' with the surface, the NPs have an affect on the anchoring energy and pretilt, as was the case here, for the $1wt\%$LCQD as well as the $0.1wt\%$ ODA$_{530}$ and ODA$_{650}$QD nanocomposites. A similar approach to that used by Urbanski et. al. was used, whereby WS fitting was used to simulate the $\epsilon(V)$ curves, including the effect of pretilt. Except in this case, a high $\Delta\epsilon$ LC has been used and thus the modified approach with a $1/V$ extrapolation was used to find $\epsilon_{||}$ which was then fixed in the WS fitting of $\epsilon(V)$ curves around V_{th}, as described in detail in chapter 3 section 3.4.

Good agreement of the simulated and measured $\epsilon(V)$ curves around V_{th} was found in all cases here. However, what appear to be erroneously large V_{th} and thus K_{11} values were found in the $0.1wt\%$ODA$_{650}$QD nanocomposite, which also gave the highest θ_p. This overestimation of V_{th} from WS fitting of the $\epsilon(V)$curves, in the high pretilt case of the $0.1wt\%$ODA$_{650}$QD nanocomposite is thought to arise from the inhomogeneous alignment and variation of pretilt across the cell that can be seen in figures 5.4(c) and 5.4(d). This is something that is not taken into consideration, as the WS approach assumes a uniform alignment through the cell and thus the θ_p found is an effective average value. An additional consideration is the 'screening' effect of the QD residing at the substrate surfaces, which can lead to an overestimation of V_{th} [195]. Similarly to the effec the ALs have on the true voltage applied across the LC, QD at the AL surface will cause a further reduction to the true voltage applied across the LC, which has not been corrected for here. Thus, in the case of the ODA$_{650}$QD nanocomposite, this could also be leading to the overestimation of V_{th} and subsequently giving rise to the erroneously large vales of K_{11} that have been calculated.

5.4 Summary

POM textures of the LCQD and both ODAQD nanocomposites have been studied at a range of concentrations between both untreated glass slides and in aligned cells. In conjunction with pretilt and dielectric spectroscopy measurements used to determine the permittivities of the nanocomposites, the alignment induced by the QDs with either side-on mesogenic or alkyl chain surface functionalisation has been deduced. Dielectric spectroscopy was also used to obtain the $\epsilon(V)$ curves of the nanocomposites which were subsequently analysed to infer the effect of the QD surface functionalisation, not only on the alignment and dielectric permittivities of the QD-LC nanocomposites, but also the elastic properties.

Between untreated glass slides, the pure LC MLC6204 produced good HT alignment at low

QD concentrations ($\sim 0.01wt\%$), all of the nanocomposites also produced HT alignment, albeit in some cases, namely the ODA$_{530}$QD and ODA$_{650}$QD produced some birefringent spots, assumed to result from alignment around QD clusters/aggregates. The LCQD, however, also gave good HT alignment up to $\sim 0.1wt\%$. At higher concentrations of $0.4wt\%$LCQD, above the concentration threshold at which QD network formation through the isotropic to nematic phase transition took place (as seen in the previous chapter 4), uniform HT alignment was lost. At these concentrations, a large number of highly birefringent regions appeared due to the QD network self-assembly. At similarly high ODA$_{530}$ and ODA$_{650}$QD concentrations, predominantly HT alignment was seen uniformly across the samples, but around QD clusters, larger birefringent spots were formed. At intermediate concentrations of $0.05wt\%$, particularly with the ODA$_{530}$QD, good HT alignment was lost and significant birefringence was seen.

The LCQD nanocomposites at all concentrations tested, both below and above the $\sim 0.1wt\%$ QD concentration threshold for phase transition driven QD self-assembly, showed good uniform PH alignment in $20\mu m$ PH LC test cells. However, at concentrations of $> 0.1wt\%$ where network formation was seen, in $20\mu m$ HT cells, alignment was deteriorated. The ODA$_{530}$QD nanocomposites in $20\mu m$ PH cells showed good PH alignment at low concentrations, but at higher concentrations, significant QD migration to the substrate surfaces resulted in HT alignment. In samples where ODA$_{530}$QD network formation was seen, thick birefringent 'strings' were formed at the location of the QD networks. The HT alignment induced in the high concentration ODA$_{530}$QD nanocomposites was also confirmed through pretilt measurements which gave a pretilt value of $\theta_p = 89°$. Pretilt measurements also revealed a significant increase of θ_p from the LCQD when compared to that of the pure LC.

Interestingly in the ODA$_{650}$ nanocomposites, a mixture of planar and HT alignment was seen in $20\mu m$ PH cells, with the HT regions situated at the location of the QD clusters or QD networks that were self-assembled through the isotropic to nematic transition. The density of HT regions was found to increase with increasing QD concentration and more significant deviations from good PH alignment was seen surrounding the HT regions. It was also found that the HT regions grew in size on heating the sample through the nematic phase until a complete HT alignment transition took place before the nematic-isotropic phase transition. This alignment transition was then later confirmed through permittivity measurements as a function of temperature, where the value of $\epsilon_\perp$ was found to increase until it reached the value of $\epsilon_\parallel$ below T_{NI}.

Dielectric spectroscopy measurements of the QD-LC nanocomposites showed radically different frequency responses of $\epsilon_\perp$, $\epsilon_{||}$, $\sigma_\perp$ and $\sigma_{||}$ as a result of the different QD types. The different surface functionalisation and QD sizes drastically altered the ionic effects in the dielectric spectroscopy measurements, which had to be considered when performing $\epsilon(V)$ measurements. The $\epsilon(V)$ curves of the QD-LC nanocomposites were then measured and analysed to find $\epsilon_\perp$, $\epsilon_{||}$, K_{11} and K_{33} as well as θ_p by using a combination of a $1/V$ extrapolation and WS fitting around V_{th}. The LCQD nanocomposites showed no change in $\epsilon_{||}$ compared to the pure LC at the same T/T_{NI}, whereas both types of ODAQD nanocomposites showed a significant reduction in $\epsilon_{||}$ as well as an increase in $\epsilon_\perp$ and thus also $\Delta\epsilon$. This result agrees well with the measurement of S in the previous chapter 4 section4.4, which revealed that both the ODAQD nanocomposites had significantly lower order than both the pure LC and the LCQD nanocomposites.

WS fitting of the $\epsilon(V)$ curves showed no change to the elastic constants K_{11} or K_{33} for the LCQD nanocomposites at any of the concentrations measured, but did show that θ_p increased with increasing QD concentration. This also agrees with the S measurements, since the LCQD were shown to preserve the order of the LC and therefore no reduction in K_{ii} should be seen since $K_{ii} \propto S^2$. The disordering nature of the ODAQD, however, leads one to expect a reduction in K_{ii}, which was not found here. An unexpected change in the gradient of K_{11} and K_{33} with T/T_{NI} was seen in the ODA$_{530}$QD nanocomposite, accompanied with an increase in θ_p as expected, but the absolute values of K_{ii} were not significantly reduced by the magnitude expected from the reduction seen in S. The ODA$_{650}$QD nanocomposite showed the most unusual K_{ii} results of all the nanocomposites measured. K_{11} was found to significantly increase compared to the pure LC, even though S is known to decrease, whereas as K_{33} was found to decrease. The largest θ_p was, however, found for the ODA$_{650}$QD nanocomposite.

It is therefore concluded that even though WS fitting of the $\epsilon(V)$ curves should account for the large θ_p, erroneous K_{ii} values can still be produced due to the variable pretilt across the test cell. Numerous studies have reported changes in K_{ii}, but do so without consideration of any change in θ_p. Most frequently, this change is a reduction [89, 90, 92], but increases have also been reported in some cases [93]. This highlights the importance of accounting for the effect that NP doping of LCs has on θ_p in LC test cells when characterising the electro-optic properties.

Chapter 6

Conclusions and Future Research

6.1 Conclusions

In this thesis, the fundamental theory underpinning the physics of NLCs and nanomaterials, required to undertake the research and understand the results was first introduced in sections 1.1 and 1.2 of chapter 1. This was followed by a detailed review of the relevant literature, covering the previously performed research on LC nanocomposites; including their overall physical properties and the self-assembly of nanomaterials driven by the ordered nature of LC materials in section 1.3 of chapter 1. In the first half of chapter 2 (section 2.2), the experimental techniques and methods used to build the LC devices and prepare the LC nanocomposites that were subsequently characterised in these devices were covered. In the second half of chapter 2 (section 2.4), the characterisation techniques used to determine the physical properties of the LC nanocomposites and study the QD self-assembly were described. Where necessary, the theoretical principles of the characterisation techniques used were also discussed in detail.

6.1.1 Dielectric Spectroscopy of LCs

The first results chapter (chapter 3) was comprised of a rigorous study and a comprehensive guide of how to correctly perform dielectric spectroscopy on LC materials and LC nanocomposites. The contribution of the LC test cells constructed for this purpose were studied, in particular, the effects of ionic impurities within the samples and the ALs that are used in such devices to provide uniform alignment of the LC. To do so, the dielectric spectra of empty LC test cells built with and without ALs were first measured. The dielectric spectra of LC test cells, again, with and without ALs filled with the isotropic promesogenic liquid PCH32, as well as PCH32 doped with the organic salt TBATPB to provide additional ionic impurities were also measured. This was done in order to study the effects of ionic impurities on the dielectric spectra, particularly at low frequencies.

To analyse and interpret the dielectric spectra, an equivalent circuit approach was used and the process of doing so described in detail. Firstly the basic equivalent circuit components comprised of the ideal capacitor, resistor and inductor were introduced, and their individual contribution to the overall frequency dependence of the complex impedance/capacitance presented. Following this, the construction process used to combine the individual components into equivalent circuits was described, including how the complex impedance/capacitance of the component combinations should be calculated. The frequency dependent complex capacitance of some fundamental component combinations were then introduced and related to the features seen in the real dielectric spectra measured using LC test cells. Following this, the more complex but versatile component, the constant phase element was introduced and subsequently used in the complete equivalent circuit that describes the dielectric spectra of PCH32 (and other dielectric liquids) in LC test cells across a frequency range of mHz - MHz including the effects of ionic impurities.

The dielectric spectra of the high $\Delta\epsilon$ NLC mixture MLC6204 was then measured and the frequency dependent complex permittivity parallel ($\epsilon_{||}(\omega)$) and perpendicular ($\epsilon_{\perp}(\omega)$) to the director was found from measurements in HT and PH cells respectively. $\epsilon_{||}(\omega)$ and $\epsilon_{\perp}(\omega)$ were then interpreted in order to perform permittivity-voltage $\epsilon(V)$ measurements at the appropriate frequency. The correct measurement procedure required to perform accurate $\epsilon(V)$ measurements was then discussed, including the determination of a suitable stabilisation time to be used following the application of a field, before performing a capacitance measurement, particularly around the threshold voltage V_{th}. The effect of the stabilisation time on the measured $\epsilon(V)$ curves around V_{th} was then shown. By not stabilising the LC for a suitable period of time following the application of a field, V_{th} shown in the $\epsilon(V)$ curve was significantly larger than the true value, which would therefore lead to overestimation of K_{11} when analysing the curves.

The effect of ALs on the measured $\epsilon(V)$ curves was then studied. An equivalent circuit approach was used to correct the curves, both in terms of the effect on the measured ϵ values and the true voltage applied across the LC. It was found, that for a high $\Delta\epsilon$ material such as MLC6204 with a low ϵ AL, the measured ϵ value is significantly lower than the true ϵ value of the LC. The magnitude of this effect was also shown to scale with increasing AL thickness and decreasing cell gap. An $\epsilon(V)$ curve fitting routine using a combination of linear and WS fitting to determine the $\epsilon_{\parallel}$, $\epsilon_{\perp}$, K_{11} and K_{33} from the corrected $\epsilon(V)$ curves whilst accounting for θ_p for high high $\Delta\epsilon$ materials such as MLC6204 was developed and described in detail. By using this fitting routine on the $\epsilon(V)$ curves of MLC6204 in $20\mu m$ PH cells corrected for different AL thicknesses, it was shown that with increasing AL thickness, K_{11} increased, whilst K_{33} decreased and $\epsilon_{\parallel}$, $\epsilon_{\perp}$ and $\Delta\epsilon$ all increased. It was shown that for high $\Delta\epsilon$ materials, to accurately measure the $\epsilon(V)$ curves and thus accurately determine the permittivities and elastic constants, AL correction must be performed prior to using an appropriate fitting routine.

6.1.2 Characterisation of QD-LC Nanocomposites

The second results chapter (chapter 4) concentrated on the phase behaviour and order of QD-LC nanocomposites as well as the QD self-assembly through the isotropic to nematic phase transition. Specifically, the effects of using side-on mesogenic and alkyl chain surface functionalisation, as well as QD size, was studied in terms of their effects on the phase transitions and order of the QD-LC nanocomposites, which was then related to the phase transition driven self-assembly processes.

The nematic-isotropic phase transition temperatures of the different QD-LC nanocomposites as a function of QD concentration were measured using DSC (in an unaligned state) and POM (in aligned $20\mu m$ PH cells). The DSC measurements showed no reduction in T_{NI} of the LCQD nanocomposites whatsoever, but the POM measurements showed an initial reduction up to a critical QD concentration, beyond which, T_{NI} reduced no further with increasing QD concentration. Unlike T_{NI} of the LCQD nanocomposites, which did not continually decrease with increasing QD concentration, in both of the ODAQD nanocomposites, T_{NI} was found to decrease with increasing QD concentration across the entire QD concentration range studied, indicating the disordering nature of the alkyl chain functionalisation. T_{NI} was reduced more so by the smaller ODA_{530}QD than the larger ODA_{650}QD at the same QD concentration by weight.

Similarly to the POM measurements of the LCQD nanocomposites, the ODAQD nanocomposites showed an initial steep reduction in T_{NI} up to a critical QD concentration. Unlike the LCQD nanocomposites, however, beyond this concentration, T_{NI} continued to decrease, but at a slower rate with increasing QD concentration. These results were then related to the theoretical model of Osipov and Gorkunov, which predicts a phase coexistence of a QD 'rich' isotropic phase and QD 'poor' nematic phase when the initial concentration of QD in the host LC is above a critical concentration threshold. Phase diagrams based on this model were then proposed for the LCQD and both ODAQD nanocomposites.

Following the determination of the phase behaviour, refractive index measurements were performed, the results of which were fit using the Haller method to find the scalar order parameter (S) of the QD-LC nanocomposites. As Indicated by the T_{NI} measurements, the LCQD showed little effect on S, whereas the ODAQDs reduced S with increasing QD concentration. Again, as the T_{NI} measurements suggested, this effect was more pronounced with the smaller ODA$_{530}$QD than the larger ODA$_{650}$QD for the same concentration by weight. This result solidifies the conclusion that the alkyl chain surface functionalisation of the ODAQDs, expected to give HT anchoring at the QD surface, are therefore disordering, whereas the LCQD are order preserving. The order preserving nature of the LCQD arises from the side-on mesogenic surface functionalisation where the mesogenic group is attached by a flexible alkyl linker, thus can orient with the director of the host LC rather than anchoring the host LC at the QD surface and therefore creating disorder due to the isotropic spherical shape of the QD.

The final part of the second results chapter investigated the phase transition driven QD self-assembly in the different QD-LC nanocomposites using FM. It was found that the LCQD formed 'hollow tubular worm-like' networks whereas both the ODAQDs formed 'solid worm-like' networks or in some case clusters. The reason for this was attributed to the effect that the surface functionalisation had on the order and subsequently the phase behaviour of the nanocomposites.

Since the LCQD are order preserving and do not reduce T_{NI} with increasing QD concentration, as the QD migrate to the remaining isotropic regions during the phase transition from isotropic to nematic, T_{NI} in these QD 'rich' isotropic regions is not reduced compared to the surrounding QD 'poor' nematic regions. This means that a second stage of nematic nucleation can take place within the isotropic regions, causing QD migration outwards into the reaming 'tubular' isotropic strands. This takes place until the entire nanocomposite has transitioned into the nematic phase, at which point, the 'hollow tubular' QD networks are 'locked' in place. Due to the disordering nature of the ODAQDs which reduce T_{NI} with increasing QD concentration, as the QD migrate to the remaining isotropic regions through the isotropic to nematic phase transition, the QD 'rich' isotropic regions experience a reduction in T_{NI} compared to the surrounding QD 'poor' nematic. This then prevents the second stage of nematic nucleation from taking place, as the QD 'rich' isotropic regions never reach $T < T_{NI}$ before the entire nanocomposite reaches nematic, thus solid QD networks or clusters are formed.

In the final results chapter (chapter 5), the alignment of the different QD-LC nanocomposites across a range of QD concentrations was studied, both between untreated glass slides and in aligned cells. Following this, dielectric spectroscopy measurements of the nanocomposites in $20\mu m$ PH cells were performed. The frequency dependence of ϵ', ϵ'' and σ' of the nanocomposites were studied and used to determine how to appropriately measure the $\epsilon(V)$ curves. The $\epsilon(V)$ curves were analysed according to the methods outlined in the first results chapter (chapter 3) to determine $\epsilon_{\|}$, $\epsilon_{\perp}$, K_{11} and K_{33} whilst accounting for the effect of θ_p, which varied significantly between the different nanocomposites.

Concentration dependent effects on the alignment between untreated glass slides was seen for each of the different QD-LC nanocomposite types. At low concentrations, good HT alignment, comparable to that of the pure LC MLC6204 was seen in the LCQD and both ODAQD nanocomposites. At concentrations above the threshold for network formation through phase transition driven self-assembly, the LCQD deteriorated the HT alignment between untreated glass of the pure LC, introducing significant birefringence, indicative of planar alignment. The ODAQDs, both showed deterioration of the HT alignment at intermediate concentrations, introducing birefringence from planar alignment but more so with the smaller ODA$_{530}$QD. At higher concentrations, good HT alignment was again seen, but with some birefringence around QD clusters formed through phase transition driven self-assembly.

In PH cells, the LCQD nanocomposites showed good PH alignment across all QD concentrations, with clear bright and dark states visible between crossed polarisers. The ODAQD nanocomposites, however, both showed concentration dependent alignment effects in PH cells. HT alignment was induced at higher concentrations of the ODA$_{530}$QD, but at lower concentrations, PH alignment was retained. This indicates that at higher QD concentrations, the ODA$_{530}$ reside at the substrate surfaces at high enough quantities to overcome the PH anchoring of the ALs and create preferentially HT anchoring instead. The ODA$_{650}$QD showed a mix of planar and and HT anchoring across the range of QD concentrations studied in PH cells. HT regions were seen at the locations of the QD networks or clusters, with planar alignment surrounding them. The birefringence colours in these planar regions surrounding the HT alignment arises from what is effectively a changing pretilt. Additionally, interesting temperature dependent alignment effects were also seen in the ODA$_{650}$QD nanocomposites, whereby the proportion of HT alignment to planar alignment increased as the temperature was increased, until a full HT alignment transition was seen below T_{NI}. This was later confirmed through $\epsilon(T)$ measurements of the same sample.

Analysis of the $\epsilon(V)$ curves revealed that the LCQD nanocomposites had the same $\epsilon_{\|}$ and as the pure LC, as to be expected due to the order preserving nature of the LCQD. Similarly, the elastic constants K_{11} and K_{33} were unchanged within error across the range of QD concentrations measured when compared to the pure LC. θ_p was found to increase with increasing QD concentration in the LCQD nanocomposites compared to the pure LC. This increase in θ_p due to the LCQD nanocomposites was not only inferred from the $\epsilon(V)$ curve fitting, but also shown through direct measurements in PH cells using the modified crystal rotation method.

Both the ODA$_{530}$ and ODA$_{650}$QD nanocomposites showed a reduction in $\epsilon_{\|}$ due to the disordering effect of the alkyl chain functionalisation, as one would expect, since both ODAQDs were found to reduce S compared to the pure LC. Conversely, however, the significant reduction of K_{ii} expected from ODAQD nanocomposites $\epsilon(V)$ curve fitting was not seen, even when accounting for the large increase in θ_p. It is thought that the K_{ii} values found for the ODA$_{650}$QD nanocomposites arose from the non-uniform pretilt through the cell, and thus, even when using the WS $\epsilon(V)$ curve fitting routine, this resulted in erroneous values K_{ii}. Table 6.1 provides a brief summary of these key findings regarding the effect of the different QD on the properties of the nanocomposites.

Table 6.1: Summary of QD-LC nanocomposite properties comparing effects of LCQD and ODAQD.

	LCQD	ODAQD
Phase Transitions	T_{NI} constant with increasing QD concentration	T_{NI} reduced significantly with increasing QD concentration
Network Formation	Hollow 'tubular' networks	Solid networks
Order	S preserved	S reduced
Alignment & Pretilt	Alignment retained in PH cells but with increased θ_p	Mixture of PH and HT alignment in PH cells large increase in θ_p
Permittivities	$\epsilon_{\parallel}$ unchanged, slight increase in $\epsilon_{\perp}$	$\epsilon_{\parallel}$ reduced, $\epsilon_{\perp}$ increased
Elastic Constants	K_{ii} unchanged	Erroneous K_{ii} due to pretilt

6.2 Future Research

The areas of future research are discussed in this section. Some of these topics of future research were originally planned to be conducted as part of the work for this thesis. However, due to the impact of COVID-19 and moving buildings, as discussed in greater detail in the impact statement, this work was unable to be completed within the time frame of the project and under the limitations imposed by COVID-19 restrictions and lab down time due to the building move.

6.2.1 Equivalent Circuit Modelling of LC Dielectric Spectroscopy Data

Part of the objective of using equivalent circuit modelling to analyse the dielectric spectra of filled and empty cells, was to be able to fit these models to the frequency dependent dielectric spectra. Equivalent circuit models for the empty as well as the filled cells could be fit to $C^*(\omega)$ and/or $Z^*(\omega)$. Rather than picking a specific frequency at which to take ϵ' at, the full frequency dependence of the filled and empty cells could be fit and the component values for C_0 and C_{LC} taken from the fitting results, which would then be, essentially frequency independent values. Thus, these values could be used to calculate ϵ_{LC} rather than picking single specific frequencies at which to take C_0 and C_{LC}.

This type of equivalent circuit fitting method would enable one to accurately and effectively determine the true ϵ_{LC} value of materials with a high concentration of ionic impurities leading to high frequency EP/IP which masks the plateau of ϵ_{LC}. Additionally, fitting of LC dielectric spectra could also be used to determine LC conductivities with greater ease and even fit for relaxation process such as the gold-stone relaxation mode in ferroelectric LCs.

6.2.2 Further Investigation into the Effects of QD Surface Functionalisation

In this work, the use of side-on mesogenic and alkyl chain QD surface functionalisation were compared in terms of their effects on the phase behaviour and physical properties of the QD-LC nanocomposites. However, only one type of side-on mesogenic surface functionalisation was used, in which the flexible alkyl linker was found to be of a sufficient length to enable the mesogenic groups to orient with **n** of the host LC. One area to be investigated further, would be the effect of the length of this alkyl linker.

It is expected that there would be a threshold length, below which, the mesogenic groups are no longer able to align freely with the host **n**. The use of short alkyl linkers could prevent the reorientation of the mesogenic groups, and would likely lead to planar anchoring of the host LC at the QD surface. Planar anchoring, similarly to HT anchoring, as seen with the alkyl chain QD functionalisation, should lead to a reduction in order of the nanocomposites compared to the pure LC and nanocomposites using side-on mesogenic surface functionalisation with longer alkyl linkers. Thus, an investigation into this alkyl linker length would be beneficial to further understand how mesogenic surface functionalisation of nanomaterials can be implemented in order to tune the properties and behaviour of LC nanocomposites.

It was shown here, that the self-assembly of QD micro-structures is strongly dependent upon the surface functionalisation used. With the disordering alkyl chain functionalisation preventing hollow QD micro-structure formation and the order preserving side-on mesogenic functionalisation enabling hollow QD micro-structure formation. By using a combination of disordering and order preserving QD surface functionalisation, it could be possible to further tune the phase transition driven self-assembly process. At present, it has only been shown that the outer diameter of the hollow QD micro-structures is determined by both the cooling rate and QD concentration in the nanocomposites. Once the second stage of nematic nucleation takes place, the outer diameter of the hollow micro-structures is fixed and as cooling continues, only the inner diameter grows.

It is therefore proposed, that by incorporating a mixture of disordering and order preserving QD surface functionalisation, where a mixture of some side-on mesogenic functionalised QD and some alkyl chain functionalised QD is used, the onset of the second stage of nematic nucleation could be delayed due to the reduction in T_{NI} within the isotropic regions from the disordering QD. This could enable the formation of smaller QD micro-structures at slower, more convenient and controllable cooling rates as well as possibly being able to tune the ratio of the inner to outer diameters of the hollow micro-structures.

6.2.3 QD Defect Confinement in Zenithal Bistable Devices

The work discussed in this section was originally planned as part of this thesis, however, due to the constraints imposed by the COVID-19 restrictions, was unable to carried out as planned, as discussed in the COVID-19 impact statement. A zenithal bistable device (ZBD) uses a surface relief grating to align an NLC in either one of two stable states that can be switched between by applying a bipolar voltage pulse [196]. The grating surface homeotropically anchors the LC and in the continuous (C) state, the LC is oriented homeotropically through the device as shown in figure 6.1(a) [197]. The other stable state is the defect (D) state, which is stabilised by $+1/2$ and $-1/2$ disclinations situated at the troughs and peaks of the surface relief grating, with the director in the planar oriented as shown in figure 6.1(c). By applying a negative then positive voltage pulse, the C state can be switched into the D state and vice versa, as can be seen in figure 6.1(b).

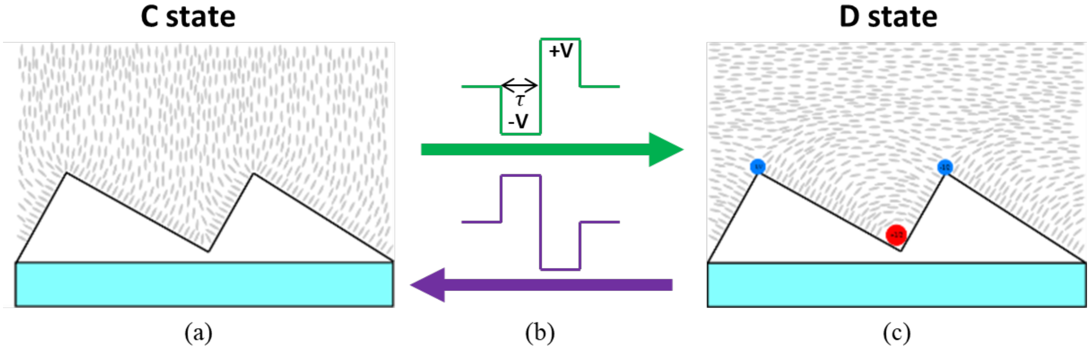

Figure 6.1: Schematic diagram of a ZBD in a) the C state which can be switched by applying b) a bipolar voltage pulse into c) the D state. The blue and red circles situated at the peaks and troughs of the surface relief grating represent the $-1/2$ and $+1/2$ disclinations respectively.

Dispersion of Indium Phosphide Zinc Sulphide (InP/ZnS) core shell QD into a host LC to form a QD-LC nanocomposite has previously shown QD self-assembly into disclinations when filled into a ZBD [198], as shown in figure 6.2(b). Using Stochastic Optical Reconstruction Microscopy, the fluorescence image shown in 6.2(a) was reconstructed to give the resolved image shown in 6.2(b). By measurement of the distance between the fluorescent lines where the QD are confined, it was found that the QD self-assembled into the the $+1/2$ disclinations at the troughs of the surface relief grating but not in the $-1/2$ disclinations at the peaks of the surface relief grating as shown schematically in figures 6.2(c) and 6.2(d).

The self-assembly of nanomaterials into defects is well known and was discussed in chapter 1 section1.3.4. Less well known, however, is how the surface functionalisation of the nanomaterials affects this self-assembly process. For instance, does the efficiency of trapping within defects depend on the type of surface functionalisation used and if so how/why? Additionally, if the surface functionalisation does have an effect on the trapping efficiency, does the efficiency change depending on the type of defect? By using a ZBD filled with QD-LC nanocomposites using side-on mesogenic and alkyl chain functionalisation, these questions could potentially be answered as within the same device, both $+1/2$ and $-1/2$ disclinations can be reliably formed and can be switched between states with and without them.

An alternative motive to further investigate QD trapping in defects using ZBD is to potentially improve the performance of reflective ZBD displays. Commercial reflective ZBD displays are used as a low-power solution for readily adaptable labels. However, one of the issues with these types of reflective displays is their contrast ratio between the bright and dark states, which in the case of ZBD corresponds to the D and C states respectively. Thus, if a QD-LC nanocomposite could be filled into a ZBD such that the QD reside in the D state areas in much higher concentrations than the C state areas as they are confined to the defects, then this could be used to improve the contrast ratio of the display, particularly by tuning the size of the QD to absorb and fluoresce at the appropriate wavelengths. This, however, relies on a high enough QD concentration in the nanocomposite without significantly affecting the material properties of the host LC, which are of paramount importance for the correct function and optimum performance of ZBD [199, 200].

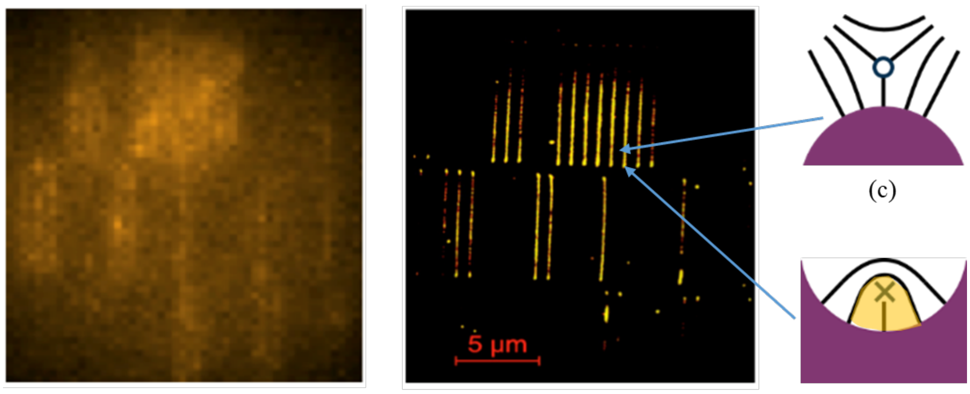

(a) (b) (c) (d)

Figure 6.2: ZBD filled with InP/ZnS QD-LC nanocomposite a) fluorescence image showing regions of lower and higher fluorescence intensity corresponding to areas of higher and lower QD concentration in regions of predominantly C or D state respectively. b) shows the resolved STORM image of the same area where lines highly fluorescent lines of QD can be seen. The regions between the highly fluorescent lines correspond to the c) $-1/2$ disclinations and the highly fluorescent lines correspond to the d) $+1/2$ disclinations where the QD are confined [198].

6.2.4 Light Scattering Measurements of LC Nanocomposites

Light scattering (LS) measurements of QD-LC nanocomposites were performed during this project. However, the systematic study into the surface functionalisation effects using this technique which was originally planned was unable to be carried out in full due to the constraints imposed through COVID-19 and moving buildings, as discussed in the impact statement. Thus, only some of the preliminary work was performed during this project. Therefore, only a discussion of how LS techniques could be used to study LC nanocomposites is given.

To characterise NP size, a range of techniques such as transmission or scanning electron microscopy (TEM or SEM) and atomic force microscopy (AFM), as well spectroscopic techniques which can be used for specific types of NPs such as fluorescence spectroscopy for QDs (as already discussed in this thesis) and optical extinction spectroscopy for metallic NPs exhibiting surface plasmon resonance. The appropriate choice of technique/s should be determined by the type of sample and characterisation required, a number of articles discuss this and the integration of multiple techniques in detail [201, 202, 203]. TEM, SEM and AFM are capable of sizing individual NPs and even resolving individual NPs within aggregates as well as deducing the shape of the NPs/NP aggregates, but must be performed with the sample deposited onto a substrate.

Spectroscopic and LS techniques on the other hand, are ensemble methods, providing information about the population of NPs dispersed in a suitable solvent. LS techniques can be used to determine the average size and size distribution of particles dispersed in a solvent, provided the dielectric constants and thus the refractive index of the particles and the surrounding solvent differ enough to produce a measurable scattering effect. For a more detailed discussion of the specific attributes of LS techniques and the development of their application, see the review articles [204, 205]. Depending on the particle sizes, either static light scattering (SLS) or dynamic light scattering (DLS) may be more effective. For colloidal dispersions, with larger μm scale particles, SLS is generally used due to the angular dependence of the scattered intensity. DLS, however, is capable of determining the size of much smaller nm scale particles [206] and even sub nm sized particles [207].

Since LS techniques acquire data from an ensemble of particles, the concentration of a dispersion can subsequently have an effect on the measurements, thus, it is necessary to control the concentration of particles in the dispersion. Too few particles and the resulting scattering will be too weak, whereas too many particles will result in particle interactions and multiple scattering[208][209], requiring further measures to be taken in order to account for, or suppress these effects [210][211]. To study both the size and size distribution of individual NPs and NP aggregates over time, a combination of SLS and DLS can be used [212]. The hetero-aggregation kinetics of an NP dispersion consisting of two types of NPs has also been studied through the use of DLS in combination with zeta potential measurements and imaging of the formed aggregates performed with TEM and SEM [213].

In NLCs, the long range nematic ordering leads to the optical anisotropy, which in an unaligned sample leads to the formation of nematic domains. In each of these nematic domains, **n** can be oriented in differently, leading to changes in the effective refractive index experienced by light passing from one domain to the other, causing significant scattering. To avoid this, the LC must be uniformly aligned as is the case in aligned LC test cells. Due to orientational fluctuations of **n**, still lead to changes in the refractive index and thus produce a measurable scattering effect. By using DLS, the timescales of these fluctuations can be measured and through careful choice of the scattering geometry, it is possible to decouple the different modes of orientational fluctuations to study orientational dynamics [214] and determine the different viscoelastic ratios of the LC[215].

Thus through the use of DLS it is therefore possible to study the different relaxation modes in LCs, such as the splay and twist modes [216], determine the three Miesowicz viscosities as well as the isotropic viscosity of 5CB [13] and even determine anchoring strengths of LCs in aligned cells [217][218]. Since each of the different relaxation modes has their own characteristic timescale, the intensity correlation function for each of these modes individually is exponential. In a polydomain sample, however, due to the change in scattering geometry between the nematic domains, a mix of the different modes is measured and thus the intensity correlation function is non-exponential [219]. Thus, a stretched exponential can instead be used to model the intensity correlation function of a polydomain LC sample.

The resulting intensity correlation function for polydomain 5CB was shown by Mertelj and Čopič to be non-exponential [219]. They developed a theoretical model for the correlation function based on a range of director orientations in the different domains which were assumed to have a small enough size such that polarisation changes through the domains could be neglected. The model agreed well with experimental data as well as a stretched exponential function with a stretching exponent of 0.8. The same group also went on to further study orientational dynamics in NLCs [214] well as the anchoring of 5CB at substrate surfaces in planar aligned LC cells [217][218].

Thus, the use of LS techniques could be a powerful tool to study both the effects of nanomaterials on the properties of the LC in the nanocomposites, as well as study the time evolution of aggregation/self-assembly behaviour of NPs in NLCs. This could help to further characterise the role of nanomaterial surface functionalisation for both tuning the properties of the LC nanocomposites and controlling the aggregation/self-assembly of NPs. Through characterisation of the elastic properties of the pure LC and LC nanocomposites, using for example dielectric spectroscopy as presented in chapter 5, it is possible to determine if nanomaterial doping of the LC causes changes to the viscosities compared to the pure LC.

References

[1] P.-G. De Gennes and J. Prost, “The physics of liquid crystals,” 1993.

[2] G. W. Gray, *Molecular structure and the properties of liquid crystals.* Academic Press, 1962.

[3] J. Goodby and S. J. Cowling, “Conception, Discovery, Invention, Serendipity and Consortia: Cyanobiphenyls and Beyond,” *Crystals*, vol. 12, 6 2022.

[4] G. W. Gray, K. J. Harrison, and J. A. Nash, “New family of nematic liquid crystals for displays,” *Electronics Letters*, vol. 9, no. 6, pp. 130–131, 1973.

[5] A. Saupe, “Recent Results in the Field of Liquid Crystals,” *Angewandte Chemie International Edition in English*, vol. 7, pp. 97–112, 2 1968.

[6] A. D. Buckingham, “Angular Correlation in Liquids,” *Discussions of the Faraday Society*, vol. 43, pp. 205–211, 1967.

[7] G. R. Luckhurst and C. Zannoni, “Why is the Maier-Saupe theory of nematic liquid crystals so successful?,” *Nature*, vol. 267, pp. 412–414, 1977.

[8] I. Haller, “Thermodynamic and static properties of liquid crytsals,” *Progress in Solid-State Chemistry*, vol. 10, pp. 103–118, 1975.

[9] P. Sherrell, D. Crellin, P. L. Sherrell, and D. A. Crellin, “Susceptibilities and Order Parameters of Nematic Liquid Crystals,” *Journal de Physique Colloques*, vol. 40, pp. 211–216, 1979.

[10] R. G. Horn, “Refractive Indices and Order Parameters of Two Liquid Crystals,” *Journal de Physique*, vol. 39, no. 1, pp. 105–109, 1978.

[11] C. J. Jones, “Lecture 9: Liquid Crystal Theories,” 2015.

[12] W. Maier and A. Saupe, “Eine einfache molekulare Theorie des nematischen kristallinflussigen Zustandes,” *Z. Naturforsch.*, vol. 13a, pp. 564–566, 1958.

[13] M. Cui and J. R. Kelly, “Temperature Dependence of Visco-Elastic Properties of 5CB,” *Molecular Crystals and Liquid Crystals Science and Technology Section A: Molecular Crystals and Liquid Crystals*, vol. 331, pp. 49–57, 1999.

[14] C. W. Oseen, “The theory of liquid crystals,” *Transactions of the Faraday Society*, vol. 29, pp. 883–899, 1 1933.

[15] F. C. Frank, “I. Liquid crystals: On the theory of liquid crystals,” *Discussions of the Faraday Society*, vol. 25, pp. 19–28, 1958.

[16] J. Nehring and A. Saupe, “On the Elastic Theory of Uniaxial Liquid Crystals,” *The Journal of Chemical Physics*, vol. 54, pp. 337–343, 2 2004.

[17] A. Saupe, “Disclinations and Properties of the Directorfield in Nematic and Cholesteric Liquid Crystals,” *Mol Cryst Liq Cryst*, vol. 21, no. 3-4, pp. 211–238, 1973.

[18] H. A. Lorentz, “Verh Kon Acad van Wetenschappen,” *Amsterdam.(1880) Ann Phys*, vol. 9, p. 641, 1879.

[19] R. Classius, *Die mechanische warmetheorie*, vol. 2. Vieweg, 1887.

[20] P. F. Mossotti, “Bibl Univ Modena 6: 193;(1850) Mem di matem e di fisica d soc Ital d scenze,” *Modena*, vol. 24, p. 49, 1847.

[21] L. Onsagbr, “Electric Moments of Molecules in Liquids,” *Journal of the American Chemical Society*, vol. 58, pp. 1486–1493, 8 1936.

[22] A. Schönhals and F. Kremer, *Theory of Dielectric Relaxation. In Broadband Dielectric Spectroscopy.* Berlin Heidelberg: Springer Berlin Heidelberg, 2003.

[23] K. S. Cole and R. H. Cole, “Dispersion and Absorption in Dielectrics I. Alternating Current Characteristics,” *The Journal of Chemical Physics*, vol. 9, pp. 341–351, 4 1941.

[24] D. W. Davidson and R. H. Cole, “Dispersion and Absorption in Dielectrics II,” *Alternating Current Characteristics The Journal of Chemical Physics*, vol. 18, p. 98, 1950.

[25] S. Havriliak and S. Negami, “A complex plane representation of dielectric and mechanical relaxation processes in some polymers,” *Polymer*, vol. 8, no. C, pp. 161–210, 1967.

[26] C. J. Jones, "Lecture 10: Electric Field Behaviour of Liquid Crystals," *PHYS5016M Soft Matter Physics: Liquid Crystals. University of Leeds*, pp. 4–6, 2015.

[27] M. F. Vuks, "Determination of the Optical Anisotropy of Aromatic Molecules from the Double Refraction of Crystals - NASA/ADS," *Optics and Spectroscopy*, vol. 20, p. 361, 4 1966.

[28] S. Chandrasekhar and N. Madhusudana, "Orientational order in p-azyoxyanisole, p-azoxyphenetole and their mixtures in the nematic phase," *Journal de Physique Colloques*, vol. 30, no. C4, 1969.

[29] K. R. Welford and J. R. Sambles, "Analysis of Electric Field Induced Deformations in a Nematic Liquid Crystal for any Applied Field," *Molecular Crystals and Liquid Crystals*, vol. 147, pp. 25–42, 1 1987.

[30] H. J. Deuling, "Deformation of Nematic Liquid Crystals in an Electric Field," *Mol Cryst Liq Cryst*, vol. 19, no. 2, pp. 123–131, 1972.

[31] R. H. Baughman, A. A. Zakhidov, and W. A. De Heer, "Carbon Nanotubes-the Route Toward Applications," *Science*, vol. 297, pp. 787–792, 2002.

[32] P. K. Jain, K. S. Lee, I. H. El-Sayed, and M. A. El-Sayed, "Calculated Absorption and Scattering Properties of Gold Nanoparticles of Different Size, Shape, and Composition: Applications in Biological Imaging and Biomedicine," *The journal of physical chemistry B*, vol. 110, pp. 7238–7248, 2006.

[33] S. Link and M. A. El-Sayed, "Size and Temperature Dependence of the Plasmon Absorption of Colloidal Gold Nanoparticles," *The Journal of Physical Chemistry B*, vol. 103, pp. 4212–4217, 1999.

[34] H. Chen, L. Shao, Q. Li, and J. Wang, "Gold nanorods and their plasmonic properties," *Chemical Society Reviews*, vol. 42, pp. 2679–2724, 3 2013.

[35] L. Dykman and N. Khlebtsov, "Gold nanoparticles in biomedical applications: recent advances and perspectives," *Chemical Society Reviews*, vol. 41, pp. 2256–2282, 2 2012.

[36] P. Ghosh, G. Han, M. De, C. K. Kim, and V. M. Rotello, "Gold nanoparticles in delivery applications," *Advanced Drug Delivery Reviews*, vol. 60, pp. 1307–1315, 8 2008.

[37] W. Lewandowski, M. Fruhnert, J. Mieczkowski, C. Rockstuhl, and E. Górecka, "Dynamically self-assembled silver nanoparticles as a thermally tunable metamaterial," *Nature Communications 2015 6:1*, vol. 6, pp. 1–9, 3 2015.

[38] J. Dintinger, S. Mühlig, C. Rockstuhl, T. Scharf, J. B. Pendry, A. J. Holden, D. J. Robbins, W. J. Stewart, S. Cai, U. K. Chettiar, H. K. Yuan, A. K. Sarychev, V. P. Drachev, and A. V. Kildishev, "A bottom-up approach to fabricate optical metamaterials by self-assembled metallic nanoparticles," *Optical Materials Express, Vol. 2, Issue 3, pp. 269-278*, vol. 2, pp. 269–278, 3 2012.

[39] K. Bi, Q. Wang, J. Xu, L. Chen, C. Lan, M. Lei, K. Bi, Q. Wang, J. Xu, L. Chen, C. Lan, and M. Lei, "All-Dielectric Metamaterial Fabrication Techniques," *Advanced Optical Materials*, vol. 9, p. 2001474, 1 2021.

[40] W. Wei, F. Bai, and H. Fan, "Oriented Gold Nanorod Arrays: Self-Assembly and Optoelectronic Applications," *Angewandte Chemie International Edition*, vol. 58, pp. 11956–11966, 8 2019.

[41] R. Griffith Freeman, K. C. Grabar, K. J. Allison, R. M. Bright, J. A. Davis, A. P. Guthrie, M. B. Hommer, M. A. Jackson, P. C. Smith, D. G. Walter, and M. J. Natan, "Self-AssembledMetalColloidMonolayers:AnApproachtoSERSSubstrates," *Science*, vol. 116, pp. 1629–1632, 1995.

[42] J. Kneipp, H. Kneipp, and K. Kneipp, "SERS—a single-molecule and nanoscale tool for bioanalytics," *Chemical Society Reviews*, vol. 37, pp. 1052–1060, 4 2008.

[43] X. M. Qian and S. M. Nie, "Single-molecule and single- nanoparticle SERS : from fundamental mechanisms to biomedical applications," *Chemical Society Reviews*, vol. 37, pp. 912–920, 4 2008.

[44] L. E. Brus, "Electron-electron and electron-hole interactions in small semiconductor crystallites: The size dependence of the lowest excited electronic state," *The Journal of Chemical Physics*, vol. 80, no. 9, pp. 4403–4409, 1984.

[45] L. Brus, "Electronic Wave Functions In Semiconductor Clusters: Experiment and Theory," *J. Phys. Chem*, vol. 90, pp. 2555–2560, 1986.

[46] Y. Shen and I. Dierking, “Perspectives in liquid-crystal-aided nanotechnology and nanoscience,” 6 2019.

[47] I. Dierking, G. Scalia, and P. Morales, “Liquid crystal-carbon nanotube dispersions,” *Journal of Applied Physics*, 2005.

[48] H. Qi and T. Hegmann, “Liquid crystal-gold nanoparticle composites,” *Liquid Crystals Today*, vol. 20, pp. 102–114, 10 2011.

[49] H. Qi, T. Hegmann, D. W. Bruce, J. W. Goodby, and J. R. Sambles, “Impact of nanoscale particles and carbon nanotubes on current and future generations of liquid crystal displays,” *Journal of Materials Chemistry*, vol. 18, no. 28, pp. 3288–3294, 2008.

[50] J. Mirzaei, M. Reznikov, and T. Hegmann, “Quantum dots as liquid crystal dopants,” *Journal of Materials Chemistry*, vol. 22, p. 22350, 10 2012.

[51] T. Hegmann, H. Qi, and V. M. Marx, “Nanoparticles in liquid crystals: Synthesis, self-assembly, defect formation and potential applications,” 2007.

[52] J. Mirzaei, T. Hegmann, . Springer, V. Berlin, O. Stamatoiu, J. Mirzaei, and X. Feng, “Nanoparticles in Liquid Crystals and Liquid Crystalline Nanoparticles,” *Top Curr Chem*, vol. 318, pp. 331–394, 2011.

[53] H. K. Bisoyi and S. Kumar, “Liquid-crystal nanoscience: An emerging avenue of soft self-assembly,” 1 2011.

[54] S. Singh, “Impact of Dispersion of Nanoscale Particles on the Properties of Nematic Liquid Crystals,” *Crystals*, vol. 9, p. 475, 9 2019.

[55] H. Stark, “Director field configurations around a spherical particle in a nematic liquid crystal,” *THE EUROPEAN PHYSICAL JOURNAL B*, vol. 10, pp. 311–321, 1999.

[56] P. Poulin and D. A. Weitz, “Inverted and multiple nematic emulsions,” *Physical Review E*, vol. 57, no. 1, pp. 626–637, 1998.

[57] T. C. Lubensky, D. Pettey, N. Currier, and H. Stark, “Topological defects and interactions in nematic emulsions,” *Physical Review E*, vol. 57, no. 1, pp. 610–625, 1998.

[58] P. Poulin, H. Stark, T. C. Lubensky, and D. A. Weitz, “Novel Colloidal Interactions in Anisotropic Fluids,” *Science*, vol. 275, pp. 1770–1773, 1997.

[59] Y. Gu and N. L. Abbott, “Observation of Saturn-Ring Defects around Solid Microspheres in Nematic Liquid Crystals,” *PHYSICAL REVIEW LETTERS*, vol. 85, no. 22, pp. 4719–4722, 2000.

[60] S. Ramaswamy, R. Nityananda, V. A. Raghunathan, and J. Prost, “Power-Law Forces Between Particles in a Nematic,” *Molecular Crystals and Liquid Crystals Science and Technology. Section A. Molecular Crystals and Liquid Crystals*, vol. 288, no. 1, pp. 175–180, 1996.

[61] M. Karabot and I. Muevi, “Direct observation of interaction of nanoparticles in a nematic liquid crystal,” *Soft Matter*, vol. 6, pp. 5476–5481, 11 2010.

[62] R. W. Ruhwandl and E. M. Terentjev, “Long-range forces and aggregation of colloid particles in a nematic liquid crystal,” *PHYSICAL REVIEW E*, vol. 55, no. 3, pp. 2958–2961, 1997.

[63] I. Musevic, M. Skarabot, U. Tkalec, M. Ravnik, and S. Zumer, “Two-Dimensional Nematic Colloidal Crystals Self-Assembledby Topological Defects,” *Science*, vol. 313, pp. 954–957, 8 2006.

[64] R. A. Drawhorn and N. L. Abbott, “Anchoring of Nematic Liquid Crystals on Self-Assembled Monolayers Formed from Alkanethiols on Semitransparent Films of Gold,” *J. Phys. Chem*, vol. 99, pp. 16511–16515, 1995.

[65] H. Qi, B. Kinkead, and T. Hegmann, “Effects of functionalized metal and semiconductor nanoparticles in nematic liquid crystal phases,” in *Emerging Liquid Crystal Technologies III*, vol. 6911, p. 691106, SPIE, 2 2008.

[66] B. Kinkead and T. Hegmann, “Effects of size, capping agent, and concentration of CdSe and CdTe quantum dots doped into a nematic liquid crystal on the optical and electro-optic properties of the final colloidal liquid crystal mixture,” *Journal of Materials Chemistry*, vol. 20, no. 3, pp. 448–458, 2010.

[67] M. F. Prodanov, N. V. Pogorelova, A. P. Kryshtal, A. S. Klymchenko, Y. Mely, V. P. Semynozhenko, A. I. Krivoshey, Y. A. Reznikov, S. N. Yarmolenko, J. W. Goodby, and V. V. Vashchenko, “Thermodynamically stable dispersions of quantum dots in a nematic liquid crystal,” *Langmuir*, vol. 29, pp. 9301–9309, 7 2013.

[68] M. Sultan Mahmud, I. Naydenova, V. Toal, H. Shiraki, S. Kundu, Y. Sakai, J. Thisayukta, T. Masumi, Y. Shiraishi, N. Toshima, and S. Kobayashi Ã, "Dielectric Properties of Frequency Modulation Twisted Nematic LCDs Doped with Silver Nanoparticles," *Japanese Journal of Applied Physics To*, vol. 43, p. 5430, 2004.

[69] S. Khatua, P. Manna, W. S. Chang, A. Tcherniak, E. Friedlander, E. R. Zubarev, and S. Link, "Plasmonic nanoparticles-liquid crystal composites," *Journal of Physical Chemistry C*, vol. 114, pp. 7251–7257, 4 2010.

[70] N. Nishida, Y. Shiraishi, S. Kobayashi, and N. Toshima, "Fabrication of liquid crystal sol containing capped Ag-Pd bimetallic nanoparticles and their electro-optic properties," *Journal of Physical Chemistry C*, vol. 112, no. 51, pp. 20284–20290, 2008.

[71] A. Lapanik, A. Rudzki, B. Kinkead, H. Qi, T. Hegmann, and W. Haase, "Electrooptical and dielectric properties of alkylthiol-capped gold nanoparticle –ferroelectric liquid crystal nanocomposites: influence of chain length and tethered liquid crystal functional groups," *Soft Matter*, vol. 8, pp. 8722–8728, 8 2012.

[72] J. Milette, V. Toader, L. Reven, and R. B. Lennox, "Tuning the miscibility of gold nanoparticles dispersed in liquid crystals via the thiol-for-DMAP reaction," *Journal of Materials Chemistry*, vol. 21, pp. 9043–9050, 7 2011.

[73] A. L. Rodarte, Z. S. Nuno, B. H. Cao, R. J. Pandolfi, M. T. Quint, S. Ghosh, J. E. Hein, and L. S. Hirst, "Tuning quantum-dot organization in liquid crystals for robust photonic applications," *ChemPhysChem*, vol. 15, pp. 1413–1421, 5 2014.

[74] A. Keshavarz, S. T. Riahinasab, L. S. Hirst, and B. J. Stokes, "New Promesogenic Ligands for Host Medium Microencapsulation by Quantum Dots via Liquid Crystal Phase Transition Templating," *Applied Nano Materials*, vol. 2, no. 4, pp. 2542–2547, 2019.

[75] S. Khatua, P. Manna, W. S. Chang, A. Tcherniak, E. Friedlander, E. R. Zubarev, and S. Link, "Plasmonic nanoparticles-liquid crystal composites," *Journal of Physical Chemistry C*, vol. 114, pp. 7251–7257, 4 2010.

[76] M. Kaczmarek, O. Buchnev, and I. Nandhakumar, "Ferroelectric nanoparticles in low refractive index liquid crystals for strong electro-optic response," *Applied Physics Letters*, vol. 92, no. 10, 2008.

[77] H. Yoshida, K. Kawamoto, H. Kubo, T. Tsuda, A. Fujii, S. Kuwabata, and M. Ozaki, "Nanoparticle-dispersed liquid crystals fabricated by sputter doping," *Advanced Materials*, vol. 22, pp. 622–626, 2 2010.

[78] S. Krishna Prasad, K. L. Sandhya, G. G. Nair, U. S. Hiremath, C. V. Yelamaggad, and S. Sampath, "Electrical conductivity and dielectric constant measurements of liquid crystal-gold nanoparticle composites," *Liquid Crystals*, vol. 33, pp. 1121–1125, 10 2006.

[79] L. M. Lopatina and J. V. Selinger, "Theory of Ferroelectric Nanoparticles in Nematic Liquid Crystals," *Physical Review Letters*, vol. 102, p. 197802, 2009.

[80] M. Gorkunov, M. Osipov, M. V. Gorkunov, and M. A. Osipov, "Mean-field theory of a nematic liquid crystal doped with anisotropic nanoparticles," *Soft Matter*, vol. 7, no. 9, pp. 4348–4356, 2011.

[81] H. Duran, B. Gazdecki, A. Yamashita, and T. Kyu, "Liquid Crystals Effect of carbon nanotubes on phase transitions of nematic liquid crystals Effect of carbon nanotubes on phase transitions of nematic liquid crystals," *Liquid Crystals*, vol. 32, no. 7, pp. 815–821, 2005.

[82] J. Mirzaei, M. Urbanski, K. Yu, H. S. Kitzerow, and T. Hegmann, "Nanocomposites of a nematic liquid crystal doped with magic-sized CdSe quantum dots," *Journal of Materials Chemistry*, vol. 21, pp. 12710–12716, 9 2011.

[83] F. Li, O. Buchnev, C. I. Cheon, A. Glushchenko, V. Reshetnyak, Y. Reznikov, T. J. Sluckin, and J. L. West, "Orientational coupling amplification in ferroelectric nematic colloids," *Physical Review Letters*, vol. 97, no. 14, 2006.

[84] J. F. Blach, S. Saitzek, C. Legrand, L. Dupont, J. F. Henninot, and M. Warenghem, "BaTiO3 ferroelectric nanoparticles dispersed in 5CB nematic liquid crystal: Synthesis and electro-optical characterization," *Journal of Applied Physics*, vol. 107, 4 2010.

[85] R. Manohar, S. P. Yadav, A. K. Srivastava, A. K. Misra, K. K. Pandey, P. K. Sharma, and A. C. Pandey, "Zinc oxide (1% Cu) Nanoparticle in nematic liquid crystal: Dielectric and electro-optical study," *Japanese Journal of Applied Physics*, vol. 48, no. 10 Part 1, pp. 1015011–1015016, 2009.

[86] R. K. Shukla, Y. G. Galyametdinov, R. R. Shamilov, and W. Haase, “Effect of CdSe quantum dots doping on the switching time, localised electric field and dielectric parameters of ferroelectric liquid crystal,” *Liquid Crystals*, vol. 41, pp. 1889–1896, 12 2014.

[87] E. A. Konshina, E. O. Gavrish, A. O. Orlova, and M. V. Artem’ev, “Effect of dispersed CdSe/ZnS quantum dots on optical and electrical characteristics of nematic liquid crystal cells,” *Technical Physics Letters*, vol. 37, pp. 1011–1014, 11 2011.

[88] C. J. Hsu, L. J. Lin, M. K. Huang, and C. Y. Huang, “Electro-optical effect of gold nanoparticle dispersed in nematic liquid crystals,” *Crystals*, vol. 7, no. 10, 2017.

[89] H. H. Elkhalgi, S. Khandka, U. B. Singh, K. L. Pandey, R. Dabrowski, and R. Dhar, “Dielectric and electro-optical properties of a nematic liquid crystalline material with gold nanoparticles,” *Liquid Crystals*, vol. 45, no. 12, 2018.

[90] U. B. Singh, R. Dhar, A. S. Pandey, S. Kumar, R. Dabrowski, and M. B. Pandey, “Electro-optical and dielectric properties of CdSe quantum dots and 6CHBT liquid crystals composites,” *AIP Advances*, vol. 4, p. 117112, 11 2014.

[91] T. Zhang, C. Zhong, and J. Xu, “CdS-Nanoparticle-doped liquid crystal displays showing low threshold voltage,” *Japanese Journal of Applied Physics*, vol. 48, pp. 0550021–0550026, 5 2009.

[92] P. Tripathi, R. Uttam, S. Kumar, R. Dabrowski, and R. Dhar, “Enhancement of the physical parameters due to the dispersion of functionalised gold nanoparticles in a room temperature nematic liquid crystal,” *Liquid Crystals*, pp. 1–9, 9 2022.

[93] S. J. Shivaraja, R. K. Gupta, S. Kumar, and V. Manjuladevi, “Effect of functionalised silver nanoparticle on the elastic constants and ionic transport of a nematic liquid crystal,” *Liquid Crystals*, vol. 46, pp. 1868–1876, 9 2019.

[94] S. Sridevi, S. K. Prasad, G. G. Nair, V. D’Britto, and B. L. Prasad, “Enhancement of anisotropic conductivity, elastic, and dielectric constants in a liquid crystal-gold nanorod system,” *Applied Physics Letters*, vol. 97, 10 2010.

[95] Y. Garbovskiy, I. Glushchenko, Y. Garbovskiy, and I. Glushchenko, “Nano-Objects and Ions in Liquid Crystals: Ion Trapping Effect and Related Phenomena,” *Crystals*, vol. 5, pp. 501–533, 11 2015.

[96] M. Urbanski and J. P. Lagerwall, “Why organically functionalized nanoparticles increase the electrical conductivity of nematic liquid crystal dispersions,” *Journal of Materials Chemistry C*, vol. 5, no. 34, pp. 8802–8809, 2017.

[97] M. Urbanski and J. P. F. Lagerwall, “Nanoparticles dispersed in liquid crystals: Impact on conductivity, low-frequency relaxation and electro-optical performance †,” *Journal of Materials Chemistry C*, vol. 4, no. 16, pp. 3485–3491, 2016.

[98] J. Mirzaei, M. Urbanski, H. S. Kitzerow, and T. Hegmann, “Hydrophobic gold nanoparticles via silane conjugation: chemically and thermally robust nanoparticles as dopants for nematic liquid crystals,” *Philosophical Transactions of the Royal Society A: Mathematical, Physical and Engineering Sciences*, vol. 371, 4 2013.

[99] H. Qi, B. Kinkead, V. M. Marx, H. R. Zhang, and T. Hegmann, “Miscibility and alignment effects of mixed monolayer cyanobiphenyl liquid-crystal-capped gold nanoparticles in nematic cyanobiphenyl liquid crystal hosts,” *ChemPhysChem*, vol. 10, pp. 1211–1218, 6 2009.

[100] H. Qi and T. Hegmann, “Formation of periodic stripe patterns in nematic liquid crystals doped with functionalized gold nanoparticles,” *Journal of Materials Chemistry*, vol. 16, pp. 4197–4205, 11 2006.

[101] M. Urbanski, B. Kinkead, T. Hegmann, and H. S. Kitzerow, “Director field of birefringent stripes in liquid crystal/nanoparticle dispersions,” *Liquid Crystals*, vol. 37, no. 9, pp. 1151–1156, 2010.

[102] H. Qi, B. Kinkead, and T. Hegmann, “Unprecedented dual alignment mode and freedericksz transition in planar nematic liquid crystal cells doped with gold nanoclusters,” *Advanced Functional Materials*, vol. 18, pp. 212–221, 1 2008.

[103] M. Reznikov, A. Sharma, and T. Hegmann, “Ink-Jet Printed Nanoparticle Alignment Layers: Easy Design and Fabrication of Patterned Alignment Layers for Nematic Liquid Crystals,” *Particle & Particle Systems Characterization*, vol. 31, no. 2, pp. 257–265, 2013.

[104] M. Urbanski, J. Mirzaei, T. Hegmann, and H. S. Kitzerow, “Nanoparticle Doping in Nematic Liquid Crystals: Distinction between Surface and Bulk Effects by Numerical Simulations,” *ChemPhysChem*, vol. 15, pp. 1395–1404, 5 2014.

[105] P. P, P. Malik, Supreet, A. Kumar, R. Castagna, and G. Singh, "Recent advances and future perspectives on nanoparticles-controlled alignment of liquid crystals for displays and other photonic devices," *Critical Reviews in Solid State and Materials Sciences*, pp. 1–36, 2 2022.

[106] D. Pires, J. B. Fleury, and Y. Galerne, "Colloid particles in the interaction field of a disclination line in a nematic phase," *Physical Review Letters*, vol. 98, 6 2007.

[107] J. B. Fleury, D. Pires, and Y. Galerne, "Self-Connected 3D architecture of microwires," *Physical Review Letters*, vol. 103, p. 267801, 12 2009.

[108] M. Škarabot, M. Ravnik, S. Žumer, U. Tkalec, I. Poberaj, D. Babič, and I. Muševič, "Hierarchical self-assembly of nematic colloidal superstructures," *Physical Review E - Statistical, Nonlinear, and Soft Matter Physics*, vol. 77, 6 2008.

[109] D. Coursault, J. Grand, B. Zappone, H. Ayeb, G. Lévi, N. Félidj, and E. Lacaze, "Linear self-assembly of nanoparticles within liquid crystal defect arrays," *Advanced Materials*, vol. 24, pp. 1461–1465, 3 2012.

[110] J. Milette, S. Relaix, C. Lavigne, V. Toader, S. J. Cowling, I. M. Saez, R. B. Lennox, J. W. Goodby, and L. Reven, "Reversible long-range patterning of gold nanoparticles by smectic liquid crystals," *Soft Matter*, vol. 8, pp. 6593–6598, 5 2012.

[111] I. Dierking, W. Blenkhorn, E. Credland, W. Drake, R. Kociuruba, B. Kayser, and T. Michael, "Stabilising liquid crystalline Blue Phases," *Soft Matter*, vol. 8, pp. 4355–4362, 3 2012.

[112] H. Yoshida, Y. Tanaka, K. Kawamoto, H. Kubo, T. Tsuda, A. Fujii, S. Kuwabata, H. Kikuchi, and M. Ozaki, "Nanoparticle-stabilized cholesteric blue phases," *Applied Physics Express*, vol. 2, 12 2009.

[113] E. Karatairi, B. Rozic, Z. Kutnjak, V. Tzitzios, G. Nounesis, G. Cordoyiannis, J. Thoen, C. Glorieux, and S. Kralj, "Nanoparticle-induced widening of the temperature range of liquid-crystalline blue phases," *Physical Review E*, vol. 81, 4 2010.

[114] B. Rozic, V. Tzitzios, E. Karatairi, U. Tkalec, G. Nounesis, Z. Kutnjak, G. Cordoyiannis, R. Rosso, E. G. Virga, I. Musevic, and S. Kralj, "Theoretical and experimental study of

the nanoparticle-driven blue phase stabilisation," *European Physical Journal E*, vol. 34, no. 2, 2011.

[115] A. Gudimalla, M. Lavric, M. Trcek, S. Harkai, B. Rozic, G. Cordoyiannis, S. Thomas, K. Pal, Z. Kutnjak, and S. Kralj, "Nanoparticle-Stabilized Lattices of Topological Defects in Liquid Crystals," *International Journal of Thermophysics*, vol. 41, no. 4, pp. 1–25, 2020.

[116] M. A. Gharbi, S. Manet, J. Lhermitte, S. Brown, J. Milette, V. Toader, M. Sutton, and L. Reven, "Reversible Nanoparticle Cubic Lattices in Blue Phase Liquid Crystals," *ACS nano*, vol. 10, no. 3, pp. 3410–3415, 2016.

[117] K. Higashiguchi, K. Yasui, M. Ozawa, K. Odoi, and H. Kikuchi, "Spatial distribution control of polymer nanoparticles by liquid crystal disclinations," *Polymer Journal*, vol. 44, pp. 632–638, 6 2012.

[118] X. Wang, D. S. Miller, E. Bukusoglu, J. J. De Pablo, and N. L. Abbott, "Topological defects in liquid crystals as templates for molecular self-assembly," *Nature Materials*, vol. 15, pp. 106–112, 1 2016.

[119] G. M. Koenig, R. Ong, A. D. Cortes, J. A. Moreno-Razo, J. J. De Pablo, and N. L. Abbott, "Single nanoparticle tracking reveals influence of chemical functionality of nanoparticles on local ordering of liquid crystals and nanoparticle diffusion coefficients," *Nano Letters*, vol. 9, pp. 2794–2801, 7 2009.

[120] J.-I. Fukuda, H. Stark, and H. Yokoyama, "Friction drag of a spherical particle in a liquid crystal above the isotropic-nematic transition," *Physical Review E*, vol. 72, no. 2, p. 021701, 2005.

[121] S. Carlotto and A. Polimeno, "Evaluation of translational friction coefficients of macroscopic probes in nematic liquid crystals," *The Journal of Chemical Physics*, vol. 128, p. 154505, 4 2008.

[122] M. Škarabot, M. Ravnik, S. Žumer, U. Tkalec, I. Poberaj, D. Babič, N. Osterman, and I. Muševič, "Interactions of quadrupolar nematic colloids," *Physical Review E - Statistical, Nonlinear, and Soft Matter Physics*, vol. 77, 3 2008.

[123] M. A. Osipov and M. V. Gorkunov, "Molecular theory of phase separation in nematic liquid crystals doped with spherical nanoparticles," *ChemPhysChem*, vol. 15, pp. 1496–1501, 5 2014.

[124] M. V. Gorkunov, G. A. Shandryuk, A. M. Shatalova, I. Y. Kutergina, A. S. Merekalov, Y. V. Kudryavtsev, R. V. Talroze, and M. A. Osipov, "Phase separation effects and the nematic-isotropic transition in polymer and low molecular weight liquid crystals doped with nanoparticles," *Soft Matter*, vol. 9, pp. 3578–3588, 4 2013.

[125] J. Milette, S. J. Cowling, V. Toader, C. Lavigne, I. M. Saez, R. Bruce Lennox, J. W. Goodby, and L. Reven, "Reversible long range network formation in gold nanoparticle - nematic liquid crystal composites," *Soft Matter*, vol. 8, pp. 173–179, 12 2011.

[126] S. T. Riahinasab, A. Keshavarz, C. N. Melton, A. Elbaradei, G. I. Warren, R. L. Selinger, B. J. Stokes, and L. S. Hirst, "Nanoparticle-based hollow microstructures formed by two-stage nematic nucleation and phase separation," *Nature Communications*, vol. 10, 12 2019.

[127] N. Atzin, O. Guzmán, O. Gutiérrez, L. S. Hirst, and S. Ghosh, "Free-energy model for nanoparticle self-assembly by liquid crystal sorting," *Physical Review E*, vol. 97, 6 2018.

[128] A. L. Rodarte, R. J. Pandolfi, S. Ghosh, and L. S. Hirst, "Quantum dot/liquid crystal composite materials: Self-assembly driven by liquid crystal phase transition templating," *Journal of Materials Chemistry C*, vol. 1, pp. 5527–5532, 9 2013.

[129] D. Meyerhofer, "Characteristics of resist films produced by spinning," *Journal of Applied Physics*, vol. 49, no. 7, pp. 3993–3997, 1978.

[130] L. E. Scriven, "Physics and Applications of DIP Coating and Spin Coating," *MRS Proceedings*, vol. 121, p. 717, 2 1988.

[131] E. W. Greenfield, "Application of guard electrodes in dielectric measurements," *Review of Scientific Instruments*, vol. 13, no. 11, pp. 489–492, 1942.

[132] J. Hoogboom, T. Rasing, A. E. Rowan, and R. J. Nolte, "LCD alignment layers. Controlling nematic domain properties," *Journal of Materials Chemistry*, vol. 16, pp. 1305–1314, 2006.

[133] M. Behdani, A. Rastegar, S. H. Keshmiri, S. I. Missat, E. Vlieg, and T. Rasing, “Submicron liquid crystal pixels on a nanopatterned indium tin oxide surface,” *Applied Physics Letters*, vol. 80, pp. 4635–4637, 6 2002.

[134] M. Behdani, S. H. Keshmiri, S. Soria, M. A. Bader, J. Ihlemann, G. Marowsky, and T. Rasing, “Alignment of liquid crystals with periodic submicron structures ablated in polymeric and indium tin oxide surfaces,” *Applied Physics Letters*, vol. 82, pp. 2553–2555, 4 2003.

[135] B. F. Macdonald, W. Zheng, and R. J. Cole, “Reflection anisotropy spectroscopy: A probe of rubbed polyimide liquid crystal alignment layers,” *Journal of Applied Physics*, vol. 93, pp. 4442–4446, 4 2003.

[136] N. A. J. M. Van Aerie and A. J. W. Tol, “Molecular Orientation in Rubbed Polyimide Alignment Layers Used for Liquid-Crystal Displays,” *Macromolecules*, vol. 27, pp. 6520–6526, 1994.

[137] J. Stöhr and M. Samant, “Liquid crystal alignment by rubbed polymer surfaces: a microscopic bond orientation model,” *Journal of Electron Spectroscopy and Related Phenomena*, vol. 98-99, pp. 189–207, 7 2002.

[138] S. W. Lee, B. Chae, H. C. Kim, B. Lee, W. Choi, S. B. Kim, T. Chang, and M. Ree, “New Clues to the Factors Governing the Perpendicular Alignment of Liquid Crystals on Rubbed Polystyrene Film Surfaces,” *Langmuir*, vol. 19, pp. 8735–8743, 10 2003.

[139] M. KACZMAREK and A. DYADYUSHA, “STRUCTURED, PHOTOSENSITIVE PVK AND PVCN POLYMER LAYERS FOR CONTROL OF LIQUID CRYSTAL ALIGNMENT,” *Journal of Nonlinear Optical Physics & Materials*, vol. 12, pp. 547–555, 1 2004.

[140] Y. D. Chen, A. Y. G. Fuh, C. K. Liu, and K. T. Cheng, “Radial liquid crystal alignment based on circular rubbing of a substrate coated with poly(N-vinyl carbazole) film,” *Journal of Physics D: Applied Physics*, vol. 44, 6 2011.

[141] F. Bruyneel, “Method for measuring the cell gap in liquid-crystal displays,” *Optical Engineering*, vol. 40, p. 259, 2 2001.

[142] K. B. Blodgett, “Use of Interference to Extinguish Reflection of Light from Glass,” *Physical Review*, vol. 55, pp. 391–404, 1939.

[143] Beer, "Bestimmung der Absorption des rothen Lichts in farbigen Flüssigkeiten," *Annalen der Physik*, vol. 162, pp. 78–88, 1 1852.

[144] D. Swinehart, "The Beer-Lambert Law," *Journal of chemical education*, vol. 39, no. 7, p. 333, 1962.

[145] Bruker, "DektakXT Stylus Profiler: 10th Generation Stylus Profiling System," 2022.

[146] Edinburgh Instruments, "FLS1000 User Guide," 1 2020.

[147] G. Höhne, J. L. McNaughton, W. Hemminger, H.-J. Flammersheim, and H.-J. Flammersheim, *Differential scanning calorimetry.* Springer Science & Business Media, 2003.

[148] J. S. Gwag, S. H. Lee, K. H. Park, W. S. Park, K. Y. Han, C. G. Jhun, T. H. Yoon, J. C. Kim, D. M. Song, and D. M. Shin, "Simple method for measuring the high pretilt angle of nematic liquid crystals," *Journal of Applied Physics*, vol. 93, pp. 4936–4938, 4 2003.

[149] J. Strutt, " XV. On the light from the sky, its polarization and colour ," *The London, Edinburgh, and Dublin Philosophical Magazine and Journal of Science*, vol. 41, pp. 107–120, 2 1871.

[150] M. Rubinstein and R. Colby, *Polymer Physics*, vol. 23. Oxford university press New York, 2003.

[151] H. Wiese and D. Horn, "Single-mode fibers in fiber-optic quasielastic light scattering: A study of the dynamics of concentrated latex dispersions," *The Journal of Chemical Physics*, vol. 94, p. 6429, 8 1998.

[152] M. Kaszuba, "The Measurement of Nanoparticles Using Photon Correlation Spectroscopy and Avalanche Photo Diodes," *Journal of Nanoparticle Research 1999 1:3*, vol. 1, no. 3, pp. 405–409, 1999.

[153] J. S. Behra, J. Mattsson, O. J. Cayre, E. S. J. Robles, H. Tang, and T. N. Hunter, "Characterization of Sodium Carboxymethyl Cellulose Aqueous Solutions to Support Complex Product Formulation: A Rheology and Light Scattering Study," *ACS Applied Polymer Materials*, vol. 1, pp. 344–358, 3 2019.

[154] S. W. Provencher, "A constrained regularization method for inverting data represented by linear algebraic or integral equations," *Computer Physics Communications*, vol. 27,

pp. 213–227, 9 1982.

[155] S. W. Provencher, "CONTIN: A general purpose constrained regularization program for inverting noisy linear algebraic and integral equations," *Computer Physics Communications*, vol. 27, pp. 229–242, 9 1982.

[156] I.-G. Marino, "RILT," 2007.

[157] H. Ayeb, S. Alaya, M. Derbali, L. Samet, J. Bennaceur, F. Jomni, and T. Soltani, "Dielectrical, electro-optical and textural studies of 5CB nematic liquid crystal doped with TiO2 and Cu-TiO2 nanoparticle," *Liquid Crystals*, vol. 48, no. 2, pp. 223–232, 2021.

[158] A. Kumar, "On the Dielectric and Splay Elastic Constants of Nematic Liquid Crystals With Positive Dielectric Anisotropy," *Mol. Cryst. Liq. Cryst*, vol. 575, no. 1, pp. 30–39, 2013.

[159] A. Sawada, Y. Nakazono, K. Tarumi, S. Naemura, K. TARUMIb, and S. NAEMURAa, "Complex Dielectric Constant of Liquid Crystal Materials Containing Ionic Impurities in Low Frequency Region," *Molecular Crystals and Liquid Crystals Science and Technology. Section A. Molecular Crystals and Liquid Crystals*, vol. 318, no. 1, pp. 22–242, 1998.

[160] M. R. Costa, R. A. C Altafim, and A. P. Mammana, "Ionic impurities in nematic liquid crystal displays," *Liquid Crystals*, vol. 28, no. 12, pp. 1779–1783, 2001.

[161] S. Naemura and A. Saivada, "Ionic conduction in nematic and smectic a liquid crystals," *Molecular Crystals and Liquid Crystals*, vol. 400, pp. 79–96, 2003.

[162] S. Dhara and N. V. Madhusudana, "Ionic contribution to the dielectric properties of a nematic liquid crystal in thin cells," *Journal of Applied Physics*, vol. 90, no. 7, pp. 3483–3488, 2001.

[163] A. Sawada, K. Tarumi, and S. Naemura, "Effects of electric double layer and space charge polarization by plural kinds of ions on complex dielectric constant of liquid crystal materials," *Japanese Journal of Applied Physics*, vol. 38, pp. 1418–1422, 1999.

[164] A. Sawada, A. Manabe, and S. Naemura, "Novel Characterization Method of Ions in Liquid Crystal Materials by Complex Dielectric Constant Measurements," *Japanese Journal of Applied Physics*, vol. 38, pp. 1423–1427, 1999.

[165] M. Iwamoto, “Maxwell-Wagner Effect,” in *Encyclopedia of nanotechnology*, pp. 1276–1285, Springer Dordrecht, The Netherlands, 2012.

[166] K. W. Wagner, “Erkl{\"a}rung der dielektrischen nachwirkungsvorg{\"a}nge auf grund maxwellscher vorstellungen,” *Archiv f{\"u}r Elektrotechnik*, vol. 2, no. 9, pp. 371–387, 1914.

[167] R. Sillars, “The properties of a dielectric containing semiconducting particles of various shapes,” *Journal of the Institution of Electrical Engineers*, vol. 80, no. 484, pp. 378–394, 1937.

[168] P. B. Ishai, M. S. Talary, A. Caduff, E. Levy, and Y. Feldman, “Electrode polarization in dielectric measurements: A review,” 2013.

[169] H. Jansson, R. Bergman, and J. Swenson, “Hidden Slow Dynamics in Water,” *Physical Review Letters*, vol. 104, no. 1, p. 017802, 2010.

[170] R. Richert, “Comment on "hidden slow dynamics in water",” *Physical Review Letters*, vol. 104, 6 2010.

[171] M. Samet, V. Levchenko, G. Boiteux, G. Seytre, A. Kallel, and A. Serghei, “Electrode polarization vs. Maxwell-Wagner-Sillars interfacial polarization in dielectric spectra of materials: Characteristic frequencies and scaling laws,” *The Journal of chemical physics*, vol. 142, no. 19, p. 194703, 2015.

[172] G. J. Brug, A. L. van den Eeden, M. Sluyters-Rehbach, and J. H. Sluyters, “The analysis of electrode impedances complicated by the presence of a constant phase element,” *Journal of Electroanalytical Chemistry*, vol. 176, no. 1-2, pp. 275–295, 1984.

[173] G. Láng and K. E. Heusler, “Remarks on the energetics of interfaces exhibiting constant phase element behaviour,” *Journal of Electroanalytical Chemistry*, vol. 457, no. 1-2, pp. 257–260, 1998.

[174] M. N. Kakaei, J. Neshati, and A. R. Rezaierod, “On the Extraction of the Effective Capacitance from Constant Phase Element Parameters,” *Protection of Metals and Physical Chemistry of Surfaces*, vol. 54, no. 3, pp. 548–556, 2018.

[175] S. Skale, V. Doleček, and M. Slemnik, "Substitution of the constant phase element by Warburg impedance for protective coatings," *Corrosion Science*, vol. 49, no. 3, pp. 1045–1055, 2007.

[176] M. G. Clark, E. P. Raynes, R. A. Smith, and R. J. Tough, "Measurement of the permittivity of nematic liquid crystals in magnetic and electric fields using extrapolation procedures," *Journal of Physics D: Applied Physics*, vol. 13, no. 11, pp. 2151–2164, 1980.

[177] R. J. Tough and E. P. Raynes, "Capacitance response of a homogeneous parallel aligned nematic sample to electric and magnetic fields," *Molecular crystals and liquid crystals*, vol. 56 (Letters), no. 1, pp. 19–24, 1979.

[178] M. J. Bradshaw, *Physical properties of nematic liquid crystals.* PhD thesis, University of Exeter, 1984.

[179] J. C. Jones, *Handbook of optoelectronics.* CRC Press, 2017.

[180] C. Giansante and I. Infante, "Surface Traps in Colloidal Quantum Dots: A Combined Experimental and Theoretical Perspective," *Journal of Physical Chemistry Letters*, vol. 8, pp. 5209–5215, 10 2017.

[181] A. Veamatahau, B. Jiang, T. Seifert, S. Makuta, K. Latham, M. Kanehara, T. Teranishi, and Y. Tachibana, "Origin of surface trap states in CdS quantum dots: Relationship between size dependent photoluminescence and sulfur vacancy trap states," *Physical Chemistry Chemical Physics*, vol. 17, pp. 2850–2858, 1 2015.

[182] D. R. Baker and P. V. Kamat, "Tuning the emission of CdSe quantum dots by controlled trap enhancement," *Langmuir*, vol. 26, pp. 11272–11276, 7 2010.

[183] R. Xie, U. Kolb, J. Li, T. Basché, and A. Mews, "Synthesis and characterization of highly luminescent CdSe-core CdS/Zn 0.5Cd0.5S/ZnS multishell nanocrystals," *Journal of the American Chemical Society*, vol. 127, pp. 7480–7488, 5 2005.

[184] X. Peng, M. C. Schlamp, A. V. Kadavanich, and A. P. Alivisatos, "Epitaxial Growth of Highly Luminescent CdSe/CdS Core/Shell Nanocrystals with Photostability and Electronic Accessibility," *Journal of the American Chemical Society*, vol. 127, no. 20, pp. 7480–7488, 1997.

[185] T. H. Forster, "Transfer Mechanisms of Electronic Excitation," *Discussions of the Faraday Society*, vol. 27, pp. 7–17, 1959.

[186] O. I. Micic, K. M. Jones, A. Cahill, and A. J. Nozik, "Optical, Electronic, and Structural Properties of Uncoupled and Close-Packed Arrays of InP Quantum Dots," *J. Phys. Chem. B*, vol. 102, pp. 9791–9796, 1998.

[187] C. R. Kagan, C. B. Murray, M. Nirmal, and M. G. Bawendi, "Electronic Energy Transfer in CdSe Quantum Dot Solids," *Physical Review Letters*, vol. 76, no. 9, pp. 1517–1520, 1996.

[188] S. A. Crooker, J. A. Hollingsworth, S. Tretiak, and V. I. Klimov, "Spectrally Resolved Dynamics of Energy Transfer in Quantum-Dot Assemblies: Towards Engineered Energy Flows in Artificial Materials," *Physical Review Letters*, vol. 89, no. 18, p. 186802, 2002.

[189] T. Uematsu, H. Kitajima, T. Kohma, T. Torimoto, Y. Tachibana, and S. Kuwabata, "Tuning of the fluorescence wavelength of CdTe quantum dots with 2nm resolution by size-selective photoetching," *Nanotechnology*, vol. 20, no. 21, 2009.

[190] J. B. Sambur and B. A. Parkinson, "Size selective photoetching of CdSe quantum dot sensitizers on single-crystal TiO2," *ACS Applied Materials and Interfaces*, vol. 6, pp. 21916–21920, 12 2014.

[191] Y. Garbovskiy, "Kinetics of Ion-Capturing/Ion-Releasing Processes in Liquid Crystal Devices Utilizing Contaminated Nanoparticles and Alignment Films," *Nanomaterials*, vol. 8, no. 2, 2018.

[192] Y. Garbovskiy, "Ion capturing/ion releasing films and nanoparticles in liquid crystal devices," *Applied Physics Letters*, vol. 110, no. 4, 2017.

[193] Y. Garbovskiy, "Switching between purification and contamination regimes governed by the ionic purity of nanoparticles dispersed in liquid crystals," *Applied Physics Letters*, vol. 108, no. 12, 2016.

[194] Y. Garbovskiy, "Ions in liquid crystals doped with nanoparticles: conventional and counterintuitive temperature effects," 2017.

[195] D. A. Vakulin, D. A. Frenkel, E. O. Gavrish, and E. A. Konshina, “Impact of Doping CdSe/ZnS Quantum Dots on the Elasticity Coefficients of Nematic,” *Molecular Crystals and Liquid Crystals*, vol. 612, pp. 110–116, 5 2015.

[196] J. C. Jones, “The Zenithal Bistable Display: From concept to consumer,” *Journal of the Society for Information Display*, vol. 16, p. 143, 12 2007.

[197] S. A. Jones, J. Bailey, D. R. Walker, G. P. Bryan-Brown, and J. C. Jones, “Method for Tuneable Homeotropic Anchoring at Microstructures in Liquid Crystal Devices,” *Langmuir*, vol. 34, pp. 10865–10873, 9 2018.

[198] J. C. Jones and M. Nagaraj, “STORM images of InP/ZnS in ZBD - To be published.” 2017.

[199] J. C. Jones, S. Beldon, P. Brett, M. Francis, and M. Goulding, “26.3: Low Voltage Zenithal Bistable Devices with Wide Operating Windows,” *SID Symposium Digest of Technical Papers*, vol. 34, no. 1, p. 954, 2003.

[200] T. J. Spencer, C. M. Care, R. M. Amos, and J. C. Jones, “Zenithal bistable device: Comparison of modeling and experiment,” *Physical Review E - Statistical, Nonlinear, and Soft Matter Physics*, vol. 82, p. 021702, 8 2010.

[201] R. D. Boyd, S. K. Pichaimuthu, and A. Cuenat, “New approach to inter-technique comparisons for nanoparticle size measurements; using atomic force microscopy, nanoparticle tracking analysis and dynamic light scattering,” *Colloids and Surfaces A: Physicochemical and Engineering Aspects*, vol. 387, pp. 35–42, 8 2011.

[202] C. M. Hoo, N. Starostin, P. West, and M. L. Mecartney, “A comparison of atomic force microscopy (AFM) and dynamic light scattering (DLS) methods to characterize nanoparticle size distributions,” *Journal of Nanoparticle Research*, vol. 10, pp. 89–96, 12 2008.

[203] R. F. Domingos, M. A. Baalousha, Y. Ju-Nam, M. M. Reid, N. Tufenkji, J. R. Lead, G. G. Leppard, and K. J. Wilkinson, “Characterizing manufactured nanoparticles in the environment: Multimethod determination of particle sizes,” *Environmental Science and Technology*, vol. 43, pp. 7277–7284, 10 2009.

[204] S. K. Brar and M. Verma, “Measurement of nanoparticles by light-scattering techniques,” *TrAC Trends in Analytical Chemistry*, vol. 30, no. 1, pp. 4–17, 2011.

[205] R. Xu, “Progress in nanoparticles characterization: Sizing and zeta potential measurement,” *Particuology*, vol. 6, pp. 112–115, 4 2008.

[206] R. Pecora, “Dynamic light scattering measurement of nanometer particles in liquids,” *Journal of Nanoparticle Research*, vol. 2, pp. 123–131, 2000.

[207] M. Kaszuba, D. McKnight, M. T. Connah, F. K. McNeil-Watson, and U. Nobbmann, “Measuring sub nanometre sizes using dynamic light scattering,” *Journal of Nanoparticle Research*, vol. 10, pp. 823–829, 5 2008.

[208] F. Gruner and W. Lehmann, “Multiple scattering of light in a system ofinteracting Brownian particles,” *J. Phys. A: Math. Gen*, vol. 13, pp. 2155–2170, 1980.

[209] S. Fraden and G. Maret, “Multiple light scattering from concentrated, interacting suspensions,” *Physical Review Letters*, vol. 65, p. 512, 7 1990.

[210] K. Schatzel, M. Drewel, and J. Ahrens, “Suppression of multiple scattering in photon correlation spectroscopy,” *Journal of Physics: Condensed Matter*, vol. 2, p. SA393, 12 1990.

[211] P. N. Pusey, “Suppression of multiple scattering by photon cross-correlation techniques,” *Colloid & Interface Science*, vol. 4, pp. 177–185, 1999.

[212] Z. Meng, S. M. Hashmi, and M. Elimelech, “Aggregation rate and fractal dimension of fullerene nanoparticles via simultaneous multiangle static and dynamic light scattering measurement,” *Journal of Colloid and Interface Science*, vol. 392, pp. 27–33, 2 2013.

[213] P. Dušak, A. Mertelj, S. Kralj, and D. Makovec, “Controlled heteroaggregation of two types of nanoparticles in an aqueous suspension,” *Journal of Colloid and Interface Science*, vol. 438, pp. 235–243, 10 2014.

[214] A. Mertelj and M. Čopič, “Dynamic light scattering as a probe of orientational dynamics in confined liquid crystals,” *Physical Review E*, vol. 61, p. 1622, 2 2000.

[215] D. Langevin and M.-A. Bouchiat, “Anisotropy of the turbidity of an oriented nematic liquid crystal,” *Le Journal de Physique Colloques*, vol. 36, no. C1, p. C1–197, 1975.

[216] R. Borsali, D. Y. Yoon, and R. Pecora, “Determination of splay and twist relaxation modes in nematic liquid crystals from dynamic light scattering experiments,” *Journal of*

Physical Chemistry B, vol. 102, pp. 6337–6341, 8 1998.

[217] M. Vilfan, A. Mertelj, and M. Čopič, "Dynamic light scattering measurements of azimuthal and zenithal anchoring of nematic liquid crystals," *Physical Review E*, vol. 65, p. 041712, 4 2002.

[218] M. Vilfan and M. Copic, "Temperature dependence of azimuthal anchoring strength measured by dynamic light scattering," *Molecular Crystals and Liquid Crystals Science and Technology Section A: Molecular Crystals and Liquid Crystals*, vol. 375, no. 1, pp. 155–164, 2002.

[219] A. Mertelj and M. Čoplč, "Light scattering intensity correlation function in disordered nematic systems," *Molecular Crystals and Liquid Crystals Science and Technology Section A: Molecular Crystals and Liquid Crystals*, vol. 282, pp. 35–41, 1996.

Appendix A

Fluorescence Spectra

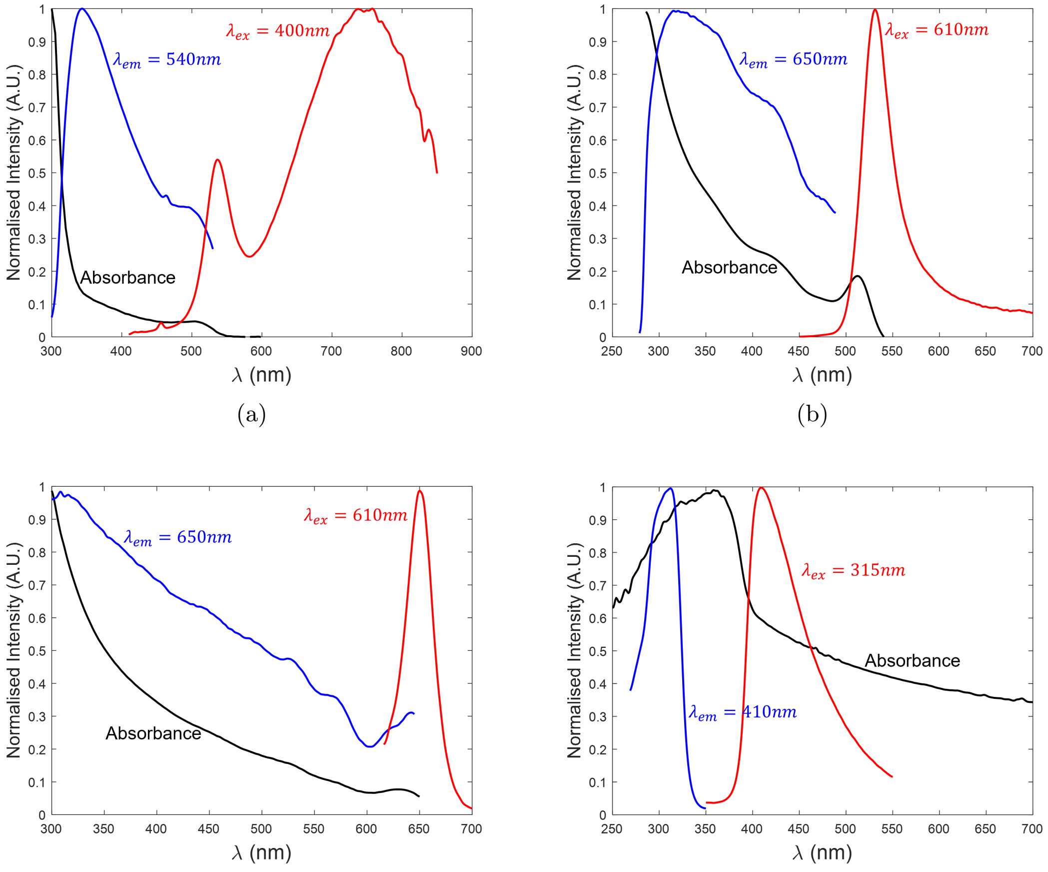

(a) (b)

(c) (d)

Figure A.1: Absorbance (black lines), fluorescence excitation (blue lines) and emission (red lines) spectra of a) LCQD, b) $ODA_{530}QD$ and c) $ODA_{650}QD$ in toluene as well as d) the pure LC MLC6204

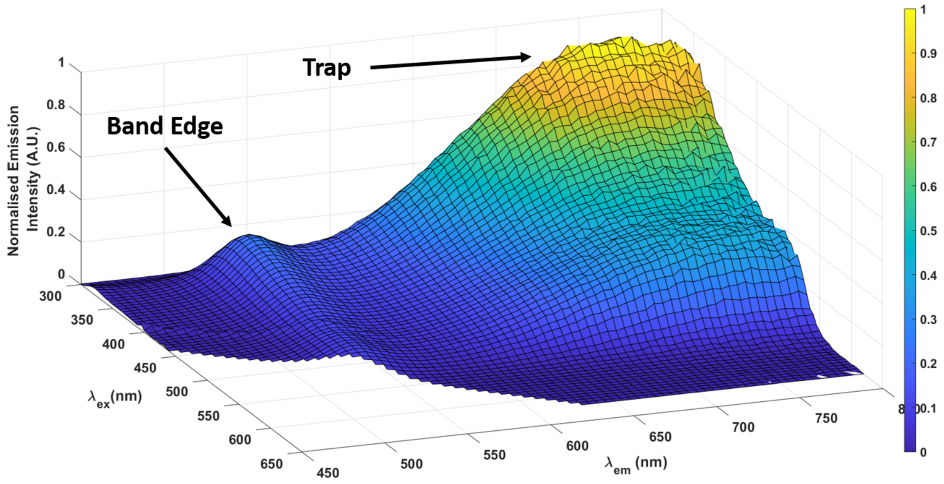

Figure A.2: Fluorescence emission map of LCQD in toluene showing both the main band edge emission peak at $\lambda_{em} \sim 537nm$ and the surface trap state emission at $\lambda \sim 745nm$ dependence on the excitation wavelength.

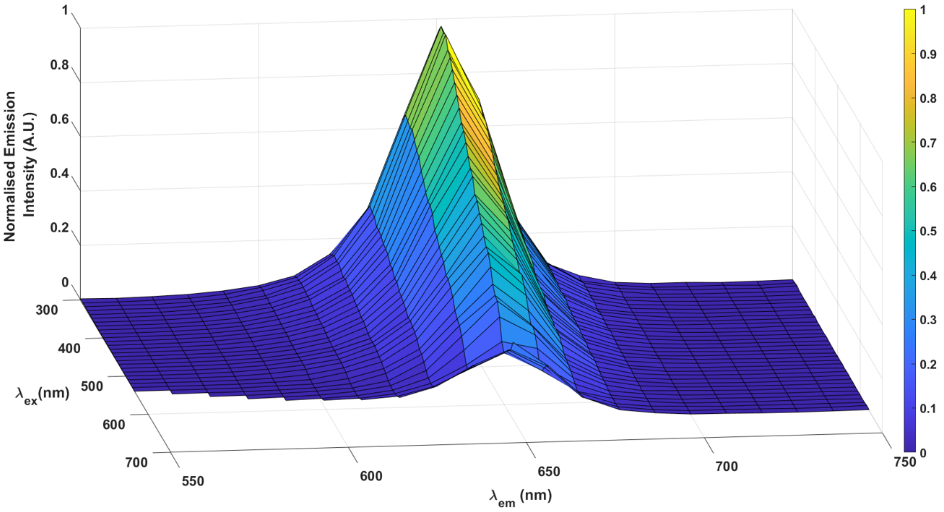

Figure A.3: Fluorescence emission map of ODA$_{650}$QD in toluene showing the single well defined emission peak at $\lambda \sim 650nm$ dependence on excitation wavelength.

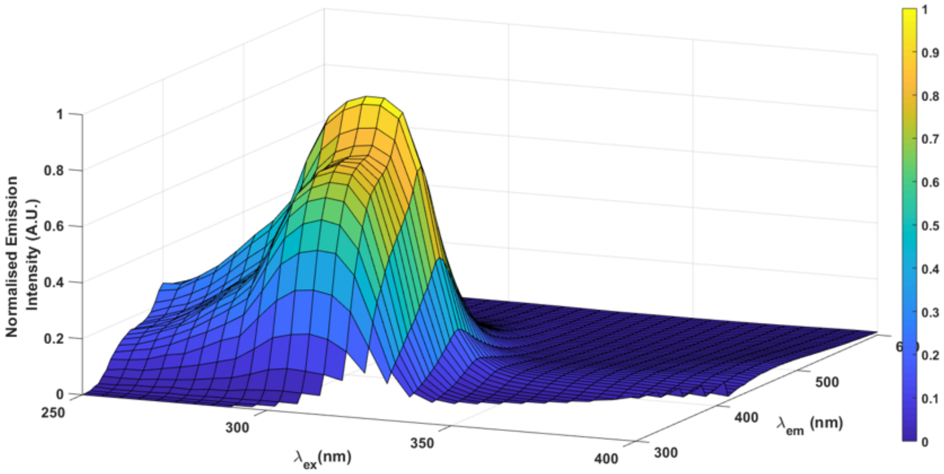

Figure A.4: Fluorescence emission map of the pure LC MLC6204.

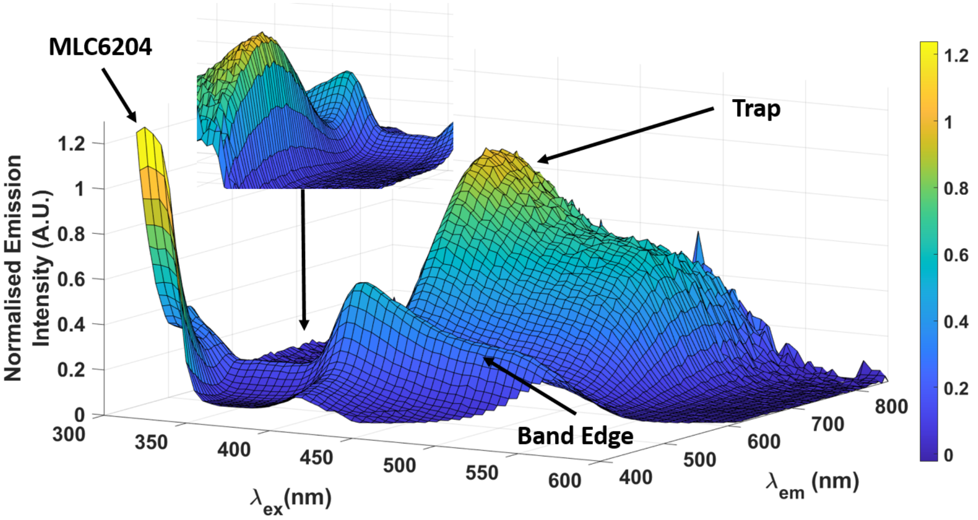

Figure A.5: Fluorescence emission map of LCQD in MLC6204 showing the reduced emission intensity at shorter excitation wavelengths due to the absorption of MLC6204. The tail end of the MLC6204 emission peak can also be seen in the left corner of the plot at short excitation and emission wavelengths.

Appendix B

QD-LC Dielectric Frequency Response

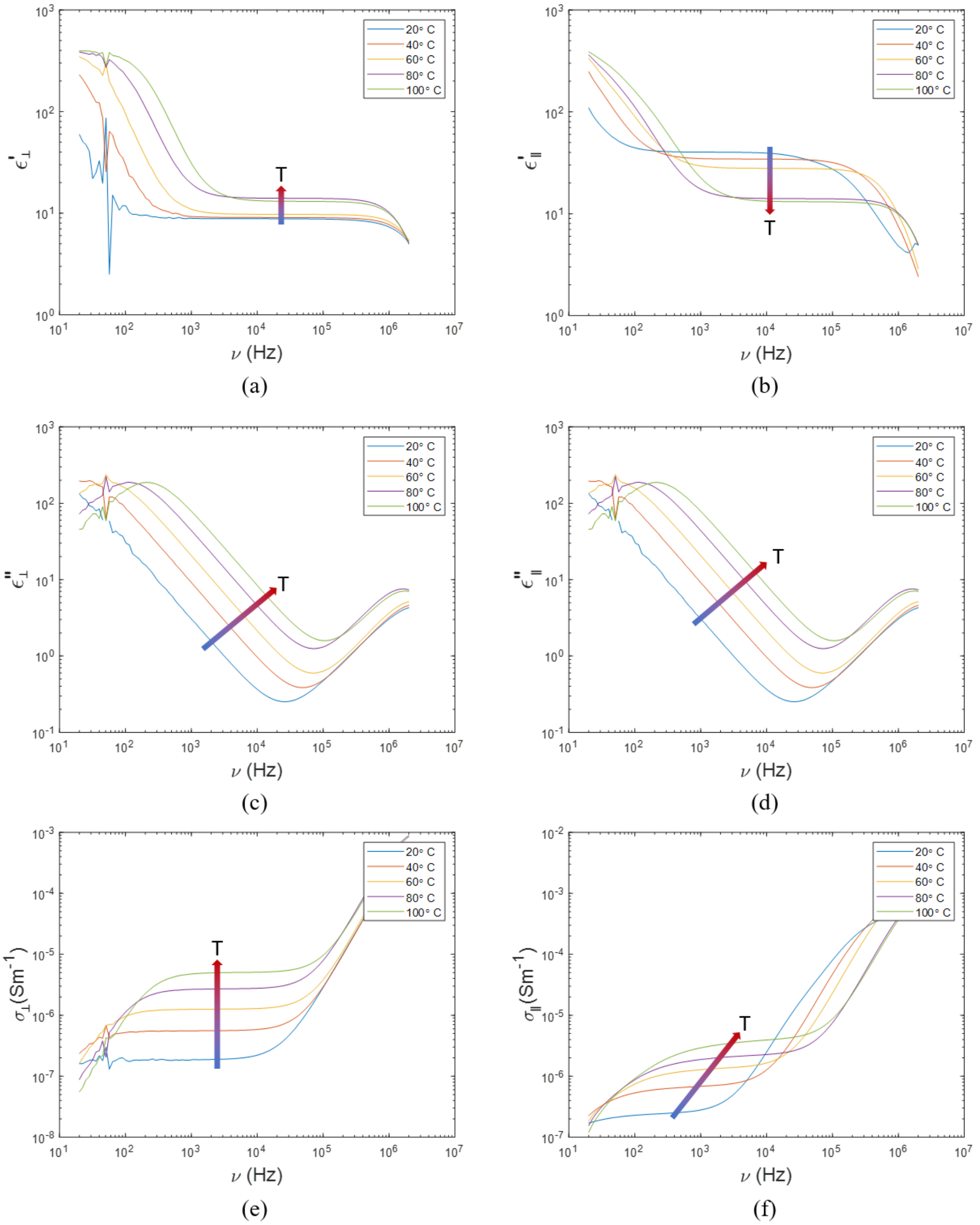

(a) (b) (c) (d) (e) (f)

Figure B.1: Dielectric spectroscopy frequency response of pure MLC6204. Real permittivity a) perpendicular and b) parallel to **n**, imaginary permittivity c) perpendicular and d) parallel to **n**, real conductivity e) perpendicular and f) parallel to **n**. $\epsilon_\perp$, $\sigma_\perp$ measured at $V = 0.05V_{rms}$ and $\epsilon_\parallel$, $\sigma_\parallel$ measured at $V = 20V_{rms}$ in a $20\mu m$ PH cell.

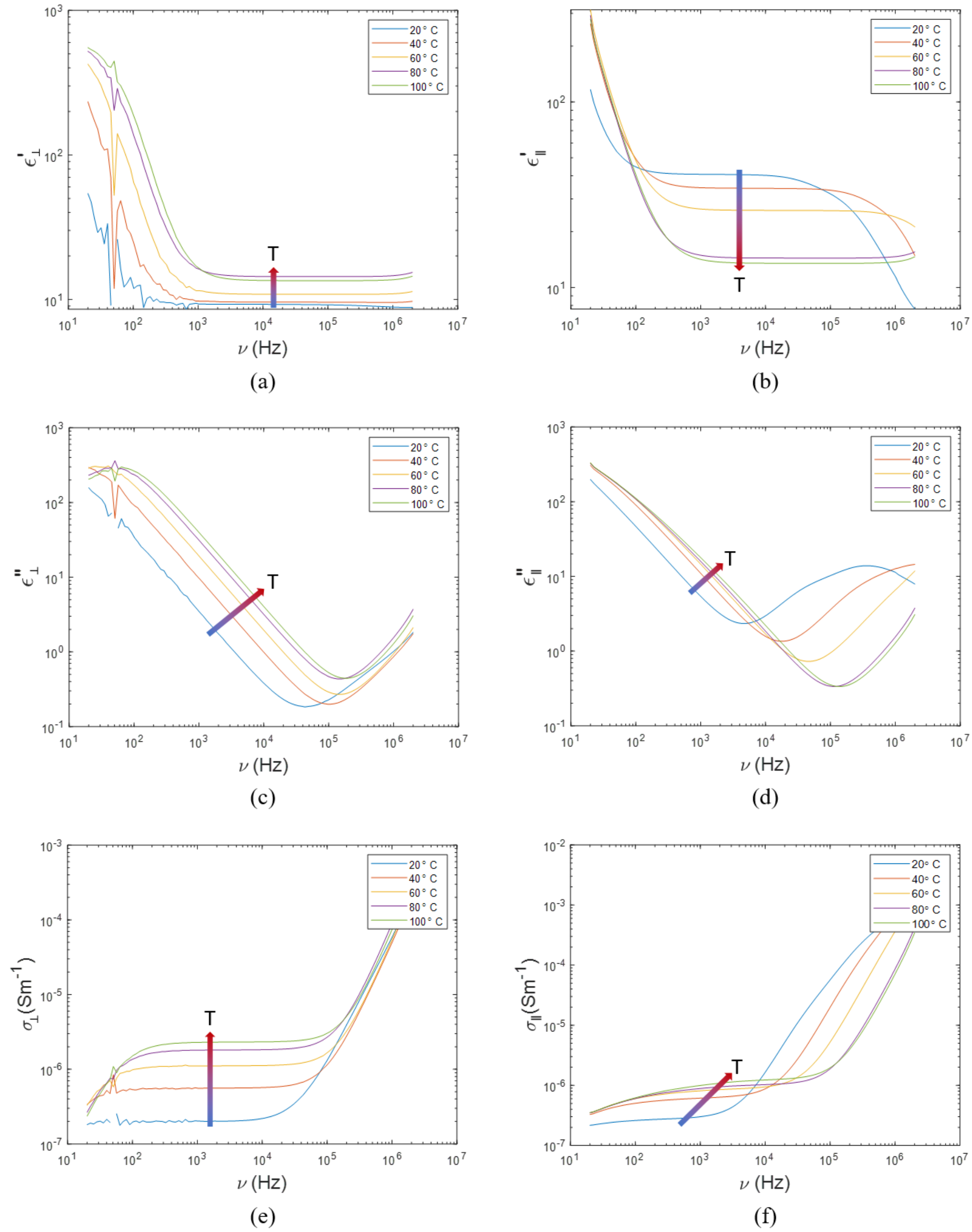

(a) (b)

(c) (d)

(e) (f)

Figure B.2: Dielectric spectroscopy frequency response of pure $0.1wt\%$LCQD nanocomposite in MLC6204. Real permittivity a) perpendicular and b) parallel to **n**, imaginary permittivity c) perpendicular and d) parallel to **n**, real conductivity e) perpendicular and f) parallel to **n**. $\epsilon_\perp$, $\sigma_\perp$ measured at $V = 0.05V_{rms}$ and $\epsilon_\parallel$, $\sigma_\parallel$ measured at $V = 20V_{rms}$ in a $20\mu m$ PH cell.

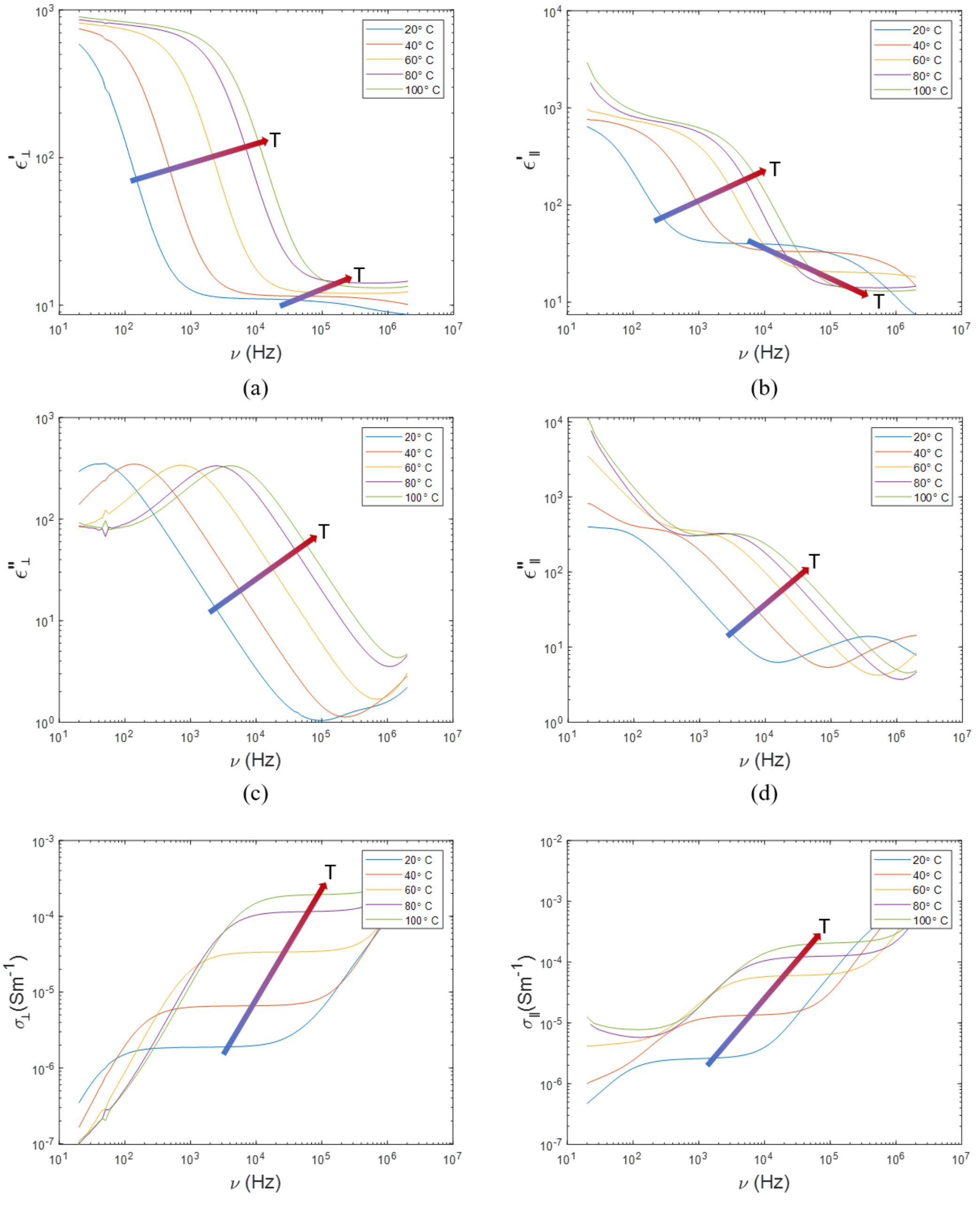

(a) (b) (c) (d) (e) (f)

Figure B.3: Dielectric spectroscopy frequency response of 0.1wt%ODA$_{530}$QD nanocomposite in MLC6204. Real permittivity a) perpendicular and b) parallel to **n**, imaginary permittivity c) perpendicular and d) parallel to **n**, real conductivity e) perpendicular and f) parallel to **n**. $\epsilon_\perp$, $\sigma_\perp$ measured at $V = 0.05V_{rms}$ and $\epsilon_\parallel$, $\sigma_\parallel$ measured at $V = 20V_{rms}$ in a $20\mu m$ PH cell.

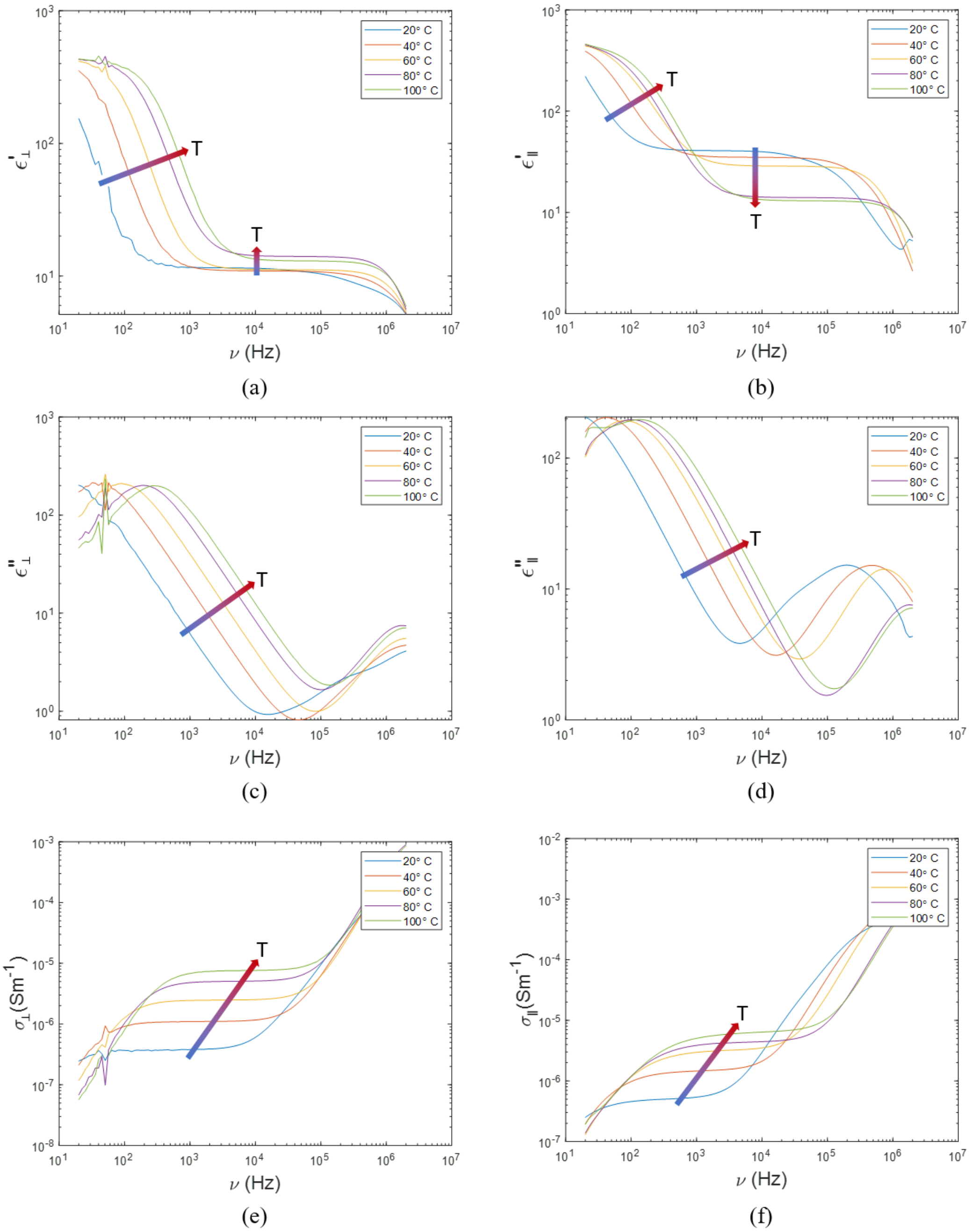

(a) (b)

(c) (d)

(e) (f)

Figure B.4: Dielectric spectroscopy frequency response of 0.1wt%ODA$_{650}$QD nanocomposite in MLC6204. Real permittivity a) perpendicular and b) parallel to **n**, imaginary permittivity c) perpendicular and d) parallel to **n**, real conductivity e) perpendicular and f) parallel to **n**. $\epsilon_{\perp}$, $\sigma_{\perp}$ measured at $V = 0.05V_{rms}$ and $\epsilon_{\parallel}$, $\sigma_{\parallel}$ measured at $V = 20V_{rms}$ in a $20\mu m$ PH cell.

Appendix C

QD-LC Permittivity-Voltage Curves and Fitting

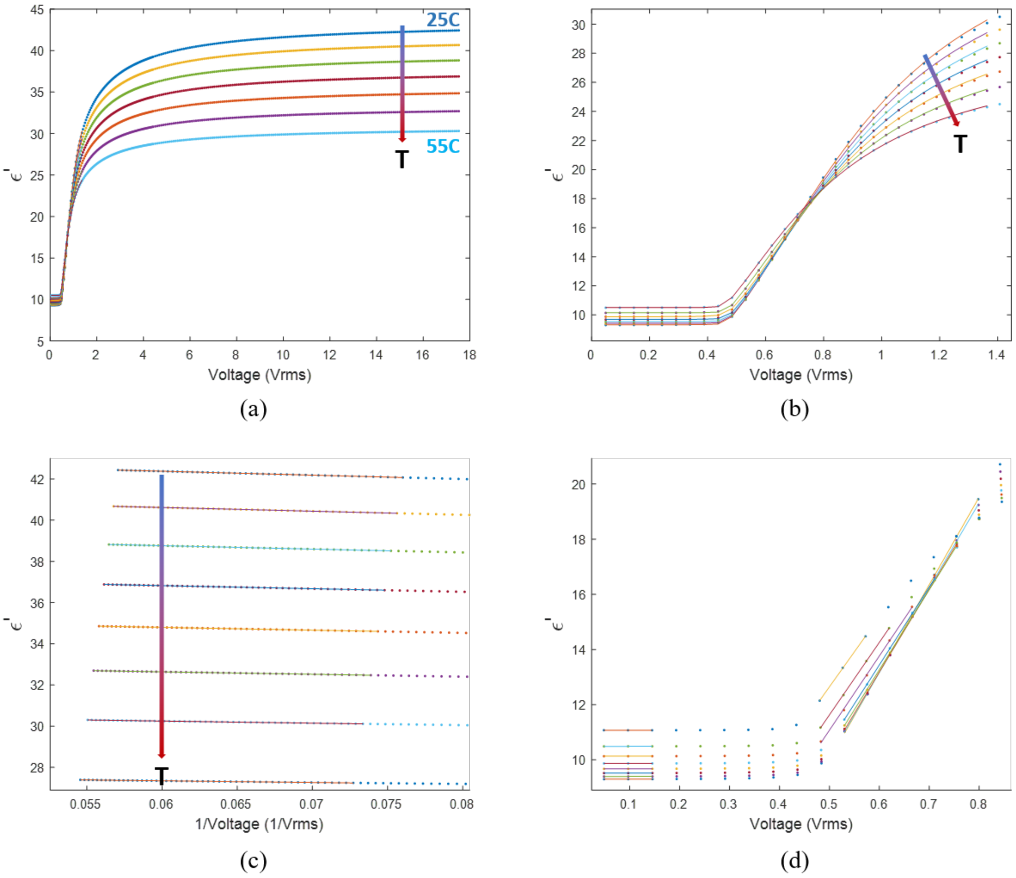

(a) (b) (c) (d)

Figure C.1: MLC6204 a) full $\epsilon(V)$ curves, b) WS fits, c) $1/V$ extrapolation and d) linear V_{th} fitting of $\epsilon(V)$ curves.

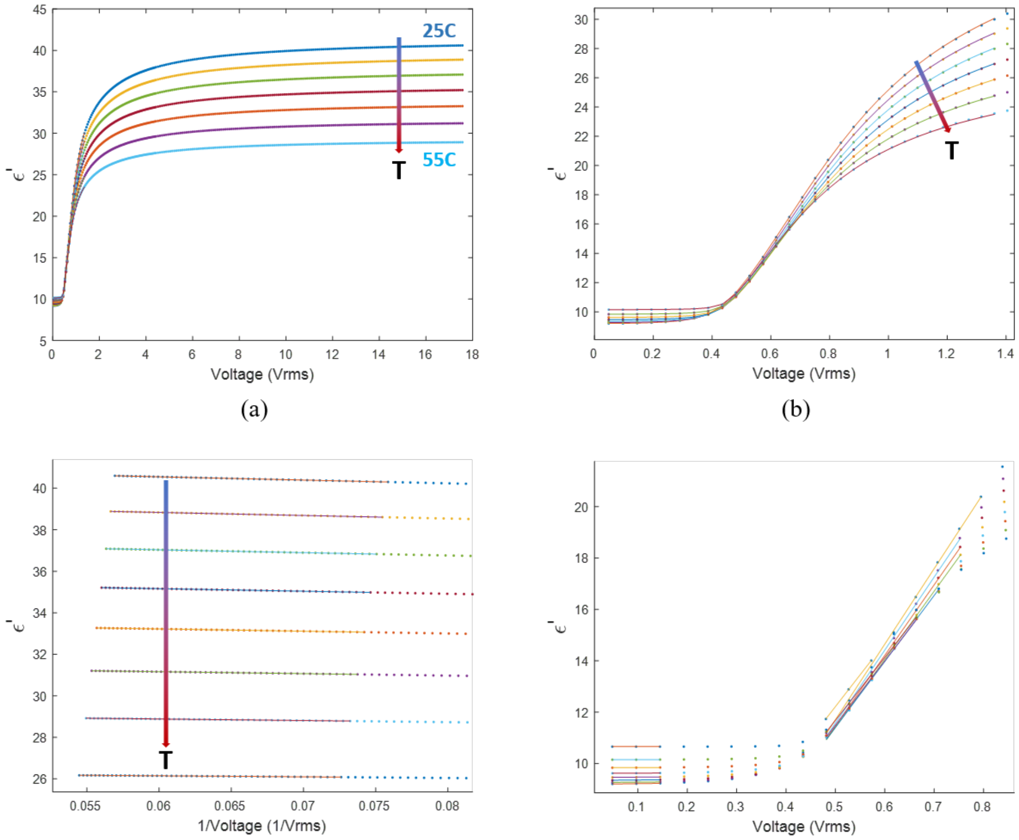

(a) (b)

(c) (d)

Figure C.2: 1wt%LCQD nanocomposite in MLC6204 a) full $\epsilon(V)$ curves, b) WS fits, c) $1/V$ extrapolation and d) linear V_{th} fitting of $\epsilon(V)$ curves.

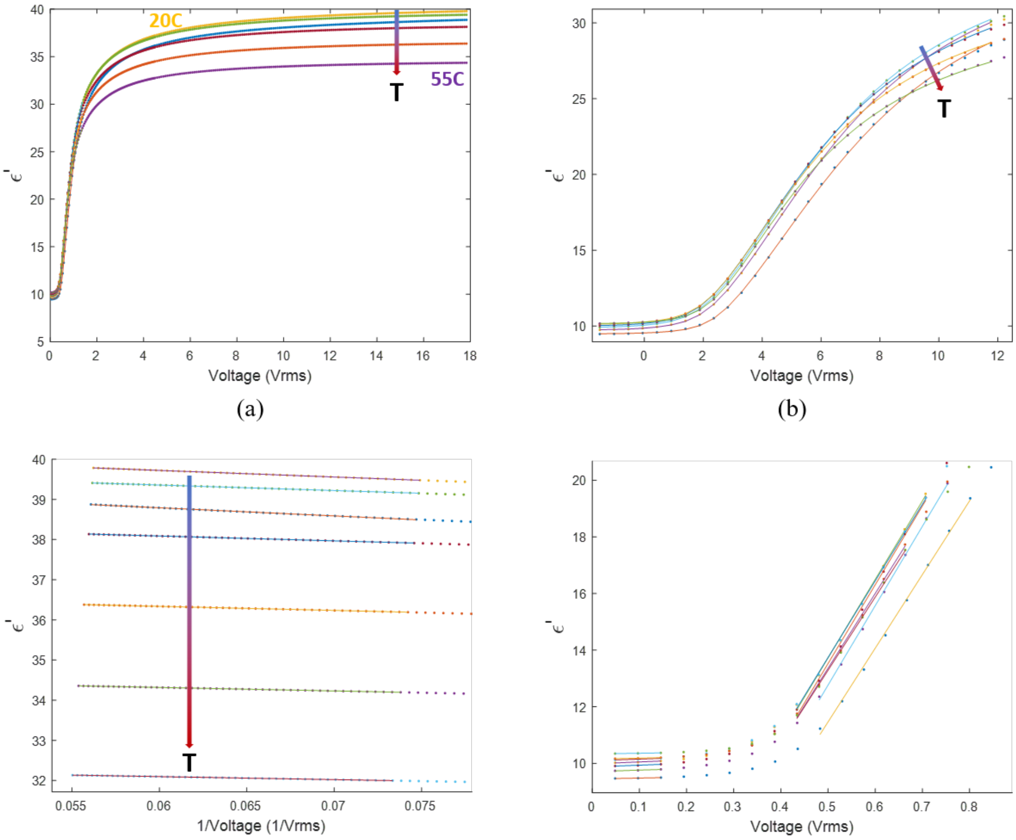

(a) (b)

(c) (d)

Figure C.3: 0.1wt%ODA$_{530}$QD nanocomposite in MLC6204 a) full $\epsilon(V)$ curves, b) WS fits, c) $1/V$ extrapolation and d) linear V_{th} fitting of $\epsilon(V)$ curves.

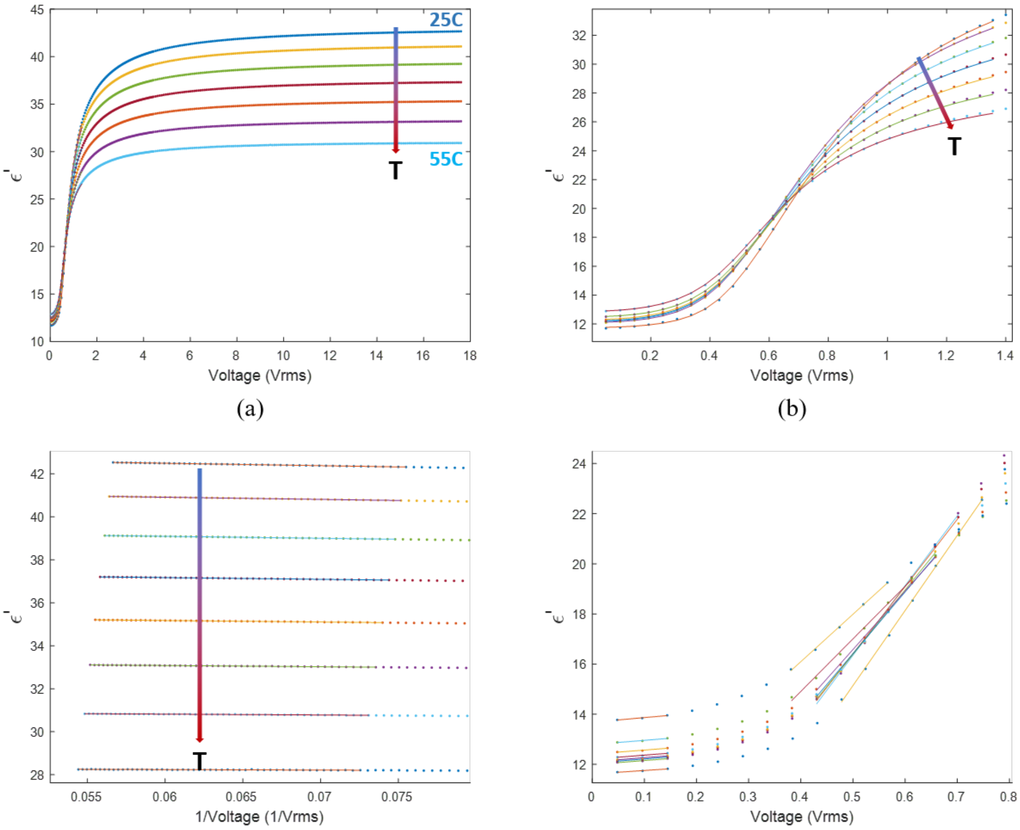

(a) (b)

(c) (d)

Figure C.4: 0.1wt%ODA$_{650}$QD nanocomposite in MLC6204 a) full $\epsilon(V)$ curves, b) WS fits, c) $1/V$ extrapolation and d) linear V_{th} fitting of $\epsilon(V)$ curves.